

---

# **EXPERIMENTAL INVESTIGATIONS, MODELING, AND ANALYSES OF HIGH-TEMPERATURE DEVICES FOR SPACE APPLICATIONS**

## **Part 1 of 2**

**Jean-Michel Tournier  
Mohamed S. El-Genk  
Lianmin Huang**

**Institute for Space and Nuclear Power Studies  
Department of Chemical and Nuclear Engineering  
University of New Mexico  
Farris Engineering Center, Room 239  
Albuquerque, NM 87131**

**January 1999**

**Final Report**

**19990817 085**

**APPROVED FOR PUBLIC RELEASE; DISTRIBUTION IS UNLIMITED.**



**AIR FORCE RESEARCH LABORATORY  
Space Vehicles Directorate  
3550 Aberdeen Ave SE  
AIR FORCE MATERIEL COMMAND  
KIRTLAND AIR FORCE BASE, NM 87117-5776**


Using Government drawings, specifications, or other data included in this document for any purpose other than Government procurement does not in any way obligate the U.S. Government. The fact that the Government formulated or supplied the drawings, specifications, or other data, does not license the holder or any other person or corporation; or convey any rights or permission to manufacture, use, or sell any patented invention that may relate to them.

This report has been reviewed by the Public Affairs Office and is releasable to the National Technical Information Service (NTIS). At NTIS, it will be available to the general public, including foreign nationals.


If you change your address, wish to be removed from this mailing list, or your organization no longer employs the addressee, please notify AFRL/VSDV, 3550 Aberdeen Ave SE, Kirtland AFB, NM 87117-5776.

Do not return copies of this report unless contractual obligations or notice on a specific document requires its return.

This report has been approved for publication.

  
Clay S. Mayberry  
Project Manager

FOR THE COMMANDER

  
CHRISTOPHER N. BURNS, Lt Col, USAF  
Chief, Vehicles Technologies Branch

  
CHRISTINE M. ANDERSON, SES  
Director, Space Vehicles

# REPORT DOCUMENTATION PAGE

Form Approved  
OMB No. 074-0188

Public reporting burden for this collection of information is estimated to average 1 hour per response, including the time for reviewing instructions, searching existing data sources, gathering and maintaining the data needed, and completing and reviewing this collection of information. Send comments regarding this burden estimate or any other aspect of this collection of information, including suggestions for reducing this burden to Washington Headquarters Services, Directorate for Information Operations and Reports, 1215 Jefferson Davis Highway, Suite 1204, Arlington, VA 22202-4302, and to the Office of Management and Budget, Paperwork Reduction Project (0704-0188), Washington, DC 20503

1. AGENCY USE ONLY (Leave blank)		2. REPORT DATE January 1999		3. REPORT TYPE AND DATES COVERED Final; June 1996 - December 1998	
4. TITLE AND SUBTITLE Experimental Investigations, Modeling, and Analyses of High-Temperature Devices for Space Applications				5. FUNDING NUMBERS C: F29601-97-K-0123 PE: 63401F PR: 682J TA: TG WU: 18	
6. AUTHOR(S) Jean-Michel Tournier Mohamed S. El-Genk Lianmin Huang					
7. PERFORMING ORGANIZATION NAME(S) AND ADDRESS(ES) University of New Mexico Institute for Space and Nuclear Power Studies Department of Chemical and Nuclear Engineering Farris Engineering Center Rm 239 Albuquerque, New Mexico 87131				8. PERFORMING ORGANIZATION REPORT NUMBER	
9. SPONSORING / MONITORING AGENCY NAME(S) AND ADDRESS(ES) Air Force Research Laboratory 3550 Aberdeen Ave. SE Kirtland AFB, NM 87117-5776				10. SPONSORING / MONITORING AGENCY REPORT NUMBER AFRL-VS-PS-TR-1998-1108, Part 1 of 2	
11. SUPPLEMENTARY NOTES					
12a. DISTRIBUTION / AVAILABILITY STATEMENT Approved for public release; distribution is unlimited				12b. DISTRIBUTION CODE	
13. ABSTRACT (Maximum 200 Words) The Institute of Space and Nuclear Power Studies at the University of New Mexico has developed a computer simulation of cylindrical geometry alkali metal thermal-to-electric converter cells using a standard Fortran 77 computer code. The objective and use of this code was to compare the experimental measurements with computer simulations, upgrade the model as appropriate, and conduct investigations of various methods to improve the design and performance of the devices for improved efficiency, durability, and longer operational life-time. The Institute of Space and Nuclear Power Studies participated in vacuum testing of PX series alkali metal thermal-to-electric converter cells and developed the alkali metal thermal-to-electric converter Performance Evaluation and Analysis Model. This computer model consisted of a sodium pressure loss model, a cell electrochemical and electric model, and a radiation/conduction heat transfer model. The code closely predicted the operation and performance of a wide variety of PX series cells which led to suggestions for improvements to both lifetime and performance. The code provides valuable insight into the operation of the cell, predicts parameters of components within the cell, and is a useful tool for predicting both the transient and steady state performance of systems of cells.					
14. SUBJECT TERMS AMTEC, Solar Thermal AMTEC, APEAM, AMTEC System, computer modeling, Spacecraft Power, Advanced Solar, Radioisotope Power Source				15. NUMBER OF PAGES 244	
				16. PRICE CODE	
17. SECURITY CLASSIFICATION OF REPORT Unclassified	18. SECURITY CLASSIFICATION OF THIS PAGE Unclassified	19. SECURITY CLASSIFICATION OF ABSTRACT Unclassified	20. LIMITATION OF ABSTRACT UL		

NSN 7540-01-280-5500

Standard Form 298 (Rev. 2-89)  
Prescribed by ANSI Std. Z39-18  
298-102





## TABLE OF CONTENT

	Page
<b>LIST OF FIGURES</b>	<b>XII</b>
<b>LIST OF TABLES</b>	<b>XX</b>
<b>ACKNOWLEDGMENTS</b>	<b>XXI</b>
<b>EXECUTIVE SUMMARY</b>	<b>XXII</b>
<b>1. INTRODUCTION</b>	<b>1</b>
<b>2. BACKGROUND</b>	<b>4</b>
2.1 NOMENCLATURE	4
2.2 TYPES of AMTEC CELLS and OPERATION PRINCIPLE	6
2.3 DESCRIPTION of PX-TYPE, VAPOR ANODE, MULTI-TUBE AMTEC CELLS	8
2.4 THERMODYNAMIC CYCLE and EFFICIENCY of an IDEAL AMTEC CYCLE	12
2.5 EFFECT of PRESSURE LOSSES on EFFICIENCY of an IDEAL AMTEC CYCLE	15
2.6 AMTEC CELL VOLTAGE and INTERNAL ELECTRICAL LOSSES	17
2.6.1 AMTEC Cell Voltage, and Concentration and Charge-Exchange Polarization Losses	17
2.6.2 Other Internal Electric Losses in an AMTEC	20
2.6.3 Electrical Efficiency of an AMTEC	20
2.7 PARASITIC RADIATION LOSSES in an AMTEC CELL	21
2.7.1 Thermal Efficiency of an AMTEC Cell with Radiation Parasitic Losses	23
2.7.2 Overall Efficiency of AMTEC Cell with Internal Electrical and Heat Losses	23
2.8 JOULE and THERMAL CONDUCTION LOSSES in CURRENT LEADS to LOAD	25
2.9 SERIES-CONNECTION of MULTI-TUBES in AMTEC CELL	28
2.10 EFFECTS of CHARGE-EXCHANGE POLARIZATION LOSSES in AMTEC CELL	30
2.11 BENCHMARK of ELECTROCHEMICAL MODEL USING EXPERIMENTAL I-V CHARACTERISTICS	32
2.12 SUMMARY	35
2.13 AMTEC PERFORMANCE AND EVALUATION ANALYSIS MODEL (APEAM)	38

2.13.1 Sodium Vapor Pressure Loss Model	39
2.13.2 Cell Electrochemical and Electric Model	40
2.13.3 Radiation/Conduction Heat Transfer Model	40
2.13.4 Method of Solution	40
<b>3. SODIUM VAPOR PRESSURE LOSSES IN A MULTI-TUBE AMTEC CELL</b>	<b>42</b>
3.1 NOMENCLATURE	42
3.2 INTRODUCTION	44
3.3 MODEL DESCRIPTION	48
3.3.1 Pressure Drop Caused by Evaporation of Sodium at BASE Surface	49
3.3.2 Pressure Drop in the Porous Electrode (Cathode)	49
3.3.3 Pressure Drop along the Base Tubes	51
3.3.4 Pressure Loss Caused by Sudden Expansion at Top of Base Tubes	54
3.3.5 Pressure Loss in Annulus Above Base Tubes	55
3.3.6 Pressure Loss Caused by Vapor Flow through Chevron's Shield	57
3.3.7 Pressure Loss in the Annulus above Chevron's Shield	61
3.3.8 Pressure Loss Caused by Condensation of Sodium	61
3.4 RESULTS AND DISCUSSION	62
3.4.1 Vapor Pressure Losses in a Vapor Anode, Multi-Tube AMTEC Cell	62
3.4.2 Optimization of Conical Chevron's shield in Multi-Tube AMTEC Cell	68
Conical Chevrons in Minimum Configuration ( $\alpha=0$ )	68
Crowded Chevrons' Configuration ( $\alpha > 0$ )	70
Pressure Losses through Separated Conical Chevrons	72
3.5 SUMMARY AND CONCLUSIONS	75
<b>4. AN ELECTRIC MODEL OF VAPOR ANODE, MULTI-TUBE AMTEC CELLS</b>	<b>77</b>
4.1 NOMENCLATURE	77
4.2 MODEL DESCRIPTION	80
4.2.1 Open-Circuit Voltage and Polarization Losses	80
4.2.2 BASE Ionic Resistance	84
4.2.3 Current Collector Losses	84
Ring Wires in Contact with Axial Bus	85
Metal Sponge in Contact with Axial Bus	87
Screen Mesh in Contact with Axial Bus	88
Wrapped Helical Wire	88
4.2.4 Calculation of Electric Current and Voltage	89
4.2.5 Equivalent External Load Resistance	90
4.3 RESULTS AND DISCUSSION	92
4.3.1 Sodium Vapor Pressure and Current Density in PX-3G	95
4.3.2 Effect of Internal Ohmic Losses	97
4.3.3 Effect of Leakage Losses	97
4.3.4 Effect of Concentration and Charge-Exchange Polarization Losses	97

<b>4.4 SUMMARY AND CONCLUSION</b>	<b>100</b>
<b>5. RADIATION/CONDUCTION HEAT TRANSFER MODEL OF PX-SERIES CELLS</b>	<b>103</b>
5.1 NOMENCLATURE	103
5.2 INTRODUCTION	104
5.3 MODEL DESCRIPTION	107
5.3.1 Modeling of Radiation Heat Transfer	108
Configuration Factors between Two Black Surfaces of Finite Areas	108
5.3.2 Radiation View Factors in Vapor-Anode, Multi-Tube, AMTEC Cells	110
5.3.3 Circumferential Radiation Heat Shield in AMTEC Cell	117
5.3.4 Conduction Stud in Hot Plenum of AMTEC Cell	117
5.3.5 Radiation Exchange between Diffuse-Gray Surfaces	118
5.3.6 Radiant Energy Balance in Enclosure	120
5.3.7 Energy Balance for Solid Elements of the AMTEC Cell	121
5.4 METHOD OF SOLUTION IN APEAM	125
5.4.1 Sodium Vapor Pressure Loss Model	125
5.4.2 Cell Electrochemical and Electric Model	125
5.4.3 Radiation/Conduction Heat Transfer Model	126
5.4.4 Method of Solution	126
5.5 PREDICTION OF THERMAL AND PERFORMANCE DATA OF PX-4C, PX-5A AND PX-3A CELLS	128
5.5.1 Heat Transfer and Temperatures in PX-4C Cell	131
5.5.2 Heat Transfer and Temperatures in PX-5A Cell	133
5.5.3 Heat Transfer and Temperatures in PX-3A Cell	133
5.6 SUMMARY AND CONCLUSIONS	135
<b>6. PRESSURE LOSSES AND CAPILLARY LIMIT IN LIQUID-RETURN ARTERY OF PX-SERIES, MULTI-TUBE AMTEC CELL</b>	<b>137</b>
6.1 NOMENCLATURE	137
6.2 INTRODUCTION	138
6.3 MODEL DESCRIPTION	140
6.4 RESULTS AND DISCUSSION	143
6.4.1 Wick Capillary Limit	146
6.4.2 Composite Liquid-Sodium Return Wick	148
6.5 SUMMARY AND CONCLUSIONS	151
<b>MEASUREMENTS OF THERMAL CONDUCTIVITIES OF ALUMINA POWDERS AND MIN-K IN VACUUM</b>	<b>152</b>

<b>7.1</b>	<b>NOMENCLATURE</b>	<b>152</b>
<b>7.2</b>	<b>INTRODUCTION</b>	<b>152</b>
<b>7.3</b>	<b>EXPERIMENTAL SETUP</b>	<b>154</b>
7.3.1	Setup of Alumina Powder Experiments	155
7.3.2	Setup of Molded Min-K Experiments	157
<b>7.4</b>	<b>EXPERIMENTAL RESULTS AND ANALYSIS</b>	<b>157</b>
7.4.1	Determination of Material Thermal Conductivity	158
7.4.2	Thermal Conductivity Values and Correlations	160
7.4.3	Comparison of Conductances of Min-K and Multi-Foils	161
<b>7.5</b>	<b>SUMMARY AND CONCLUSIONS</b>	<b>162</b>
<b>8.</b>	<b>EXPERIMENTAL SETUP AND PROCEDURES</b>	<b>165</b>
<b>8.1</b>	<b>NOMENCLATURE</b>	<b>165</b>
<b>8.2</b>	<b>SINGLE-CELL TEST SETUP</b>	<b>165</b>
<b>8.3</b>	<b>VACUUM SYSTEM</b>	<b>170</b>
<b>8.4</b>	<b>COOLING SYSTEM</b>	<b>176</b>
<b>8.5</b>	<b>CELL ELECTRIC CIRCUIT</b>	<b>176</b>
<b>8.6</b>	<b>DATA ACQUISITION SYSTEM AND WATCH DOG</b>	<b>178</b>
<b>8.7</b>	<b>EXPERIMENTAL METHODOLOGY</b>	<b>182</b>
<b>8.8</b>	<b>EXPERIMENTAL PROCEDURES</b>	<b>185</b>
8.8.1	Test setup Assembly	185
8.8.2	Data Acquisition System and Power Supply	186
8.8.3	Initialization of Tests	187
8.8.5	Ending of Test	187
8.8.6	Response to "Watch Dog" Warning	187
<b>8.9</b>	<b>PARTICULARITIES OF SINGLE-CELL EXPERIMENTAL SETUPS</b>	<b>189</b>
8.9.1	Design of PX-1A Cell Experimental Setup	189
8.9.2	Design of PX-1B and PX-1C Cell Experimental Setups	191
8.9.3	Experimental Setup for PX-2A and PX-2C Cells with Molded Min-K Insulation	191
8.9.4	Experimental Setup for PX-4 and PX-5 Series Cells	192
8.9.5	Experimental Setup for PX-3 Series Cells	194
<b>8.10</b>	<b>MULTI-CELL GROUND DEMO EXPERIMENTAL SETUP</b>	<b>194</b>
<b>9.</b>	<b>EXPERIMENTAL UNCERTAINTIES IN VACUUM TESTS OF PX-SERIES CELLS</b>	<b>202</b>
<b>9.1</b>	<b>NOMENCLATURE</b>	<b>202</b>

9.2	VACUUM TEST APPARATUS AT AFRL	203
9.3	UNCERTAINTIES IN VACUUM TESTS OF PX-CELLS	205
9.4	FIN MODEL OF TC GUIDE TUBES IN THE BASE AND EVAPORATOR CAVITIES	206
9.5	COMPARISON OF FIN MODEL WITH EXPERIMENTAL MEASUREMENTS	214
9.6	EFFECT OF THERMOCOUPLE PLACEMENT	216
9.7	SUMMARY AND CONCLUSIONS	216
10.	EVALUATION OF HEAT LOSSES IN PX-SERIES CELL TESTS	219
10.1	BORO-ELECTRIC HEATER RESISTIVITY CALIBRATION EXPERIMENT	220
10.2	HEAT CONDUCTION MODEL FOR PREDICTING INSULATION LOSSES	224
10.2.1	NOMENCLATURE	225
10.2.2	GOVERNING EQUATIONS AND BOUNDARY CONDITIONS	228
10.2.3	THERMOPHYSICAL PROPERTIES	229
10.2.4	DISCRETIZATION OF GOVERNING EQUATIONS	230
10.2.5	SOLUTION PROCEDURE	233
10.3	HEAT CONDUCTION MODEL BENCHMARK	237
10.4	HEAT LOSSES IN ALUMINA POWDER INSULATION OF PX-1 CELLS	243
10.5	HEATER CALORIMETER EXPERIMENT TO EVALUATE HOT SIDE LOSSES	252
10.6	SUMMARY AND CONCLUSION	257
11.	SINGLE-CELL TEST RESULTS AND PERFORMANCE DATA ANALYSIS	260
11.1	NOMENCLATURE	260
11.2	CELLS DESIGNS, OPERATING CONDITIONS AND PERFORMANCE DATA	262
11.3	PX-1A CELL DATA ANALYSIS	267
11.3.1	Liquid-Return Artery Capillary Limit	267
11.3.2	Effective Thermal Conductivity of Sintered Metal Wick and Conduction Losses along the Artery	268
11.3.3	Heat Balance in the PX-1A Cell	271
11.3.4	Heat Flow to the Evaporator End of the Artery	276
11.4	PX-2C CELL DATA ANALYSIS	277
11.4.1	Local Sodium Pressure in PX-2C	278
11.4.2	PX-2C Cell Electrical Power	279
11.4.3	PX-2C Cell I-V Characteristic	281
11.4.4	Load-Following Characteristic of PX-2C Cell	281
11.4.5	Effects of Internal Radiation Shields	281
11.4.6	Vapor Pressure Losses in PX-2C Cell	285

11.4.7 Electrode Current Density in PX-2C	287
11.4.8 BASE Tubes Temperature in PX-2C	287
11.4.9 Evaporator Temperature and Temperature Margin in PX-2C	289
11.4.10 PX-2C: Summary and Conclusion	289
<b>11.5 PX-4C CELL DATA ANALYSIS</b>	<b>291</b>
<b>11.6 PX-5A CELL DATA ANALYSIS</b>	<b>296</b>
<b>11.7 PX-4C AND PX-5A CELLS: THE VALUE OF BASE AND EVAPORATOR TEMPERATURE MEASUREMENTS</b>	<b>296</b>
11.7.1 Effect of Electrode Characteristics	296
11.7.2 Effect of Increased Pressure Losses on the Cathode Side	297
11.7.3 Electronic Leakage Between Electrodes and BASE Tubes Support Plate	298
11.7.4 Heat Transfer in Evaporator and BASE Tube Thermocouple Wells	298
<b>11.8 REVISED ANALYSIS OF PX-4C CELL DATA</b>	<b>299</b>
<b>11.9 REVISED ANALYSIS OF PX-5A CELL DATA</b>	<b>307</b>
<b>11.10 PX-3A CELL DATA ANALYSIS</b>	<b>307</b>
<b>11.11 EFFECT OF DESIGN CHANGES ON PERFORMANCE OF PX-4C, PX-5A, AND PX-3A CELLS</b>	<b>311</b>
<b>11.12 PX-3C CELL DATA ANALYSIS</b>	<b>313</b>
<b>11.13 SUMMARY AND CONCLUSIONS</b>	<b>316</b>
<b>12. ANALYSIS OF TEST RESULTS OF 8-CELL PX-GENERATOR GROUND</b>	<b>318</b>
12.1 NOMENCLATURE	318
12.2 A MULTI-CELL GENERATOR FOR THE PLUTO/EXPRESS MISSION	319
12.3 DESCRIPTION OF PX-3G CELLS	319
12.4 DESCRIPTION OF 8-CELL GROUND DEMO	323
12.5 RESULTS AND ANALYSES	323
12.6 SUMMARY AND CONCLUSIONS	331
<b>13. PERFORMANCE ANALYSES OF PLUTO/EXPRESS, MULTI-TUBE CELLS</b>	<b>334</b>
13.1 NOMENCLATURE	334
13.2 PARAMETRIC ANALYSIS AND DESIGN RECOMMENDATIONS	335
13.2.1 Effect of Heat Losses through the Cell Wall	335
13.2.2 Effect of Condenser Design	338

13.2.3 Effect of Number of BASE Tubes and Length of Electrodes	338
13.2.4 Effect of Electrode Material	343
13.2.5 Effect of Hot-Side Structural Material and High-Reflectivity Coatings	343
13.2.6 Improved Performance Parameters of an Adiabatic, PX-Series Cell	345
<b>13.3 SUMMARY AND CONCLUSIONS</b>	<b>347</b>
<b>14. ANALYSIS OF RADIOISOTOPE POWER SYSTEMS USING IMPROVED CELLS</b>	<b>351</b>
14.1 NOMENCLATURE	351
14.2 INTRODUCTION	352
14.3 DESCRIPTION OF PX-3G CELLS	352
14.4 IMPROVED PX-3G CELL DESIGN	353
14.5 MULTI-CELL POWER SYSTEMS INTEGRATION ANALYSIS	357
14.6 SUMMARY AND CONCLUSIONS	362
<b>15. SUPER-ALLOY, AMTEC CELLS FOR THE PLUTO/EXPRESS MISSION</b>	<b>364</b>
15.1 NOMENCLATURE	364
15.2 INTRODUCTION	365
15.3 VALIDATION OF APEAM WITH PX-3G GROUND DEMO DATA	370
15.4 IMPROVED DESIGN OF PX-3G TYPE CELL	371
15.5 ANALYSIS AND DISCUSSION	376
15.5.1 Effect of Condenser Temperature	376
15.5.2 PX-Power Systems Integration Options	378
15.5.3 Effect of Cell Length on Generator Specific Power	386
15.6 SUMMARY AND CONCLUSIONS	386
<b>16. SUMMARY AND CONCLUSIONS</b>	<b>390</b>
<b>REFERENCES</b>	<b>400</b>
<b>APPENDIX A: SODIUM VAPOR FLOW PROPERTIES AND CHARACTERISTICS</b>	<b>409</b>
A.1 DYNAMIC VISCOSITY OF SODIUM VAPOR	409
A.2 MEAN FREE PATH AND KNUDSEN NUMBER OF SODIUM VAPOR	409

<b>A.3</b>	<b>REYNOLDS NUMBER OF SODIUM VAPOR FLOW</b>	<b>410</b>
<b>A.4</b>	<b>MACH NUMBER OF SODIUM VAPOR FLOW</b>	<b>411</b>
<b>APPENDIX B:</b>	<b>FLOW CONDUCTANCES IN THE FREE-MOLECULAR</b>	
	<b>VAPOR FLOW REGIME</b>	<b>412</b>
<b>B.1</b>	<b>CONDUCTANCE OF A LONG CHANNEL AT LOW PRESSURE</b>	<b>412</b>
<b>B.2</b>	<b>CONDUCTANCE OF AN APERTURE AT LOW PRESSURE</b>	<b>412</b>
<b>B.3</b>	<b>CONDUCTANCE OF A CHANNEL AT LOW PRESSURE, CORRECTED</b>	
	<b>FOR END EFFECTS</b>	<b>413</b>
<b>APPENDIX C:</b>	<b>RADIATION VIEW FACTORS IN PX MULTI-TUBE AMTEC CELL</b>	<b>417</b>
<b>C.1</b>	<b>ELEMENTARY RADIATION VIEW FACTORS</b>	<b>417</b>
C.1.1.	View Factor between Inside Surface of Right Cylinder and itself (C-37, Howell 1982)	417
C.1.2.	View Factor between Inside Surface of Right Cylinder and Base Disk	417
C.1.3	View Factor between Finite Section of Right Cylinder and another Separated Section (C-82, Howell 1982)	418
C.1.4.	View Factor between Finite Section of Right Cylinder and Separated Base Ring (C-80, Howell 1982)	419
C.1.5.	View Factor between Disk and Coaxial Parallel Ring (C-44, Howell 1982)	420
C.1.6.	View Factor between Interior Surface of Outer Coaxial Cylinder and itself (Sparrow and Cess 1970, Appendix A)	421
C.1.7.	View Factor between Interior Surface of Outer Coaxial Cylinder and Exterior Surface of Inner Coaxial Cylinder (Sparrow and Cess 1970, Appendix A)	422
C.1.8.	View Factor between Interior Surface of Outer Coaxial Cylinder and Annular Base of Coaxial Enclosure	422
C.1.9.	View Factor between Exterior Surface of Inner Coaxial Cylinder and Annular End between Coaxial Cylinders	422
C.1.10.	View Factor between Annular Base of Coaxial Cylindrical Enclosure and Opposit Annular End	423
C.1.11.	View Factor between Ring on Base of Coaxial Cylindrical Enclosure and Inner Surface of Outer Cylinder	423
C.1.12.	View Factor between Ring on Base of Coaxial Cylindrical Enclosure and Separated Inner Shell of Outer Cylinder	424
C.1.13.	View Factor between Outer Surface of Cylinder and Annular Disk at End of Cylinder (Rea 1975)	426
C.1.14.	View Factor between Outer Surface of Cylinder and Coaxial Annular Disk Separated from Cylinder	426
C.1.15.	View Factor between Ring on Base of Coaxial Cylindrical Enclosure and Outer Surface of Inner Cylinder	427
C.1.16.	View Factor between Ring on Base of Coaxial Cylindrical Enclosure and Opposit Annular End between Cylinders	427
C.1.17.	View Factor between Outer Surface of Inner Cylinder and Separated Inner Section of Outer Cylinder (Rea 1975)	428
C.1.18.	View Factor between Interior Shell of Outer Coaxial Cylinder and Another Interior Shell of Different Length (Reid and Tennant 1973)	429
C.1.19.	View Factors between Two Infinitely-Long Parallel and Opposed Cylinders of Unequal Radii	430
C.1.20.	View Factor between Two Infinitely-Long Parallel and Opposed Cylinders of Identical Radii Partially Obstructed by Another Parallel Cylinder of Different Radius	433



C.1.21. View Factor between Two Parallel and Opposed Cylinders of Unequal Radii and Equal Length (Juul 1982)	435
C.1.22. View Factor between Two Parallel Cylindrical Sections at Different Levels and of Different Length	439
<b>C.2 CALCULATION OF RADIATION VIEW FACTORS IN PX-SERIES, MULTI-TUBE AMTEC CELLS</b>	<b>441</b>
C.2.1. Calculation of Radiation View Factors in the Hot Plenum Enclosure	441
C.2.2. Calculation of View Factors in a Coaxial Cylindrical Cavity with a Bottom End Constituted of Three Concentric Rings	444
C.2.3. Calculation of View Factors in the Evaporator Standoff / $\beta$ -Tubes Bundle Cavity	445
C.2.4. Radiative Coupling between $\beta$ -Tubes Bundle Cavity and Artery Annular Cavity Above	454
C.2.5. Inclusion of Side-Wall Circumferential Radiation Heat Shield in AMTEC Cell	460
C.2.6. Inclusion of Conduction Stud in Hot Plenum of AMTEC Cell	461
C.2.7. Conservation of Radiant Energy in AMTEC Cell	461
<b>APPENDIX D: THERMAL CONDUCTIVITY MEASUREMENT DATA AND PROCESSING</b>	<b>462</b>
<b>APPENDIX E: CALCULATION OF MEASUREMENT UNCERTAINTIES IN VACUUM TESTS OF PX-SERIES CELLS</b>	<b>474</b>
E.1 CELL ELECTRIC OUTPUT	475
E.2 HEATING POWER, $Q_{in}$	477
E.3 TEMPERATURE, T	478
E.4 HEAT REJECTION AT THE CELL CONDENSER, $Q_{air}$	479

## LIST OF FIGURES

	Page
Figure 2.1. A Schematic Diagram of Sodium AMTEC Operating Cycle Showing Microscopic Processes.....	7
Figure 2.2. Cross Section Views of Vapor Anode, Multi-Tube AMTEC Cell (Not to Scale). ....	9
Figure 2.3. Condenser wick types employed in PX-Series AMTEC Cells. ....	11
Figure 2.4. Pressure-Volume Thermodynamic Diagram of a Sodium AMTEC Cycle. ....	14
Figure 2.5. Temperature-Entropy Thermodynamic Diagram of a Sodium AMTEC Cycle. ....	14
Figure 2.6. Thermodynamic Efficiency of an Ideal Liquid-Anode Sodium AMTEC as a Fraction of Carnot Efficiency.....	16
Figure 2.7. Thermodynamic Efficiency of an Ideal Vapor-Anode Sodium AMTEC as a Fraction of Carnot Efficiency.....	16
Figure 2.8. Effect of Cathode Vapor Pressure Losses on the Efficiency of an Ideal Sodium AMTEC. ....	18
Figure 2.9. Electrical Efficiency of a Sodium AMTEC as a Function of BASE Ionic Resistance. ....	21
Figure 2.10. Thermal Efficiency of a Sodium AMTEC as a Function of Radiation Factor, $Z$ . ....	23
Figure 2.11. Conversion Efficiency and Power Density of a Sodium AMTEC with Zero Charge-Exchange Polarization Losses. ....	25
Figure 2.12. Dimensionless Temperature Profile along Conducting Lead.....	27
Figure 2.13. Dimensionless Joule Heating and End Heat Fluxes in Conducting Lead as a Function of Electrical Current. ....	27
Figure 2.14. Ratio of Joule Heating to Conduction Heat Loss in Conducting Lead as a Function of its Geometric Ratio.....	29
Figure 2.15. Sum of Joule Heating and Conduction Heat Loss in Conducting Lead as a Function of its Geometric Ratio.....	29
Figure 2.16. Effect of Charge-Exchange Polarization Losses on the Conversion Efficiency of a Sodium AMTEC. ....	31
Figure 2.17. Effect of Charge-Exchange Polarization Losses on the Power Density of a Sodium AMTEC. ....	31
Figure 2.18. I-V Characteristic of a Molybdenum Electrode with $G=47$ and Comparison with Experimental Data (Sievers and Bankston 1988). ....	33
Figure 2.19. I-V Characteristic of a Molybdenum Electrode with $G=42$ and Comparison with Experimental Data (Sievers and Bankston 1988). ....	33
Figure 2.20. Effect of BASE Temperature on I-V Characteristic of a 3 $\mu\text{m}$ -Thick NbN Electrode and Comparison with Experimental Data (Kato et al. 1992). ....	34
Figure 2.21. Cathode Polarization Losses of a Thin TiN Electrode and Comparison with Experimental Data (Kato et al. 1993). ....	34
Figure 2.22. I-V Characteristic of a Thin TiN Electrode with $G=0$ and Comparison with Experimental Data (Kato et al. 1993). ....	36
Figure 2.23. I-V Characteristic of a Thin TiN Electrode with $G=5$ and Comparison with Experimental Data (Kato et al. 1993). ....	36
Figure 3.1. A Schematic of a Vapor Anode, Multi-Tube, AMTEC Cell (Not To Scale). ....	46
Figure 3.2. Resistance Coefficient $\xi$ for Sudden Expansion, as a Function of Area Ratio. ....	55

Figure 3.3.	Schematic of (Unseparated) Conical Chevrons Radiation Shield .....	58
Figure 3.4.	Calculated Vapor Pressure on Cathode Side of a Multi-Tube AMTEC Cell ( $I = 1.39$ A, $\dot{m}_z = 8.3$ gm/hr).....	63
Figure 3.5.	Effect of Chevron's Shield on AMTEC Cell Electrical Power Output, at Fixed Evaporator and BASE Tubes Temperatures ( $T_{cd} = 550$ K, $T_B = T_{ev} = 1050$ K). ....	65
Figure 3.6.	Sodium vapor Flow Characteristics in a Vapor Anode, Multi-Tube AMTEC cell with a Chevron's Shield ( $T_{cd} = 550$ K, $T_B = 1050$ K, 30 mm Shield Clearance, $I =$ $1.39$ A, $\dot{m}_z = 8.3$ gm/hr). (a) Vapor Temperature; (b) Knudsen Number, $Kn$ ; (c) Flow Diffusion Coefficients; (d) Mass Flow Rate, $\dot{m}_z$ ; (e) Reynolds Number, $Re$ ; (f) Mach Number, $Ma$ .....	67
Figure 3.7.	Effects of Chevrons' Angle $\theta$ and Number of Chevrons $N$ on the Viscous and Knudsen Flow Diffusion Coefficients ( $\alpha=0$ ).....	69
Figure 3.8.	Shield Flow Conductance $\chi$ and Chevrons' Height as a Function of Angle $\theta$ and Number of Chevrons $N$ ( $\alpha=0$ ).....	69
Figure 3.9.	Pressure Loss Through Unseparated Radiation Shield as a Function of Angle $\theta$ and Number of Chevrons $N$ ( $\alpha=0$ ).....	71
Figure 3.10.	Effects of Temperature and Number of Chevrons on the Pressure Loss Through Radiation Shield ( $\alpha=0$ , $\theta=60^\circ$ ).....	71
Figure 3.11.	Shield Flow Conductance, $\chi$ as a Function of Packing Factor $\alpha$ and Number of Chevrons $N$ ( $\theta=60^\circ$ ).....	73
Figure 3.12.	Calculated Pressure Loss Through Radiation Shield as a Function of Packing Factor $\alpha$ and Number of Chevrons $N$ ( $\theta=60^\circ$ ).....	73
Figure 3.13.	Pressure Loss Through Separated Chevron's Shield as a Function of Angle $\theta$ and Number of Chevrons, $N$ ( $\alpha=0$ ).....	74
Figure 3.14.	Effects of Temperature and Number of Chevrons, $N$ on the Pressure Loss Through Separated Chevron's Shield ( $\alpha=0$ , $\theta=62^\circ$ ).....	74
Figure 4.1.	Cross Sections of a PX-Series, Multi-Tube AMTEC Cell (Not to Scale).....	79
Figure 4.2.	Current Collector Designs in Vapor Anode, Multi-Tube AMTEC Cell.....	83
Figure 4.3.	Electric Circuit Model of BASE Tube's Current Collectors.....	86
Figure 4.4.	Electrons' Conduction Path in a Screen Mesh Current Collector.....	89
Figure 4.5.	Electrical Connection of BASE Tubes and External Load in PX-Series Cell.....	91
Figure 4.6.	Electric Circuit Model of BASE Tubes and External Load in PX-Series Cell.....	91
Figure 4.7.	Fraction of Electrical Loss Processes in PX-3G Cell.....	94
Figure 4.8.	Theoretical Nernst Power in PX-3G Cell.....	94
Figure 4.9.	Sodium Vapor Pressure on Low-Pressure Side of PX-3G Cell.....	96
Figure 4.10.	BASE Tubes' Temperature and Current Density in PX-3G Cell.....	96
Figure 4.11.	Effect of Contact Resistance on Performance of PX-3G Cell.....	98
Figure 4.12.	Effect of Braze Leakage Current on Performance of PX-3G Cell.....	99
Figure 4.13.	Effect of Charge-Exchange Coefficient, $B$ , on Performance of PX-3G Cell.....	101
Figure 5.1a.	A Schematic of Vapor Anode, Multi-Tube AMTEC Cell and Heat Transfer Processes (Not to Scale).....	105
Figure 5.1b.	A Schematic of Vapor Anode, Multi-Tube AMTEC Cell (Section A-A).....	106
Figure 5.2.	Geometry for Radiant Energy Exchange between Finite Areas.....	108

Figure 5.3.	Numerical Grid Layout of Multi-Tube AMTEC Cell, without Thermal Shield nor Conduction Stud.....	111
Figure 5.4.	Calculation of View Factor Between Infinitely-Long Parallel Cylinders Partially Obstructed by Another Parallel Cylinder, Using Hottel's Crossed-String Method; (a) No Obstruction; (b) Small, Partial Obstruction ( $\beta \leq \phi$ , $H \leq 1$ ); (c) Large, Partial Obstruction ( $\beta \geq \phi$ , $H \geq -1$ , $X > R + 1$ ) .....	114
Figure 5.5.	Radiant Energies Incident Upon and Leaving a Gray-Diffuse Surface. ....	119
Figure 5.6.	Schematic of APEAM Model's Architecture.....	128
Figure 5.7.	Predicted Heat Transfer and Temperatures in PX-4C AMTEC Cell, at the Peak Conversion Efficiency.....	130
Figure 5.8.	Predicted Heat Transfer and Temperatures in PX-5A AMTEC Cell, at the Peak Conversion Efficiency.....	132
Figure 5.9.	Predicted Heat Transfer and Temperatures in PX-3A AMTEC Cell, at the Peak Conversion Efficiency.....	134
Figure 6.1.	A Schematic of Vapor Anode, Multi-Tube AMTEC Cell (Not to Scale). ....	139
Figure 6.2.	Saturation Pressure of Liquid Sodium.....	141
Figure 6.3.	Surface Tension of Liquid Sodium.....	142
Figure 6.4.	Kinematic Viscosity of Liquid Sodium.....	142
Figure 6.5.	Pressure Loss as a Function of Wick Porosity and Average Pore Size. ....	144
Figure 6.6.	Calculated Wick Temperature Profile in PX-2C AMTEC Cell.....	144
Figure 6.7.	Wick Pressure Losses in PX-2C Cell.....	145
Figure 6.8.	A Line Diagram of the Local Pressure in PX-2C Cell ( $Q_{in} = 39$ W, $T_{cd} = 600$ K, $T_{ev} = 950$ K, $\dot{m} = 9$ gm/hr, $P_e = 4.5$ We). ....	145
Figure 6.9.	Minimum Wick Porosity at an Evaporator Temperature of 975 K. ....	147
Figure 6.10.	Minimum Wick Porosity at an Evaporator Temperature of 1025 K. ....	147
Figure 6.11.	Minimum Wick Porosity at a Sodium Flow Rate of 10 gm/hr. ....	149
Figure 6.12.	Maximum Pore Radius as a Function of Evaporator Temperature. ....	149
Figure 7.1.	Multi-Foil Insulation for a PX-Series AMTEC Cell (Shock et al. 1997b).....	154
Figure 7.2.	Test Section for Alumina Powder Thermal Conductivity.....	155
Figure 7.3.	Test Section for Min-K Thermal Conductivity Experiments. ....	156
Figure 7.4.	Measured Radial Temperature Distribution in 1 $\mu$ m Alumina Powders. ....	158
Figure 7.5.	Measured Thermal Conductivities of Alumina Powders in Vacuum.....	159
Figure 7.6.	Measured Thermal Conductivities of Molded Min-K.....	159
Figure 7.7.	Comparison of Thermal Conductivity Correlations.....	162
Figure 7.8.	Comparison of Thermal Conductance of Multi-Foils Insulation and Min-K. (a) in Perpendicular Direction; (b) in Axial Direction. ....	163
Figure 8.1.	Experimental Flow Chart for Single-Cell Tests at AFRL. ....	166
Figure 8.2a.	Schematic of Single-Cell Test with Min-K Insulation.....	167
Figure 8.2b.	Photograph of Single-Cell Test Setup. ....	168
Figure 8.3a.	Boroelectric Heater Block.....	169
Figure 8.3b.	Photograph of Cell's Heater Block.....	170
Figure 8.3c.	Photograph of Cell's Cold Plate and Air Calorimeter Loop. ....	171
Figure 8.3d.	Photograph of Test Setup Support Structure. ....	172
Figure 8.3e.	Photograph of Cell's Insulation Package. ....	173
Figure 8.3f.	Photograph of Cell's Min-K Insulation Disks.....	174

Figure 8.3g. Photograph of Vacuum Chamber.....	175
Figure 8.4. Electric Circuit Measurement for Single-Cell Test.....	177
Figure 8.5. Power Measurement Control Panel.....	177
Figure 8.6a. Safety Chart for Condenser Temperature Control, $T_{low,1} > T_{low,2}$ .....	179
Figure 8.6b. Safety Chart for Condenser Temperature Control, $T_{high,2} > T_{high,1}$ .....	180
Figure 8.6c. Safety Chart for BASE Tube Temperature Control, $T_{\beta} > T_{\beta,1}$ .....	181
Figure 8.6d. Safety Chart for Vacuum Level $> 10^{-4}$ torr.....	181
Figure 8.7a. Cell Load Safety Circuit.....	183
Figure 8.7b. Cell Heater Safety Circuit.....	184
Figure 8.7c. Data Acquisition System Crash Protection Circuit.....	184
Figure 8.8a. Photograph of Boron Nitride Heater Block.....	188
Figure 8.8b. Thermocouples Arrangement in Insulation Package of PX-1B and PX-1C Cells..	189
Figure 8.8c. Photograph of Thermocouples Arrangement Along Cell Wall.....	190
Figure 8.9. Multi-Foil Insulation of Cell's Heater.....	193
Figure 8.10a. Shroud Design for Multi-Cell Ground Demo.....	195
Figure 8.10b. Photograph of Shroud for Multi-Cell Ground Demo.....	196
Figure 8.11. Photograph of Eight-Cell Ground Demo Test Setup.....	198
Figure 8.12. Schematic of Test Setup for Four-Cell Ground Demo.....	200
Figure 8.13. Photograph of Four-Cell Ground Demo Test Setup.....	201
Figure 9.1. Flow Chart of Experimental Setup of Single-Cell Test at AFRL.....	204
Figure 9.2a. Experimental Measurement on a PX-series Cell.....	206
Figure 9.2b. A Schematic of Thermocouple's Guide Tube Arrangement.....	209
Figure 9.3. A Schematic of Thermocouple's Guide Tube "FIN" Model.....	210
Figure 9.4. Comparison of Predicted and Measured Evaporator Temperatures in PX-5A.....	213
Figure 9.5. Comparison of Predicted and Measured BASE Tube Temperatures in PX-5A.....	215
Figure 9.6. Effect of Guide Tube Length in Evaporator of PX-5A.....	217
Figure 9.7. Effect of Guide Tube Length in BASE Tube of PX-5A.....	218
Figure 10.1a. Heater Resistance versus Lightpipe Temperature Reading.....	221
Figure 10.1b. Heater Resistance versus K-Type Thermocouple Reading.....	222
Figure 10.1c. Heater Resistance versus Average Temperature Reading.....	222
Figure 10.2. Heater Electrical Resistivity.....	223
Figure 10.3. Heater Geometric Factor.....	223
Figure 10.4. Thermocouples Arrangement in Insulation Package of PX-1B and PX-1C Cells..	226
Figure 10.5. Thermal Model of Insulation Package of PX-1B and PX-1C Cells.....	227
Figure 10.6. Illustration of Band Storage of a Linear system Matrix which Results from the Discretization of Conservation Equations on a Two-Dimensional Domain.....	234
Figure 10.7. Flow Chart of Two-Dimensional Conduction Model.....	236
Figure 10.8. Comparison of Analytical and Predicted Axial Temperature Distributions for the Case of One-D Axial Conduction with Constant Thermal Conductivity.....	239
Figure 10.9. Comparison of Analytical and Predicted Axial Temperature Distributions for the Case of One-D Axial Conduction with Linear Thermal Conductivity.....	239
Figure 10.10. Comparison of Analytical and Predicted Radial Temperature Distributions for the Case of One-D Radial Conduction with Constant Thermal Conductivity.....	241
Figure 10.11. Comparison of Analytical and Predicted Radial Temperature Distributions for the Case of One-D Radial Conduction with Linear Thermal Conductivity.....	241

Figure 10.12. Thermocouple Temperature Measurements in the Alumina Powder Insulation of PX-1B ( $T_{heater}=1220\text{ K}$ )	244
Figure 10.13. Temperature and Heat Flux Profiles along the Bottom Surface of PX-1B Insulation ( $T_{heater}=1220\text{ K}$ )	245
Figure 10.14. Temperature and Heat Flux Profiles along PX-1B Cell Wall ( $T_{heater}=1220\text{ K}$ )	246
Figure 10.15. Temperature and Heat Flux Profiles along PX-1B Heater Top ( $T_{heater}=1220\text{ K}$ )	247
Figure 10.16. Temperature and Heat Flux Profiles along the Side Surface of PX-1B Insulation ( $T_{heater}=1220\text{ K}$ )	248
Figure 10.17. Temperature and Heat Flux Profiles along the Top Surface of PX-1B Insulation ( $T_{heater}=1220\text{ K}$ )	249
Figure 10.18. Predicted Isotherms and Heat Losses in the Insulation of PX-1B Cell ( $T_{heater}=1220\text{ K}$ )	250
Figure 10.19a. Schematic of Calorimeter Experiment for Cell Heater Calibration	253
Figure 10.19b. Photograph of Calorimeter Experiment for Cell Heater Calibration	254
Figure 10.20a. Thermocouples Arrangement in Boron Nitride Heater Block	255
Figure 10.20b. Photograph of Boron Nitride Heater Block	256
Figure 11.1. Minimum Wick Porosity at a Sodium Flow Rate of 10 gm/hr	268
Figure 11.2. Volume Porosity of Sintered Porous Wick as a Function of $R_c/R_s$	270
Figure 11.3. Prime Porosity of Sintered Porous Wick as a Function of Volume Porosity	270
Figure 11.4. Effective Thermal Conductivity of SS Wick Saturated with Liquid Sodium as a Function of Wick Volume Porosity	272
Figure 11.5a. Effective Thermal Conductivity of Fully-Saturated Porous Wick with a 20% Volume Porosity	272
Figure 11.5b. Effective Thermal Conductivity of Stainless Steel Sintered Wick Saturated with Liquid Sodium, with a 20% Volume Porosity	273
Figure 11.6. Heat Supply to Cell Evaporator as a Function of Sodium Mass Flow Rate	274
Figure 11.7. Heat Conducted to Evaporator as a Function of Standoff Wall Thickness	274
Figure 11.8. Estimate of Heat Radiated to Evaporator from Cell's Hot Plate in PX-1A	275
Figure 11.9. Calculated Values of Local Pressure in PX-2C Cell ( $Q_{in}=39\text{ W}$ , $T_{cd}=600\text{ K}$ , $T_{ev}=950\text{ K}$ , $\dot{m}=9\text{ gm/hr}$ , $I=1.5\text{ A}$ , $Pe=4.5\text{ W}_e$ )	278
Figure 11.10. PX-2C Cell Electrical Power as a Function of Current	280
Figure 11.11. Estimate of PX-2C Cell Input Power Versus Electrical Current	280
Figure 11.12. PX-2C Cell Voltages as a Function of Electrical Current	282
Figure 11.13. PX-2C Cell Electrical Power as a Function of External Load Resistance	282
Figure 11.14. Predicted Heat Transfer and Temperatures in PX-2C, Near the Peak Power	284
Figure 11.15. Calculated Vapor Pressure in PX-2C on Low-Pressure Side	286
Figure 11.16. Calculated Vapor Knudsen Number on Cathode Side of PX-2C	286
Figure 11.17. BASE Tubes Temperature and Current Density in PX-2C	287
Figure 11.18. Measured and Predicted Temperatures in PX-2C, as Function of Load Resistance	288
Figure 11.19. Measured and Predicted Temperatures in PX-2C, as Function of Cell Current	288
Figure 11.20. Temperature Margins and Conversion Efficiency in PX-2C	290
Figure 11.21. Predicted Heat Transfer and Temperatures in PX-4C, at $R_L=3.15\ \Omega$	292
Figure 11.22. Measured and Predicted Temperatures in PX-4C, as Function of Load Resistance	293

Figure 11.23. Measured and Predicted Temperatures in PX-4C, as Function of Cell Current. .	293
Figure 11.24. Temperature Margins and Conversion Efficiency in PX-4C. ....	294
Figure 11.25. Temperature Margins in PX-2C and PX-4C Cells. ....	294
Figure 11.26. Comparison of PX-2C and PX-4C Electric Power Outputs. ....	295
Figure 11.27. Comparison of PX-2C and PX-4C Electrode Power Densities. ....	295
Figure 11.28a. Electric Power Output of PX-4C Cell ( $T_{hot} = 1130$ K, $T_{cd} = 565$ K). ....	300
Figure 11.28b. Electric Voltage Output of PX-4C Cell ( $T_{hot} = 1130$ K, $T_{cd} = 565$ K). ....	300
Figure 11.28c. Heat Removed at Condenser of PX-4C Cell ( $T_{hot} = 1130$ K, $T_{cd} = 565$ K). ....	301
Figure 11.28d. BASE Tube's Cold End Temperature in PX-4C Cell ( $T_{hot} = 1130$ K, $T_{cd} = 565$ K). .....	301
Figure 11.28e. Evaporator Temperature in PX-4C Cell ( $T_{hot} = 1130$ K, $T_{cd} = 565$ K). ....	302
Figure 11.28f. Predicted Conversion Efficiency of PX-4C Cell ( $T_{hot} = 1130$ K, $T_{cd} = 565$ K). ....	302
Figure 11.29a. Electric Power Output of PX-5A Cell ( $T_{cd} = 623$ K). ....	304
Figure 11.29b. Electric Voltage Output of PX-5A Cell ( $T_{cd} = 623$ K). ....	304
Figure 11.29c. Heat Removed at Condenser of PX-5A Cell ( $T_{cd} = 623$ K). ....	305
Figure 11.29d. BASE Tube's Cold End Temperature in PX-5A Cell ( $T_{cd} = 623$ K). ....	305
Figure 11.29e. Evaporator Temperature in PX-5A Cell ( $T_{cd} = 623$ K). ....	306
Figure 11.29f. Predicted Conversion Efficiency of PX-5A Cell ( $T_{cd} = 623$ K). ....	306
Figure 11.30a. Electric Power Output of PX-3A Cell ( $T_{cd} = 623$ K). ....	308
Figure 11.30b. Electric Voltage Output of PX-3A Cell ( $T_{cd} = 623$ K). ....	308
Figure 11.30c. Heat Removed at Condenser of PX-3A Cell ( $T_{cd} = 623$ K). ....	309
Figure 11.30d. BASE Tube's Cold End Temperature in PX-3A Cell ( $T_{cd} = 623$ K). ....	309
Figure 11.30e. Evaporator Temperature in PX-3A Cell ( $T_{cd} = 623$ K). ....	310
Figure 11.30f. Predicted Conversion Efficiency of PX-3A Cell ( $T_{cd} = 623$ K). ....	310
Figure 11.31. Electric Power Output of PX-3C Cell and Comparison with APEAM's Results. ....	314
Figure 11.32. Electric Voltage Output of PX-3C Cell and Comparison with APEAM's Results. .....	314
Figure 11.33. Effect of Cell Current on Evaporator and BASE Tube Temperatures in PX-3C. ....	315
Figure 11.34. Effect of Cell Current on Temperature Margin in PX-3C. ....	315
Figure 11.35. Predicted BASE Brazes Temperature in PX-3C Cell. ....	316
Figure 12.1. Orbital Sciences Corporation's PX-Generator Design, with 2 GPHS Modules Stack and Sixteen AMTEC Cells (Schock et al. 1997b). ....	320
Figure 12.2. Cross Sections of PX-3G Cell (Not to Scale). ....	321
Figure 12.3. Effects of $R_{cont}$ , $R_{leak}$ and $B$ parameters on I-V Characteristic and Electrical Power Output of PX-3G Cell #1. ....	326
Figure 12.4. I-V Characteristic of PX-3G Cell #1. ....	327
Figure 12.5. Electric Power Output of PX-3G Cell #1. ....	327
Figure 12.6. Load-Following Characteristic of PX-3G Cell #1. ....	329
Figure 12.7. I-V Characteristic of Ground Demo. ....	329
Figure 12.8. Electric Power Output of Ground Demo. ....	330
Figure 12.9. Predicted Leakage Current in the Average PX-3G Cell. ....	330
Figure 12.10. Effect of Cell Current on Evaporator and BASE Tube Temperatures in the Average PX-3G Cell. ....	332
Figure 12.11. Effect of Cell Current on Temperature Margin in the Average PX-3G Cell. ....	332
Figure 13.1. Cell Wall Heat Losses and Conversion Efficiency (Cases #1, 2 and 3). ....	337

Figure 13.2. Effect of Condenser Type on Cell Electrical Power and Conversion Efficiency (Cases #2 and 4).....	339
Figure 13.3. Effects of Changing the Number of BASE Tubes and the Electrode Length, $L_E$ , on Cell Performance (Cases #5, 2, 6 and 7).....	341
Figure 13.3. Effects of Changing the Number of BASE Tubes and the Electrode Length, $L_E$ , on Cell Performance (Cases #5, 2, 6 and 7) (Cont.).....	342
Figure 13.4. Effect of Electrode Material on Cell Performance (Cases #7, 8 and 9).....	344
Figure 13.5. Effect of Changing Structure Material and Using High-Reflectivity Coatings on Cell Performance (Cases #7, 10 and 11).....	346
Figure 13.6. Performance of Adiabatic PX-Series AMTEC Cells (Cases #12, 13, 14 and 15).....	348
Figure 13.6. Performance of Adiabatic PX-Series AMTEC Cells (Cases #12, 13, 14 and 15) (Cont).....	349
Figure 14.1. Predicted Temperatures and Heat Flow in BASE Tubes of Cell Design #6 (3.5 V, $Q_{in}=31.3\text{ W}_{th}$ ).....	356
Figure 14.2. Predicted Temperatures and Heat Flow in BASE Tubes of Cell Design #7 (3.5 V, $Q_{in}=31.3\text{ W}_{th}$ ).....	356
Figure 14.3. Calculated Performance of an Improved 1.25-in Diameter, PX-3G Type Cell Design.....	358
Figure 14.4. Peak Electric power of Improved 1.25-in Diameter, PX-3G Type Cell.....	360
Figure 14.5. Number of Improved 1.25-in Diameter Cells and Total Heat Input for a Multi-cell Generator with 156 W <sub>e</sub> Output at EOM.....	360
Figure 14.6. Maximum Electric Power Output of 16-Cell Generator Power Systems at EOM.....	362
Figure 15.1. Cross-sectional Views of PX-3G Type Cell (Not to Scale).....	366
Figure 15.2. OSC's PX-Generator Design, with 2 GPHS Modules and Sixteen 31.75 mm (1.25") Dia. Cells (Schock et al. 1998c).....	367
Figure 15.3. AMPS's PX-Generator Design, with 4 GPHS Modules and Sixteen 44.45 mm (1.75") Dia. AMTEC Cells (Hendricks et al. 1998).....	368
Figure 15.4. I-V Characteristic of Cell Design #1.....	372
Figure 15.5. Electrical Power of Cell Design #1.....	372
Figure 15.6. Predicted Temperatures and Heat Flow in the Cell's BASE Tubes. (a) Cell Design #7; (b) Cell Design #8.....	375
Figure 15.7. Effect of Condenser Temperature on Conversion Efficiency of Cell B.....	377
Figure 15.8. Effect of Condenser Temperature on Sodium Vapor Pressure on Cathode Side of the BASE in Cell B.....	377
Figure 15.9. Peak Electric Power and Peak efficiency of Cell C.....	379
Figure 15.10. Number of C-Type Cells and Total Thermal Energy Requirements for a Power System Generating 156 W <sub>e</sub> @ EOM.....	379
Figure 15.11. Electrical Power of Generators at EOM for Different Cell Designs.....	383
Figure 15.12. BASE Tubes' Braze Temperature at BOM for Different Cell Designs.....	383
Figure 15.13. Electrical Power of Generator #2 at EOM as a Function of Cell Length.....	387
Figure 15.14. Specific Power of Generator #2 at EOM as a Function of Cell Length.....	387
Figure B1. Free-Molecular Flow Conductance Ratio, $C/C_0$ , for a Circular Tube (Levenson et al. 1961).....	414
Figure B2. Free-Molecular Flow Conductance Ratio, $C/C_0$ , for a 90° Bent Elbow (Levenson et al. 1961).....	414



Figure B3.	Free-Molecular Flow Conductance Ratio, $C/C_0$ , for a Cylindrical Annulus (Levenson et al. 1961).	415
Figure B4.	Free-Molecular Flow Conductance Ratio, $C/C_0$ , for Rectangular Louvers (Levenson et al. 1961).	416
Figure B5.	Free-Molecular Flow Conductance Ratio, $C/C_0$ , for Chevrons Baffles (Levenson et al. 1961).	416
Figure C20.	Schematic of Vapor Anode, Multi-Tube AMTEC Cell and Discretization (Shown: $N_c=2$ , $N=5$ , $N_w=4$ ).	442
Figure D1.	Radial Temperature Profiles in 1- $\mu\text{m}$ Alumina Powder (Group 1).	463
Figure D2.	Radial Temperature Profiles in 1- $\mu\text{m}$ Alumina Powder (Group 2).	463
Figure D3.	Radial Temperature Profiles in 1- $\mu\text{m}$ Alumina Powder (Group 3).	464
Figure D4.	Radial Temperature Profiles in 1- $\mu\text{m}$ Alumina Powder (Group 4).	464
Figure D5.	Radial Temperature Profiles in 0.01- $\mu\text{m}$ Alumina Powder (Group 1).	465
Figure D6.	Radial Temperature Profiles in 0.01- $\mu\text{m}$ Alumina Powder (Group 2).	465
Figure D7.	Radial Temperature Profiles in 0.01- $\mu\text{m}$ Alumina Powder (Group 3).	466
Figure D8.	Radial Temperature Profiles in 0.01- $\mu\text{m}$ Alumina Powder (Group 4).	466
Figure D9.	Radial Temperature Profiles in Molded Min-K (Group 1).	467
Figure D10.	Radial Temperature Profiles in Molded Min-K (Group 2).	467
Figure D11.	Radial Temperature Profiles in Molded Min-K (Group 3).	468
Figure D12.	Radial Temperature Profiles in Molded Min-K (Group 4).	468
Figure E1.	Electric Circuit Measurement for Single-Cell Test.	475

## LIST OF TABLES

Page

Table 3.1.	Measured and Selected Values of the Resistance Coefficient $\xi$ for Sudden Expansions of Different Area Ratios (Idelchik 1986, Figure 4.9, page 155). .....	56
Table 3.2.	Sodium Vapor Pressure Losses in PX-1A Cell with Four 45°-angle Chevrons Placed 48 mm from Condenser ( $T_{cd} = 550$ K, $T_B = 1050$ K, $R_L = 2 \Omega$ , $I = 1.39$ A). .....	63
Table 4.1.	Electrical Losses in PX-Series Cells near their Peak Electric Power. ....	93
Table 5.1.	Predicted Heat Transfer and Performance Parameters for PX-Series Cells. ....	136
Table 9.1.	Measurement Uncertainty Analysis of PX-Series Cell Tests at AFRL. ....	207
Table 9.2.	Comparison of BASE and Evaporator TC Readings and Predictions of APEAM Model and Fin Model for PX-5A. ....	214
Table 10.1.	Experimental Data Collected in Heater Calibration Experiment. ....	221
Table 10.2.	Predicted Heat Losses in Insulation of PX-1 Series Cells. ....	243
Table 11.1.	Design Parameters of PX-Series Cells Tested at AFRL. ....	263
Table 11.2.	Measured and Predicted Performance Characteristics of PX-Series Cells Tested at AFRL. ....	264
Table 11.3.	Effect of Internal Radiation Shields on PX-2C Cell Performance ( $R_L = 2 \Omega$ ). ....	283
Table 11.4.	Predicted Performance of Some PX-Series Cells Tested at AFRL. ....	312
Table 12.1.	Design Parameters of PX-5 Series Cells. ....	322
Table 12.2.	Performance Parameters of PX-3G Cells Tested at $T_{hot} = 1123$ K and $T_{cd} = 553$ K. ....	325
Table 13.1.	Predicted Performance of a PX-5A Type Cell due to Various Design Changes ( $T_{hot} = 1200$ K, $T_{cond} = 623$ K, $\Delta T = 50$ K). ....	336
Table 14.1.	Predicted Performance of PX-3G type Cells ( $Q_{in} = 31.25$ W <sub>th</sub> and 3.5 V). ....	354
Table 14.2.	Predicted Performance of Radioisotope Power Systems with Improved 1.25-in Diameter, PX-3G Cells. ....	361
Table 15.1.	Predicted Performance of Improved PX-3G Type Cell Design ( $Q_{in} = 40$ W, $T_{cond} = 640$ K, and $V_L = 2.8$ V). ....	373
Table 15.2.	Design parameters of the Super-Alloy, Multi-Tube AMTEC Cells Investigated in the Present Study. ....	376
Table 15.3.	Predicted Performance of PX-Power Systems with 6 Fresh-Fuel GPHS Modules and 48 Cells ( $V_L = 28$ V). ....	381
Table 15.4.	Predicted Performance of the Top Performing PX-Power Systems in this Study ( $V_L = 28$ V). ....	382
Table 15.5.	Mass Breakdown of Pluto/Express Power Systems #3 (with C-Type Cells). ....	384
Table D1.	Experimental Data and Processing of Thermal Conductivity of 1- $\mu$ m Alumina Powder. ....	469
Table D2.	Experimental Data and Processing of Thermal Conductivity of 0.01- $\mu$ m Alumina Powder. ....	471
Table D3.	Experimental Data and Processing of Thermal Conductivity of Molded Min-K. ....	473
Table E1.	Measurement Uncertainty Analysis of PX-Series Cell Tests at AFRL. ....	482

## ACKNOWLEDGMENTS

This research was funded by the VSDV Power and Thermal Group of the Air Force Research Laboratory (AFRL), Phillips Site, Kirtland Air Force Base, Albuquerque, New Mexico, USA, under contract F29601-96-K-0123, to the University of New Mexico's Institute for Space and Nuclear Power Studies (UNM-ISONPS). The authors wish to thank John Merrill and Matt Clark, Nichols Research, Inc., Troy Diagle, SA, USAF, who conducted the vacuum tests, and provided the experimental data and some thermophysical properties upon which some outputs of this work were based. The authors are also grateful to Dr. Michael Schuller, former chief, Power Management Division, William Ralph James, AFRL/VSDV, DR/2, DAF, Power and Thermal Group Leader, Clay Mayberry, AFRL/VSDV, AMTEC Program Manager, and to Bob Sievers, Chendong Huang and Chris Borkowski at AMPS for providing details on AMTEC cell design and dimensions. Thanks are also due to Jeff King, UNM-ISONPS, who generated some of the artwork in this report using the SolidWorks CAD package and performed some of the parametric analyses using APEAM.

Finally, the authors wish to thank the UNM-ISONPS administrative staff, Mary Bragg and Maureen Alaburda, for their assistance in the final preparation and production of this document.

Without the effort of all these individuals, this work would not have been possible.

## EXECUTIVE SUMMARY

The objectives of this work were to: (a) participate in the vacuum testing of vapor anode Multi-tube, Alkali Metal Thermal-to-Electric conversion (AMTEC) cells performed at the Air Force Research Laboratory (AFRL) during the past three years and evaluate the performance of various test articles; (b) analyze and examine the experimental data collected in the tests; (c) develop appropriate phenomenological modeling capabilities of vapor anode, multi-tube AMTEC test articles and thermal models of the experimental setup; (d) compare the experimental measurements with models predictions and upgrade models as appropriate; and (e) conduct investigations of various methods to improve the design and performance of these devices, and based on the results, provide technical feedback and recommendations for improving the capabilities of the test setup and the design of next generation devices for higher efficiency and power density.

The thermal conductivity of a number of insulation materials used in the experiments (alumina powders and molded Min-K) was measured experimentally using a setup that was designed and instrumented for that purpose. The thermal conductivity data for these materials were correlated and compared as functions of temperature. The thermal conductance of Min-K was compared with those of 60 and 240 multi-foils insulation, both in the axial and perpendicular directions.

A test shroud was also designed for conducting the multi-cell system tests. The shroud was cooled with liquid nitrogen and proved adequate for the conduct of the multi-cell vacuum tests.

The uncertainties associated with the different experimental measurements in the single-cell vacuum tests performed at AFRL were determined. These uncertainties include those associated with the measurements of temperature, load electric current and voltage, and flow rate of air through the heat rejection coil. Other important uncertainties determined were those associated with the placement of the thermocouples within the cavities of the BASE tube and evaporator inside some of the PX-series cells, for measuring their respective temperature.

A comprehensive AMTEC Performance Evaluation and Analysis Model (APEAM) of vapor anode, multi-tube AMTEC cells was developed and benchmarked successfully using data generated in the vacuum tests performed at AFRL of both single cell and multi-cell systems. APEAM was used extensively to perform parametric analyses of test articles and identify key design changes to reduce internal heat and electrical losses, optimize the performance, and increase the conversion efficiency of the cells.

APEAM consists of the following building blocks, developed in the course of this research: (a) a *sodium vapor pressure loss model*, which predicts free-molecular, transition and continuum vapor flow regimes and calculates the sodium vapor pressure at the interface between the cathode electrode and the BASE; (b) a *cell electrochemical and electric model*, which calculates the effective potential developed across the BASE due to the isothermal expansion of sodium ions, determines the resistances of the BASE, electrodes, current collectors and conductor leads to the

external load, and calculates the cell's electrical potentials, electrode current density, and the cell's total electric current; and (c) a *radiation/conduction heat transfer model*, which accounts for all heat exchanges between the different components of the cell and calculates the temperatures throughout the cell. The radiation/conduction model used an approximate algebraic view factor database developed in this work, for computational efficiency. The radiation/conduction heat flow model in APEAM was also modified to include a variety of thermal boundary conditions and the potential to more accurately mimic and predict the cell wall losses through the insulation package surrounding the cell. An efficient iterative solution procedure was developed, which ensured good couplings between the different physical models in APEAM. As a result, APEAM was extremely fast-running; a typical steady-state, 200 nodes full AMTEC cell analysis would take less than 10 s CPU to complete on a 200-MHz Pentium Personal Computer.

Based on the analyses performed using APEAM, several design changes were investigated, proposed and implemented, which improved the performance of next generation AMTEC cells. For example, we proposed adding conduction studs between the hot side and the BASE tubes' metal support plate to enhance heat conduction to the BASE tubes and the cell evaporator. This design modification was implemented in next generation cells (PX-2A cell and following cells) that were tested at AFRL.

The radiation heat loss from the BASE tubes to both the condenser and the cell wall surface was found to be most significant. Results showed that substantial gain in cell performance could be achieved by reducing the radiation losses in the cell using internal radiation shield. Also, the use of a Creare type condenser wick, which maintains a continuous film of liquid sodium on its surface, improves the cell conversion efficiency due to the very high reflectivity of liquid sodium (0.95).

APEAM's predictions of the performance parameters of a number of PX-series, single cells and of a Pluto/Express electric power generator ground demo tested in vacuum at AFRL compared well with experimental data. These parameters were the load electrical power output, the cell I-V characteristic, the hot and cold end temperatures, the condenser heat rejection, and, in some cases, the evaporator and BASE tubes' cold end temperatures. Such good agreement confirmed the soundness of the modeling approach and the solution procedure used.

Analyses of the vacuum test results of the Pluto/Express electric power generator ground demo showed that, at the operating conditions expected on board the Pluto/Express spacecraft ( $T_{hot} \sim 1200$  K,  $T_{cd} \sim 573$  K), the best performing PX-3G cell #1 would have delivered 5  $W_e$  at a output voltage of 3 V. These values, however, were still significantly lower than those needed (8.2  $W_e$  at 3.5 V, per cell) to meet the Pluto/Express mission power requirements in the Orbital Sciences Corporation's (OSC) 16-cell power system configuration. The ground demo test article produced a peak electrical power of 27  $W_e$  at a voltage of 16 V, when tested at hot and cold side temperatures of 1123 K and 553 K, respectively. Detailed analysis of the test results using APEAM has shown that the electric power outputs and terminal voltages of the individual PX-3G cells differed by as much as 25%, from 2.94 to 3.76  $W_e$ , and 1.73 to 2.21 V, respectively. These variations in the individual cells' performance parameters were attributed, in an order of decreasing importance, to differences in: (a) the contact resistances between the BASE/metal electrodes and the electrodes/current collectors ( $R_{cont}$ ); (b) the current leakage between anode and

cathode electrodes through the metal-ceramic braze joint between BASE tubes and SS support plate ( $R_{leak}$ ); and (c) the charge-exchange polarization losses ( $B$ ). The values of  $B$ ,  $R_{cont}$ , and  $R_{leak}$  for the individual PX-3G cells, deduced from the comparison of measured and calculated I-V characteristics, varied between 64 – 75 A.K<sup>1/2</sup>/Pa.m<sup>2</sup>, 0.06 – 0.12  $\Omega$ . cm<sup>2</sup>, and 1.3 – 6.0  $\Omega$ , respectively.

Design changes in the cell design and the multi-cell power system configuration, for meeting the power requirement of the Pluto/Express spacecraft, were investigated using APEAM. The parametric analyses performed evaluated the effects of a number of design changes: (a) reducing the heat losses through the cell wall; (b) using a Creare type condenser; (c) changing the number of BASE tubes and the electrode length; (d) changing the electrode material; (e) using Mo or Ni structure on the hot side of the cell; and (f) using reflective rhodium coatings in the low vapor pressure cavity of the cell.

Results showed that a radioisotope power system configured as proposed by Orbital Sciences Corporation (OSC), that uses the improved cell design, can meet the power requirement of the Pluto/Express mission, but at the expense of high metal-to-ceramic brazes and evaporator temperatures in the cell. A major concern in this case was the potential acceleration of the performance degradation of the cells. Analysis showed that the PX-generator configuration proposed by Advanced Modular Power Systems (AMPS), where the cells are mounted onto the 4 sides of the GPHS stack (instead of mounting the cells on the top and bottom faces of the GPHS stack, in OSC design), does not suffer from a limitation in the number of cells that could be used in the system. The larger surface area of the four sides of the GPHS stack also offers greater flexibility in the integration of the cells with the heat source.

Finally, nickel structure cells of improved performance were designed and various options of integrating these cells with GPHS modules in the generator configuration proposed by AMPS were explored. Design options investigated included: (a) changing the number of GPHS modules and the number of cells per generator; (b) using either fresh or aged <sup>238</sup>PuO<sub>2</sub> fuel; (c) increasing the BASE and electrode lengths (to 2 inch and 1.5 inch, respectively); and (d) varying the number of BASE tubes in the cell (5 – 9) by changing the cell diameter (1.25 – 1.75 inch). Results showed that when the number of cells in the PX-generator was reduced, or when cells with a smaller number of BASE tubes were used, the total mass of the generator decreased, and the total electric power output increased. However, these changes also caused the evaporator and the BASE tubes' brazes temperatures in the cells to increase. The analysis identified a number of power systems with higher specific power, which used the proposed nickel AMTEC cells and could meet the electric power requirement for the Pluto/Express mission, while operating at a relatively cool evaporator ( $T_{ev} < 1023$  K) and low metal-to-ceramic braze temperatures ( $T_{braz} < 1073$  K).

## 1. INTRODUCTION

Alkali-Metal Thermal-to-Electric Converters (AMTEC) are being considered for a number of potential space missions, requiring low mass, low cost, long life, and high-efficiency power systems. These devices are very attractive for these applications because they are static and can provide efficiencies that are a large fraction of the theoretical Carnot efficiency at relatively low operating temperatures (Weber 1974 and Cole 1983), efficiencies that are substantially higher than other static energy conversion power systems. For example, an optimized AMTEC can potentially provide a theoretical conversion efficiency between 20 and 30% when operated at hot-side temperatures between 1000 K and 1300 K and a cold-side temperature in the range 400 K-700 K. AMTEC devices have no moving parts with the resulting potential for low maintenance and high durability, are modular in nature, and have the ability to use high-temperature nuclear heat sources.

Since the mid-1980s, a number of programs to develop the technology of liquid- and vapor-anode AMTECs have been initiated at several organizations: the Ford Motor Company (Weber 1974 and Sievers et al. 1988); the Jet Propulsion Laboratory (Sievers and Bankston 1988, Williams et al. 1990, and Underwood et al. 1992); the Electrotechnical Laboratory and Kyushu University in Japan (Kato et al. 1992 and 1993, and Tanaka et al. 1992); Advanced Modular Power Systems (AMPS) and the Environmental Research Institute of Michigan (Sievers et al. 1993, and Ivanenok et al. 1994); the U.S. Air Force Research Laboratory/Phillips Site (Schuller and LeMire 1994, Schuller et al. 1996, and Merrill et al. 1997 and 1998). While these programs have successfully resolved a number of key technology issues associated with the fabrication and design of AMTECs, the performance levels achieved to-date in laboratory tests are still below the theoretical potential of these devices.

A comprehensive modeling and testing program at the Air Force Research Laboratory/Phillips Site (AFRL/PS), jointly with AMPS and the University of New Mexico's Institute for Space and Nuclear Power Studies (UNM-ISONPS), has demonstrated the readiness of AMTEC technology for flight on the National Aeronautics and Space Administration's (NASA) Pluto/Express (PX) and Europa spacecraft and future U.S. Air Force space missions. The goal of this program was to improve the design and performance of AMTECs and demonstrate system efficiencies in excess of 20%. An important component of this collaborative effort was the development of a comprehensive performance model of liquid-anode single-tube and vapor-anode multi-tube cells, to support the ongoing cell testing, perform parametric analyses and evaluate cell design changes to improve the converter performance. The details of the AMTEC modeling and simulation effort as well as the model's comparison results with single-cell and multi-cell vacuum tests performed at AFRL are presented in the following chapters.

This report is organized as follows. Chapter 2 reviews the different types of AMTEC cells, describes their principle of operation, and describes in details the geometry of Pluto/Express (PX) series cells being tested at AFRL/PS. Some of the performance limiting factors in vapor anode, multi-tube AMTEC cells are also discussed. Chapters 3 – 5 describe the AMTEC Performance

Evaluation and Analysis Model (APEAM) developed by UNM-ISONPS in details. Particular attention is given to the major submodels in APEAM: the sodium vapor pressure drop model in the low-pressure cavity of the PX-cell (Chapter 3, and Appendices A and B), the AMTEC electrochemical and electrical model (Chapter 4), which includes 4 different options of current collectors, and the thermal radiation/conduction model (Chapter 5), which incorporates an algebraic radiation view factor database (Appendix C). Chapter 5 also describes the efficient iterative solution procedure which was developed to couple the models of the different physical processes in the cell.

In Chapter 6, a thermal-hydraulic model is developed to calculate the pressure losses and determine the capillary limit of the liquid-sodium return wick in the PX-series, vapor anode, multi-tube AMTEC cell. The model is used to examine the effects of the wick parameters and evaporator temperature on the liquid sodium circulation.

In Chapter 7, the experimental setup and data analysis for measuring the thermal conductivity of insulation materials (alumina powders and Min-K) are presented, and conductivity correlations are developed for these materials, based on measurements.

Chapter 8 describes the single-cell and multi-cell experimental setups at AFRL/PS. The experimental uncertainties in the vacuum tests are evaluated in Chapter 9.

In Chapter 10, a number of calibration experiments were designed to attempt to evaluate the heat losses in the heater block of the cell and the surrounding insulation, identify critical loss paths, and improve the experimental setup at AFRL. An indirect-heat-loss measurement technique was devised, to evaluate the conduction heat losses in the single-cell test from the measured temperature profiles along the insulation surface and the cell wall. A two-dimensional, transient heat conduction model was developed, and benchmarked, using a number of sample thermal problems with known analytical solution. This 2-D heat conduction model was then used in conjunction with temperature measurements to predict the heat losses in the alumina powder insulation of the PX-1 series of cells. Next, a heater calorimeter experiment was designed to calibrate the heat losses in the heater Boron Nitride block. The heat from the bottom of the cell heater was removed and measured by the calorimeter, which had the shape and dimensions of a typical, 1.25-inch diameter PX-series cell. The heat input to the calorimeter was removed by an impinging air jet inside the confinement.

Experimental data of a number of single-cell tests (PX-1A, PX-2C, PX-4C, PX-5A, PX-3A and PX-3C) obtained at AFRL/PS are analyzed and compared with APEAM's predictions in Chapter 11. Recent Experimental data of a multi-cell ground demo generator tests (which used 8 identical PX-3G cells) obtained at AFRL/PS are analyzed and compared with APEAM's predictions in Chapter 12.

In Chapter 13, parametric analyses are performed using APEAM to evaluate the effect of some design changes and important parameters on the performance of PX-series cells, and identify some of the performance and lifetime limitations in current cell designs. Finally, in Chapters 14 and 15, improved designs of super-alloy cells are proposed and a number of radioisotopic power



generators are designed to meet the requirements for the Pluto/Express mission. Both Orbital Sciences Corporation (OSC)'s (Chapter 14) and Advanced Modular Power Systems (AMPS)'s (Chapter 15) configurations are investigated.

Finally, important findings and results of this research are compiled in Chapter 16, and recommendations are given for possible future work.

## 2. BACKGROUND

This chapter reviews the different types of Alkali-Metal Thermal-to-Electric Conversion (AMTEC) cells since the patent for liquid sodium anode cell by the Ford Motor Company in 1968 (Kummer and Weber 1968). The thermodynamic cycle of AMTEC is described in detail to demonstrate the theoretical potential of these cells for static energy conversion. For high power space applications, vapor anode, multi-tube cells were introduced. The attribute of these cells and technical challenges that need to be addressed to approach the theoretical potential of these devices are discussed.

This chapter provides the necessary background information on AMTEC operation, and describes the electrochemical and thermal-lumped model developed by UNM-ISONPS during the first phase of this effort. The electrochemical model results agreed well with experimental data for Mo, NbN and TiN electrodes. The processes which significantly affect the performance of AMTEC cells and several design suggestions for improving cell electric power output and conversion efficiency were identified. Results indicated the need to develop an accurate model for predicting the vapor pressure losses on the cathode side and the parasitic radiation and conduction losses in the cell. Such a model was developed in the second phase of the UNM-ISONPS modeling effort.

The objective of this chapter is to report on the first phase of the modeling effort by UNM-ISONPS. In this phase, an electrochemical and thermal-lumped model is developed and used to predict the performance of both liquid- and vapor-anode AMTEC devices. The model assumes uniform axial temperature and current density distributions along the BASE tubes and the electrodes, and accounts for pressure losses, parasitic radiation heat losses, and internal electric losses in the AMTEC cell. Vapor pressure losses between the cathode electrode and the heat rejection condenser are calculated using an effective dimensionless factor,  $G$  (the pressure losses on the high-pressure side of the AMTEC cell are negligible compared to the anode pressure). Parasitic radiation heat losses between the BASE tubes and both the condenser and the side wall are evaluated using a dimensionless radiation factor,  $Z$ .

The present AMTEC lumped model is benchmarked by comparing its predictions with the experimental data of Sievers and Bankston (1988) and Kato et al. (1992 and 1993) for oxide-free molybdenum, NbN and TiN electrodes. The processes which significantly affect the performance of AMTEC cells are identified. Areas for further studies, which have strong potential for improving the cell electrical power output and efficiency, are identified.

### 2.1 NOMENCLATURE

#### English

$A_E$	Cathode electrode area on one BASE tube ( $\text{m}^2$ )
$A_l$	Cross-section area of connecting lead ( $\text{m}^2$ )
$B$	Temperature-independent, charge-exchange coefficient ( $\text{A.K}^{1/2} / \text{Pa.m}^2$ )
$C_p$	Heat capacity of liquid sodium ( $\text{J} / \text{kg.K}$ )
$F$	Faraday's constant ( $F = 96,485. \text{C} / \text{mole}$ )

$f_B$	Coefficient, $f_B = F / (R_g T_B)$ (C / J)
$G$	Dimensionless morphology factor for vapor pressure losses on the cathode side, Equation (2.4)
$h_L$	Enthalpy of liquid sodium (J / kg)
$h_{LV}$	Latent heat of vaporization of sodium (J / kg)
$I$	Total cell current, $I = A_E \times J$ (A)
$J$	Electrode current density (A / m <sup>2</sup> )
$J^{ex}$	Charge-exchange current density (A / m <sup>2</sup> )
$J_{sat}^{ex}$	Saturated equilibrium charge-exchange current density (A / m <sup>2</sup> )
$k$	Thermal conductivity of lead (W / m.K)
$L$	length of one electric lead (m)
$M$	Molecular weight of sodium ( $M = 23$ g/mol)
$N_S$	Number of series-connected BASE tubes
$P$	Pressure (Pa)
$Q_{cd}$	Heat conduction loss in one lead (W)
$Q_J$	Joule heating in one lead (W)
$Q_{rad}''$	Parasitic radiation heat loss (W / m <sup>2</sup> )
$r$	Sodium massic gas constant, $r = R_g / M$ ( $r = 361.5$ J / kg.K)
$R'_B$	Ionic resistance of the BASE ( $\Omega \cdot m^2$ )
$R'_{cont}$	Cell internal resistance other than $R'_B$ , or contact resistance ( $\Omega \cdot m^2$ )
$R_g$	Perfect gas constant ( $R_g = 8.314$ J / mol.K)
$T$	Temperature (K)
$t_B$	Thickness of BASE tube (m)
$V$	electrical voltage (V)
$Z$	Geometric factor for radiation heat losses, Equation (2.15)

#### Greek

$\alpha$	Electrochemical transfer coefficient ( $\alpha = 1/2$ )
$\delta$	Current lead dimensionless factor, $\delta = LI\sqrt{\lambda} / (kA_l)$
$\Delta T_{evap}$	Evaporator subcooling or temperature margin, $\Delta T_{evap} = T_B - T_{evap}$ (K)
$\varepsilon$	Radiative emissivity
$\zeta$	concentration and charge-exchange polarization losses (V)
$\eta$	Conversion efficiency
$\lambda$	Franz-Lorenz's number, $\lambda = 2.45 \times 10^{-8}$ W. $\Omega$ / K <sup>2</sup>
$\rho$	Electrical resistivity ( $\Omega \cdot m$ )

#### Subscript / Superscript

a	Anode electrode / BASE interface
B	Beta"-Alumina Solid Electrolyte (BASE)
c	Cathode electrode / BASE interface
Carnot	Carnot thermodynamic cycle

cc	Closed-circuit
cond	Condenser
e	Electric
evap	Evaporator
G	Includes effect of vapor pressure losses on the cathode side
ideal	Ideal thermodynamic cycle
l	Conducting lead
o	Effective electromotive force
oc	Open-circuit
sat	Liquid-vapor saturation line
th	Thermal

## 2.2 TYPES of AMTEC CELLS and OPERATION PRINCIPLE

Using Beta-Alumina solid electrolytes in conjunction with liquid sodium (Na) to convert heat to electricity had been demonstrated in a patent assigned to the Ford Motor Company (Kummer and Weber 1968). In 1974, the operating principle of a liquid anode, Alkali-Metal Thermal-to-Electric Converter (AMTEC) cell, was described by Weber (1974). AMTEC converters are high-temperature regenerative concentration cells, which employ an alkali metal (such as sodium or potassium) and directly convert heat to electricity. The key component in an AMTEC is the Beta"-Alumina Solid Electrolyte (BASE), a sodium-ion conductor whose ionic conductivity is much larger than its electronic conductivity (Weber 1974 and Cole 1983). The BASE, a crystalline solid with a nominal composition  $\text{Na}_{5/3}\text{Li}_{1/3}\text{Al}_{32/3}\text{O}_{17}$ , is usually fabricated as a dense micro-crystalline sintered ceramic. Early work at the Ford Motor Company has shown that the BASE was durable and trouble-free at temperatures as high as 1300 K, which is 700 K higher than that in sodium-sulfur batteries.

The BASE divides the cell into two separate regions: (a) a heated region filled with high pressure (10-100 kPa) sodium vapor or liquid (at  $\sim 1100$  K); and (b) a cooled (low-pressure) sodium vapor region (Figure 2.1). A porous metal electrode (cathode) covers the low-pressure (outer) side of the BASE, to provide a conduction path for the electrons to the external load. In a vapor-anode AMTEC cell, the inner surface of the BASE tube (anode) is also covered with a porous electrode. In liquid-anode cells, the anode electrode is not needed, since liquid sodium is a good electric conductor.

A substantial amount of work has been devoted to developing and understanding the limiting processes of the AMTEC electrode. The role of the cathode electrode is to provide a conductive path for the electrons to the low-pressure side of the BASE, where they recombine with the sodium ions exiting the surface. These electronic currents are relatively large due to the low voltage / high current nature of AMTEC devices. The sheet resistance (in the plane) of the electrode must be kept small in order to avoid compromising the cell output power. At the same time, the electrode must be highly permeable to the neutral sodium atoms in order to prevent a back pressure buildup (concentration losses) at the BASE/cathode interface, which would

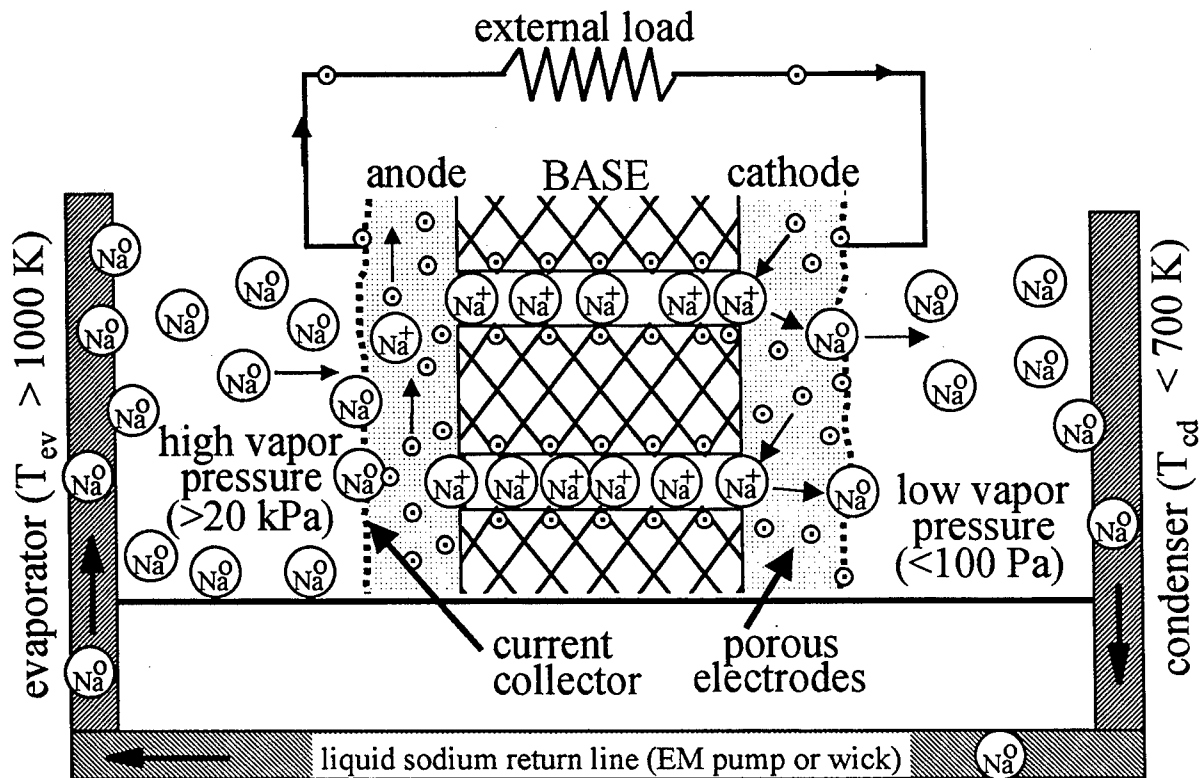


Figure 2.1. A Schematic Diagram of Sodium AMTEC Operating Cycle Showing Microscopic Processes.

decrease the cell effective voltage. A high-performance electrode therefore: (a) has good electrical conductivity; (b) makes a strong physical bond with the BASE, with a low contact resistance; (c) is highly permeable to sodium vapor; (d) resist corrosion by sodium; (e) has low material loss rate due to chemical reaction with metallic and gaseous impurities or by sublimation at BASE temperatures of  $\sim 1200$  K; and (f) experiences slow grain growth and material migration (Ryan et al. 1998). Current electrodes are made of refractory metal particles (titanium nitride, TiN), few  $\mu\text{m}$  in diameter, that are applied onto the BASE tube's outer surface by Chemical Vapor Deposition or sputtering techniques. A special (Weber) process is used to paste a (thicker) TiN electrode on the inside surface of the BASE tube.

Electrical leads connect the anode and cathode to the external electric load. The pressure differential across the BASE causes electrochemical expansion of sodium ions ( $\text{Na}^+$ ). The thermodynamic potential across the BASE causes ionization of the sodium atoms on the hot-side. The Na ions diffuse through the BASE toward the cathode, while the electrons circulate through the external load, producing electrical work. The electrons then return to the cathode, where they recombine with the sodium ions at the interface between the BASE and the cathode porous electrode (Figure 2.1). The resulting low-pressure, neutral sodium vapor (20–60 Pa) diffuse through the cathode electrode, traverse the vapor space and reach the radiator (or heat sink,  $\sim 600$  K), where it condenses. A wick structure or electromagnetic pump returns the liquid

condensate from the radiator (or condenser) to the high temperature (or anode) side of the BASE to complete its circulation (Figure 2.1).

The AMTECs developed in the 1980s were liquid anode, single-tube converters and employed sodium working fluid. In these converters, liquid sodium was in direct contact with the high-pressure side of the BASE, and there was no need for an anode electrode, since liquid sodium is a good electrical conductor. Liquid anode converters, however, have a limited volumetric power density. To reduce the size and the mass of the cell and improve its efficiency, the amount of BASE tube surface area that can be located in a given volume must be increased. Volumetric power density ( $W_e/\text{cm}^3$ ) can be increased by reducing the diameter and increasing the number of the BASE tubes. This design approach is used in vapor anode, multi-tube cells. In a liquid-anode cell, since liquid sodium is a good electrical conductor, it is difficult to electrically insulate the BASE tubes in a multi-tube cell from the cell wall and from each other. Series connection of liquid anode BASE tubes within one cell wall is a challenging engineering problem that has not yet been solved. On the other hand, in a vapor anode, multi-tube AMTEC cell, several BASE tubes can be easily connected in series, consequently increasing the volumetric power density of the cell. Such multi-tube cell designs are being developed for launch on board the NASA Pluto/Express mission, early next century.

In a vapor-anode cell, the liquid condensate is returned to the evaporator end of the wick by capillary action, and is converted into a high pressure vapor, with the heat input to the evaporator (Figs. 2.1 and 2.2). This vapor then travels to the anode side of the BASE tube, which is maintained at a slightly higher temperature than the evaporator, to prevent condensation of the working fluid onto the anode side of the BASE tube and possibly electrically shorting the BASE tubes of the cell.

### **2.3 DESCRIPTION of PX-TYPE, VAPOR ANODE, MULTI-TUBE AMTEC CELLS**

In a vapor anode, multi-tube AMTEC cell employing sodium working fluid, the BASE electrodes are connected in series to increase the output voltage of the cell (2-3.5 V), and the BASE tubes are electrically insulated from each other and from the cell wall. This, however, is not possible in liquid-anode cells, since liquid sodium is a good electrical conductor. Consequently, vapor anode, multi-tube cells have lower specific mass ( $\text{kg}/W_e$ ) than single tube cells, and are attractive for potential space applications.

During the past two years, several vapor anode, multi-tube cells have been fabricated by AMPS and tested in vacuum at AFRL (Merrill et al. 1997 and 1998). A parallel effort included developing an accurate physical model of these cells. This comprehensive testing and modeling program has been underway at AFRL, jointly with UNM-ISNPS and Nichols Research, Inc., since 1996, to advance the technology of multi-tube AMTEC cells for flight on future US Air Force missions.

These cells are also being considered for providing electric power on board the NASA's Pluto Express (PX) flyby and Europa spacecraft, scheduled for launch early next century. The power

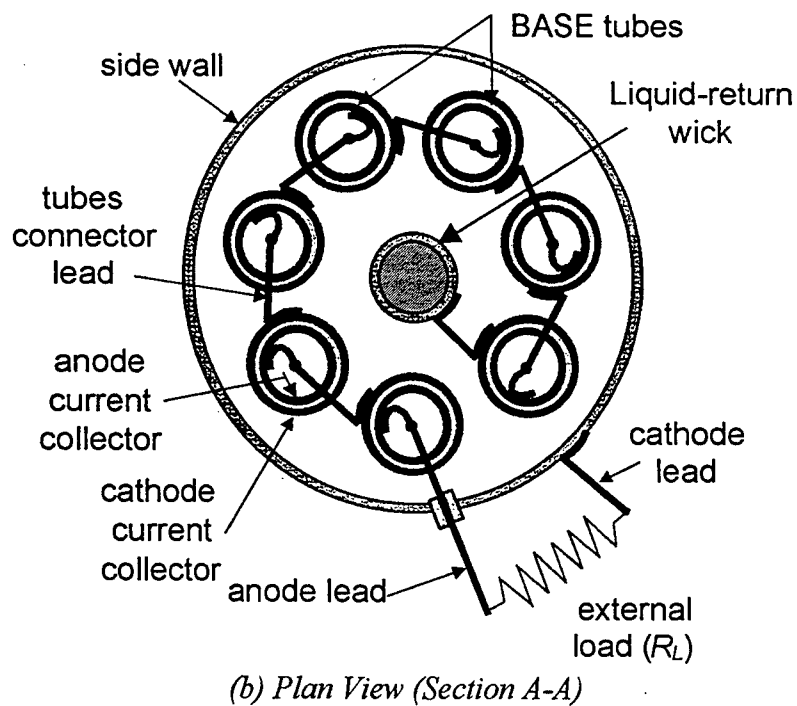
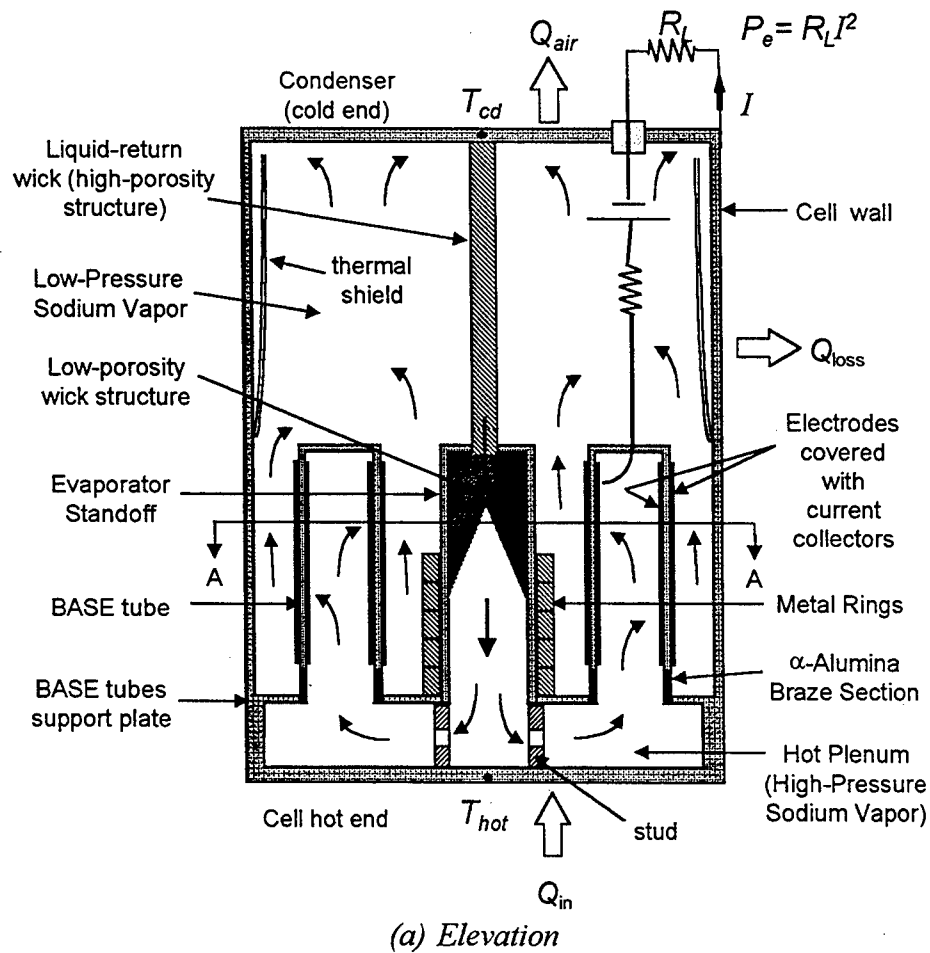


Figure 2.2. Cross Section Views of Vapor Anode, Multi-Tube AMTEC Cell (Not to Scale).

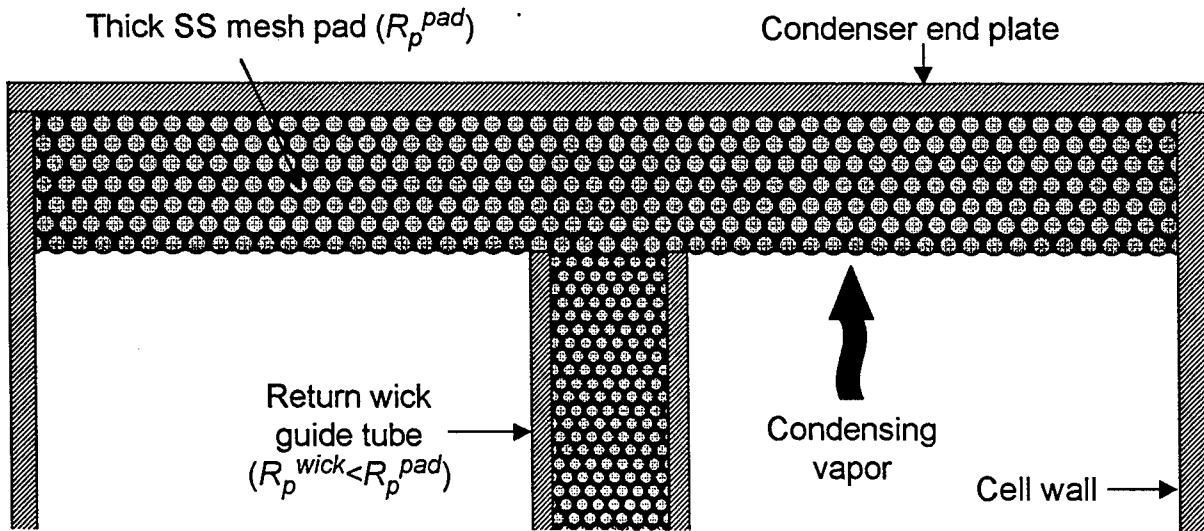
requirement for the PX-mission is 130 W<sub>e</sub> for 14 years, at a load voltage of 28 V d.c.. One proposed PX power system consists of 2 or 3 <sup>238</sup>PuO<sub>2</sub> radioisotope heat source modules (each provides ~220 W<sub>th</sub>) and 8-16 AMTEC cells, in two parallel strings (Schock et al. 1998). The PX-type cells tested at AFRL incorporated several design changes such as: (a) number and dimensions of BASE tubes and length of electrodes; (b) interior structure design and materials; (c) geometry and material of heat shield; (d) condenser wick type; and (e) characteristics and shape of the evaporator wick.

As shown in Fig. 2.2, the PX-series cells designed by AMPS had five, six or seven BASE tubes each and a central felt-metal wick for returning the liquid sodium working fluid to the cell evaporator. The BASE tubes and the housing of the evaporator assembly are brazed to a stainless steel (SS) support plate. The low-pressure side (cathode) and high-pressure side (anode) of the BASE tubes are covered with titanium nitride (TiN) porous electrodes and molybdenum mesh current collectors (to minimize internal electrical losses), and the BASE tubes are electrically connected in series. Series connection of AMTEC cells provides the desired d.c. load voltage for the spacecraft bus. The heat input to the cell hot plate is transported by conduction and radiation to the BASE tubes and the evaporator structure. The PX-series cells use a circumferential radiation shield, laid against the cell wall above the tubes, to reduce parasitic heat losses to the cell wall. Some of the PX-cells employ a solid conduction stud to enhance heat conduction from the hot plate to the evaporator and the BASE tubes's support plate. In addition, several solid metallic rings are placed around the evaporator standoff. These rings enhance the conduction path between the BASE tubes support plate and the cell evaporator, increasing the evaporator temperature and the sodium anode pressure in the cell. The conical evaporator structure provides a larger surface area for evaporating the liquid sodium returning from the condenser (Fig. 2.2a), and the depth of the evaporator cone can be adjusted commensurate with the desired cell performance. The BASE tubes temperature is kept slightly higher than that of the evaporator, to prevent condensation of the working fluid onto the anode side of the BASE tube and electrically shorting the BASE tubes in the cell.

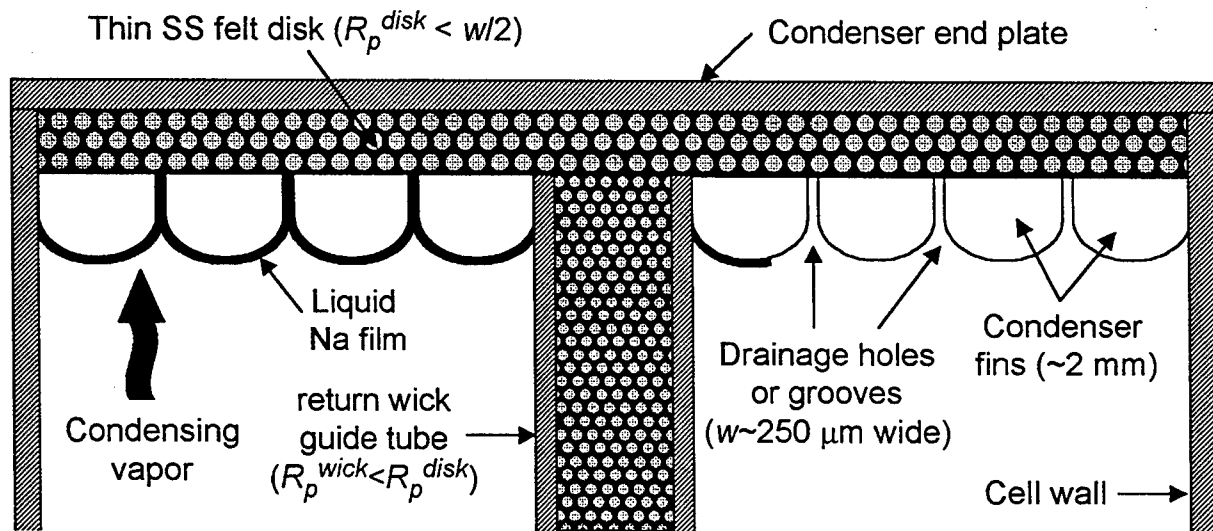
Also, the condenser's wick structure, which maintains a continuous thin film of liquid sodium on its surface, effectively reflects thermal radiation toward the interior, hence reducing parasitic heat losses. Figure 2.3 shows two types of condenser wick structures that have been used in PX-cells. The SS mesh pad has been shown to develop dry patches and hence, increase parasitic heat losses, resulting in lower cell electric power output and conversion efficiency (Fig. 2.3a). The Creare wick, however, ascertains that a continuous film of sodium is maintained on its surface (Fig. 2.3b). It provides a capillary force one order of magnitude larger than the hydrostatic force at earth gravity, forcing liquid sodium to spread uniformly on the surface of the wick (Crowley and Izenzon 1993). The small longitudinal grooves facilitate the flow of condensed liquid sodium to the underlying thin SS felt wick structure (Fig. 2.3b). This wick structure is hydro- dynamically coupled to that of the liquid return wick in the central guide tube. The cells equipped with a Creare condenser wick have performed markedly better than those with a SS mesh pad condenser.

The liquid-return wick has a smaller pore size than the condenser wick structure. However, the pore size and the permeability of the former must be selected carefully, since they have competing effects. For example, decreasing the pore size of the wick increases its capillary pumping power,





(a) Stainless-steel Mesh Pad Condenser Wick



(b) Creare Condenser Wick

Figure 2.3. Condenser wick types employed in PX-Series AMTEC Cells.

but reduces its effective permeability, hence increasing the pressure losses in the wick. Such increase in pressure losses might exceed the capillary pressure head of the wick, causing the evaporator to dry out. Therefore, in order to keep the pressure losses in the liquid-return wick low, while providing high capillary pressure head, composite wick structures are being used (Fig. 2.2a).

The liquid transport section of the wick, that extends from the cell condenser to near the evaporator surface, is made of a relatively large pore size, high permeability metal wick structure.

The evaporator wick, however, is made of a very small pore size structure to provide high capillary pumping power and generate higher vapor. The maximum capillary pressure rise across the liquid-vapor meniscus is directly proportional to the surface tension of liquid sodium at the evaporator temperature, and inversely proportional to the maximum radius of evaporator wick pores.

Another key component is the ceramic-metal brazes between the BASE tubes and the SS support plate. Because the BASE supports the sodium pressure differential between the high vapor pressure plenum and the low pressure cathode region, these joints must be sealed well. These brazes must have a good thermal conductance, but very low electrical conductance. High quality, high purity  $\alpha$ -alumina, which is compatible with sodium, is used to electrically insulate the BASE tubes from the SS support plate (Fig. 2.2a). Tantalum and molybdenum metals have a thermal expansion coefficient close to that of  $\alpha$ -alumina, and can be used in the joints. The BASE and the  $\alpha$ -alumina insulator are brazed to a molybdenum or tantalum tube using active-metal braze joints with nickel-titanium (NiTi) or nickel-zirconium (Ni-Zr) alloy filler materials. Tests have showed that NiTi active-metal brazed joints can perform well at temperatures as high as 1123 K.

When operating at high terminal voltage, some electrical (or electron) leakage between the anode and cathode electrodes can occur through the ceramic-metal braze, lowering the electric power output and conversion efficiency of the cell. The effect of such current leakage, however, has been found to be negligible in cells with properly fabricated braze joints, or when operating in the low-voltage region.

## 2.4 THERMODYNAMIC CYCLE and EFFICIENCY of an IDEAL AMTEC CYCLE

The efficiency of an ideal AMTEC cell can be calculated from the thermodynamic diagram of the cycle. The Pressure-Volume diagram of a sodium AMTEC cycle is shown in Figure 2.4. In a vapor-anode AMTEC (without condensation of sodium on the surface of BASE tubes), sodium is vaporized at a temperature  $T_{evap} = T_B - \Delta T_{evap}$ , below the BASE temperature, and remains in the vapor state as it heats up to the BASE temperature. The ideal thermodynamic cycle for a vapor-anode AMTEC is represented by the path [f',g',a'',a',c,d,e,f'], and is comprised of the following processes:

- [f',g']: pressurized liquid sodium is heated from condenser temperature to evaporator temperature at constant pressure ( $P=P_a$ );
- [g',a'']: the saturated liquid is vaporized at constant evaporator temperature and pressure ( $T=T_{evap}$ ,  $P=P_a$ );
- [a'',a']: the saturated vapor is heated further to the BASE temperature at constant pressure ( $P=P_a$ );
- [a',c]: sodium ions undergo isothermal expansion through the Beta"-Alumina Solid Electrolyte ( $T=T_B$ );
- [c,d]: low-pressure vapor leaving the BASE cools down to the heat sink temperature;
- [d,e]: condensation of vapor onto the surface of the radiator ( $T=T_{cond}$ ,  $P=P_{cond}$ ); and
- [e,f]: liquid condensate is pumped from the condenser to the evaporator pressure at constant temperature ( $T=T_{cond}$ ).

The ideal cycle for a liquid-anode AMTEC (or with liquid sodium in contact with the hot surface of the BASE) is represented by the path [f,g,a,c,d,e,f] in Figure 2.4. Liquid sodium is vaporized at the BASE temperature ( $\Delta T_{\text{evap}} = 0$ ), and the states [a'] and [a''] coalesce into the saturated state [a].

The ideal thermodynamic efficiency of a vapor-anode AMTEC cycle,  $\eta_{\text{ideal}}$ , is the ratio of the useful work to the total heat input,  $Q_{\text{in}}$ , the latter being equal to the area under [f',g',a'',a',c] in the Temperature-Entropy Diagram (Figure 2.5):

$$Q_{\text{in}} = \int_{f'}^{g'} dh + \int_{g'}^{a''} dh + \int_{a''}^{a'} dh \quad (2.1a)$$

From classical thermodynamics (Saad 1966), one finds ( $Tds = dh - vdP$ ):

$$\begin{aligned} W_{\text{work}} &= \int_{a'}^c Tds = \int_c^{a'} vdP = rT_B \ln(P_{a'}/P_c), \quad W_{\text{pump}} = \int_{f'}^e Tds = \int_e^{f'} vdP = v_L(P_{a'} - P_{\text{cond}}), \\ \int_{f'}^{g'} Tds &= \int_{f'}^{g'} dh = h_L(T_{\text{evap}}) - h_L(T_{\text{cond}}), \quad \int_{g'}^{a''} Tds = \int_{g'}^{a''} dh = h_V(T_{\text{evap}}) - h_L(T_{\text{evap}}) = h_{LV}(T_{\text{evap}}), \\ \int_{a''}^{a'} Tds &= \int_{a''}^{a'} dh = h_V(T_B) - h_V(T_{\text{evap}}) = h_L(T_B) + h_{LV}(T_B) - [h_L(T_{\text{evap}}) + h_{LV}(T_{\text{evap}})]. \end{aligned} \quad (2.1b)$$

Therefore, the cycle efficiency has the following expression:

$$\eta_{\text{ideal}} = \frac{W_{\text{work}} - W_{\text{pump}}}{Q_{\text{in}}} = \frac{rT_B \ln(P_{a'}/P_c) - W_{\text{pump}}}{h_L(T_B) - h_L(T_{\text{cond}}) + h_{LV}(T_B)} \quad (2.2)$$

This expression assumes that the vapor obeys the perfect gas law ( $Pv = rT$ ) and that the enthalpies are solely functions of temperature. The pumping work in Equation (2.2) can be neglected in practice due to the small specific volume of the liquid,  $v_L$  ( $W_{\text{pump}}$  is about 4 orders of magnitude smaller than the expansion work).

The ideal AMTEC cycle described here is very close to the Carnot cycle. The actual AMTEC efficiency is lower than the Carnot efficiency as a result of the irreversibility of the process [c,d]. In theory, the sensible heat of the low-pressure vapor could be converted to mechanical energy by an adiabatic expansion. However, the vapor density is so low at state [c] that this sensible heat cannot be recuperated in practice.

The working fluid pressure at state [a'], at the anode electrode/BASE interface (see Figure 2.4), is equal to the saturation vapor pressure at the evaporator temperature:  $P_{a'} = P_{\text{sat}}(T_B - \Delta T_{\text{evap}})$ . The pressure at state [c], at the cathode electrode/BASE interface, is a function of the mass flow rate of sodium. Because of the very low vapor pressure of sodium and the relatively low condenser

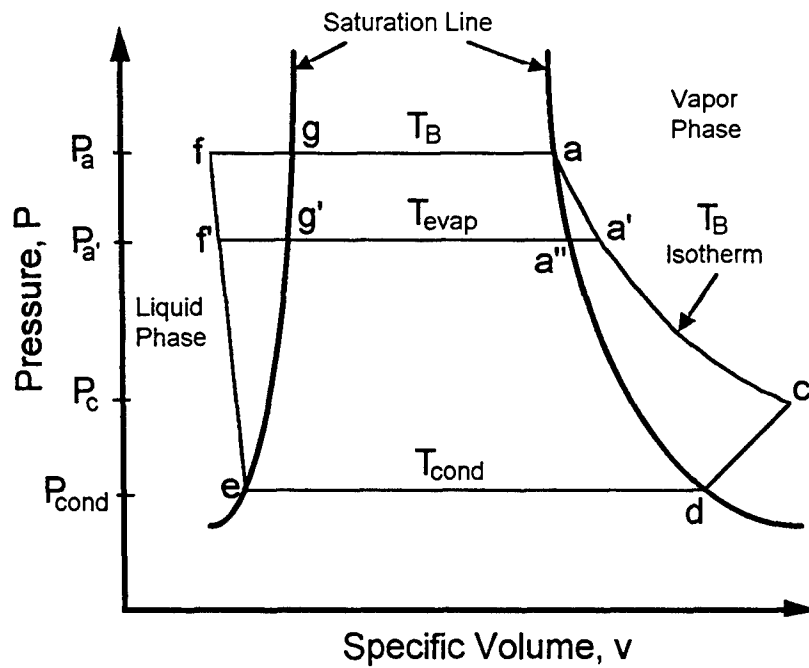


Figure 2.4. Pressure-Volume Thermodynamic Diagram of a Sodium AMTEC Cycle.

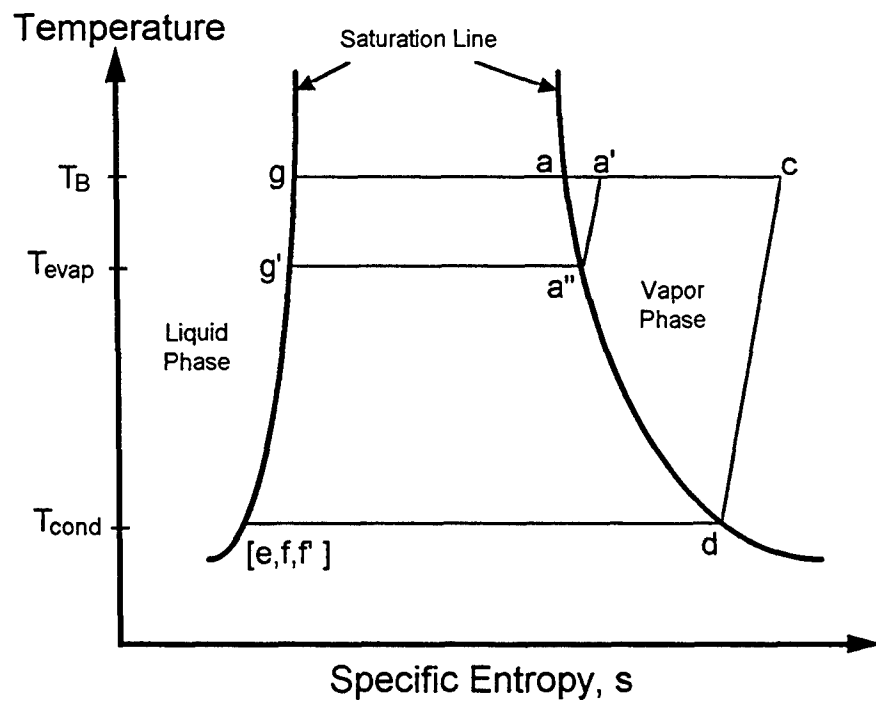


Figure 2.5. Temperature-Entropy Thermodynamic Diagram of a Sodium AMTEC Cycle.

temperatures of interest (450 K to 650 K), the vapor flow is in the transition or free-molecular regime (Tournier and El-Genk 1996) along the path [c,d]. This is also true in the microscopic pores of the cathode electrode. For an open circuit, there is no net sodium flow between the cathode electrode and the heat rejection condenser, and the vapor pressure at state [c] is controlled by molecular effusive flow, and is given by the Langmuir relation (Kennard 1938):

$$\dot{m}_{cd}'' = \frac{1}{\sqrt{2\pi r}} \left[ \frac{P_c^{oc}}{\sqrt{T_B}} - \frac{P_{cond}}{\sqrt{T_{cond}}} \right] = 0, \quad \text{or} \quad P_c^{oc} = P_{cond} \sqrt{\frac{T_B}{T_{cond}}} \quad (2.3)$$

The following properties were used herein. The heat capacity of liquid sodium is essentially constant over the temperature range of interest, and is taken equal to  $C_p = 1,285$  J / kg.K. The vapor pressure of sodium is expressed by the relation:  $\log_{10}(P_{sat}) = 9.678 - 5,383.2/T$ , with an error of less than 4%, when compared to Ditchburn's correlation of experimental data of 11 investigators (Bomelburg and Smith 1972). The latent heat of vaporization, determined by the Clausius-Clapeyron equation (Saad 1966), has a constant value  $h_{LV} = r \times \ln(10) \times 5,383.2 = 4,480$  kJ / kg.

Figure 2.6 shows the thermodynamic efficiency of an ideal liquid-anode ( $\Delta T_{evap} = 0$ ) AMTEC cycle (with no internal polarization, concentration nor parasitic heat losses), as a function of BASE and condenser temperatures. This efficiency is greater than 89.5% of the Carnot efficiency ( $\eta_{carnot} = 1 - T_{evap} / T_{cond}$ ) over the entire range of temperatures of interest. At representative BASE and condenser temperatures of 1200 K and 550 K, respectively, the Carnot efficiency is 54.2% and the ideal cycle efficiency is 49.1%, or 90.6% of Carnot. AMTEC devices have the highest intrinsic efficiency of all known heat engines (static and dynamic), which makes them very attractive, particularly for space applications.

Figure 2.7 shows the thermodynamic efficiency of an ideal vapor-anode AMTEC cycle (with no internal polarization, concentration nor parasitic heat losses) as a function of BASE and evaporator temperatures, for a condenser temperature of 550 K. For a fixed value of  $\Delta T_{evap}$ , the efficiency of an ideal vapor-anode AMTEC increases with increasing BASE temperature, and is very comparable to that of an ideal liquid-anode AMTEC for a BASE temperature above 1100 K. For representative values of  $T_B = 1200$  K and  $\Delta T_{evap} = 40$  K, the ideal cycle efficiency is 48.4%, or 89.3% of Carnot. Clearly, ideal vapor-anode AMTEC cycles can be as efficient as liquid-anode AMTEC cycles, given that  $(T_B - T_{cond})$  is large compared to  $\Delta T_{evap}$ .

## 2.5 EFFECT of PRESSURE LOSSES on EFFICIENCY of an IDEAL AMTEC CYCLE

When the external electric circuit is closed, there is a net sodium flow and the pressure at state [c] is augmented by the pressure losses,  $\Delta P_{cd}$ , between the cathode electrode/BASE interface and the condenser, along the path [c,d] (Figure 2.4). The effect of sodium flow on the AMTEC cell voltage is often referred to as concentration loss or concentration overpotential. In the free-molecular flow regime of sodium vapor in the cell, this vapor pressure loss is proportional to the flow rate. If  $\Delta P_{cd}$  is approximated by the pressure losses through the porous electrode, the

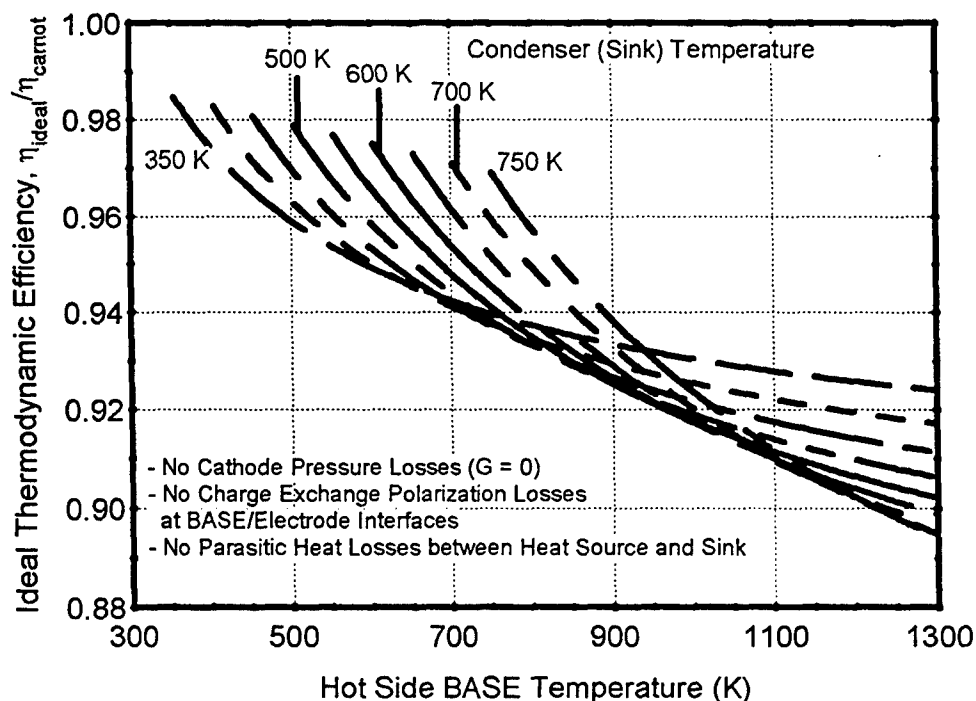


Figure 2.6. Thermodynamic Efficiency of an Ideal Liquid-Anode Sodium AMTEC as a Fraction of Carnot Efficiency.

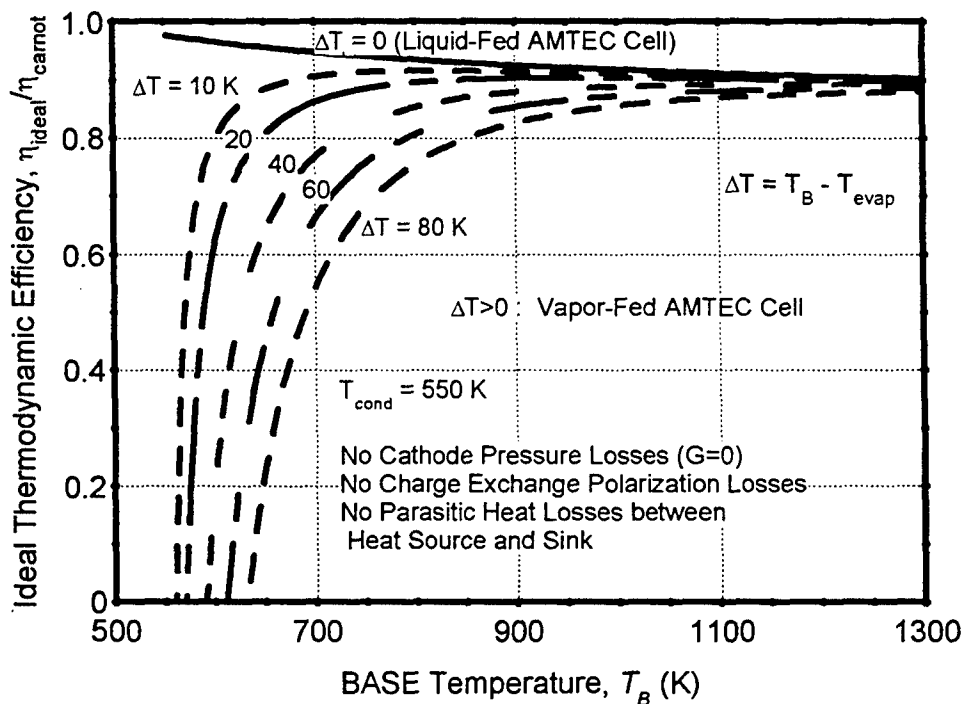


Figure 2.7. Thermodynamic Efficiency of an Ideal Vapor-Anode Sodium AMTEC as a Fraction of Carnot Efficiency.

sodium pressure at state [c], the interface between the cathode electrode and the BASE, has the expression:

$$P_c = P_c^{oc} + \Delta P_{cd} = P_c^{oc} + \sqrt{2\pi r T_B} \left( \frac{3G}{8\pi} \right) \frac{MJ}{F}, \quad (2.4)$$

where  $G$  is a dimensionless geometric factor that should be determined experimentally.

Figure 2.8 shows the efficiency of the AMTEC cycle (as a fraction of ideal cycle efficiency) as a function of the geometric factor  $G$  and electrode current density  $J$ . For values of  $G$  less than 10, the cycle efficiency is above 90% of ideal cycle efficiency. Such values are typical for thin electrodes in early cell designs, in which the cylindrical cell wall constituted the condenser. However, such designs were characterized by very large radiation parasitic losses, and hence low conversion efficiency. To reduce these parasitic losses and improve the efficiency of the cell, advanced designs have used internal radiation shields between the heat source and condenser, a remotely located condenser, or a combination of these two (Ivanenok et al. 1994). While significantly reducing the radiation parasitic losses, these new designs are characterized by higher vapor pressure losses on the cathode side, with typical values of the geometrical factor  $G$  between 50 and 150 (the new design resulted in an improved overall efficiency, however). As shown in Figure 2.8, the cycle efficiency decreases with increasing  $G$ , and can be as low as 76% of ideal cycle efficiency at  $G = 100$  and a current density of  $2 \text{ A/cm}^2$ . At representative values of  $G = 50$  and  $J = 2 \text{ A/cm}^2$ , the AMTEC cycle theoretical efficiency is 39.9%, or 81.2% of ideal cycle efficiency.

## 2.6 AMTEC CELL VOLTAGE and INTERNAL ELECTRICAL LOSSES

The open-circuit voltage in a AMTEC is given by the well-known Nernst equation, described later (Cole 1983). The internal electrical losses of the device consist of the charge exchange polarization losses at the BASE/electrode interfaces, the ionic resistance of the BASE, the contact resistance of the electrodes, the sheet resistance in the plane of the electrodes, and the resistances of the current collectors, bus wires and conductor leads to the load. These losses are discussed in the following subsections.

### 2.6.1 AMTEC Cell Voltage, and Concentration and Charge-Exchange Polarization Losses

Neglecting the Seebeck voltage generated by the radial temperature gradient across the BASE (Weber 1974), the effective electromotive force of the cell can be written as:

$$V_o^{cc} = V^{oc} - \zeta_a - (-\zeta_c), \quad (2.5)$$

where the open-circuit voltage is proportional to the isothermal expansion work of sodium ions in the BASE, and is given by the Nernst equation (Cole 1983):

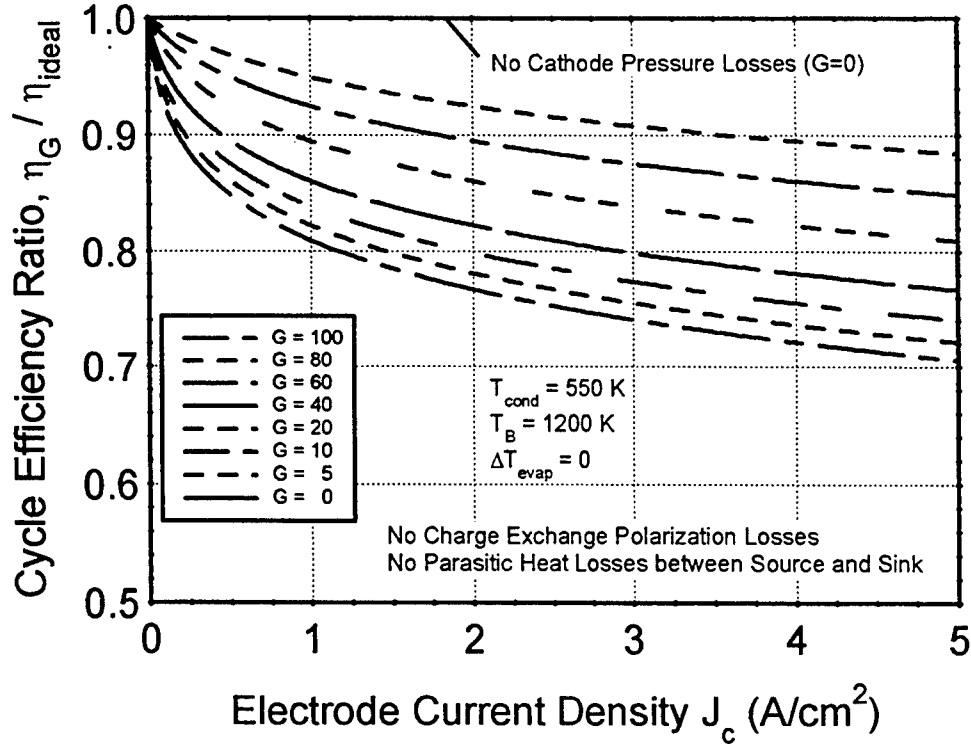


Figure 2.8. Effect of Cathode Vapor Pressure Losses on the Efficiency of an Ideal Sodium AMTEC.

$$V^{oc} = \frac{R_g T_B}{F} \ln(P_a^{oc} / P_c^{oc}) = \frac{1}{f_B} \ln(P_a^{oc} / P_c^{oc}) \quad (2.6)$$

The concentration and charge-exchange polarization overpotentials at the anode and cathode are given by the Butler-Volmer equation (Williams et al. 1990a, Underwood et al. 1992):

$$\frac{J_i}{J_i^{ex}} = \exp[-\alpha f_B \zeta_i] - \frac{P_i^{cc}}{P_i^{oc}} \exp[(1 - \alpha) f_B \zeta_i]. \quad (2.7)$$

The subscript 'i' in Equation (2.7) stands for either 'a' (anode) or 'c' (cathode). For a symmetric barrier, the electrochemical transfer coefficient  $\alpha = 1/2$ , and Equation (2.7) can be inverted to give the polarization overvoltage explicitly in terms of the cell's current density (see Section 4.2):

$$\zeta_i = -\frac{2R_g T_B}{F} \ln \left\{ \frac{1}{2} \left[ \left( \frac{J_i}{J_i^{ex}} \right)^2 + 4 \frac{P_i^{cc}}{P_i^{oc}} \right]^{1/2} + \frac{1}{2} \frac{J_i}{J_i^{ex}} \right\}. \quad (2.8)$$



The overpotential,  $\zeta_i$ , increases logarithmically with the cell current, reducing the voltage potential across the BASE. In Equation (2.8),  $\zeta_c < 0$ ,  $\zeta_a > 0$ , and  $J_c = -J_a$  for a thin BASE membrane. The charge-exchange current densities,  $J_i^{ex}$ , a measure of the effective local conductance at the BASE/sodium ions/electrode grains triple points, are related to the saturated equilibrium exchange-current density,  $J_{sat}^{ex}$ , as (Williams et al. 1990a and 1990b):

$$J_i^{ex} = J_{sat}^{ex} \left[ \frac{P_i^{oc}}{P_{sat}(T_B)} \right]^\alpha \quad (2.9)$$

Since the sodium vapor pressure at the cathode ( $P_c^{cc} < 50$  Pa) is several orders of magnitude smaller than that at the anode ( $P_a^{cc} \sim 15\text{--}60$  kPa), the anode exchange-current density is much larger than the cathode exchange-current density, hence the polarization overpotential on the anode side,  $\zeta_a$ , is negligible. Experimental investigations have shown that the saturated equilibrium exchange-current density,  $J_{sat}^{ex}$ , is essentially a function of the BASE temperature and of the type of electrodes. It can be expressed as (Williams et al. 1990a, Underwood et al. 1992):

$$J_{sat}^{ex} = B \times \frac{P_{sat}(T_B)}{\sqrt{T_B}}, \quad (2.10a)$$

where  $B$  is the temperature-independent charge-exchange coefficient, expressed in units of  $\text{A.K}^{1/2}/\text{Pa.m}^2$ . As a result:

$$J_i^{ex} = B \times \left[ P_i^{oc} P_{sat}(T_B) / T_B \right]^{1/2}. \quad (2.10b)$$

As shown in Equation (2.8), the concentration losses, or the effect of increased pressure at the BASE/cathode electrode interface (due to sodium vapor pressure losses in the low pressure cavity of the cell, Fig. 2.2a), increase with cell current or sodium flow rate. The pressure drop across the cathode electrode is expressed in terms of an empirical dimensionless factor  $G_E$ . Both  $B$  and  $G_E$  are characteristic of the type of electrodes used, and are determined experimentally. Typical TiN electrodes have  $B \sim 80$  SI and  $G_E \sim 50$  (Ryan et al. 1998).

When the charge-exchange polarization losses are negligible (i.e.  $B$  is infinite), the Nernst electromotive force of the AMTEC cell is reduced only by the concentration losses, and is proportional to the expansion work by sodium ions through the BASE, under load:

$$V_o^{cc} = V_o^{cell} \equiv \frac{1}{f_B} \ln \left[ P_a^{cc} / P_c^{cc} \right]. \quad (2.11)$$

### 2.6.2 Other Internal Electric Losses in an AMTEC

Current manufacturing processes allow deposition of mature electrodes with small contact resistances when compared to the BASE ionic resistance. To assess the importance of the sheet resistance, and resistances of the current collectors and bus wires, a one-dimensional electrical model was developed in this work, which included four current collector configurations (see Chapter 4). The first configuration consisted of a single wire wrapped around the BASE tube in a helix. The second configuration consisted of circular wires wrapped around the BASE tube at different heights, and connected to a larger axial collector lead (bus). The third configuration consisted of a metal sponge wrapped around the BASE tube and held in place by circular wires connected to an axial bus. Finally, the fourth current collector configuration consisted of one layer of wire screen mesh wrapped around the BASE tube and held in place by circular wires connected to an axial bus. The same current collectors could be used on the anode side of vapor-anode AMTEC cells. Results showed that, except for the case of a rather thick sponge collector, all current collectors investigated performed extremely well, with insignificant internal losses (see Chapter 4). These collectors provide enough contact points with the electrode to overcome the sheet resistance in the plane of the electrode. The main contributors to the electrical internal losses in the AMTEC, therefore, were found to be the BASE ionic resistance, the contact resistances between BASE/electrode/current collector, and the concentration and charge-exchange polarization losses on the cathode side.

### 2.6.3 Electrical Efficiency of an AMTEC

The electrical efficiency of the AMTEC cycle has the expression:

$$\eta_e = \frac{V_o^{cc} - (R'_B + R'_{cont})J}{V_o^{cell}}, \quad (2.12)$$

where the BASE ionic resistance is given by:

$$R'_B = \rho_B \times t_B. \quad (2.13)$$

The ionic resistivity of BASE is calculated using the correlation developed by Steinbruck et al. (1993):

$$\rho_B = T \left( 1.62 \times 10^{-5} e^{-45.5/T} + 1.55 \times 10^{-7} e^{+3,722./T} \right), \quad (2.14)$$

where  $T$  is expressed in Kelvin and  $\rho_B$  is in ( $\Omega \cdot m$ ). The contact resistance,  $R_{cont}$ , in Equation (2.12), accounts for the other electrical internal losses in the cell. Note that the concentration polarization losses at the BASE/electrode interfaces have already been included in the model through the pressure losses on the cathode side (on the anode side, the pressure losses are negligible when compared to the vapor pressure at the evaporator). The polarization overvoltage given by Equation (2.8) includes both the concentration and charge exchange polarization losses.

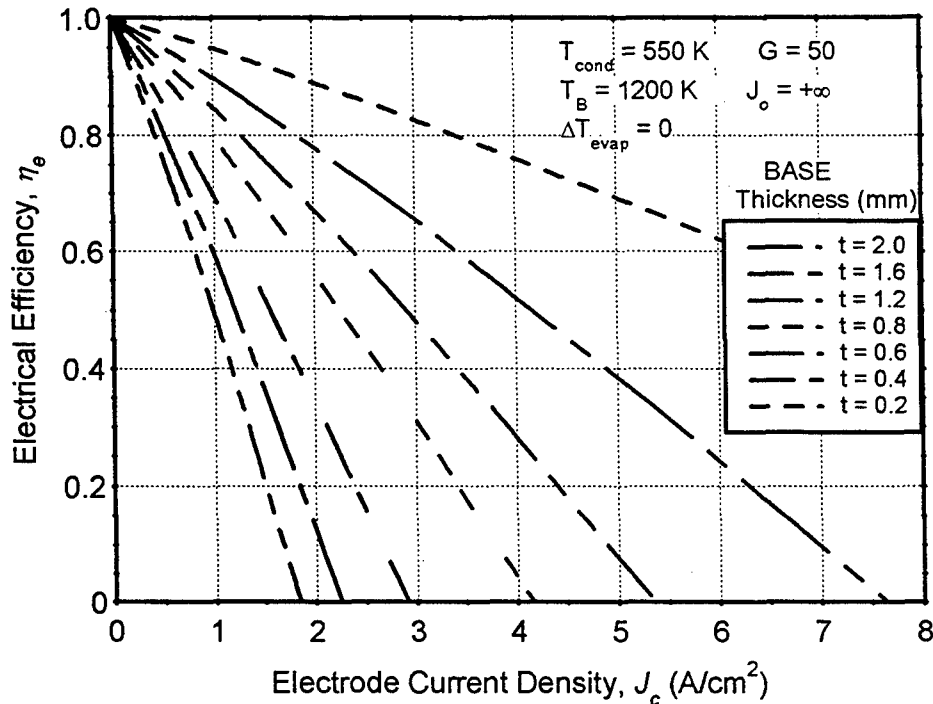


Figure 2.9. Electrical Efficiency of a Sodium AMTEC as a Function of BASE Ionic Resistance.

Figure 2.9 shows the electrical efficiency of a AMTEC with zero charge-exchange polarization losses ( $B$  is infinite) as a function of BASE thickness and electrode current density, for a geometric factor  $G=50$ , and BASE and condenser temperatures of 1200 K and 550 K, respectively. The efficiency decreases very rapidly with current density and BASE thickness. However, reducing the BASE wall thickness has adverse effects on the reliability of conventional seals. Thinner BASE walls are not strong enough to accommodate the stress caused by the thermal expansion mismatch between the BASE and the braze filler material. The failure of BASE tubes is promoted by improper electrical loading, thermal shock, or mechanical stress. In order to reduce stresses on the BASE tubes, electrical leads and mounting fixtures have been redesigned. Current collector leads, once solid copper bus bars, have been replaced with flexible braided copper wires.

BASE tubes of thickness 0.6 mm are commonly manufactured and can withstand the stresses, and this value is chosen in our analysis. At this thickness and a current density of 2 A/cm<sup>2</sup>, the electrical efficiency of the AMTEC is 67.2%, which gives an overall efficiency of  $\eta_G \times \eta_e = 26.8\%$ .

## 2.7 PARASITIC RADIATION LOSSES in an AMTEC CELL

In an AMTEC cell, parasitic thermal losses between heat source and heat sink cannot be fully avoided, and contribute greatly to reducing the efficiency of the cell. In the AMTEC cell, the

radiation heat loss from the BASE tubes to both the condenser and the cell wall surface is most significant (Underwood et al. 1990), and can be expressed as:

$$Q''_{rad} = \frac{\sigma}{Z} (T_B^4 - T_{cond}^4), \quad (2.15)$$

where  $Z$ , a geometric dimensionless factor, is function of surface emissivities and view factors. Early coaxial cell designs relied upon the assumption that evaporated sodium would coat the condenser surface and reflect radiation (the reflectivity of liquid sodium in the infrared is greater than 98%). In such case (Siegel and Howell 1981):

$$Z = \frac{1}{\varepsilon_B} + \frac{1}{\varepsilon_{cond}} - 1, \quad (2.16)$$

where  $\varepsilon_{cond}$  is equal to 0.02, the specular emissivity of liquid sodium, and  $\varepsilon_B$  is the effective emissivity of the BASE. Because the BASE is covered with the cathode electrode and the current collector, it has a rough surface which acts as a blackbody. Radiation experiments have shown that  $\varepsilon_B$  is typically 0.90 above 1100 K (Ryan et al. 1993), which gives a value  $Z = 50$ . However, AMTEC experiments revealed that sodium did not uniformly wet the stainless steel surface at the low condenser temperatures. With a stainless steel emissivity of 0.2, the  $Z$  factor could be as low as 5. The use of a condenser coating can further reduce the condenser effective emissivity. Present AMTEC cells employ a micro-machined (CREARE) condenser surface or a wire-mesh fixed to the condenser wall which acts as a wick to hold a substantial layer of liquid sodium on the surface, therefore reducing the effective emissivity (or absorptivity) of the condenser surface.

If a radiation shield made of  $N$  concentric metal foils with a surface emissivity  $\varepsilon_s$  were placed between the BASE tubes and the condenser, the  $Z$  factor would become (Siegel and Howell 1981):

$$Z = \frac{1}{\varepsilon_B} + \frac{1}{\varepsilon_{cond}} - 1 + N \left( \frac{2}{\varepsilon_s} - 1 \right). \quad (2.17)$$

For a radiation shield using thin molybdenum foils,  $\varepsilon_s = 0.15$ , and  $Z$  could be as much as 50 with only  $N = 4$ . It must be remembered, however, that such shields would impede the sodium vapor flow on the cathode side and could somewhat reduce the efficiency.

Numerical and experimental studies have shown that using a remote condenser has the potential of improving the cell efficiency even more (Ivanenok et al. 1994). In such a configuration, the hot and cold zones (high-temperature BASE tubes and low-temperature condenser surface) are isolated from one another, geometrically and thermally, significantly reducing the view factor and therefore increasing  $Z$ . The increase in vapor flow resistance between the BASE tubes and the condenser is more than compensated by the reduction in the radiation losses between the two surfaces. This configuration also improves the cell's reliability by reducing the thermal stresses on the BASE tubes.

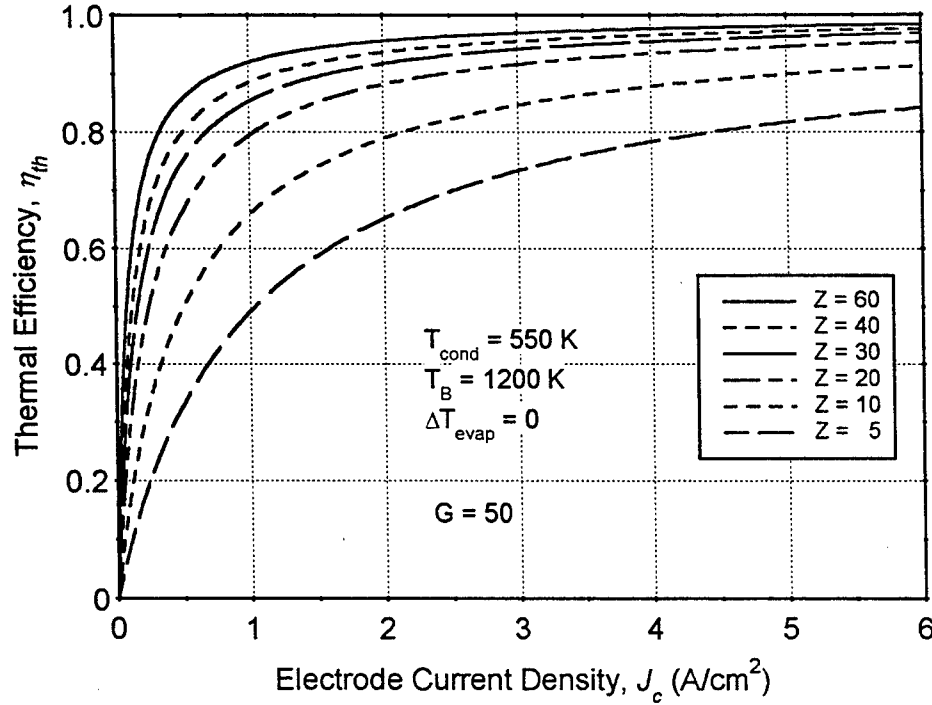


Figure 2.10. Thermal Efficiency of a Sodium AMTEC as a Function of Radiation Factor,  $Z$ .

### 2.7.1 Thermal Efficiency of an AMTEC Cell with Radiation Parasitic Losses

When radiation parasitic losses are accounted for, the thermal efficiency of the AMTEC cycle can be calculated as:

$$\eta_{th} = \frac{C_p^L(T_B - T_{cond}) + h_{LV}(T_B)}{C_p^L(T_B - T_{cond}) + h_{LV}(T_B) + Q_{rad}'' \times F / (MJ)} \quad (2.18)$$

This thermal efficiency is basically the ratio of the heat input of an ideal AMTEC cycle given by Equation (2.1) to the heat input of a cell with radiation parasitic heat losses. Figure 2.10 shows the effect of the geometric factor  $Z$  on the thermal efficiency of the AMTEC cycle as a function of the electrode current density  $J$ . The thermal efficiency increases with current density since the radiation heat loss is a constant function of the BASE and condenser temperatures only, while all other thermodynamic heat terms (such as heat of vaporization) are proportional to the current.

### 2.7.2 Overall Efficiency of AMTEC Cell with Internal Electrical and Heat Losses

When internal electrical and thermal losses are accounted for, the overall efficiency of the AMTEC cell can be expressed as:

$$\eta = \eta_G^{ideal} \times \eta_e \times \eta_{th} = \frac{I \times [V_o^{cc} - (R'_B + R'_{cont})J]}{[C_p^L(T_B - T_{cond}) + h_{LV}(T_B)] \times (IM)/F + A_E \times Q_{rad}''} \quad (2.19)$$

where  $\eta_G^{ideal}$  is the conversion efficiency of an ideal AMTEC cycle with sodium vapor pressure losses on the cathode side:

$$\eta_G^{ideal} = \frac{I \times V_o^{cell}}{[C_p^L(T_B - T_{cond}) + h_{LV}(T_B)] \times (IM)/F} \quad (2.19a)$$

$\eta_e$  is the electrical efficiency of the AMTEC cycle:

$$\eta_e = \frac{V_o^{cc} - (R'_B + R'_{cont})J}{V_o^{cell}} \quad (2.19b)$$

and  $\eta_{th}$  is the thermal efficiency of the AMTEC cycle:

$$\eta_{th} = \frac{C_p^L(T_B - T_{cond}) + h_{LV}(T_B)}{C_p^L(T_B - T_{cond}) + h_{LV}(T_B) + Q_{rad}'' \times F/(MJ)} \quad (2.19c)$$

The predicted thermodynamic efficiency and power density of a sodium AMTEC cycle with zero charge-exchange polarization losses and zero contact electrical resistances are shown in Figure 2.11 as a function of electrode current density and radiation geometric factor. Representative values of  $T_B = 1200$  K,  $T_{cond} = 550$  K,  $t_B = 0.6$  mm, and  $G=50$  were used for this calculation. BASE tubes of thickness 0.6 mm are commonly manufactured and can withstand the stresses caused by the thermal expansion mismatch between the BASE and the braze filler material, and this value was chosen in our analysis. As Figure 2.11 shows, the peak efficiency occurs at a lower current density than the peak electrical power density. For a Z factor of 20 and a current density  $J = 2$  A/cm<sup>2</sup>, the thermal efficiency is 88% and the overall thermodynamic efficiency of the cell is 23.6%. If the radiation factor is increased to  $Z = 40$ , the thermal and overall thermodynamic efficiencies of the cell increase to 93.7% and 25.1%, respectively. Assuming an electrode area of 10 cm<sup>2</sup>, the total cell current is  $I = 20$  A. The cell provides an expansion work rate of 16.68 W, which is converted into 11.2 We of electric power in the external load; the remainder, 5.48 We, represents the internal electrical losses (ionic losses in the BASE). The sensible and vaporization heats of sodium in the cell amount to 25.12 W, and the parasitic radiation heat losses amount to 5.62 W for  $Z = 20$ , and to 2.81 W for  $Z = 40$ .

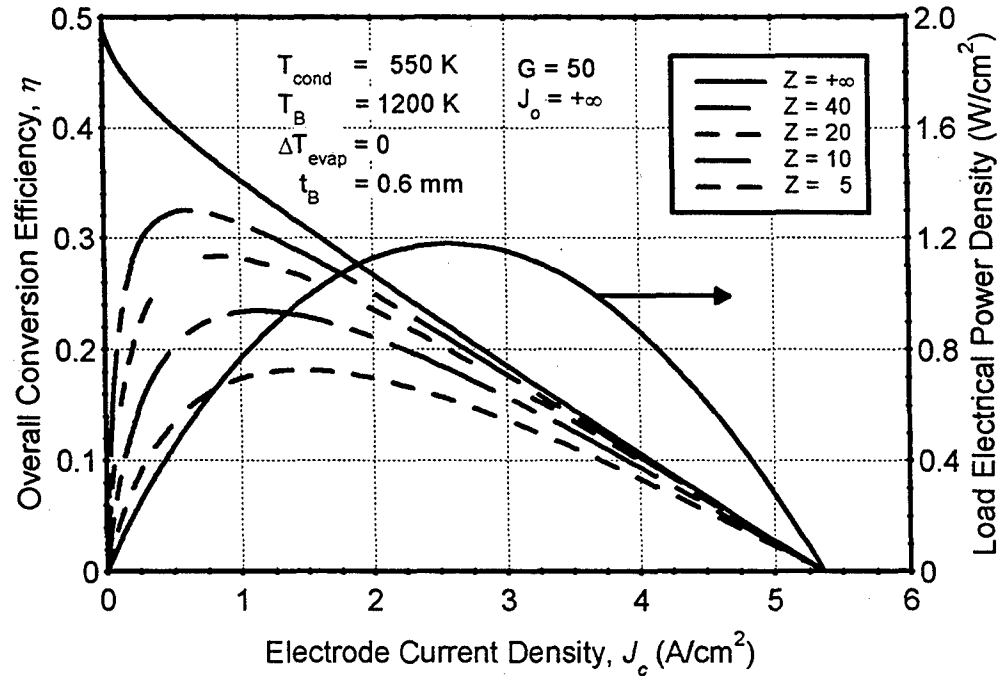


Figure 2.11. Conversion Efficiency and Power Density of a Sodium AMTEC with Zero Charge-Exchange Polarization Losses.

## 2.8 JOULE and THERMAL CONDUCTION LOSSES in CURRENT LEADS to LOAD

Parasitic heat conduction losses in the AMTEC cell occur in the current leads, the liquid-sodium return wick and the cell wall. Most of these losses can be reduced to negligible values by careful design. For example, a cell wall made from low-conductivity materials, such as stainless steel or Inconel, reduces the conduction heat loss between the hot and cold ends of the cell. There is however a particular concern with the current leads, which connect the hot electrodes to the external load. The temperature of the latter is low, below the condenser temperature, and the current leads provide a heat conduction loss path to the load. While these conduction losses could be reduced by decreasing the leads cross section area, this would also increase the electrical resistance of the leads, increasing Joule losses. Therefore, there is an optimum value of the lead cross section which maximizes the efficiency of the cell. A model was developed to optimize the connecting lead dimensions.

The current leads are assumed to be thermally insulated on the outside, their thermal conductivity assumed constant, and their electrical resistivity is calculated as a function of temperature using the Wiedemann-Franz-Lorenz law (Angrist 1965):

$$\rho = \frac{\lambda T}{k}, \quad (2.20)$$

which holds over a wide range of temperatures for a variety of metal lead materials. The steady-state, one-dimensional conduction equation, with internal Joule heating in the lead can be written as:

$$k \frac{\partial^2 T}{\partial x^2} + \rho \left( \frac{I}{A_l} \right)^2 = 0. \quad (2.21)$$

Analytical solution of Equation (2.21), with the boundary conditions  $T(0) = T_B$  and  $T(L) = T_{cond}$  gives the following temperature profile along a current lead having a length  $L$  and cross section area  $A_l$ :

$$T(x) = T_B \cos(\delta x / L) + [T_{cond} - T_B \cos(\delta)] \frac{\sin(\delta x / L)}{\sin(\delta)}, \quad \text{where } \delta = \frac{\sqrt{\lambda}}{k} \frac{L}{A_l} I. \quad (2.22)$$

Figure 2.12 shows the effect of the dimensionless parameter  $\delta$  on the temperature profile along the lead. The temperature profile can deviate significantly from a linear profile as the current (or the parameter  $\delta$ ) is increased. The parameter  $\delta$  varies typically between 0.2 and 0.5 in an AMTEC cell. The resulting heat conduction loss at the lead's hot end and Joule heating in one lead are given by:

$$Q_{cd} = -kA_l \frac{dT(0)}{dx} = \frac{I\sqrt{\lambda}}{\sin(\delta)} [T_B \cos(\delta) - T_{cond}], \quad \text{and}$$

$$Q_J = \frac{I^2}{A_l} \int_0^L \rho dx = \frac{I\sqrt{\lambda}}{\sin(\delta)} (T_B + T_{cond}) \times [1 - \cos(\delta)]. \quad (2.23)$$

Figure 2.13 shows the variation of the heats conducted at the ends of the lead and of the heat dissipated in the lead by Joule effect as a function of  $\delta$ , when the BASE tube temperature is twice that of the cold end. As shown in this figure, a fraction of the Joule heating is conducted back to the hot end of the lead, while the remaining fraction is lost by conduction at the cold end. This arises from the energy balance in the thermally insulated lead. Therefore, the actual heat loss by conduction at the hot end decreases with increasing  $\delta$ , reaching zero at  $\delta = 1.04$  (Figures 2.12 and 2.13). At higher values of  $\delta$ , higher Joule heating in the lead would cause the maximum lead temperature to increase above the hot end temperature, causing a net thermal energy gain by the BASE tube. However, the electrical losses in the lead would be so large that the electrical efficiency of the cell would be negligibly small. In practice,  $\delta$  is less than 0.5, meaning that the current leads would always cause a net heat conduction loss for the BASE tube. When  $\delta$  is equal to 0.65, the Joule losses in the lead and the conduction heat loss at the hot end are equal (Figure 2.13). For smaller values of  $\delta$ , the Joule losses in the lead are smaller than the heat conduction loss.

When the joule and conduction losses in the leads are accounted for in a cell having  $N_s$  BASE tubes connected electrically in series (in a multi-tube cell configuration), Joule heating in one



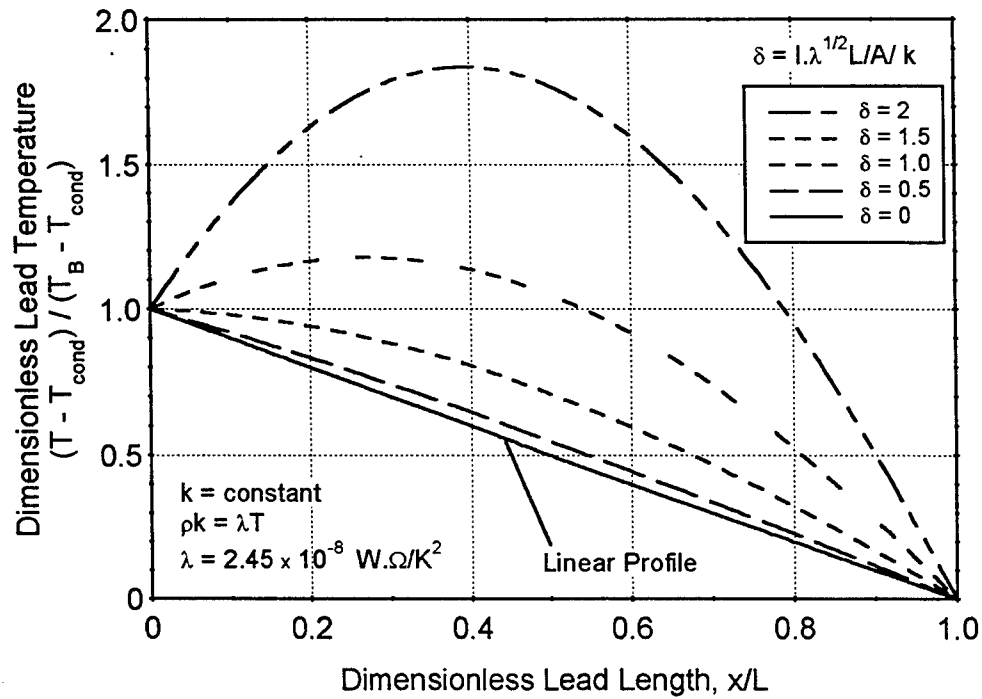


Figure 2.12. Dimensionless Temperature Profile along Conducting Lead.

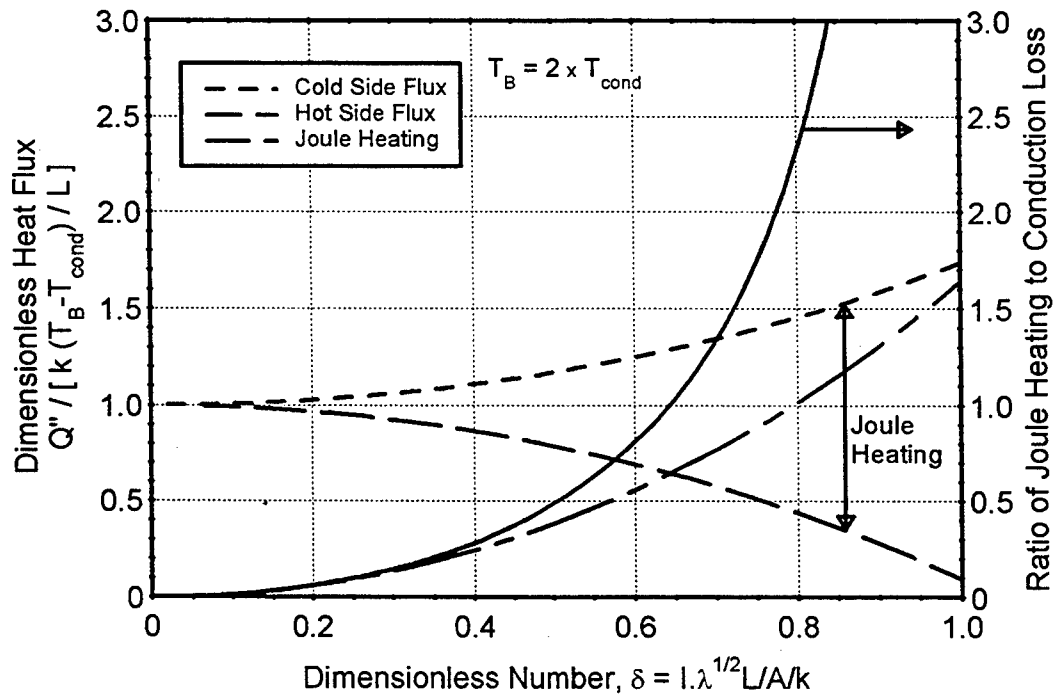


Figure 2.13. Dimensionless Joule Heating and End Heat Fluxes in Conducting Lead as a Function of Electrical Current.

connecting lead to the load is given by  $Q_J$  (Equation 2.23), and all the other parasitic losses in the AMTEC cell are included in the contact resistance,  $R'_{cont}$ . The load voltage can therefore be calculated as:

$$N_S V = N_S [V_o - (R'_B + R'_{cont})J] - 2 \times Q_J / (JA_E), \quad (2.24)$$

where  $A_E$  is the electrode area on one BASE tube. The overall conversion efficiency of the AMTEC cell becomes then:

$$\eta = \frac{I \times [V_o - (R'_B + R'_{cont})J] - 2 \times Q_J / N_S}{[C_p^L (T_B - T_{cond}) + h_{LV} (T_B)] \times (IM) / F + A_E \times Q_{rad} + 2 \times Q_{cd} / N_S} \quad (2.25)$$

Note that, when the BASE tubes in the cell are connected electrically in series, the total cell current is the same as the current for each individual BASE tube ( $I = J \times A_E$ ).

Figures 2.14 and 2.15 show the ratio and the sum of Joule heating and conduction heat loss in an lead, as a function of the lead geometric ratio  $L/A_l$  and cell current. The lead is assumed to be made of copper, with a thermal conductivity of 350 W / m.K. As show in Figure 2.14, the ratio of Joule heating to heat conduction loss decreases with the lead cross section area. Since the cell electric power is about a fifth of the total heat input, the optimum ratio for maximum efficiency will be close to 0.2. For  $I = 20$  A and  $N_S = 1$ , a ratio of 0.2 is obtained with a geometric ratio of about  $4 \times 10^4 \text{ m}^{-1}$ . Figure 2.15 shows that the total energy loss in the lead is minimum at a much higher geometric ratio of the lead. At the minimum, however, the total loss is made up mostly of Joule heating, which amounts to about half of the electrical power available. With a geometric factor of  $4 \times 10^4 \text{ m}^{-1}$ , the total loss in the two leads of the cell is about  $2 \times 6.2 \text{ W} = 12.4 \text{ W}$ , of which the conduction losses are  $12.4 / 1.2 = 10.3 \text{ W}$  and the Joule losses are 2.1 W. At a radiation Z factor of 20, the load electrical power decreases from 11.2 We to 9.1 We, and the overall efficiency of the cell decreases from 23.6% to 15.8%.

## 2.9 SERIES-CONNECTION of MULTI-TUBES in AMTEC CELL

Increasing the power density in AMTEC cells is an important development because it reduces the size and the mass of the system and improves the efficiency. Because the electrical power produced in the cell is proportional to the surface area of electrodes on the BASE tubes, volumetric power density depends on the amount of BASE tube surface area that can be located in a given volume. Volumetric power density ( $\text{We}/\text{cm}^3$ ) can be increased by reducing the diameter and increasing the number of the BASE tubes. This design approach is used in the multi-tube cell. Note that because the electrical losses increase with the electrical current, it is preferable to connect the BASE tubes in series, at the expense of redundancy and reliability. Series connection of AMTEC cells also provides the desired d.c. load voltage for the spacecraft bus.

Because liquid sodium is a good electrical conductor, it is difficult to electrically insulate the BASE tubes from the cell outer wall and from each other in a liquid-anode cell. Series connection

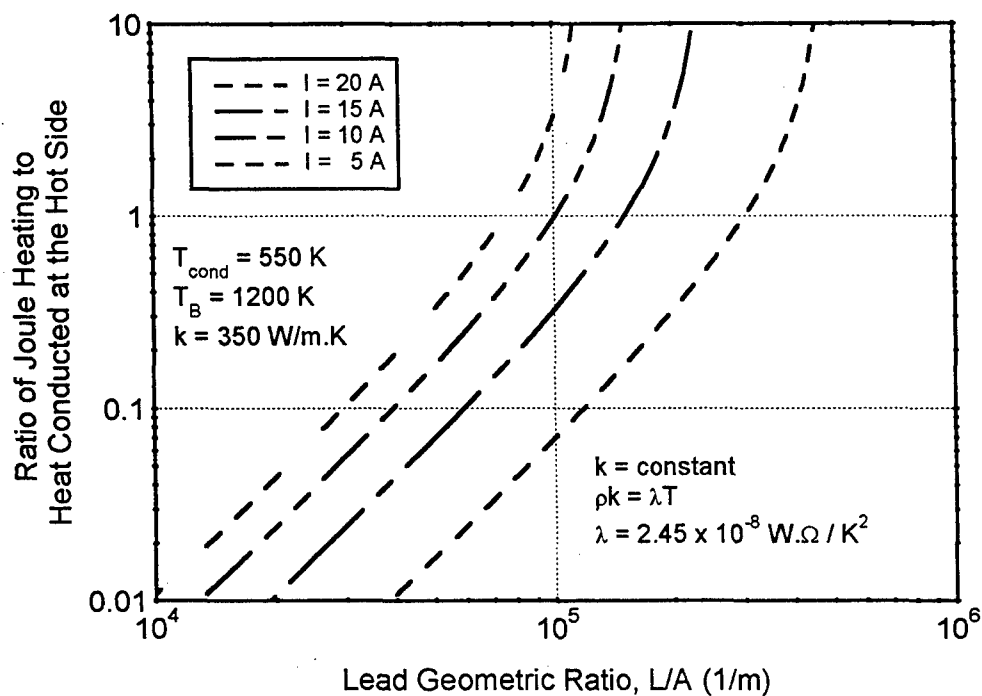


Figure 2.14. Ratio of Joule Heating to Conduction Heat Loss in Conducting Lead as a Function of its Geometric Ratio.

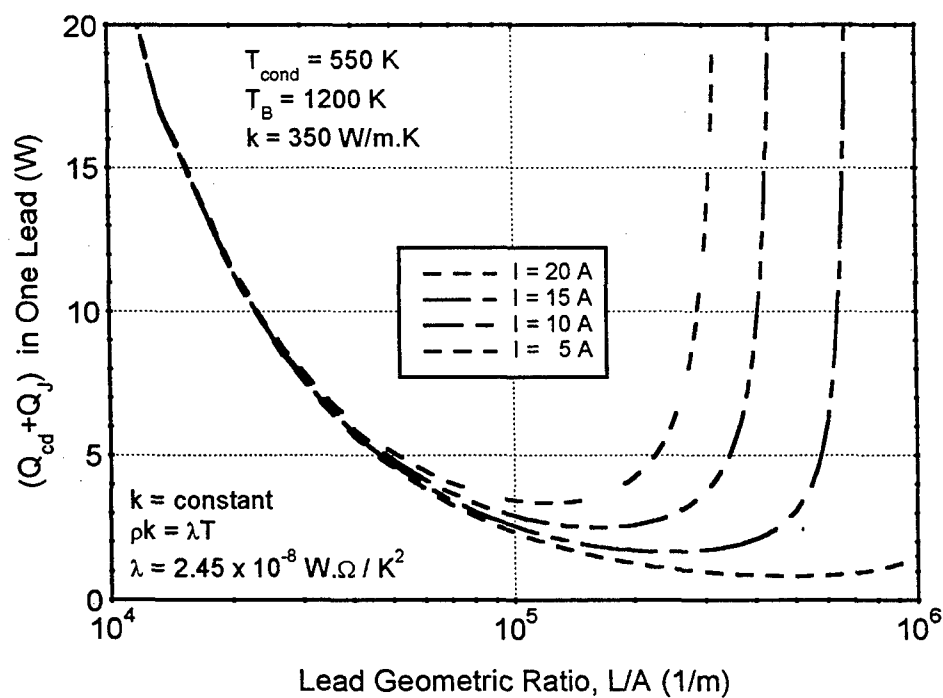


Figure 2.15. Sum of Joule Heating and Conduction Heat Loss in Conducting Lead as a Function of its Geometric Ratio.

of liquid-anode BASE tubes within one cell wall is a challenging engineering problem that has not yet been solved. On the other hand, several vapor-anode BASE tubes can be connected in series in a vapor anode, multi-tube AMTEC cell, consequently increasing the volumetric power density of the cell.

Another advantage of connecting several BASE tubes in series in AMTEC cells is that the overall conversion efficiency of the cell also increases, because the conduction and electrical parasitic losses in the connecting leads remain constant while all other terms, such as the power produced and the radiation losses, increase proportionally with the number of tubes, as shown in Equation (2.25). If 4 BASE tubes are connected in series, the heat conduction losses in the leads contribute only  $10.3 / 4 = 2.6$  W and the Joule losses only  $2.1 / 4 = 0.53$  W. The load electrical power increases from 9.1 to  $10.7 \times 4 = 42.8$  W, and the overall efficiency of the cell increases from 15.8% to 21.3%, with a radiation  $Z$  factor of 20. In summary, the effects of conduction and electrical parasitic losses in the current leads of the cell are reduced dramatically by connecting several BASE tubes in series. This arrangement also increases the cell radiation  $Z$  factor, by reducing the view factor between the BASE tubes and the condenser, and increasing the volumetric and massic power densities of the AMTEC converter.

Note that the cross section area of the electric leads connecting the different BASE tubes electrodes in series in the cell can be designed as large as necessary to insure that Joule losses are negligible. Because they connect hot cathode and anode electrodes of fairly identical temperatures, heat conduction losses in these leads are negligible.

## 2.10 EFFECTS of CHARGE-EXCHANGE POLARIZATION LOSSES in AMTEC CELL

When the charge-exchange polarization losses cannot be neglected, the overall conversion efficiency of the AMTEC cell  $\eta$  is given by Equation (2.25); in the present analysis, we assume that a number of BASE tubes are connected in series, so that the heat conduction and Joule losses in the current leads ( $Q_{cd}$  and  $Q_J$ ) can be neglected. Figures 2.16 and 2.17 show the overall efficiency of the AMTEC cell and the load electrical power density, as a function of current density and temperature-independent exchange current,  $B$ . The radiation geometric factor,  $Z$ , was taken as 20. As  $B$  decreases, the charge-exchange polarization losses increase, resulting in a decrease in peak power density, a shift of the optimum current density to lower value, and a reduction in overall efficiency. As show in Figures 2.16 and 2.17, electrodes with temperature-independent charge-exchange currents  $B$  between 400 and 600 (typical of new molybdenum and NbN electrodes) have the potential for peak power densities slightly above  $1 \text{ W/cm}^2$ , and efficiencies as high as 28%. By contrast, electrodes of lower temperature-independent exchange currents  $B$  between 100 and 150 (typical of TiN electrodes) have lower peak power densities in the range  $0.5 - 0.75 \text{ W/cm}^2$ , with efficiencies below 24%.

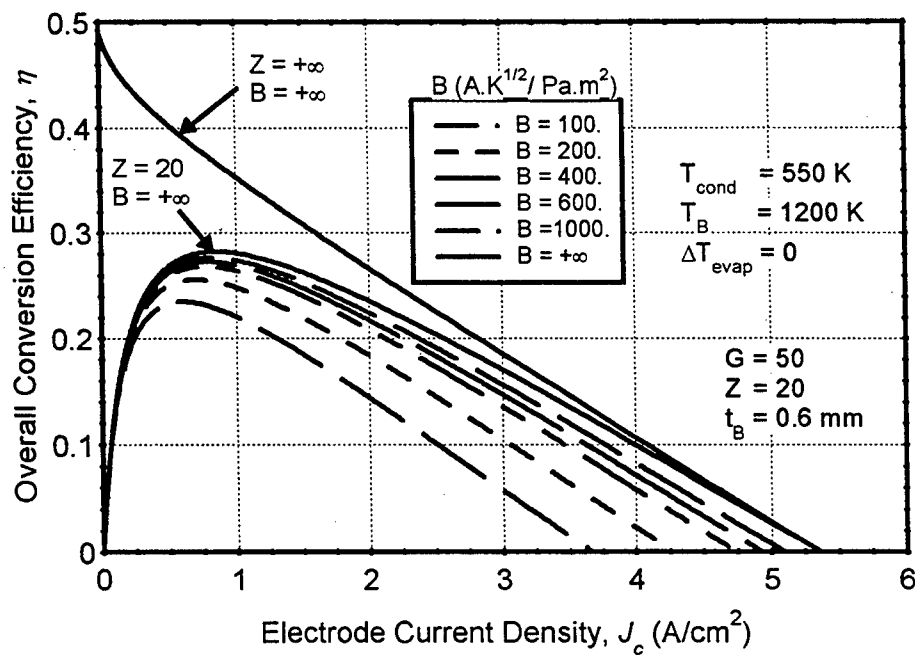


Figure 2.16. Effect of Charge-Exchange Polarization Losses on the Conversion Efficiency of a Sodium AMTEC.

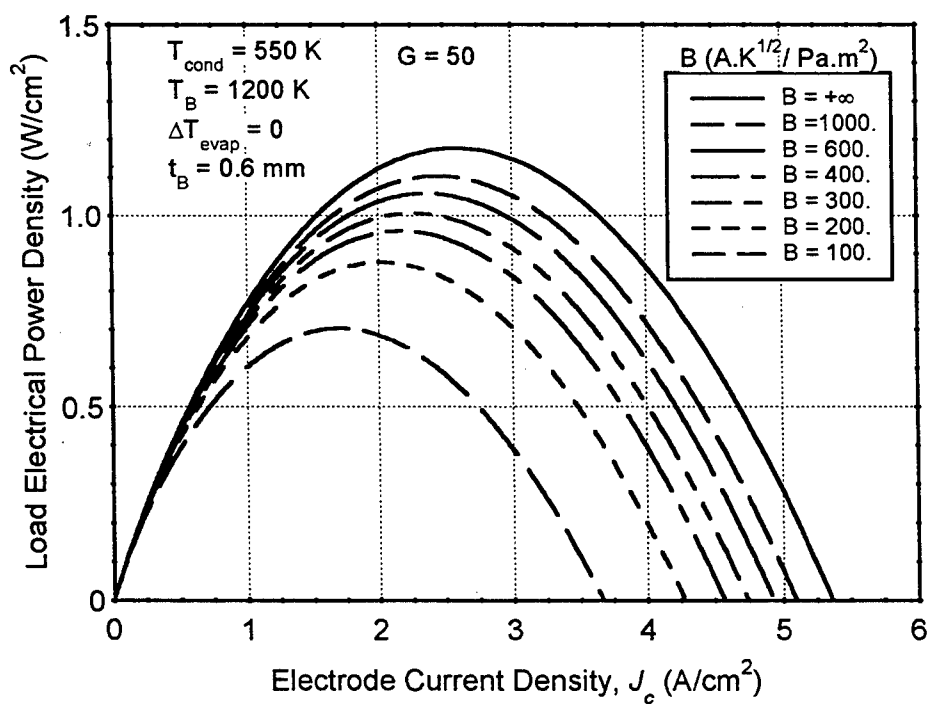


Figure 2.17. Effect of Charge-Exchange Polarization Losses on the Power Density of a Sodium AMTEC.

## 2.11 BENCHMARK of ELECTROCHEMICAL MODEL USING EXPERIMENTAL I-V CHARACTERISTICS

In this section, the AMTEC electrochemical model described in Section 2.5 is benchmarked with the experimental data for several Mo, NbN and TiN electrodes ((Sievers and Bankston 1988, Kato et al. 1992 and 1993). A fit of the model results to the experimental I-V characteristic allowed determination of the temperature-independent exchange current,  $B$ , the geometrical factor,  $G$ , for cathode pressure losses, and the internal electrical resistance other than the BASE ionic resistance,  $R'_{cont}$ . This was possible because of the unique way each of these parameters affect the I-V characteristic (see Chapter 4).

Figures 2.18 and 2.19 compare the calculated and measured I-V characteristics of a molybdenum electrode (Sievers and Bankston 1988), for the extreme range of parameters which offered best fits to the experimental data. According to Sievers and Bankston (1988), the electrode performance was that of an oxide-free, stable electrode, and was not enhanced by the presence of sodium molybdate (Sievers et al. 1988). The BASE was 1.2 mm-thick, and had a calculated ionic resistance  $R_B = 0.267 \Omega \cdot \text{cm}^2$  at 1125 K. The calculated geometrical factor  $G$  of the electrode, which offered best fits to the experimental data, varied between 42 and 47. The pressure losses through the porous cathode electrode are very large, mostly because sputtered molybdenum films have small porosity, usually less than 25%, and offer large resistance to the molecular diffusion of sodium atoms. These pressure losses could be reduced by reducing the thickness of the electrode, at the expense of increasing the electronic sheet resistance in the plane of the electrode, requiring the use of more extensive current collector grids. The contact resistance varied between 0 and  $0.014 \Omega \cdot \text{cm}^2$ , and was only a small fraction of the BASE ionic resistance (less than 6%). The temperature-independent exchange current,  $B$ , which best fitted the data, was found in the range  $385\text{--}600 \text{ A} \cdot \text{K}^{1/2} / \text{Pa} \cdot \text{m}^2$ . The fact that the range in  $B$  is large must not be misinterpreted. At such high values of temperature-independent exchange current, increases in the value of  $B$  do not affect the cell performance significantly (see Figure 2.16). Such high values of  $B$  suggest that the performance of the Mo electrode was probably enhanced by the presence of sodium molybdate (Sievers et al. 1988). One would expect the sodium molybdate to slowly disappear during the maturation period of the electrode, causing a large decrease in cell performance within the first ~400 hours of operation, to a more stable but much smaller level.

Molybdenum electrodes contact well with the solid electrolyte and offer an extensive triple-phase interface with sodium vapor. They have the smallest charge-exchange polarization losses of all electrodes, and hence the potential for best performance, if the pressure losses through the electrode can be reduced (the electrode porosity increased). Unfortunately, Mo electrodes degrade quickly, when operated at high temperature. The Mo electrode delivered a peak power density of  $0.47 \text{ W/cm}^2$ , at an electrode current density of about  $1 \text{ A/cm}^2$ .

Figure 2.20 shows the effect of BASE temperature and current density on the voltage of a cell using  $3 \mu\text{m}$ -thick NbN electrode (Kato et al. 1992). The BASE was 1 mm-thick, and had an ionic resistance  $R_B = 0.23 \Omega \cdot \text{cm}^2$  at a temperature of 1073 K. The electrode had a high temperature-independent exchange current  $B$  of about  $400 \text{ A} \cdot \text{K}^{1/2} / \text{Pa} \cdot \text{m}^2$ , and small pressure losses on the cathode side ( $G = 5$ ). However, internal losses other than BASE resistance were very high,  $0.135$

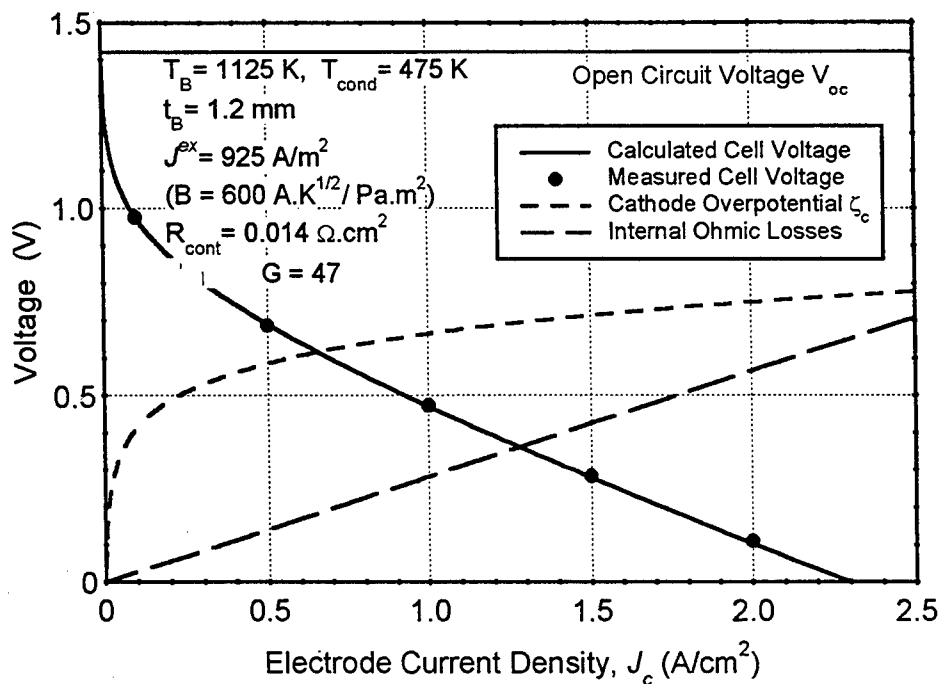


Figure 2.18. I-V Characteristic of a Molybdenum Electrode with  $G=47$  and Comparison with Experimental Data (Sievers and Bankston 1988).

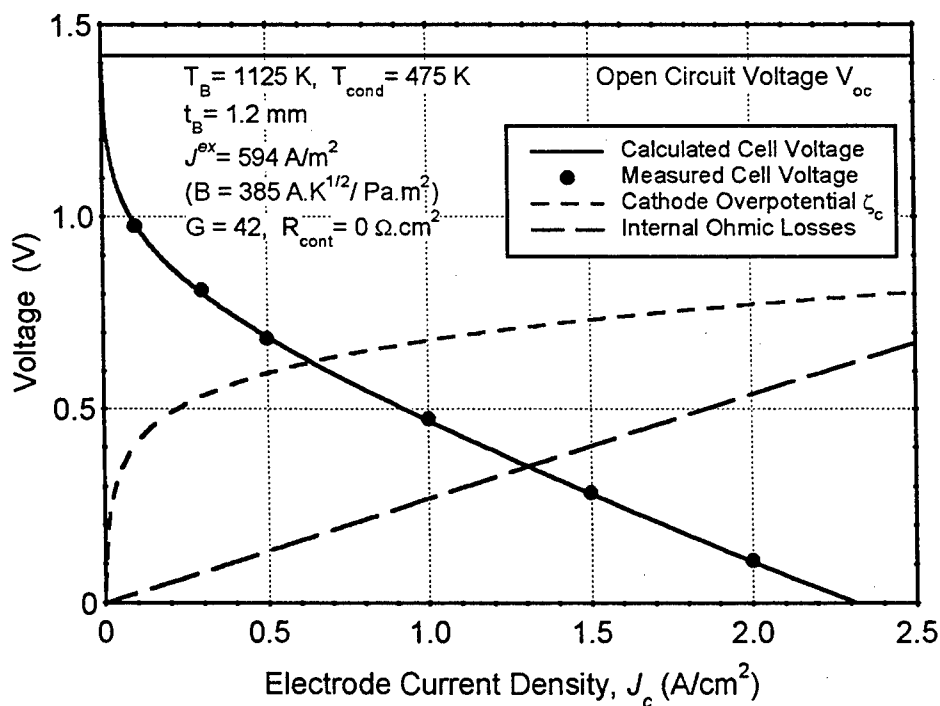


Figure 2.19. I-V Characteristic of a Molybdenum Electrode with  $G=42$  and Comparison with Experimental Data (Sievers and Bankston 1988).

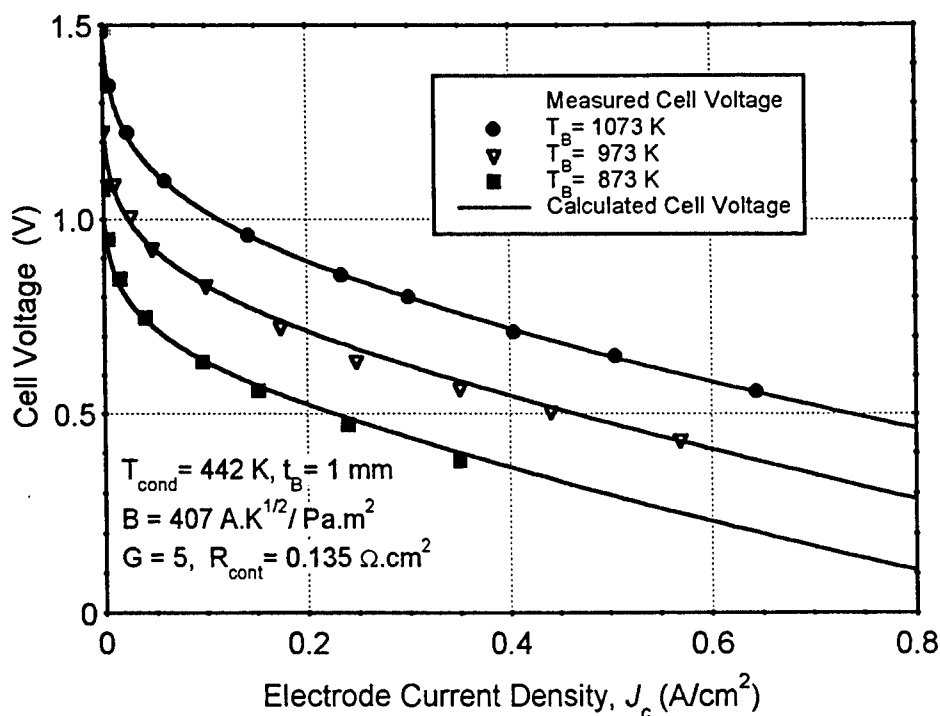


Figure 2.20. Effect of BASE Temperature on I-V Characteristic of a 3  $\mu$ m-Thick NbN Electrode and Comparison with Experimental Data (Kato et al. 1992).

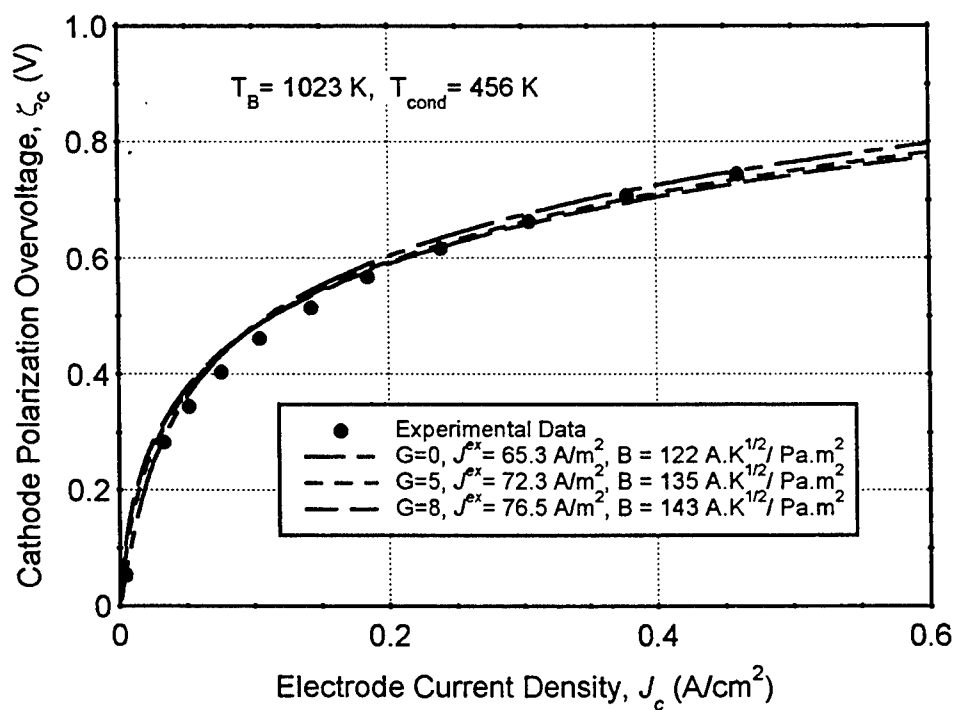


Figure 2.21. Cathode Polarization Losses of a Thin TiN Electrode and Comparison with Experimental Data (Kato et al. 1993).



$\Omega\cdot\text{cm}^2$ , or about 59% of  $R'_B$ . At the hottest BASE temperature of 1073 K, the NbN electrode delivered a peak power density of  $0.37\text{ W/cm}^2$ , at a current density of  $0.8\text{ A/cm}^2$ . As shown in Figure 2.20, the model predictions compared well with the experimental data of Kato et al. (1992). The very high value of  $B$  again suggest the existence of an enhanced transport mechanism of sodium ions in the electrode, probably caused by the presence of oxygen or other impurities in the system. One would expect such enhancement mechanism to slowly disappear during the maturation period of the electrode, within the first few hundred hours of operation.

The model predictions were also compared with the experimental data of Kato et al. (1993) for a TiN electrode. These investigators performed current interruption measurements in order to obtain the cathode polarization overvoltage in the cell. This technique uses a.c. impedance analysis to separate the ohmic resistance losses from the total voltage loss. Figure 2.21 compares the measured and calculated cathode polarization overvoltages as a function of current density. The calculated values, based on the Butler-Volmer Equation (2.8), compared well with the experimental data. Using their measurements at very low current density (in the linear range), Kato et al. (1993) deduced a cathodic exchange current density  $J_c^{ex} = 64\text{ A/m}^2$ . Calculated values of  $J_c^{ex}$  that best fitted the data were found in the range  $65.3$  to  $72.3\text{ A/m}^2$ .

Figures 2.22 and 2.23 compare the calculated and measured I-V characteristics of the TiN electrode, for the extreme range of parameters which offered best fits to the data. The BASE was 1 mm-thick, and had an ionic resistance  $R'_B = 0.219\text{ }\Omega\cdot\text{cm}^2$ . The calculated geometrical factor  $G$  of the electrode, which offered best fits to the data, varied between 0 and 5, meaning that the pressure losses through the porous electrode and current collector were small. The temperature-independent exchange current,  $B$ , which best fitted the data, was found in the range  $122$ - $135\text{ A}\cdot\text{K}^{1/2}/\text{Pa}\cdot\text{m}^2$ , which is comparable with values reported by other investigators for TiN electrodes. The electrical internal losses other than BASE resistance varied between  $0.11$  and  $0.14\text{ }\Omega\cdot\text{cm}^2$ , a large fraction of the BASE ionic resistance (50% and 64%). The TiN electrode delivered a peak power density of  $0.18\text{ W/cm}^2$ , at a current density of  $0.5\text{ A/cm}^2$ .

$B$  values of 120 for these TiN electrodes suggest that the experimental data were taken during early operation of the cell. More recent experiments at JPL, AMPS and AFRL and analyses performed in this work (see Chapters 4, 11 and 12) have shown that one should expect a  $B$  value in the range 60-80 for a matured TiN electrode/BASE system.

## 2.12 SUMMARY

An analytical, electrochemical and thermal-lumped model was developed to evaluate the performance of AMTEC cells for both liquid- and vapor-anode modes of operation. The charge-exchange polarization losses in the cell were modeled with the Butler-Volmer equation using the temperature-independent exchange current  $B$ . The model was benchmarked using electrical experimental data for oxide-free Mo, NbN and TiN electrodes. Results showed that Mo and NbN electrodes initially exhibit high  $B$  values between 400 and  $600\text{ A}\cdot\text{K}^{1/2}/\text{Pa}\cdot\text{m}^2$ , and have the potential for peak power densities slightly above  $1\text{ W/cm}^2$ , with efficiencies as high as 28%. In contrast, TiN electrodes have lower temperature-independent exchange currents, between 120

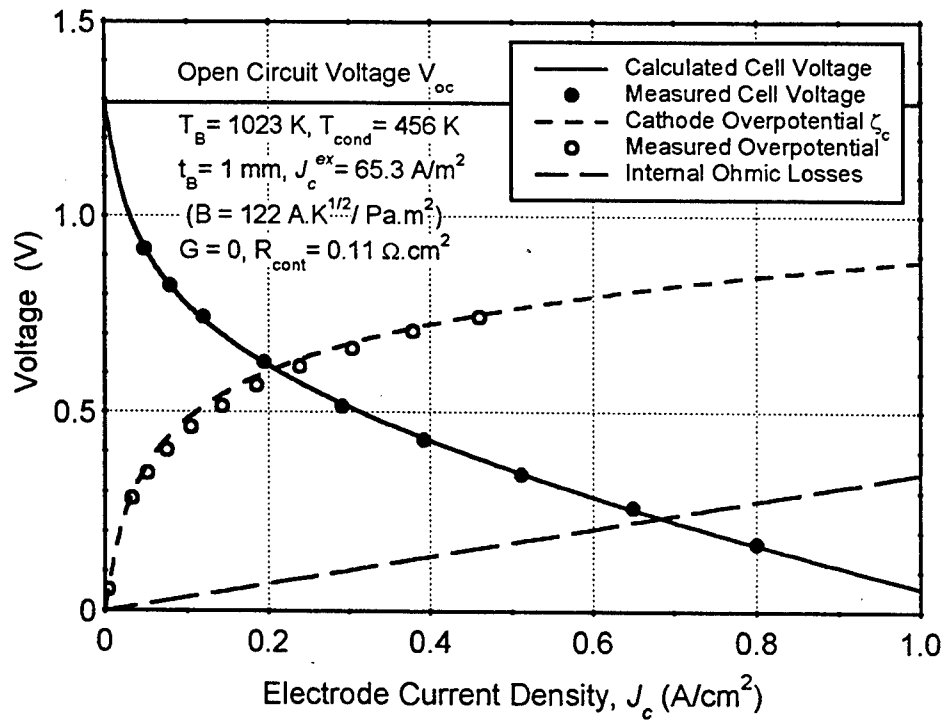


Figure 2.22. I-V Characteristic of a Thin TiN Electrode with  $G=0$  and Comparison with Experimental Data (Kato et al. 1993).

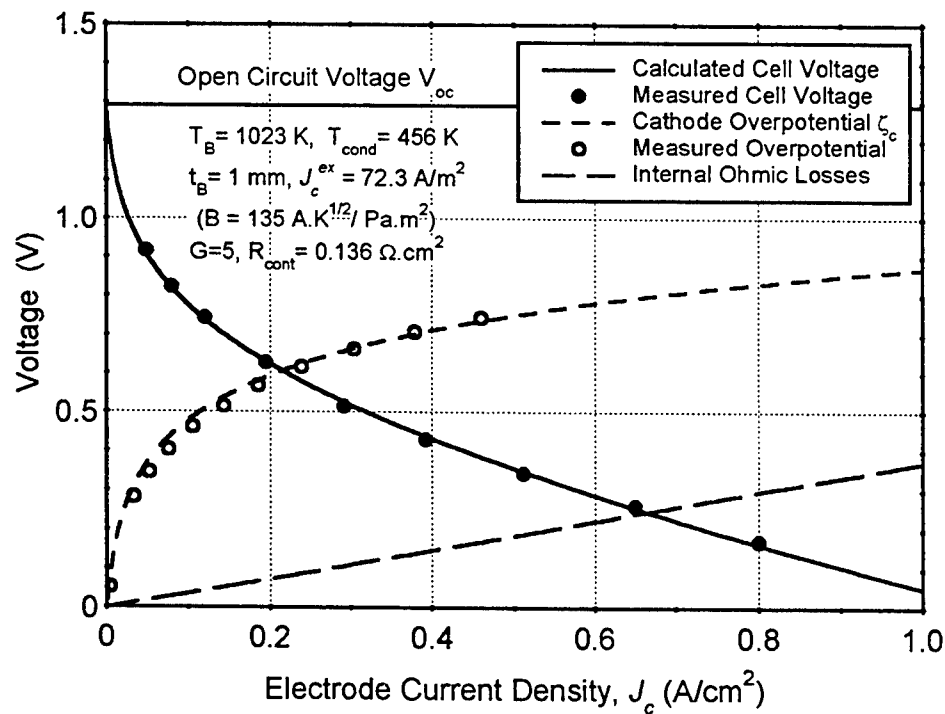


Figure 2.23. I-V Characteristic of a Thin TiN Electrode with  $G=5$  and Comparison with Experimental Data (Kato et al. 1993).

and  $135 \text{ A.K}^{1/2} / \text{Pa.m}^2$ , before maturation, corresponding to lower peak power densities between  $0.5$  and  $0.75 \text{ W/cm}^2$ , and efficiencies below  $24\%$  at a BASE temperature of  $1200 \text{ K}$ . These values of  $B$  compare well with that reported by other investigators for new electrodes/BASE systems.

While TiN electrodes have lower performance than Mo and NbN electrodes, lifetime studies at high temperature have shown that they are more stable for long-term operation (Williams et al. 1990c). At temperatures above  $1100 \text{ K}$ , Molybdenum electrodes sinter and experience significant grain growth, particularly in sodium vapor environment. As voids open in the electrode, the electronic sheet resistance increases and the exchange current density decreases with time, degrading the performance of the AMTEC cell.

Results also showed that ideal AMTEC devices have the highest theoretical thermodynamic efficiency of all known heat engines (static and dynamic), above  $90\%$  of Carnot efficiency at BASE temperatures below  $1200 \text{ K}$ . The efficiency of vapor-anode cells can approach that of liquid-anode cells, and offer the possibility of much improved volumetric power density through the use of series-connection of several BASE tubes within one common enclosure. Series connection of multi-tubes also allows larger voltage outputs, with the potential to reduce the need for extensive power conditioning, and reduces the heat conduction and Joule heating losses in the electric leads to the load.

The present electrochemical and thermal-lumped model was used to analyze the effects of pressure losses, parasitic heat losses and internal electrical losses on the power density and efficiency of the AMTEC. The pressure losses between the cathode electrode/BASE interface and the condenser were characterized by a geometric factor  $G$ . The heat exchanged by radiation between the BASE tubes and the condenser, the most significant parasitic heat loss in the cell, was characterized by a dimensionless factor  $Z$ . Advanced designs with improved efficiency use radiation shields between the heat source and sink, a remotely located condenser, or a combination of these two. While reducing the radiation losses very significantly (with representative  $Z$  values between  $20$  and  $60$ ), these designs are characterized by increased vapor pressure losses on the cathode side, with an effective geometrical factor  $G$  between  $50$  and  $200$ .

Analyses performed in another Chapter (4) of the internal losses in the AMTEC cell have showed that the BASE ionic resistance, the contact resistances between the BASE, the electrodes, and the current collectors, and the charge-exchange polarization overvoltage on the cathode side were the major contributors to the cell's electric losses. Present designs of current collector networks have insignificant electrical resistance and easily overcome the sheet resistance in the plane of the electrode. The ionic resistance is limited by the thickness of the solid electrolyte. BASE tubes as thin as  $0.5 \text{ mm}$  are commonly manufactured, which can withstand the pressure and thermal stresses encountered in AMTEC operation.

This preliminary analysis has shown that because the performance of AMTEC is strongly dependent on the values of  $G$  and  $Z$ , further modeling and experimental studies are needed to obtain accurate values of these parameters. The designs of interest are state-of-the-art, vapor anode, multi-tube cells using remote condensing and internal radiation shields. Also, design studies are needed to insure that the evaporator temperature remains close to the BASE temperature but below it, to avoid condensation of sodium onto the solid electrolyte. Such

condensation could cause electrical shorting of the BASE tubes in the cell and/or thermal shocking of the BASE tubes.

The present lumped model assumed uniform vapor pressure, temperature and current density axial distributions along the BASE tubes. In reality, radiation losses from the cathode electrode, Joule heating in the BASE membrane, conduction heat transfer and end effects contribute to producing non-uniformities in the BASE temperature. Also, vapor flow in the free-molecule and transition regimes on the cathode side of the BASE tubes challenges the prediction of sodium vapor pressure losses and contribute to producing non-uniformities in the vapor pressure axial distribution along the electrodes. These issues are addressed in the following Chapter 3.

Cell operating lifetime depends on the stability and behavior of the cell materials. Materials in components such as porous electrode and BASE must have similar thermal expansion coefficients and be well bonded to withstand many thermal cycles. These same materials must not undergo chemical or physical changes caused by diffusion processes that take place at high temperatures. Key components include the BASE, electrodes, BASE-to-metal braze, feedthrough, and cell wall. While TiN electrodes have lower performance than Mo and NbN electrodes, lifetime studies at high temperature have shown that they are much more stable for long-term operation (Williams et al. 1990c). At temperatures above 1100 K, Molybdenum electrodes sinter and experience significant grain growth, particularly in sodium vapor environment. As voids are opened in the electrode, the electronic sheet resistance increases with time, degrading the performance of the AMTEC cell.

## **2.13 AMTEC PERFORMANCE AND EVALUATION ANALYSIS MODEL (APEAM)**

The following Chapters (3 – 5) describe in details the AMTEC Performance and Evaluation Analysis Model (APEAM) of PX-series cells developed at UNM-ISNPS. This integrated cell model was developed to support ongoing tests at AFRL and evaluate the performance of PX-series AMTEC cells. The model was developed in Standard Fortran 77, and runs on a PC Compatible DOS machine. It can also run on a UNIX or VMS operating system machine, without any modification. It uses a modular input file, and automatically generates output files, and graphs which are readable by the Easy-Plot plotting package.

In order to select the software platform best suited for developing a model for predicting the performance of vapor anode, multi-tube AMTEC cells, the following packages were evaluated: Math-CAD (a software very similar to Mathematica), TK-Solver (package initially used by Advanced Modular Power Systems), Fortran 77, I-DEAS, and other commercially available thermal analyzer codes such as SINDA/FLUINT. In the end, Standard Fortran 77 was selected, for the following reasons:

- easy transportability to various machines and/or operating systems;
- algorithmic flexibility, which allows for close control of iterative solution algorithms with the potential of best computation time;
- virtually no limitation on data structure and numerical grid refinement, allowing for growth of

physical model and geometry complexity as necessary.

The use of alternative, commercially available thermal analyzer codes, such as SINDA/FLUINT, coupled with view factor calculation codes which use contour integration or Monte Carlo ray tracing, has the advantage of requiring relatively less development work (depending on the learning curve) and providing very accurate view factors (accuracy at the expense of CPU time). However, this approach suffers from the difficulties to efficiently resolve the strong couplings between the various physical processes in the AMTEC cell, and from the difficulty of verifying these physical submodels separately. As a result, the use of commercially available thermal analyzer codes would have been prohibitively CPU intensive, and would not have efficiently served one of the objectives of the present effort to identify the major and key physical processes in a vapor anode, multi-tube AMTEC cell which limit their performance.

It was therefore recommended that a Lahey Fortran 77 compiler package and an EasyPlot plotting and curve-fitting package be purchased for the 486 Personal Computer. These software served as a base software development platform for the AMTEC cell numerical model.

APEAM consists of three major building blocks, which are interactively coupled: (a) a *sodium vapor pressure loss model*, which calculates the sodium vapor pressure at the interface between the cathode electrode and the BASE (Chapter 3); (b) a *cell electrochemical and electric model*, which calculates the effective potential developed across the BASE due to the isothermal expansion of sodium ions, determines the resistances of the BASE, electrodes, current collectors and conductor leads to the external load, and calculates the cell's electrical potentials, electrode current density, and the cell's total electric current (Chapter 4); and (c) a *radiation/conduction heat transfer model*, which accounts for all heat exchanges between the different components of the cell and calculates the temperatures throughout the cell (Chapter 5). An efficient iterative solution procedure was developed, that ensured good couplings between the different submodels (Chapter 5, Section 5.4). These submodels are described in more details in the following subsections.

### 2.13.1 Sodium Vapor Pressure Loss Model

At an evaporator temperature above 900 K, the vapor pressure losses on the anode side of a PX-type cell are negligible, compared to the sodium vapor pressure ( $> 5$  kPa). By contrast, the sodium vapor pressure on the cathode side is 2 to 3 orders of magnitude lower than on the anode side ( $< 100$  Pa), at a typical condenser temperature below 650 K. The actual pressure of sodium vapor at the interface between the BASE and the cathode electrode depends on the Na saturation pressure at the condenser temperature,  $T_{cond}$ , and the pressure losses due to sodium vapor flow between the BASE and the condenser. The pressure losses due to sodium vapor flow through the cathode porous electrode; along the BASE tubes (with axial mass addition and vapor compressible effects); due to the change in flow area at the top of the BASE tubes; in the region above the BASE tubes (annular space with centerline artery); and due to condensation at the cold end of the cell (Figure 2.2a), are all accounted for in the model. The vapor diffusion coefficients in the free-molecular flow regime are calculated using the Knudsen and Dushman formulas, while those for the continuum regime are obtained from an analytical solution (when available), or by using the equivalent hydraulic diameter approximation. The Dusty-Gas-Model (DGM) is used to determine the flow diffusion coefficients for the different vapor flow regimes: free-molecule,

transition, and continuum. All necessary temperatures in the cell are calculated by the radiation/conduction heat transfer model. The sodium vapor flow rate, which is proportional to the cell electric current, is obtained from the cell electrical model.

### 2.13.2 Cell Electrochemical and Electric Model

The cell electric model is comprised of: (a) an *electrochemical model*, which calculates the effective potential developed across the BASE due to the isothermal expansion of sodium ions; (b) a *resistance model*, which determines the electric resistances of the BASE, electrodes, current collectors, bus wires and the conductor leads to the external load; and (c) an *electrical circuit model*, which calculates the electrical potentials, electrode current density, and the cell total electrical current. The one-dimensional electrochemical model accounts for the axial variation of the current density along the BASE tube. The concentration and charge-exchange polarization losses are calculated using the Butler-Volmer Equation (2.8). The cell electric model accounts for the effects on the current density of non-uniform axial temperature and vapor pressure profiles along the BASE tubes. It also accounts for radial and axial electrical losses in the current collector network. The electric model incorporates various current collector configurations, such as helical wire, circumferential wires, and metallic sponge or wire-screened mesh held in place with circumferential wires in combination with an axial bus collector. The sodium vapor pressure on the cathode side of the BASE is obtained from the vapor pressure loss model.

### 2.13.3 Radiation/Conduction Heat Transfer Model

The cell thermal model calculates internal parasitic heat losses and temperatures throughout the AMTEC cell. The model discretizes the cell components into many elements and accounts for conduction, radiation, convection and phase change heat transfers between them (Figure 2.2a). All surfaces that exchange radiant energy in the interior of the cell are assumed gray and diffuse. The radiation/conduction model can easily handle between 100 and 200 temperature nodes in the cell and the surrounding insulation package. The cell wall thickness, and the volume porosities of the liquid-return artery and the evaporator wick, are allowed to vary axially. The model can handle both transient and steady-state calculations. The input file allows the user to specify the type of boundary conditions at the hot and cold end of the cell, and at the side wall of the cell, such as adiabatic, or thermally coupled to the surrounding insulation through a radiation gap. The radiative emissivities and thermophysical properties of all structure materials, BASE tubes and sodium working fluid are calculated as functions of temperature. The heats of vaporization and condensation in the cell, and the sensible heats of the liquid sodium flowing in the artery and the evaporator wick, are calculated based on the cell current given by the electric model.

### 2.13.4 Method of Solution

An efficient iterative solution procedure was developed, that ensured good couplings between the different submodels. An energy balance was performed for every element in the cell. The source term in the resulting Poisson equation included the energy losses by radiation at the face(s) of the

element. In order to solve the energy balance equations for the temperatures, the net radiant energy loss terms were expressed in terms of temperatures. These net loss terms were expressed in terms of the rates of outgoing radiant energy, which were related to the surface temperatures, by the radiant energy balances for surface areas. The cell model formed a matrix of view factors which related the rates of outgoing radiant energy to the temperatures in the cell. A routine was developed to inverse the radiation matrix using the Gauss-Jordan elimination algorithm.

The next chapter describes in details the vapor pressure loss model used in APEAM for calculating the vapor pressure losses and characterizing the flow regimes on the cathode side of a Pluto/Express vapor anode, multi-tube AMTEC cell, with internal chevron's radiation shields.

### 3. SODIUM VAPOR PRESSURE LOSSES IN A MULTI-TUBE AMTEC CELL

In this chapter, the APEAM submodel for calculating the vapor pressure losses and characterizing the flow regimes on the cathode side of a Pluto/Express vapor anode, multi-tube AMTEC cell, with internal chevron's radiation shields, is described in details. The model predicts the vapor flow over a wide range of pressures, including the free-molecular, transition, and continuum flow regimes, using the Dusty-Gas-Model. Results showed that the vapor flow on the cathode side of a multi-tube AMTEC cell is typically in the transition regime, and that the pressure loss through the chevron's shield accounts for about 50% of the total pressure losses. Such an increase in the vapor pressure drop, due to the presence of the chevron's shield, however, decreased the cell electrical power output by only about 5%. This was because, in a cell using TiN metal electrodes, the concentration losses were small compared to the charge-exchange polarization and internal ohmic losses of the cell. An analysis is also performed to optimize the conical chevrons' geometry for minimum pressure loss.

#### 3.1 NOMENCLATURE

##### English

$A$	Surface area ( $\text{m}^2$ )
$a_{cc}$	Accommodation coefficient, Eqs. (3.1) and (3.63)
$A_E$	Electrode area on one BASE tube ( $\text{m}^2$ )
$\bar{A}_k$	Average effective flow area of passage ( $k$ ) in chevron's radiation shield ( $\text{m}^2$ ), Fig. 3.3
$b$	Perpendicular distance between chevrons (m), Figure 3.3
$C$	Flow conductance ( $\text{m}^3 / \text{s}$ ), see Appendix A
$d$	Separation distance between conical chevrons (m), Figure 3.3
$D$	Flow diffusion coefficient ( $\text{m}^2/\text{s}$ )
$D_a$	Diameter of centerline liquid-return artery ( $D_a = 3.18 \times 10^{-3} \text{ m}$ )
$D_B$	BASE tubes outer diameter ( $D_B = 6.35 \times 10^{-3} \text{ m}$ )
$D_e$	Equivalent hydraulic diameter of flow channel (m)
$D_s$	Outer diameter of evaporator standoff ( $D_s = 6.35 \times 10^{-3} \text{ m}$ )
$D_w$	Cell wall inner diameter ( $D_w = 33.2 \times 10^{-3} \text{ m}$ )
$D_k^{in}$	Effective inner diameter of conical flow passage $k$ (m), Equation (3.49)
$D_k^{out}$	Effective outer diameter of conical flow passage $k$ (m), Equation (3.49)
$F$	Faraday's constant ( $F = 96,485$ . Coulomb / mole)
$f$	Laminar friction coefficient
$G$	Dimensionless factor for pressure losses, Equation (3.0)
$I$	Total cell electrical current (A)
$J_r$	Electrode current density ( $\text{A} / \text{m}^2$ )
$k$	Boltzmann constant ( $k = 1.3806 \times 10^{-23} \text{ J} / \text{K}$ )
$K$	Loss form coefficient for sudden expansion, Equations (3.31) and (3.32)
$Kn$	Knudsen number of sodium vapor, Equation (B4)



$L$	Effective flow path length through chevrons (m)
$L_B$	Distance between bottom of electrode and top of BASE tube (m)
$L_C$	Distance between top of BASE tube and chevron's shield (m)
$L_S$	Height of chevron's shield (m)
$L_T$	Distance between chevron's shield and cell condenser (m)
$M$	Molecular weight of sodium ( $M = 22.99 \times 10^{-3}$ kg / mol)
$m$	Molecular mass of sodium ( $m = M / N_a$ )
$Ma$	Axial Mach number of sodium vapor, Equation (B9)
$\dot{m}''_{pore}$	Vapor mass flux in electrode pores (kg / m <sup>2</sup> .s)
$\dot{m}''_k$	Average mass flux in passage (k) of chevron's radiation shield (kg / m <sup>2</sup> .s), Figure 3.3
$\dot{m}'_r$	Vapor mass flow rate per unit length of channel (kg / m.s)
$\dot{m}''_r$	Average sodium mass flux through the BASE (kg / m <sup>2</sup> .s)
$\dot{m}_z$	Vapor axial mass flow rate (kg / s)
$\dot{m}''_z$	Vapor axial mass flux (kg / m <sup>2</sup> .s)
$N$	Number of conical chevrons in radiation shield
$N_a$	Avogador number ( $N_a = 6.022 \times 10^{23}$ atoms / mole)
$N_B$	Number of (series-connected) BASE tubes ( $N_B = 7$ )
$N_{pore}$	Number density of pores in electrode (pores / m <sup>2</sup> )
$P$	Sodium vapor pressure (Pa)
$R_a$	Outer Radius of centerline liquid-return artery (m), $R_a = D_a / 2$
$Re$	Axial Reynolds number of sodium vapor, Equation (B6)
$R_w$	Cell wall inner radius (m), $R_w = D_w / 2$
$R_g$	Perfect gas constant ( $R_g = 8.314$ J / mol.K)
$R_p$	Average hydraulic radius of electrode pores (m), $R_p = 10 \mu\text{m}$
$T$	Temperature (K)
$T^*$	Dimensionless temperature, Equation (B2)
$t_E$	Thickness of cathode electrode times pore tortuosity (m), $t_E = 5 \mu\text{m}$
$\bar{U}_z$	Average axial vapor velocity (m / s)
$z$	Axial coordinate (m)

### Greek

$\alpha$	Chevrons' packing factor, Figure 3.3
$\bar{\alpha}_2$	Coefficient for advection of axial momentum, Equation (3.16)
$\beta$	Expansion area ratio at top of BASE tubes ( $\beta = A_3/A_4$ )
$\gamma$	Specific heat ratio of sodium vapor ( $\gamma = 5/3$ )
$\Delta P$	Pressure loss through conical chevron's shield (Pa)
$\Delta P_{cd}$	Pressure loss due to condensation of sodium (Pa)
$\Delta P_E$	Pressure loss through cathode electrode (Pa)
$\Delta P_{evap}$	Pressure loss due to evaporation of sodium at BASE surface (Pa)
$\varepsilon_E$	Volume porosity of cathode electrode, $\varepsilon_E = 0.9$
$\zeta$	Correction factor for laminar flow in annular channel
$\theta$	Angle of conical chevrons, Figure 3.3
$\lambda$	Mean free path of sodium vapor molecules (m), Equation (B5)

$\mu$	Dynamic viscosity of sodium vapor (kg / m.s), Equation (B1)
$\xi$	Resistance coefficient for sudden expansion, Equations (3.32) and (3.33)
$\rho$	Sodium vapor density (kg / m <sup>3</sup> ), Equation (3.26)
$\sigma$	Molecular diameter of sodium ( $\sigma = 3.58 \times 10^{-10}$ m)
$\tau_w$	Wall stress (Pa / m <sup>2</sup> )
$\varphi$	Compressible factor (Equation 3.65)
$\chi$	Flow conductance of chevron's shield (m <sup>3</sup> / s), Equation (3.62)
$\Omega^*$	Collision integral for Lennard-Jones energy potential, Equations (B1)-(B3)

### Subscript / Superscript

a	Anode electrode / BASE interface
B	Beta"-Alumina Solid Electrolyte (BASE)
c	Cathode electrode / BASE interface
cd	Condenser
comp	Compressible
E	Cathode electrode
exp	Sudden expansion of flow at top of BASE tubes
evap	Evaporator
incomp	Incompressible
K	Knudsen flow regime
oc	Open-circuit condition
r	Radial direction
sat	Liquid-vapor saturation line
vis	Viscous (continuum) flow regime
z	Axial direction
1	BASE tubes/evaporator standoff bundle
2	Annular space above BASE tubes

## 3.2 INTRODUCTION

Alkali-Metal Thermal-to-Electric Converters (AMTEC) are being considered for future planetary exploration missions, because of their potential for delivering electrical power at relatively high conversion efficiency, in excess of 20-25%. Such a high conversion efficiency is due to the fact that the expansion of sodium vapor through the  $\beta''$ -Alumina Solid Electrolyte (BASE) is nearly isothermal. The electrical power output of an AMTEC cell, which equals the work of isothermal expansion, is a logarithmic function of the ratio of the sodium vapor pressure on the anode (high-pressure) side to that on the cathode (low-pressure) side of the BASE (Cole 1983). At evaporator temperatures between 950 K and 1100 K, vapor pressure losses on the anode side are negligible compared to the sodium vapor pressure (15 – 60 kPa); thus, the vapor pressure on the anode side is essentially equal to the evaporator saturation pressure. By contrast, the sodium vapor pressure on the cathode side is orders of magnitude lower (< 50 Pa), at typical sink (or condenser) temperatures < 650 K. The sodium pressure at the interface between the BASE and cathode electrode is equal to the saturation pressure at the condenser plus the pressure losses due to sodium vapor flow from the BASE outside surface to the condenser.

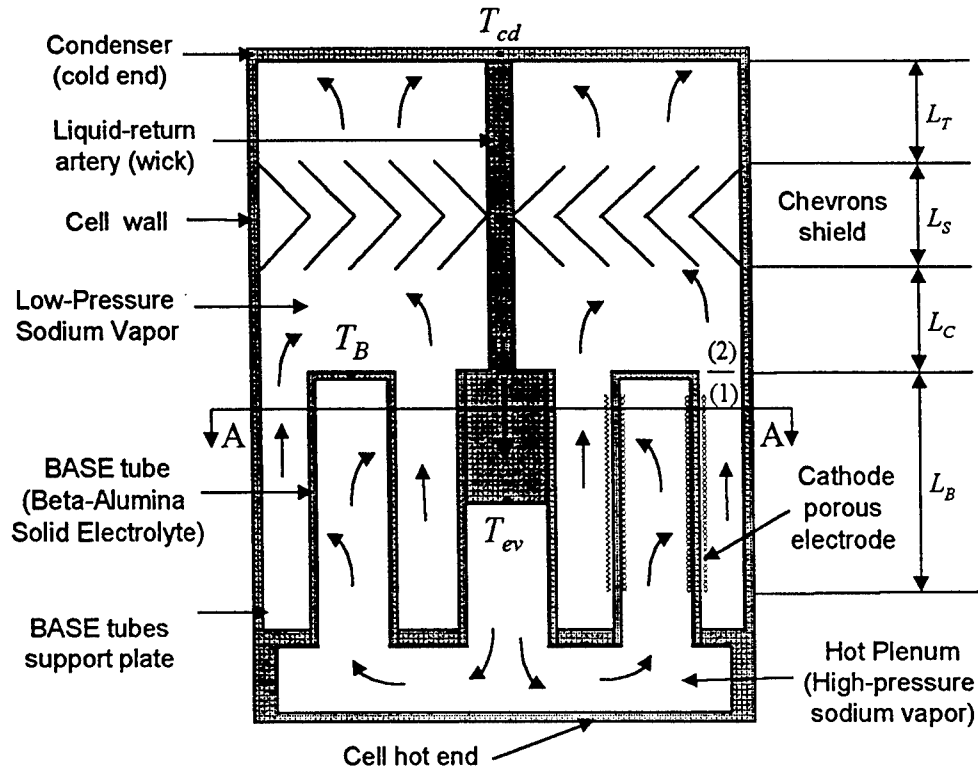
An important input to the modeling of vapor-anode, multi-tube AMTECs is determining the pressure drop on the cathode side of the cell. As indicated earlier, the electric power output of the cell is a logarithmic function of the ratio of the anode vapor pressure to the cathode pressure. Therefore, the lower the pressure losses on the cathode side, the higher is the cell's electric power output.

Only a few investigators have attempted to calculate the vapor pressure losses between the BASE and the condenser, owing to the complexity of the cell geometry (Fig. 3.1) and the fact that the vapor flow could be in the transition or the free-molecular regime (Tournier and El-Genk 1996). Johnson (1994) solved the Boltzmann conservation equation using a Monte Carlo method to calculate the vapor pressure losses in a single-tube AMTEC cell, with a remotely-located condenser, internal heat shields, and a coaxial liquid return artery. Results showed that the vapor pressure drop on the cathode side of the cell varied proportionally with the sodium vapor mass flow rate, which is indicative of the free-molecular flow regime. Based on these results, many investigators expressed the vapor pressure at the BASE/cathode interface as a linear function of the vapor mass flow rate. In order to fit such a linear relationship to experimental measurements, they introduced an effective dimensionless factor,  $G$ , that was determined empirically from the best fit of experimental data (Underwood et al. 1988 and 1992; Williams et al. 1993). Thus, the sodium vapor pressure at the BASE / cathode electrode interface was expressed as:

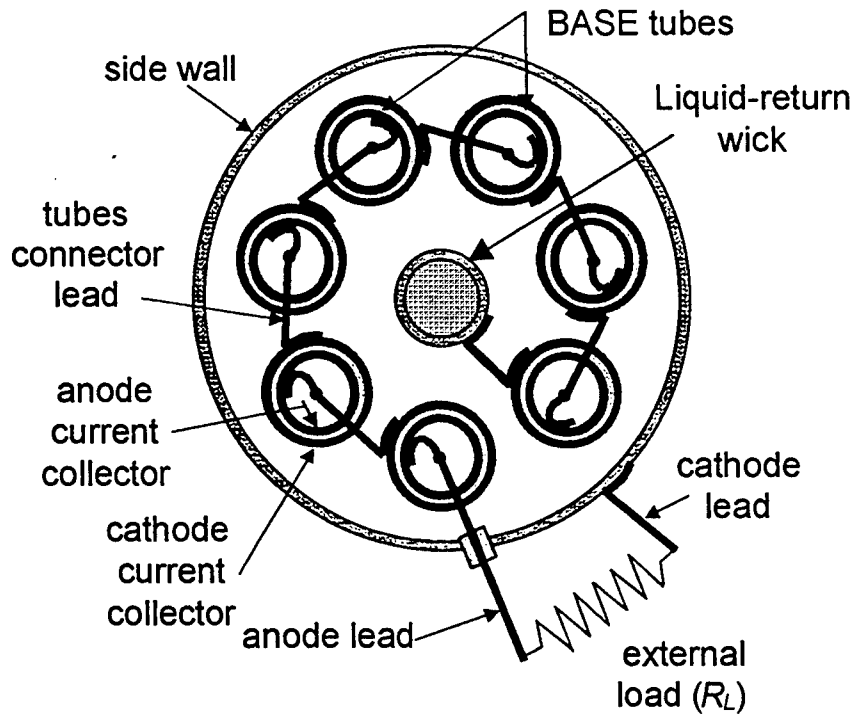
$$P_c = P_c^{oc} + \Delta P_{c,loss} = P_{cd}^{sat} \sqrt{\frac{T_B}{T_{cd}}} + \sqrt{2\pi R_g T_B / M} \left( \frac{3G}{8\pi} \right) \frac{MJ_r}{F} \quad (3.0)$$

The first term in Equation (3.0), the open-circuit vapor pressure at the BASE/cathode electrode interface, is given by the Langmuir relation for molecular effusive flow (Kennard 1938, and van Atta 1965). The second term,  $\Delta P_{c,loss}$ , is the vapor pressure loss between the cathode electrode/BASE interface and the condenser. Typical values of  $G$  less than 10 were reported for thin electrodes used in early AMTEC cell designs, in which the side wall functioned as the condenser. However, in an attempt to reduce radiation parasitic losses, recent cell designs employed a radiation shield between the heat source and sink of the cells, and a remote condenser (Ivanenok et al. 1994). The reduction in radiation parasitic losses in these cells, however, came at the expense of increased vapor pressure losses on the cathode side, for which the geometrical factor  $G$  could be as high as 150.

Recently, Ivanenok et al. (1994) developed a vapor pressure loss model for a single-tube AMTEC, with an internal heat shield (disk) and a remote coaxial condenser tube. They assumed a continuum vapor flow with a parabolic radial velocity profile and corrected the laminar friction coefficient correlation for a slip flow condition. The effect of increasing mass flow rate along the BASE tube, due to vapor perspiration at the BASE/cathode interface, was neglected. The transition between the vapor transition and free-molecular flow regimes was assumed to occur in the condenser tube. The pressure drop there was calculated by weighting the calculated pressure drops for the continuum and free-molecular regimes. Model results compared reasonably well with measurements for the cases where the vapor flow upstream of the condenser was continuum or near continuum, which is the validity limit of the slip flow approximation. In PX-series cell designs, however, where the vapor flow is expected to be in the transition or free-molecular



(a) elevation



(b) plan view (section A-A)

Figure 3.1. A Schematic of a Vapor Anode, Multi-Tube, AMTEC Cell (Not To Scale).

regime, this approach is invalid, and can erroneously underpredict the vapor pressure losses. Ivanenok et al. have also shown that using a remote condenser can potentially improve the AMTEC cell efficiency. The increase in vapor pressure losses between the BASE tube and the condenser would be more than compensated for by the reduction in the parasitic radiation losses in the cell.

In an attempt to model the entire vapor-anode, multi-tube AMTEC cell, Schock et al. (1997a and 1997b) developed complex thermal, electrical and vapor flow models using the SINDA Thermal Analyzer software and the ITAS Radiation Interchange code to calculate all radiation view factors in the cell. Schock et al. used a baseline cell designed by AMPS in February 1996 as a reference point for their study. The cell was constituted of a hot plenum cavity feeding 7 series-connected BASE tubes with high-pressure sodium vapor, a remotely-located condenser at the top end of the cell, and an off-centered liquid return artery. Orbital Sciences Corporation's (OSC) initial analyses showed that the geometry of the standoff between the evaporator end of the wick and the BASE tube support plate was of critical importance in providing adequate temperature margin between the evaporator and the coolest point of the BASE tubes (Schock et al. 1997b). A hotter evaporator could trigger condensation of sodium on the inside of the BASE tubes, causing internal electrical shorting of the BASE tubes in the cell. A cooler evaporator would result in reduced electrical power output, since the sodium pressure on the anode side is equal to the saturation pressure at the evaporator temperature. The OSC analysis revealed that providing adequate temperature margin required impractically small standoff dimensions. The standoff length would increase if the standoff's wall cross-sectional area could be increased. However, this option was prevented due to the close proximity of the neighboring BASE tubes. To avoid this problem, Schock et al. proposed a revised cell design, in which the liquid return artery was moved to the center of the cell, and the BASE tubes were relocated symmetrically on a coaxial ring. This design change allowed to increase both the diameter and the wall thickness of the evaporator standoff, resulting in a much more practical and fabricable standoff geometry for a temperature margin of 50 K.

In the OSC model, however, the vapor pressure losses in the multi-tube AMTEC cell were calculated using a simplified approach based on the equivalent hydraulic diameter approximation and a general equation for all flow regimes derived by the senior author in the 1970's (Schock et al. 1997a). This equation, which expresses the pressure gradient simply in terms of the local dimensionless pressure and mass flow rate, is basically a first approximation of the Dusty Gas Model (DGM) when the flow rate is small (Tournier and El-Genk 1996). Schock et al. results showed that both the dimensionless pressure and mass flow rate were typically on the order of unity, a situation for which the form of the vapor pressure loss equation cannot be identified. Their calculated vapor pressure along the BASE tubes bundle dropped very quickly, from 43 Pa to 14 Pa, causing the current density along the BASE tubes to vary by a factor as large as 4. These results were in disagreement with the findings of the present authors, that the current density along the BASE tubes is closer to uniform. It is believed that the vapor pressure equation of Schock et al. (1997a), developed for vapor flow through tubes connecting a continuum region and a vacuum, does not properly predict the effect of increasing mass flow rate along the BASE tubes. The change in flow rate would cause the axial vapor pressure along the tubes to have a parabolic profile that is much less steeper than that calculated by Schock et al. (1997a).

Therefore, there is a need to develop a more appropriate vapor flow and pressure loss model for these cells.

Evaluating the vapor pressure losses on the cathode side of an AMTEC cell is a difficult problem owing to the non-continuum vapor flow, and the complexity of the cell geometries. In this section, a vapor flow model is developed for calculating the pressure losses on the cathode side of a vapor anode, multi-tube AMTEC cell. This model is based on the dusty-Gas-Model, which has been verified for all vapor flow regimes of interest, continuum, transition, and molecular flow (Tournier and El-Genk 1996). The cell geometry used herein, which is the same as that used by Schock et al. (1997b), has a hot plenum cavity that feeds 7 BASE tubes with high-pressure sodium vapor, a remotely-located condenser, and a centerline liquid return artery (Figure 3.1). Also, the AMTEC cell has an internal chevron's radiation shield to reduce internal parasitic heat losses. The vapor pressure drop between the BASE/cathode interface and the remote condenser is calculated as the sum of that due to: (a) sodium evaporation at the BASE/electrode interface; (b) vapor perspiration through the cathode porous electrode; (c) vapor flow along the BASE tubes / evaporator standoff bundle; (d) change in the cross section flow area at the top of the BASE tubes; (e) vapor flow in the annulus of the liquid-return artery and cell wall; (f) vapor flow through the conical chevron's radiation shields; and (g) condensation of sodium vapor. The vapor flow diffusion coefficients in the free-molecular regime are calculated using the Knudsen and Dushman formulas (Appendix B), while those in the continuum regime are determined using an exact analytical solution (when available) or the equivalent hydraulic diameter approximation. The Dusty-Gas-Model (DGM), which has been verified for all vapor pressures and flow regimes of interest (free-molecule, transition, and continuum), is used to calculate the flow diffusion coefficients in the transition regime.

The present vapor flow model is used to calculate the pressure losses on the cathode side of the cell, and assess the effect of using a conical chevrons shield above the BASE tubes on the vapor pressure losses. For simplicity, the present analysis assumes uniform electrode current density and BASE temperature distributions. In a real cell, however, the electrode current density is slightly non-uniform and the temperature gradient along the BASE tubes is typically  $\sim 2$  K/mm. The present vapor flow model has been successfully integrated into a full multi-tube AMTEC cell model, in which the predicted distributions of electrode current density and temperature along the BASE tubes are incorporated.

### 3.3 MODEL DESCRIPTION

The sodium vapor flow model calculates the local sodium vapor pressure on the cathode side of the AMTEC cell shown in Figure 3.1. The vapor pressure drop between the BASE/cathode interface and the remote condenser is calculated as the sum of the following contributions:

- evaporation of sodium at the BASE outer surface,  $\Delta P_{\text{evap}}(z)$ ;
- vapor perspiration through the porous cathode electrode,  $\Delta P_E(z)$ ;
- vapor flow along the BASE tubes/evaporator standoff bundle,  $[P_1(0) - P_1(L_B)]$ ;
- sudden change in the cross section flow area at the top of BASE tubes,  $[P_1(L_B) - P_2(L_B)]$ ;
- vapor flow in the annulus above the BASE tubes, below the conical chevrons shield,

- $[P_2(L_B) - P_2(L_B + L_C)]$ ;
- vapor flow through the conical chevrons radiation shield,  $\Delta P = [P_2(L_B + L_C) - P_2(L_B + L_C + L_S)]$ ;
- vapor flow in the annulus between the top of the chevrons shield and the cell condenser; and
- condensation of sodium vapor at the cold end of the cell,  $\Delta P_{cd}$ .

### 3.3.1 Pressure Drop Caused by Evaporation of Sodium at BASE Surface

The pressure drop caused by evaporation of sodium along the BASE/cathode interface is given by the kinetic theory of gases (Tournier and El-Genk 1996), as:

$$P_1(z) - P_2(z) = a_{cc} \left( \frac{2\pi R_g T}{M} \right)^{1/2} \dot{m}''_{pore}(z). \quad (3.1)$$

The accommodation coefficient,  $a_{cc}$ , for liquid metals is close to unity in well evacuated, clean systems, such as in heat pipes or AMTEC (Tournier and El-Genk 1996). The sodium vapor mass flux in the pores of the cathode electrode,  $\dot{m}''_{pore}(z)$ , is related to the average local mass flux through the BASE tube,  $\dot{m}''_r(z)$ , by:

$$\dot{m}''_r(z) = \pi R_p^2 \times \dot{m}''_{pore}(z) \times N_{pore} = \varepsilon_E \times \dot{m}''_{pore}(z), \quad (3.2)$$

where  $R_p$  is the pores average hydraulic radius,  $N_{pore}$  is the number density of pores [pores/m<sup>2</sup>], and  $\varepsilon_E$  is the volume porosity of the electrode. The average mass flux of sodium through the BASE,  $\dot{m}''_r(z)$ , changes axially and is related to the local current density,  $J_r(z)$ , at the cathode side along the BASE tubes, as:

$$\dot{m}''_r(z) = \frac{M}{F} J_r(z). \quad (3.3)$$

The vapor mass flux in the pores of the cathode electrode is then given by:

$$\dot{m}''_{pore}(z) = \frac{M}{\varepsilon_E F} J_r(z). \quad (3.4)$$

Substituting Equation (3.4) into Equation (3.1) yields the following relation for the pressure drop due to evaporation of sodium along the BASE/cathode interface:

$$P_1(z) - P_2(z) = a_{cc} \left( \frac{2\pi R_g T}{M} \right)^{1/2} \frac{M}{\varepsilon_E F} J_r(z). \quad (3.5)$$

### 3.3.2 Pressure Drop in the Porous Electrode (Cathode)

The pressure drop caused by vapor flow through the porous electrode (cathode) is calculated using the Dusty-Gas-Model (Tournier and El-Genk 1996):

$$\Delta P_E = \frac{t_E}{D} \left( \frac{R_g T}{M} \right) \times \dot{m}_{pore}''(z), \quad (3.6)$$

where  $t_E$  is the thickness of the porous electrode times the tortuosity of the pores (effective pore length), and the flow diffusion coefficient,  $D$ , is given by:

$$D = D^{vis} + D^K \times \frac{1 + c_1^K \bar{P}}{1 + c_2^K \bar{P}}. \quad (3.7a)$$

In Equation (3.7a),  $\bar{P}$  is the average vapor pressure in the pores of the cathode electrode. The viscous and free-molecular flow diffusion coefficients are given, respectively, as (Tournier and El-Genk 1996, and van Atta 1965):

$$D^{vis} = \alpha^K \bar{P} = \frac{R_p^2}{8\mu} \bar{P}, \quad (3.7b)$$

$$D^K = \frac{C_{cl}}{C_o} D_o^K = \frac{20 + 8(t_E / R_p)}{20 + 19(t_E / R_p) + 3(t_E / R_p)^2} \times \frac{t_E}{4} \times \left( \frac{8R_g T}{\pi M} \right)^{1/2},$$

and

$$c_2^K = \frac{4R_p}{\mu} \times \left( \frac{M}{R_g T} \right)^{1/2}, \quad c_1^K = 0.81 \times c_2^K. \quad (3.7c)$$

The Dusty Gas Model has been shown to accurately predict the pressure drop for gas flow in capillary tubes, in all 3 flow regimes (Tournier and El-Genk 1996). These equations show that at very low vapor pressure, the flow diffusion coefficient,  $D$ , reduces to the Knudsen diffusion coefficient for free-molecular regime, which is independent of pressure. At high pressure ( $Kn < 0.02$ ), however, the Knudsen diffusivity is small compared to the viscous flow diffusivity, which increases proportionally with the vapor pressure, and the flow becomes essentially continuum. The pressure dependence of the term multiplying the Knudsen diffusivity in Equation (3.7a) explains the minimum in the flow diffusion coefficient at intermediate vapor pressure, for the transition flow regime.

Some metal electrodes do not have an apparent porosity, and the sodium atoms are transpired to the surface of the electrode by molecular diffusion. In such cases, the pressure drop in the electrode is expressed in terms of the empirical dimensionless factor  $G_E$  (Underwood et al. 1988 and 1992; Williams et al. 1993), as:

$$\Delta P_E = \frac{3G_E}{8\pi} \left( \frac{2\pi R_g T}{M} \right)^{1/2} \dot{m}_r''(z). \quad (3.8)$$

The factor  $G_E$  is determined experimentally, and varies typically between 10 and 60. For the case of free-molecular flow transport through the electrode, a comparison of Equations (3.6) and (3.8) provides the following expression for  $G_E$ :



$$G_E = \frac{8\pi}{3} \times \frac{t_E}{\varepsilon_E D} \left( \frac{R_g T}{2\pi M} \right)^{1/2} \quad (3.9)$$

It is worth noting that for a value of  $G_E = 8\pi/3 = 8.4$ , the vapor pressure drop in the porous cathode electrode,  $\Delta P_E$ , equals that due to evaporation of sodium at the BASE surface,  $[P_1(z) - P_2(z)]$ .

### 3.3.3 Pressure Drop along the Base Tubes

The vapor space between the BASE tubes and the evaporator standoff in the AMTEC cell (Figure 3.1) is treated as a single channel with an equivalent hydraulic diameter  $D_e$  (White 1991), for which:

$$D_e = \frac{4 \times \text{Flow Area}}{\text{Wetted Perimeter}} = \frac{D_w^2 - N_B D_B^2 - D_s^2}{D_w + N_B D_B + D_s} \quad (3.11)$$

The axial vapor flow area,  $A$ , is:

$$A = \frac{\pi}{4} (D_w^2 - N_B D_B^2 - D_s^2) \quad (3.12)$$

The increase in vapor mass flow rate per unit length of the BASE tubes is given by:

$$\frac{d\dot{m}_z(z)}{dz} = \dot{m}'_r(z) = (N_B \pi D_B) \times \dot{m}''_r(z) = (N_B \pi D_B) \times \frac{M}{F} J_r(z) \quad (3.13)$$

The conservation of axial momentum is expressed as (Tournier and El-Genk 1996):

$$\bar{\alpha}_2 \frac{d}{dz} (\rho \bar{U}_z^2) = -\frac{dP_3(z)}{dz} - \frac{4\tau_w}{D_e} \quad (3.14)$$

where, the average vapor velocity,  $\bar{U}_z$ , is related to the mass flow rate as:

$$\bar{U}_z = \frac{\dot{m}_z(z)}{\rho A} = \frac{\dot{m}''_z(z)}{\rho} \quad (3.15)$$

The coefficient  $\bar{\alpha}_2$  in Equation (3.14), which accounts for the non-uniform axial velocity profile of the vapor flow, is defined by (Tournier and El-Genk 1996):

$$\bar{\alpha}_2 = \frac{\iint_A (U_z)^2 dA}{\left( \iint_A U_z dA \right)^2} = \frac{\iint_A (U_z)^2 dA}{\bar{U}_z^2 A} \quad (3.16)$$

For a fully-developed laminar flow in a circular channel,  $\bar{\alpha}_2 = 4/3$ , while for a fully-developed turbulent flow,  $\bar{\alpha}_2 = 1.020$  (White 1991). In the free-molecular flow,  $\bar{\alpha}_2 = 1$  (El-Genk and Tournier 1995), because this flow regime is limited by the molecular collisions with the wall

(hence, molecules only transfer momentum to the wall as they go along their path, unaware of the presence of other molecules, and their velocity profile is flat). Therefore,  $\bar{\alpha}_2$  is a function of the Knudsen number. However, a value  $\bar{\alpha}_2=1$  is used in this work, since in all practical cases of interest, the advection of axial momentum represents less than 8% of the total pressure losses, so that an error in  $\bar{\alpha}_2$  is of little consequence (note the mistake of using the coefficient for advection of kinetic energy of vapor,  $\bar{\alpha}_3$ , in place of the coefficient for advection of axial momentum,  $\bar{\alpha}_2$ , in the work of Ivanenok et al. 1994).

The second term on the right-hand side of Equation (3.14), the pressure losses per unit volume, can be expressed in terms of the friction factor,  $f$ , as:

$$\frac{4\tau_w}{D_e} = \frac{f}{D_e} \frac{1}{2} \rho \bar{U}_z^2, \quad (3.17)$$

or in terms of the flow diffusion coefficient,  $D$ , as:

$$\frac{4\tau_w}{D_e} = \frac{P \bar{U}_z}{D} = \left( \frac{R_g T}{M} \right) \frac{\rho \bar{U}_z}{D}. \quad (3.18)$$

Since no general expression for the pressure tensor deviatoric,  $\tau_w$ , is available as a function of Knudsen number, we used the first approximation of the Dusty-Gas-Model (Tournier and El-Genk 1996), for which  $c_1^K = c_2^K = 0$ . Thus:

$$D = D^{vis} + D^K. \quad (3.19)$$

For flow in circular channels, the first approximation results in a maximum error of less than 10% in the transition flow region (Tournier and El-Genk 1996). Therefore, the first approximation is expected to provide reasonably accurate results.

The vapor pressure at the top of the BASE tubes is typically less than 20 Pa, and Mach numbers greater than 0.2 can be encountered, thus the vapor flow is compressible (see Appendix A). Therefore, the laminar viscous friction coefficient in Equation (3.17) is corrected for the effect of compressibility using the von Kármán correction (White 1991), as:

$$f_{comp} = \frac{f_{incomp}}{\sqrt{1 + \frac{\gamma - 1}{2} Ma^2}}. \quad (3.20)$$

Combining Equations (3.17) and (3.18) gives the viscous flow diffusion coefficient,  $D^{vis}$ , in terms of the friction coefficient, as:

$$D^{vis} = \left( \frac{R_g T}{M} \right) \frac{2D_e}{f_{comp} \bar{U}_z} = \frac{2D_e}{\dot{m}_z'' f_{comp}} P. \quad (3.21)$$

The viscous friction coefficient,  $f_{incomp}$ , is calculated using the equivalent diameter approximation (White 1991), as:

$$f_{incomp} = \frac{64\mu}{D_e \dot{m}_z''} \quad (3.22)$$

Substituting Equations (3.20) and (3.22) into Equation (3.21) gives:

$$D^{vis} = \frac{D_e^2}{32\mu} \sqrt{1 + \frac{\gamma-1}{2} Ma^2} \times P \quad (3.23)$$

Approximate formulas for molecular flows through channels and apertures of any shapes were developed principally by Knudsen using the kinetic theory of gases. When the mean free path of the gas molecules is large compared to the cross-sectional dimension of the channel, the flow diffusion coefficient is independent of the gas pressure. For most purposes, the formulas derived by Knudsen are sufficiently accurate. The diffusion coefficient for free-molecular flow through a channel of length  $L$  and arbitrary cross section  $A$ , is expressed as (Appendix B):

$$D^K = \frac{L}{A} C = \frac{L}{1 + \frac{3L}{4D_e}} \left( \frac{R_g T}{2\pi M} \right)^{1/2} \quad (3.24)$$

Although Equation (3.24) is only approximate, it agrees well with experimental data and Monte-Carlo calculation results for flow channels of various cross sections and shape (Appendix B). Therefore, Equation (3.24) is used to calculate the free-molecular flow diffusion coefficient,  $D^K$ , along the BASE tubes, in Equation (3.19).

Assuming that the vapor temperature is equal to that of the cathode electrode, the compressible term on the left-hand side of Equation (3.14) can be written:

$$\frac{d}{dz} (\rho \bar{U}_z^2) = \frac{d}{dz} \left( \frac{\dot{m}_z''^2}{\rho} \right) = \frac{\dot{m}_z''^2}{\rho} \left\{ \frac{1}{T} \frac{dT}{dz} - \frac{1}{P} \frac{dP}{dz} + \frac{2}{\dot{m}_z''} \frac{d\dot{m}_z''}{dz} \right\} \quad (3.25)$$

The vapor density is calculated using the perfect gas law:

$$\rho = \left( \frac{M}{R_g T} \right) P, \quad (3.26)$$

where  $R_g = 8.314$  J/mol.K is the gas constant, and  $M = 22.99 \times 10^{-3}$  kg/mol is the molecular weight of sodium. Combining Equations (3.14), (3.18) and (3.25), the conservation of axial momentum along the BASE tubes could be written as:

$$\bar{\alpha}_2 \left( \frac{R_g T}{M} \right) \frac{\dot{m}_z''^2}{P_1} \left\{ \frac{1}{T} \frac{dT}{dz} - \frac{1}{P_1} \frac{dP_1}{dz} + \frac{2}{\dot{m}_z''} \frac{d\dot{m}_z''}{dz} \right\} = - \frac{dP_1}{dz} - \left( \frac{R_g T}{M} \right) \frac{\dot{m}_z''}{D}, \quad (3.27)$$

where

$$\frac{d\dot{m}_z''}{dz} = \frac{N_B \pi D_B}{A} \times \frac{M}{F} J_r(z), \quad (3.28)$$

and

$$D = D^{vis} + D^K = \frac{D_e^2}{32\mu} \sqrt{1 + \frac{\gamma-1}{2} Ma^2} \times P_3 + \frac{L_B}{1 + \frac{3L_B}{4D_e}} \left( \frac{R_g T}{2\pi M} \right)^{1/2} \quad (3.29)$$

Rearranging Equation (3.27) gives the following expression for the sodium vapor pressure gradient:

$$\frac{dP_1}{dz} = \frac{1 + \bar{\alpha}_2 \frac{\dot{m}_z'' D}{P_1} \left\{ \frac{1}{T} \frac{dT}{dz} + \frac{2}{\dot{m}_z''} \frac{d\dot{m}_z''}{dz} \right\}}{1 - \bar{\alpha}_2 \left( \frac{R_g T}{M} \right) \left( \frac{\dot{m}_z''}{P_1} \right)^2} \left( \frac{R_g T}{M} \right) \frac{\dot{m}_z''}{D} = \Phi(P_1, z). \quad (3.30)$$

Equation (3.30) expresses the vapor pressure gradient in terms of the local vapor pressure,  $P_1(z)$ . Since the current density and BASE temperature distributions are known, the local sodium vapor mass flow rate can be calculated by integrating Equation (3.13). Therefore, all terms on the right-hand-side of Equation (3.30) are known, except the local vapor pressure. Equation (3.30) was integrated numerically using the trapezoidal rule to obtain the axial distribution of the vapor pressure along the BASE tubes. The total length of the BASE tubes was discretized into  $n$  identical sections. Results showed that the pressure drop obtained with  $n = 20$  was within  $< 1\%$  of the value calculated with an arbitrarily large number of elements ( $n = 500$ ).

### 3.3.4 Pressure Loss Caused by Sudden Expansion at Top of Base Tubes

The pressure drop caused by the sudden expansion in the flow area at the top of BASE tubes is classically expressed in terms of the loss form coefficient,  $K$ , as (Idelchik 1986):

$$P_1(L_B) - P_2(L_B) = K \frac{1}{2} (\rho \bar{U}_z^2)_1 = K \frac{1}{2} \left( \frac{\dot{m}_z''^2}{\rho} \right)_1, \quad (3.31)$$

where the subscript (1) refers to the upstream flow (channel between the BASE tubes/evaporator standoff bundle). At typical AMTEC operating conditions, the vapor flow Reynolds number is less than 13, and the loss form coefficient,  $K$ , is expressed as (Idelchik 1986):

$$K = \frac{\xi}{Re_1^{\max}} = \xi \left( \frac{\mu}{D_e \dot{m}_z''^{\max}} \right)_1. \quad (3.32)$$

Measured values of the resistance coefficient,  $\xi$ , are listed in Table 3.1 for expansion area ratio of 0.05, 0.16, 0.43 and 0.64. The selected values of  $\xi$  in Table 3.1 are used to obtain the following empirical relation as a function of expansion area ratio,  $\beta = A_1/A_2$  (Figure 3.2):

$$\xi = 1908 \times (\beta - 0.145)^{-0.05812} - 1923., \quad (3.33)$$

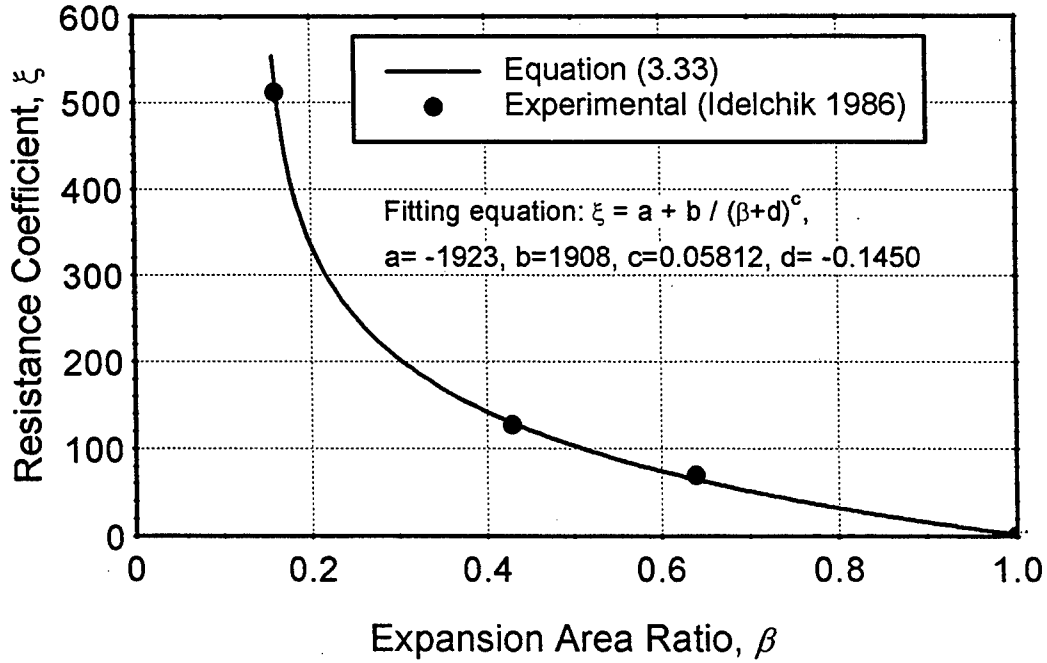


Figure 3.2. Resistance Coefficient  $\xi$  for Sudden Expansion, as a Function of Area Ratio.

so that finally:

$$P_1(L_B) - P_2(L_B) = \Delta P_{\text{exp}} = \frac{\xi}{2} \left( \frac{\mu \dot{m}_z^2}{\rho D_e} \right)_1 \quad (3.34)$$

For an example, consider an AMTEC cell operating at  $I = 1.5$  A, a BASE tube temperature  $T_B = 1050$  K, and an upstream sodium vapor pressure  $P_1(L_B) = 20$  Pa. At these conditions, the sodium mass flow rate  $\dot{m}_z = 9$  gm/hr  $= 2.5 \times 10^{-6}$  kg/s, the vapor density  $\rho = 5.27 \times 10^{-5}$  kg/m<sup>3</sup>, and the vapor dynamic viscosity  $\mu = 1.5 \times 10^{-5}$  kg/m.s. The upstream Reynolds number of the sodium vapor,  $Re_1 = 2.53$ . With  $A_1 = 612. \times 10^{-6}$  m<sup>2</sup> and  $A_2 = 858. \times 10^{-6}$  m<sup>2</sup>, the expansion ratio is  $\beta = 0.713$ , and  $\xi = 52$ . The loss form coefficient  $K = 20.6$ , and the pressure loss due to sudden expansion at the top of the BASE tubes is  $\Delta P_{\text{exp}} = 3.2$  Pa.

### 3.3.5 Pressure Loss in Annulus Above Base Tubes

The vapor space above the BASE tubes is an annulus having an outer diameter  $D_w$  and inner diameter  $D_a$  (the diameter of the centerline liquid-return artery). The annular vapor flow area,  $A$ , and equivalent hydraulic diameter,  $D_e$ , of this annulus, are given by:

$$A = \frac{\pi}{4} (D_w^2 - D_a^2), \text{ and } D_e = \frac{4A}{\pi(D_w + D_a)} = D_w - D_a \quad (3.35)$$

Table 3.1. Measured and Selected Values of the Resistance Coefficient  $\xi$  for Sudden Expansions of Different Area Ratios (Idelchik 1986, Figure 4.9, page 155).

area ratio $\beta=A_1/A_2$	$Re_1 = 1$		$Re_1 = 5$		$Re_1 = 10$		$\xi$ selection
	$K$ (exp)	$\xi^*$ (exp)	$K$ (exp)	$\xi^*$ (exp)	$K$ (exp)	$\xi^*$ (exp)	
0.05	3714.	3714.	740.	3700.	340.	3400.	3700.
0.16	512.	512.	110.	550.	51.	510.	512.
0.43	127.	127.	27.4	137.	11.9	119.	127.
0.64	66.3	66.3	15.0	75.0	7.05	70.5	69.

\*:  $\xi = K \times Re_1$

The vapor flow rate in the annulus above the BASE tubes is constant and equal to that at the top of BASE tubes. In this annulus, the conservation of axial momentum can also be expressed by Equation (3.14), as:

$$\bar{\alpha}_2 \frac{d}{dz} \left( \frac{\dot{m}_z^{*2}}{\rho} \right) = -\frac{dP_2}{dz} - \left( \frac{R_g T}{M} \right) \frac{\dot{m}_z^*}{D} \quad (3.36)$$

The flow diffusion coefficient in this region,  $D$ , is obtained from the first approximation of the Dusty Gas Model, and is given by Equation (3.29), as:

$$D = D^{vis} + D^K = \frac{D_e^2}{32\mu} \sqrt{1 + \frac{\gamma-1}{2} Ma^2} \times \frac{P_2}{\zeta} + \frac{L_C}{1 + \frac{3L_C}{4D_e}} \left( \frac{R_g T}{2\pi M} \right)^{1/2} \quad (3.37)$$

For viscous laminar flow in annular channel, the correction factor,  $\zeta$ , has the expression (White 1991):

$$\zeta = \frac{(D_w - D_a)^2}{D_w^2 + D_a^2 - \frac{D_w^2 - D_a^2}{\ln(D_w / D_a)}} \quad (3.38)$$

This factor varies between 1.0 and 1.5, which indicates that, for laminar flow, the calculated vapor pressure losses based on the equivalent diameter approximation could be in error by as much as 33%, if  $\zeta$  is not included (i.e.  $\zeta=1$ ).

The diffusion coefficient for free-molecular flow,  $D^K$ , is calculated using the Dushman formula, Equation (3.24). For annular flow, this equation is within 10% of numerical results obtained by the Monte-Carlo method (Appendix B).

The vapor temperature above the BASE tubes changes with axial position. Therefore, the gradient of the vapor specific volume in Equation (3.36) is expressed in terms of the pressure and temperature gradients, as:

$$\frac{d}{dz} \left( \frac{1}{\rho} \right) = \frac{R_g}{M} \frac{d}{dz} \left[ \frac{T}{P_2} \right] = \left( \frac{R_g T}{M} \right) \frac{1}{P_2} \left[ \frac{1}{T} \frac{dT}{dz} - \frac{1}{P_2} \frac{dP_2}{dz} \right]. \quad (3.39)$$

By combining Equations (3.36) and (3.39), the pressure gradient in the annulus above the BASE tubes is expressed as:

$$\frac{dP_2}{dz} = - \frac{1 + \bar{\alpha}_2 \frac{\dot{m}_z'' D}{P_2} \left\{ \frac{1}{T} \frac{dT}{dz} \right\} \left( \frac{R_g T}{M} \right) \frac{\dot{m}_z''}{D}}{1 - \bar{\alpha}_2 \left( \frac{R_g T}{M} \right) \left( \frac{\dot{m}_z''}{P_2} \right)^2} \Phi(P_2, z). \quad (3.40)$$

Equation (3.40) expresses the vapor pressure gradient in the annulus in terms of the local vapor pressure,  $P_2(z)$ . All other terms on the right-hand-side of Equation (3.40), which involve the sodium mass flow rate and temperature distribution, are known. Equation (3.40) was integrated numerically to obtain the axial distribution of the sodium vapor pressure,  $P_2(z)$ , in the annulus above the BASE tubes. Numerical results showed that the pressure distribution obtained with  $n = 20$  was within  $< 1\%$  of that calculated with an arbitrarily large number of elements ( $n = 500$ ).

### 3.3.6 Pressure Loss Caused by Vapor Flow through Chevron's Shield

In the annular space, mid-way between the BASE tubes and condenser,  $N$  conical chevrons that are  $(1 + \alpha)d$  wide and separated by a distance  $d$ , are placed to reduce parasitic radiation losses from the BASE tubes to the cell wall and condenser (Figure 3.1). The conical chevrons are arranged such that  $(N + \alpha) = (R_w - R_d)/d$ , and there are  $(N - 1)$  conical flow passages (Figure 3.3). Therefore, the conservation of sodium vapor flow through the chevrons is expressed as:

$$\dot{m}_z = \sum_{k=1}^{N-1} \bar{A}_k \dot{m}_k'', \quad (3.41)$$

where  $\dot{m}_z$  is the total mass flow rate, and  $\dot{m}_k''$  is the average mass flux in passage (k). The perpendicular distance between two adjacent chevrons,  $b = d \sin(\theta)$ , and the effective path length in every passage,  $L = (1 + \alpha)2d / \cos(\theta)$ . From a hydrodynamic point of view, every conical flow passage (k) is equivalent to an effective annulus that has a flow area  $\bar{A}_k$ , average perimeter  $\bar{S}_k$ , equivalent hydraulic diameter  $D_{ek}$ , and inner and outer diameters  $D_k^{in}$  and  $D_k^{out}$ . The projected area of an inclined annulus having an inner radius  $R$ , is:

$$A^{proj}(R) = \pi \left[ (R + b \sin \theta)^2 - R^2 \right] = \pi b \sin \theta [2R + b \sin \theta]. \quad (3.42)$$

The effective flow area of the inclined annulus is:

$$A(R) = \frac{A^{proj}(R)}{\sin \theta} = \pi b [2R + b \sin \theta]. \quad (3.43)$$

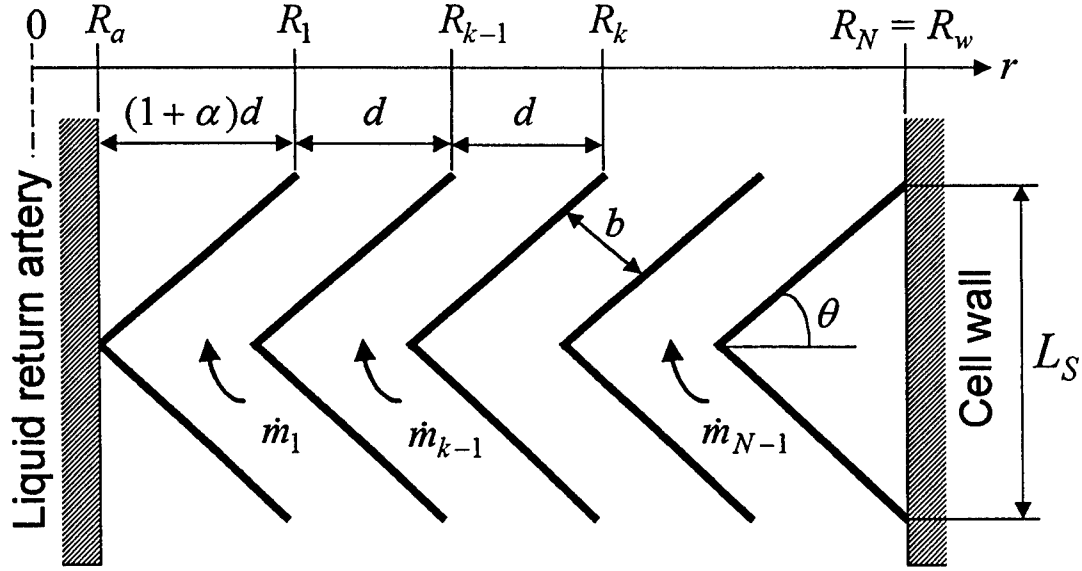


Figure 3.3. Schematic of (Unseparated) Conical Chevrons Radiation Shield.

Introducing  $R_k = R_a + d \times (k + \alpha)$ , as the radius of the chevron (k) at the entrance or exit of the shield, the average effective flow area of the passage (k) can be calculated by averaging  $A(R)$  between  $R_k - (1 + \alpha)d$  and  $R_k$ , as:

$$\bar{A}_k = \frac{1}{(1 + \alpha)d} \int_{R_k - (1 + \alpha)d}^{R_k} A(R) dR = \pi b [2R_k - d(\alpha + \cos^2 \theta)] \quad (3.44)$$

The perimeter of an equivalent chevron annulus with an inner radius,  $R$ , is:

$$S(R) = 2\pi R + 2\pi[R + b \sin \theta] = 2\pi[2R + b \sin \theta] \quad (3.45)$$

and the average perimeter of the flow passage (k), calculated by averaging  $S(R)$  between  $R_k - (1 + \alpha)d$  and  $R_k$ , is:

$$\bar{S}_k = \frac{1}{(1 + \alpha)d} \int_{R_k - (1 + \alpha)d}^{R_k} S(R) dR = 2\pi[2R_k - d(\alpha + \cos^2 \theta)] \quad (3.46)$$

The equivalent hydraulic diameter of flow passage (k) is then given as:

$$D_{ek} = 4\bar{A}_k / \bar{S}_k = 2b \quad (3.47)$$

which is twice the perpendicular distance between two adjacent chevrons. Finally, making use of the relations:

$$D_{ek} = D_k^{out} - D_k^{in} \quad , \quad \text{and} \quad (3.48)$$

$$\bar{A}_k = \frac{\pi}{4} [(D_k^{out})^2 - (D_k^{in})^2]$$



for an annulus, the following expressions for the effective inner and outer diameters of the chevron flow passage (k) are obtained:

$$\begin{aligned} D_k^{in} &= 2R_k - b - d(\alpha + \cos^2 \theta), \\ D_k^{out} &= 2R_k + b - d(\alpha + \cos^2 \theta). \end{aligned} \quad (3.49)$$

The conservation of axial momentum in the annular passage (k) of the chevron's shield can be expressed as:

$$\bar{\alpha}_2 \frac{d}{dz} \left( \frac{\dot{m}_k''^2}{\rho} \right) = - \frac{dP_k}{dz} - \left( \frac{R_g T}{M} \right) \frac{\dot{m}_k''}{D_k}, \quad (3.50)$$

where the flow diffusion coefficient,  $D_k$ , in this region, is given by Equation (3.29), as:

$$D_k = D_k^{vis} + D_k^K = \frac{b^2}{8\mu} \sqrt{1 + \frac{\gamma - 1}{2} Ma_k^2} \times \frac{P_k}{\zeta_k} + \frac{L}{1 + \frac{3L}{8b}} \left( \frac{R_g T}{2\pi M} \right)^{1/2}. \quad (3.51)$$

Note that the Knudsen diffusion coefficient,  $D^K$ , is identical for all flow passages. The annulus correction factor,  $\zeta_k$ , is given by:

$$\zeta_k = \frac{(D_k^{out} - D_k^{in})^2}{(D_k^{out})^2 + (D_k^{in})^2 - \frac{(D_k^{out})^2 - (D_k^{in})^2}{\ln(D_k^{out} / D_k^{in})}}. \quad (3.52)$$

Assuming that the vapor temperature is constant and equal to that of the chevrons, the compressible term in Equation (3.50) is written as:

$$\frac{d}{dz} \left( \frac{\dot{m}_k''^2}{\rho} \right) = \dot{m}_k''^2 \left( \frac{R_g T}{M} \right) \frac{d}{dz} \left( \frac{1}{P_k} \right) = - \frac{\dot{m}_k''^2}{P_k^2} \left( \frac{R_g T}{M} \right) \frac{dP_k}{dz}, \quad (3.53)$$

and Equation (3.50) reduces to:

$$\left[ 1 - \bar{\alpha}_2 \left( \frac{R_g T}{M} \right) \frac{\dot{m}_k''^2}{P_k^2} \right] \frac{dP_k}{dz} = - \left( \frac{R_g T}{M} \right) \frac{\dot{m}_k''}{D_k}. \quad (3.54)$$

Equation (3.54) must be integrated along the chevrons' effective flow path length,  $L$ , to determine the vapor pressure loss across the shield.

The solution of Equations (3.54) is very involved, since the mass flow rates in every flow passage,  $\dot{m}_k''$ , are not equal and are unknown. However, the vapor flow through the different chevron passages is subjected to the same pressure drop. The pressure drop across a flow passage (k),  $\Delta P_k$ , can be obtained by integrating Equation (3.54) along the effective flow path length,  $L$ . The integration is complicated, since the compressible term and the flow diffusion coefficient,  $D_k$ , are functions of the vapor pressure and the mass flow rate.

For the sodium flow rates typically encountered in PX-series AMTEC cells, however, the solution can be greatly simplified. For example, for the maximum mass flux of sodium vapor in a PX-series AMTEC cell:

$$\dot{m}_{\max}'' \approx \frac{\dot{m}_z^{\max}}{A} = \frac{L_B(N_B\pi D_B)}{A} \times \frac{M}{F} J_r(z) = J_r[A/cm^2] \times 6.422 \times 10^{-3} \quad [kg/m^2s], \quad (3.55)$$

and for an average vapor temperature of 900 K in the chevrons, the maximum value of the compressible term in Equation (3.54) is:

$$\left(\frac{R_g T}{M}\right) \frac{\dot{m}_{\max}''^2}{P_k^2} \approx 13.41 \times \frac{J_r^2 [A/cm^2]}{P_k^2 [Pa]}. \quad (3.56)$$

This value is less than 6% at the maximum current densities in a typical PX-series AMTEC cell,  $J_r = 0.5 \text{ A/cm}^2$ , when the sodium vapor pressure is  $> 8 \text{ Pa}$ . For pressures below 8 Pa, the sodium vapor flow in the chevrons passages is in the free-molecular regime, and the compressible term for isothermal flow is non-existent. Therefore, for practical purposes, the compressible term in Equation (3.54) can be neglected.

Also, at a vapor temperature of 900 K and a maximum current density,  $J_r = 0.5 \text{ A/cm}^2$ , the vapor Mach number is less than 0.283 at sodium pressures above 5 Pa, for which the von Kármán compressible factor varies within a very narrow range:

$$1 \leq \sqrt{1 + \frac{\gamma - 1}{2} Ma_k^2} \leq 1.013. \quad (3.57)$$

Therefore, this compressible factor can also be neglected in Equation (3.51), hence the expression for the flow diffusion coefficient,  $D_k$ , is simplified as:

$$D_k = D_k^{\text{vis}} + D_k^K = a_k^K P_k + D^K, \quad (3.58)$$

where the coefficient  $a_k^K$  and the Knudsen diffusion coefficient,  $D^K$ , are independent of the sodium vapor pressure and mass flux.

With the above two simplifications, the integration of Equation (3.51) along a chevron's flow passage (k) having a length,  $L$ , gives the vapor pressure loss term as:

$$\Delta P_k = \left(\frac{R_g T}{M}\right) \frac{L}{D_k} \dot{m}_k'' = \Delta P, \quad \text{for } k=1 \text{ to } (N-1). \quad (3.59)$$

The flow diffusion coefficient,  $\overline{D_k}$ , is evaluated at the average vapor pressure in the chevrons,  $\overline{P_k} = P_2(L_B + L_C) - \Delta P/2$ . The sodium vapor flow rate in passage (k) is written in terms of the pressure loss,  $\Delta P$ , using Equation (3.59), as:

$$\dot{m}_k'' = \left( \frac{M}{R_g T} \right) \frac{\overline{D}_k}{L} \Delta P, \quad (3.60)$$

and the sodium vapor mass balance, Equation (3.41), is written as:

$$\dot{m}_z = \sum_{k=1}^{N-1} \overline{A}_k \dot{m}_k'' = \frac{\Delta P}{L} \left( \frac{M}{R_g T} \right) \sum_{k=1}^{N-1} \overline{A}_k \overline{D}_k, \quad (3.61)$$

so that the pressure loss through the chevron's radiation shield is expressed as:

$$\Delta P = \frac{L}{\sum_{k=1}^{N-1} \overline{A}_k \overline{D}_k} \left( \frac{R_g T}{M} \right) \dot{m}_z = \frac{1}{\chi} \left( \frac{R_g T}{M} \right) \dot{m}_z. \quad (3.62)$$

An iterative solution procedure is required to resolve the dependence of the flow diffusion coefficients on the local sodium pressure.

### 3.3.7 Pressure Loss in the Annulus above Chevron's Shield

The geometry and governing equations for calculating the vapor pressure loss in the annulus between the chevron's shield and the condenser are identical to those used for the annulus between the top of the BASE tubes and the inlet of the chevron's shield, Equations (3.37) to (3.40).

### 3.3.8 Pressure Loss Caused by Condensation of Sodium

The pressure drop due to condensation of sodium vapor onto the condenser surface (Figure 3.1) is obtained from the kinetic theory (Tournier and El-Genk 1996), as:

$$\Delta P_{cd} = a_{cc} \left( \frac{2\pi R_g T_{cd}}{M} \right)^{1/2} \dot{m}_z'' \quad (3.63)$$

### 3.4 RESULTS AND DISCUSSION

The present sodium vapor pressure loss model was used to characterize the flow regime and calculate the pressure losses on the cathode side of a multi-tube AMTEC cell (Figure 3.1). Also, the effect of a conical chevrons shield above the BASE tubes on the vapor pressure losses was evaluated. The sodium vapor pressure loss model was also coupled to an electrical circuit model of a multi-tube AMTEC cell, described in details in Chapter 4, which allows the current density to vary axially along the BASE tubes. The coupled model is used to predict the electrical performance of a vapor anode, multi-tube AMTEC cell. The analyses, however, were performed at fixed evaporator, BASE tubes and condenser temperatures. For simplicity, the vapor temperature along the BASE tubes was assumed uniform and equal to the evaporator temperature. Also, the vapor temperature above the BASE tubes (on the cathode side) was assumed to vary linearly between the BASE and the condenser temperatures.

The vapor anode, multi-tube AMTEC cell analyzed had 7 series-connected BASE tubes (outer diameter of 6.35 mm), covered with 15.88 mm-high electrodes, having an effective  $G_E = 11.7$  (Equation 3.9 with  $t_E = 5 \mu\text{m}$ ,  $R_p = 10 \mu\text{m}$ , and  $\varepsilon_E = 0.9$ ). The outer diameter of the evaporator standoff was equal to that of BASE tubes (Figure 3.1). The diameters of the cell wall and liquid-return artery were 33.2 mm and 3.18 mm, respectively, and the condenser was placed 61 mm away from the top of the BASE tubes. A chevrons radiation shield, consisting of 4 conical chevrons with a  $45^\circ$  angle, was placed above the BASE tubes. In the minimum shielding configuration of direct radiation between BASE tubes and condenser,  $\alpha=0$ , and  $L_S = 7.5 \text{ mm}$ . As the analysis of the next section will show, this chevrons' geometry is close to the optimum design for minimizing the vapor pressure loss through the shield. The temperature-independent exchange current and the contact resistance between current collector, electrode and BASE were taken equal to  $120 \text{ A.K}^{1/2}/\text{Pa.m}^2$  and  $0.08 \Omega.\text{cm}^2$ , respectively, in the model. The external load resistance was taken as  $R_L = 2 \Omega$ .

#### 3.4.1 Vapor Pressure Losses in a Vapor Anode, Multi-Tube AMTEC Cell

Figure 3.4 shows the calculated sodium vapor pressure on the cathode side of the multi-tube AMTEC cell, operating at condenser and BASE tube temperatures of 550 K and 1050 K, respectively, for three different placements of the chevrons, and without thermal shield. The predicted cell electric current was  $I \sim 1.39 \text{ A}$ , which corresponded to a sodium mass flow rate of 8.3 gm/hr. Calculated pressure losses for a shield clearance of 48 mm (the distance between condenser and top of radiation shield) are also listed in Table 3.2. As shown in Figure 3.4, the axial pressure profile of sodium vapor along the BASE tubes was parabolic, owing to continuous mass addition at the BASE tubes' outer surface. The major contributions to the pressure losses between the condenser and BASE surface were those due to, in order of decreasing magnitude: vapor flow through the chevron's shield (50.6%), condensation of sodium vapor (11.1%), and sudden expansion at the top of BASE tubes (9.7%). For a radiation shield clearance of 48 mm, the AMTEC cell has an effective dimensionless factor for vapor pressure losses of:

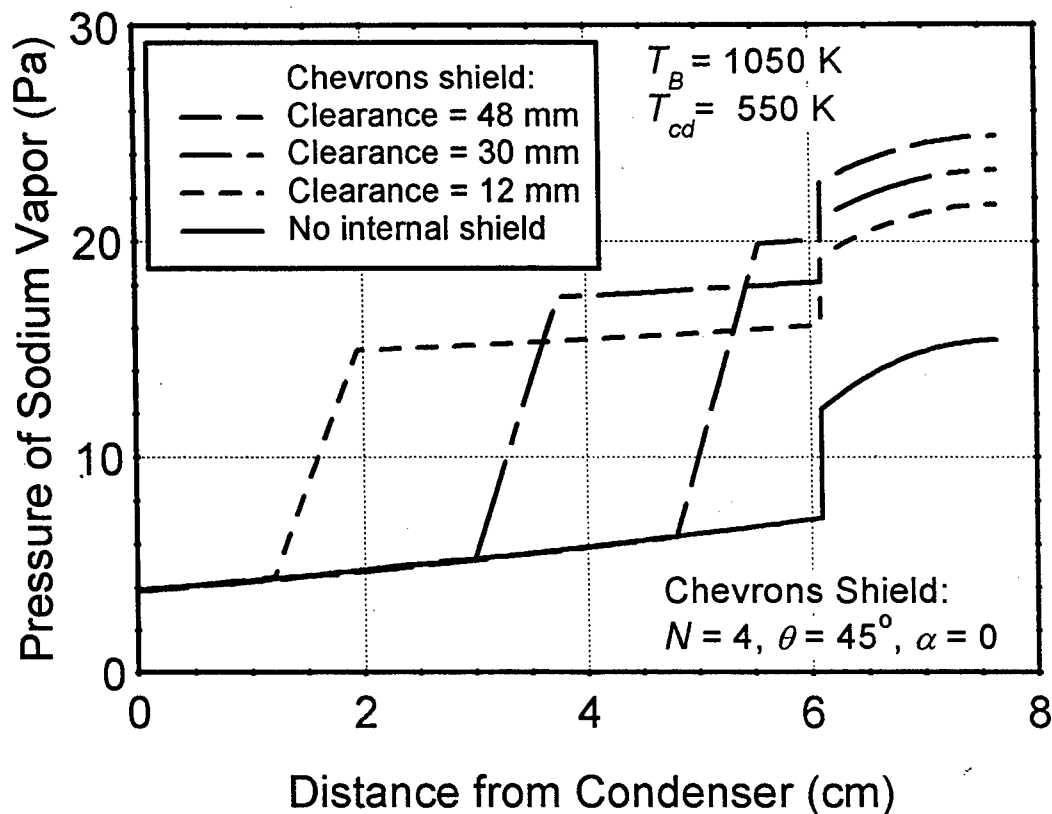


Figure 3.4. Calculated Vapor Pressure on Cathode Side of a Multi-Tube AMTEC Cell ( $I = 1.39$  A,  $\dot{m}_z = 8.3$  gm/hr).

Table 3.2. Sodium Vapor Pressure Losses in PX-1A Cell with Four 45°-angle Chevrans Placed 48 mm from Condenser ( $T_{cd} = 550$  K,  $T_B = 1050$  K,  $R_L = 2$   $\Omega$ ,  $I = 1.39$  A).

Region / Process*	pressure drop (Pa)	Contribution (%)
Condensation	3.0	11.1
Between Condenser and Chevrans	2.5	9.3
through chevrans	13.6	50.6
Between chevrans and BASE tubes	0.2	0.7
Expansion above BASE tubes	2.6	9.7
along BASE tubes	2.0	3.7
through cathode electrode	2.2	8.2
Evaporation at BASE outer surface	1.8	6.7
Total pressure drop between condenser and BASE at mid-plane of electrode	26.9 Pa	100%

\* condenser vapor pressure = 0.8 Pa

$$G = \frac{\Delta P_{c,loss}}{\Delta P_E} \times G_E = \frac{26.9}{2.2} \times 11.7 = 143 . \quad (3.64)$$

Results showed that the total pressure drop on the cathode side of the multi-tube AMTEC cell varied linearly with the cell current,  $I$ , which is a characteristic of free-molecule and transition flow regimes. An examination of Equations (3.7), (3.29), (3.37), (3.51), and (3.58)-(3.62) indicates that the flow diffusion coefficients are very weak functions of the vapor mass flow rate in these regimes. The present findings are in agreement with that of Johnson (1994), who solved the Boltzmann equation using a Monte Carlo method to calculate the vapor pressure losses in a single-tube cell. The present results show that the total pressure drop on the cathode side of a multi-tube cell can be reasonably well predicted using Equation (3.0).

Since the vapor pressure losses through the chevron's shield are very large, the location (or temperature) of the shield will affect the cell electrical performance. As Figure 3.4 shows, the closer the shield was to the BASE tubes, the larger the total vapor pressure losses on the cathode side. Displacing the shield 18 mm closer to the tubes would result in a 2 Pa increase in the pressure drop. This is because the vapor pressure losses through the chevrons increase with the vapor temperature in the shield.

The condenser saturation pressure also contributes to the value of the sodium pressure at the BASE/cathode electrode interface. To maximize the electrical power output of the cell, while keeping the BASE and evaporator constant, the condenser temperature should be low enough so that the sodium saturation pressure is negligible compared to the vapor pressure losses. At 550 K, the condenser saturation pressure is only 0.8 Pa. Decreasing the condenser temperature below 550 K, however, would not improve the electrical performance of the cell, but rather reduce the overall conversion efficiency. This is because radiation and conduction losses in the cell increase with the temperature difference between BASE tubes and condenser.

Figure 3.4 also shows the sodium vapor pressure on the cathode side of the multi-tube AMTEC cell with no internal shield. In this case, the sodium pressure at the BASE/cathode electrode interface was much lower (by about 8 Pa) than in the cases with internal shields.

The effect of vapor pressure losses on the cell electrical power output of the multi-tube AMTEC cell is illustrated in Figure 3.5. The calculated cell current at a load resistance  $R_L = 2 \Omega$  was 1.387 A and 1.424 A for the cases with a 30-mm clearance shield and without shield, respectively, corresponding to cell electrical power output of 3.85 We and 4.05 We. As Figure 3.5 shows, the increase in vapor pressure losses due to the conical chevron's shield results in a 5% decrease in predicted cell electrical power output. It is a rather small change considering that the pressure loss through the shield amounts to about 50% of the total pressure losses on the cathode side of the multi-tube AMTEC cell. These results suggest that the cell electrical power output is not very sensitive to the vapor pressure losses on the cathode side. This is because the concentration losses in the cell (the effect of sodium vapor pressure at the BASE/cathode interface) were small compared to the charge-exchange polarization and internal ohmic losses of the cell (see Chapter 4). The cell used TiN electrodes with relatively low temperature-independent exchange current and large contact resistance between current collector and BASE. With a BASE tube thickness of 0.508 mm, the cell internal resistance was  $0.27 \Omega \cdot \text{cm}^2$ . At a cell current of 1.4 A, the

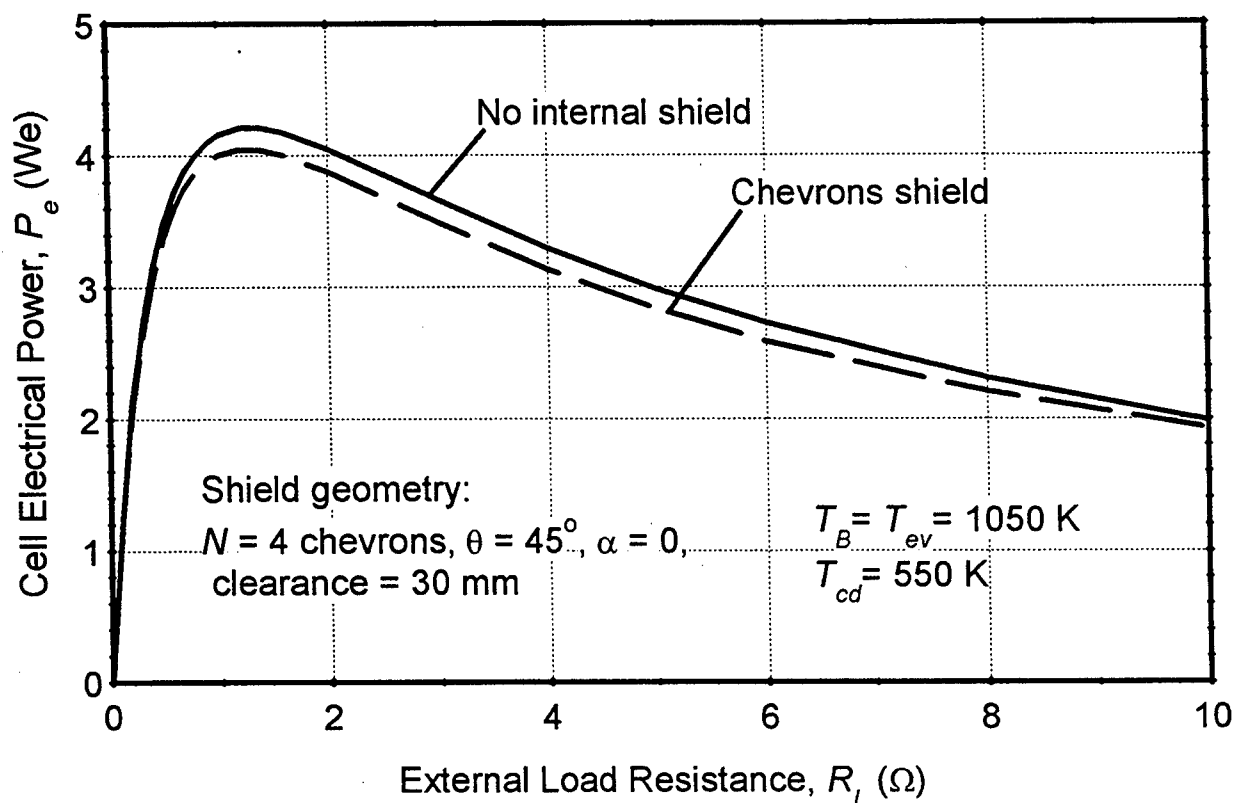


Figure 3.5. Effect of Chevron's Shield on AMTEC Cell Electrical Power Output, at Fixed Evaporator and BASE Tubes Temperatures ( $T_{cd} = 550$  K,  $T_B = T_{ev} = 1050$  K).

concentration and charge-exchange polarization overpotential (0.40 V) was a large fraction of the cell open-circuit voltage (0.942 V). Note that the present analysis, performed at fixed evaporator, BASE tubes and condenser temperatures, is only indicative of the relative effect of vapor pressure losses on the cell performance. In a real cell, the cell input power and temperatures would vary with the cell electrical current.

The calculated sodium vapor flow characteristics on the cathode side of the multi-tube AMTEC cell with chevron's shield are shown in Figure 3.6 for  $T_{cd} = 550$  K,  $T_B = 1050$  K,  $I = 1.39$  A and a 30 mm clearance between chevrons and condenser. The vapor temperature in the pores of the cathode electrode and in the bundle of BASE tubes/evaporator standoff was assumed equal to that of the BASE tubes. Above these tubes, the vapor temperature is assumed to vary linearly between  $T_B$  and  $T_{cd}$  (Figure 3.6a). The sodium vapor flow regime in the AMTEC cell is characterized by the value of the Knudsen number,  $Kn$ , ratio of the molecules mean free path,  $\lambda$ , to the channel equivalent diameter  $D_e$  (Appendix A). A Knudsen number below 0.01 indicates a continuum flow regime, whereas the free-molecular regime typically occurs at  $Kn > 1$ . As shown in Figure 3.6b, the vapor flow in the multi-tube AMTEC cell was in the transition regime, with  $Kn$  ranging between 0.04 and 0.4. As Equation (A5) indicates,  $Kn$  is proportional to the vapor temperature, and inversely proportional to the vapor pressure and the channel equivalent hydraulic diameter,  $D_e$ . The Knudsen number decreased sharply above the BASE tubes because of the increase in  $D_e$  (Figure 3.6b). It increased again as the vapor flowed through the chevron's shield.

In the annular space above the BASE tubes,  $Kn$  decreased slowly because of the decrease in vapor temperature (the vapor pressure remained essentially constant because pressure losses were small in the annulus, Figure 3.4). However,  $Kn$  was higher between the shield and the condenser because the vapor pressure was much smaller there, than between the BASE tubes and the chevron's shield. Figure 3.6c shows the calculated flow diffusion coefficients along the cell. These coefficients are functions of vapor temperature and pressure, mass flow rate and channel equivalent hydraulic diameter,  $D_e$ . The total flow diffusion coefficient is the sum of the viscous and Knudsen flow coefficients. As Figure 3.6c shows, the viscous and Knudsen flow diffusion coefficients were of same magnitude in the channels of small equivalent hydraulic diameter (BASE tubes' bundle and chevron's shield), whereas the viscous flow diffusion coefficient was about one order of magnitude larger than the Knudsen flow diffusion coefficient in the wider annulus above the BASE tubes, where the flow was more viscous.

The sodium mass flow rate increased almost linearly along the cathode electrode, reaching its maximum value of 8.3 gm/hr at the top of the BASE tubes, which corresponded to a cell electrical current,  $I = 1.39$  A (Figure 3.6d). The current density varied between 0.435 A/cm<sup>2</sup> and 0.448 A/cm<sup>2</sup>, and was almost uniform along the electrodes. This is because the temperature of the BASE tubes was assumed uniform and the electrical losses were negligible in the current collectors.

The axial Reynolds number of the vapor flow varied proportionally with the mass flow rate, and was inversely proportional to the channel wetted perimeter and dynamic viscosity, which increased with temperature. As shown in Figure 3.6e,  $Re$  increased with the mass flow rate along the BASE tubes. Above the BASE tubes,  $Re$  was higher because of the smaller wetted perimeter of the annular can, but increased steadily toward the condenser, because of the decrease in the vapor temperature. The vapor Reynolds number was much lower in the chevron's shield, because of the change in geometry (the smaller channels of the shield have lower equivalent hydraulic diameter). The maximum Reynolds number,  $Re = 10$ , occurred at the condenser. The flow of sodium vapor was laminar throughout the cell, and was slow enough to justify the use of Idelchik's relation (Equation 3.32) for evaluating the pressure drop due to sudden expansion at the top of BASE tubes.

The vapor Mach number is proportional to the mass flow rate and the square root of temperature, and inversely proportional to the flow cross section area and vapor pressure (Equation A9). As shown in Figure 3.6f, the vapor Mach number reached its largest value of 0.25 at the condenser. At such Mach number, the von Kármán correction factor for compressible effects varied between 1 and 1.01 and could be neglected. The compressible factor  $\phi$ :

$$\phi = \bar{\alpha}_2 \left( \frac{R_g T}{M} \right) \left( \frac{\dot{m}''}{P} \right)^2 \quad (3.65)$$

appearing in the axial momentum conservation Equations (3.30), (3.40) and (3.54), was less than 1.3% in the bundle of BASE tubes/evaporator standoff, and less than 1.0% in the annulus between BASE tubes and chevron's shield. The calculated value of  $\phi$  in the chevron's channels was only 7.0%, which justifies neglecting it in the development of the shield pressure drop model (Section 3.3.6). The compressible factor reached its larger values in the annular space between



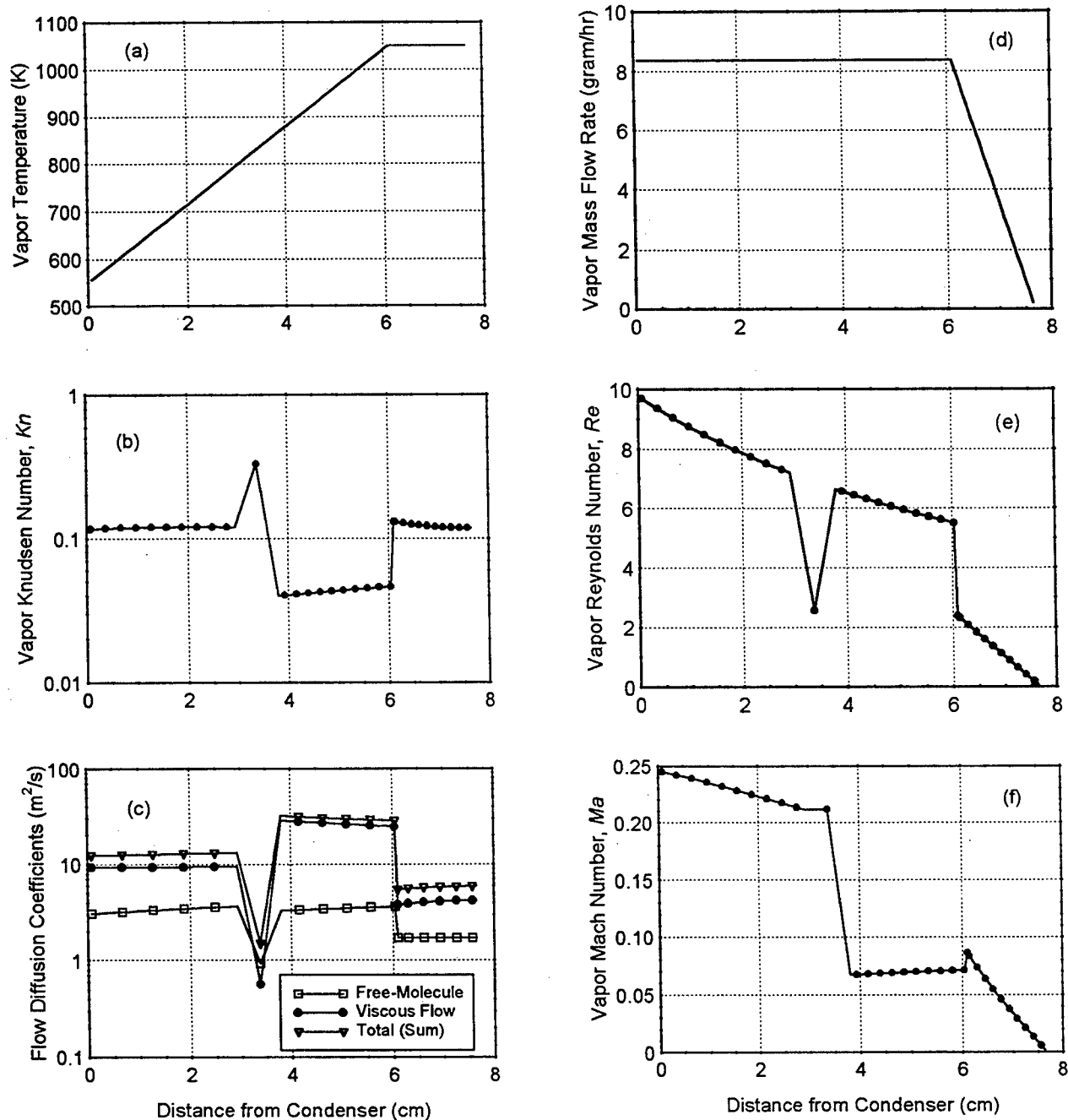


Figure 3.6. Sodium vapor Flow Characteristics in a Vapor Anode, Multi-Tube AMTEC cell with a Chevron's Shield ( $T_{cd} = 550$  K,  $T_B = 1050$  K, 30 mm Shield Clearance,  $I = 1.39$  A,  $\dot{m}_z = 8.3$  gm/hr). (a) Vapor Temperature; (b) Knudsen Number,  $Kn$ ; (c) Flow Diffusion Coefficients; (d) Mass Flow Rate,  $\dot{m}_z$ ; (e) Reynolds Number,  $Re$ ; (f) Mach Number,  $Ma$ .

the chevrons and the condenser, where the pressure was lowest. In this zone,  $\phi$  varied between 7.0% and 10.0%, and reached its largest value at the condenser.

### 3.4.2 Optimization of Conical Chevron's shield in Multi-Tube AMTEC Cell

The vapor pressure loss model described in the previous section was used to evaluate the effect of chevrons' geometry on the sodium vapor pressure drop through the shield. Several configurations were investigated.

#### Conical Chevrons in Minimum Configuration ( $\alpha=0$ )

The first case investigated was that of the configuration that ensured minimum blockage of all direct radiation between BASE tubes and condenser, for which the distance between chevrons,  $d$ , is equal to the width of the conical chevrons, that is when  $\alpha=0$  (Figure 3.3). Figure 3.8 shows the required height of the chevrons as a function of number of chevrons,  $N$ , and angle of chevrons,  $\theta$ . The larger the angle of chevrons, the taller the shield must be for the chevrons to cover the annular space for any direct radiation path. Similarly, the smaller the number of chevrons, the taller they must be (Figure 3.3).

Let us now examine the effect of chevrons' geometry on the flow diffusion coefficients. According to Equation (3.62), the vapor pressure drop decreases with increasing flow diffusion coefficients. The Knudsen flow diffusion coefficient,  $D^K$ , is identical for all flow passages, and is proportional to (Equation 3.51):

$$\frac{L}{1 + \frac{3L}{8b}} = \frac{1}{N} \frac{2(R_w - R_a)}{\cos\theta + \frac{3}{4\sin\theta}} \quad (3.66)$$

Therefore,  $D^K$  is inversely proportional to  $N$  and increases with  $\theta$  (Figure 3.7). The viscous flow diffusion coefficient,  $D_k^{vis}$ , is proportional to  $b^2 / \zeta_k$  (Equation 3.51), and also increases with  $\theta$  (Figure 3.7); it is roughly proportional to  $1/N^2$  since the annulus correction factor  $\zeta_k$  is a weak function of  $N$ . Therefore, all flow diffusion coefficients increase with increasing chevrons angle but decrease with increasing  $N$ . Since the flow area to path length ratio reaches a maximum at an angle of about  $47^\circ$  and increases with  $N$ , the flow conductance of the chevron's shield,  $\chi$ , peaks at an angle between  $47^\circ$  and  $90^\circ$ , for a finite value of  $N$ . This conductance,  $\chi$ , is plotted in Figure 3.8 as a function of  $\theta$  and  $N$ , at typical temperature and pressure of 950 K and 10 Pa, respectively. As this figure shows, the conductance  $\chi$  peaked at a chevron angle of  $60^\circ$ . This maximum was virtually independent of the number of chevrons  $N$ , for values of  $N$  greater than 3.

Figure 3.9 shows the resulting pressure drop in the chevron's shield at a typical cell current of 1.67 A (or a sodium mass flow rate of 10 gm/hr), as a function of  $\theta$  and  $N$ . The minimum pressure drop of 14 Pa occurred at a chevron angle of  $60^\circ$ . This minimum pressure drop is not particularly sensitive to the angle near the optimum, allowing some tolerance in manufacturing.

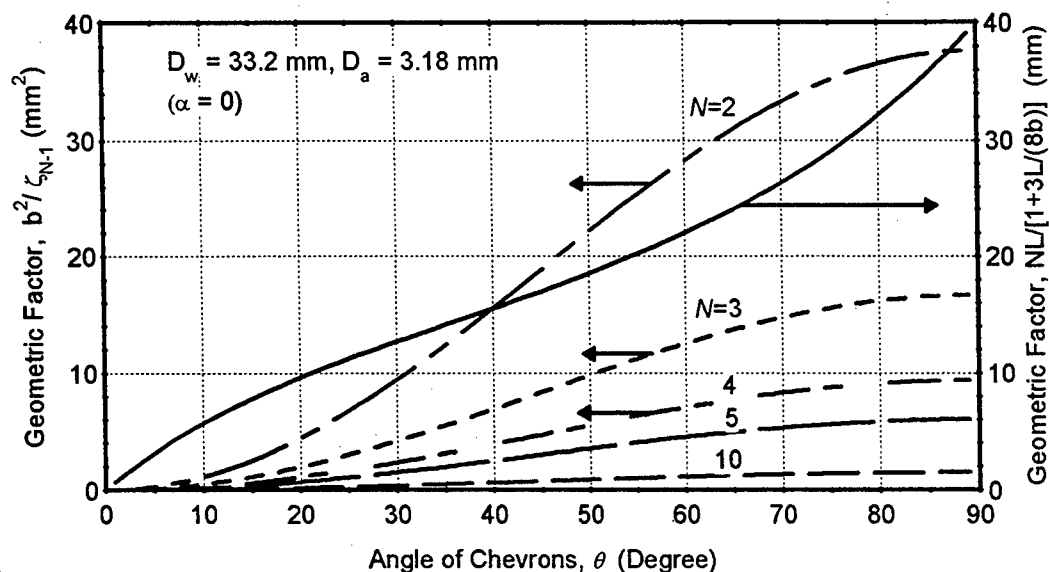


Figure 3.7. Effects of Chevrons' Angle  $\theta$  and Number of Chevrons  $N$  on the Viscous and Knudsen Flow Diffusion Coefficients ( $\alpha=0$ ).

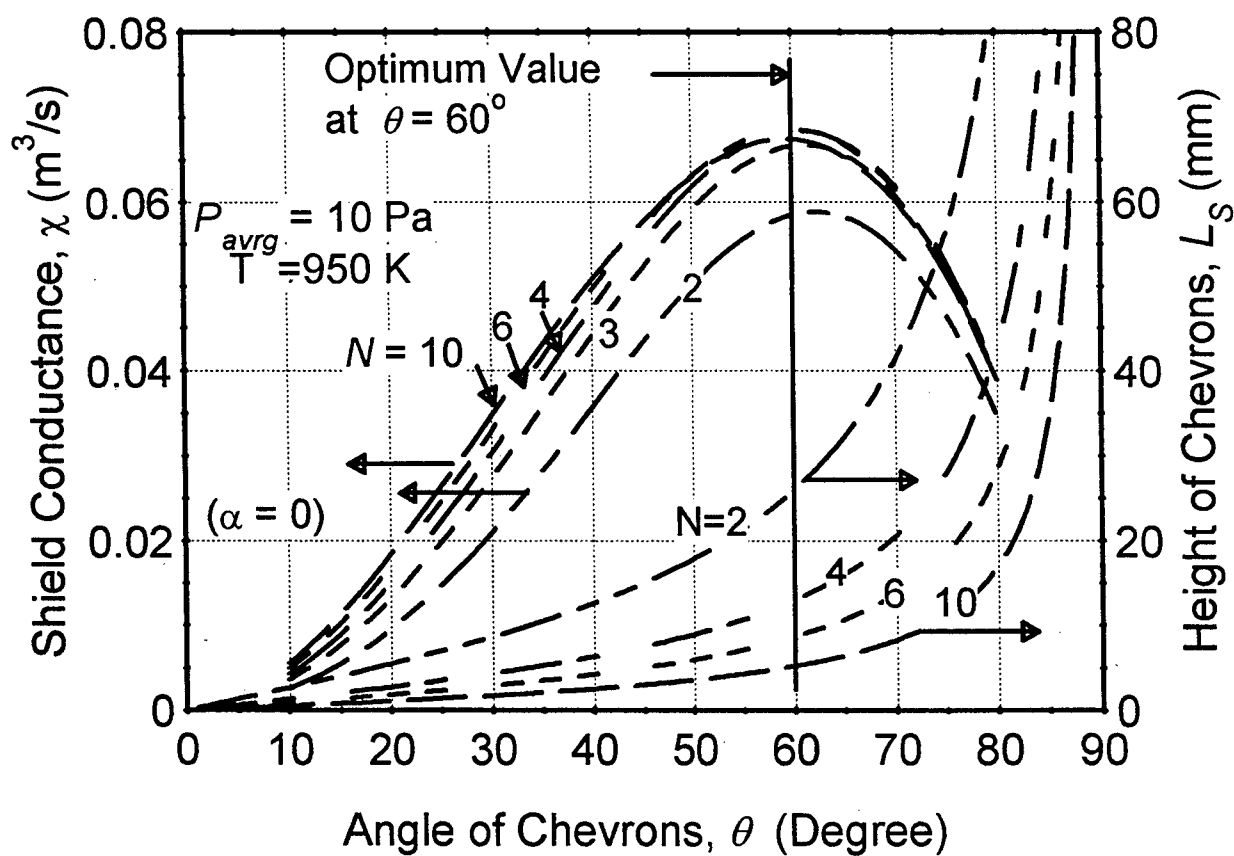


Figure 3.8. Shield Flow Conductance  $\chi$  and Chevrons' Height as a Function of Angle  $\theta$  and Number of Chevrons  $N$  ( $\alpha=0$ ).

For example, using a shield with angle of 50° or 70° only resulted in an increase in pressure drop of 1 Pa, or 7% of the minimum pressure drop (Figure 3.9). Also, the minimum pressure drop was independent of the number of chevrons  $N$ , for  $N > 3$ . Because of the difficulty of manufacturing a multi-chevron shield in a relatively small annular space, the use of 4 or 5 chevrons is recommended.

Let us now examine the effect of temperature on the pressure drop through the chevron's shield. Equation (3.62) indicates that the pressure drop is proportional to the temperature and inversely proportional to the flow diffusion coefficients. The Knudsen flow diffusion coefficient increased with the square root of temperature, while the viscous flow diffusion coefficient decreased with temperature, through the dependence of vapor dynamic viscosity on temperature (Equations 3.51 and B1). The effect of temperature on the flow conductance of the chevron's shield is illustrated by Figure 3.10, for a shield with optimum 60°-angle chevrons. The pressure drop through the chevron's shield increased with temperature, and therefore with the distance between the shield and the condenser. For example, a 75 K increase in chevrons' temperature increased the pressure drop by 8%. Figure 3.10 also shows the effect of  $N$  on the chevrons' flow conductance,  $\chi$ . It peaked at  $N=4$  or 5, then decreased slowly with increasing  $N$ . This decrease was almost insignificant at shield temperatures above 950 K, but became more pronounced at lower shield temperatures.

### **Crowded Chevrons' Configuration ( $\alpha > 0$ )**

The case investigated previously was that of the configuration geometry that ensured minimum blockage of all direct radiation between BASE tubes and condenser ( $\alpha=0$ ). However, one would expect the radiative function of the shield to improve as the chevrons are packed closer to each other,  $\alpha>0$  (Figure 3.3). The effects of the packing factor,  $\alpha$ , and the number of chevrons,  $N$ , on the flow conductance of the chevron's shield ( $\chi$ ) and the vapor pressure loss through the shield are shown in Figures 3.11 and 3.12 for a 60°-angle chevron's shield. The pressure drop increased with increasing  $\alpha$ . The larger the value of  $\alpha$ , the larger the optimum number of chevrons  $N$ . As an illustration, consider first the optimum case of four 60°-angle chevrons with  $\alpha=0$  ( $N=4$ ). The conical chevrons would be 13 mm in height, and the flow path  $L = 15$  mm.

Consider now a configuration of five 60°-angle chevrons of identical height,  $L_s = 13$  mm ( $N=5$ ). To make room for the additional (fifth) chevron, it is necessary to move the chevrons closer to each other, with a packing factor of  $\alpha=1/3$ . The addition of a fifth chevron of identical height caused a 25% decrease in the flow conductance  $\chi$ , and a 36% increase in the vapor pressure drop, from 14 Pa to 19 Pa (Figures 3.11 and 3.12). For a packing factor  $\alpha=1/3$ , the optimum number of chevrons was  $N=10$  (with a height of 6.5 mm). However, an increase in the number of chevrons from 5 to 10 only resulted in a 0.7 Pa decrease in the vapor pressure drop (from 19 Pa to 18.3 Pa).

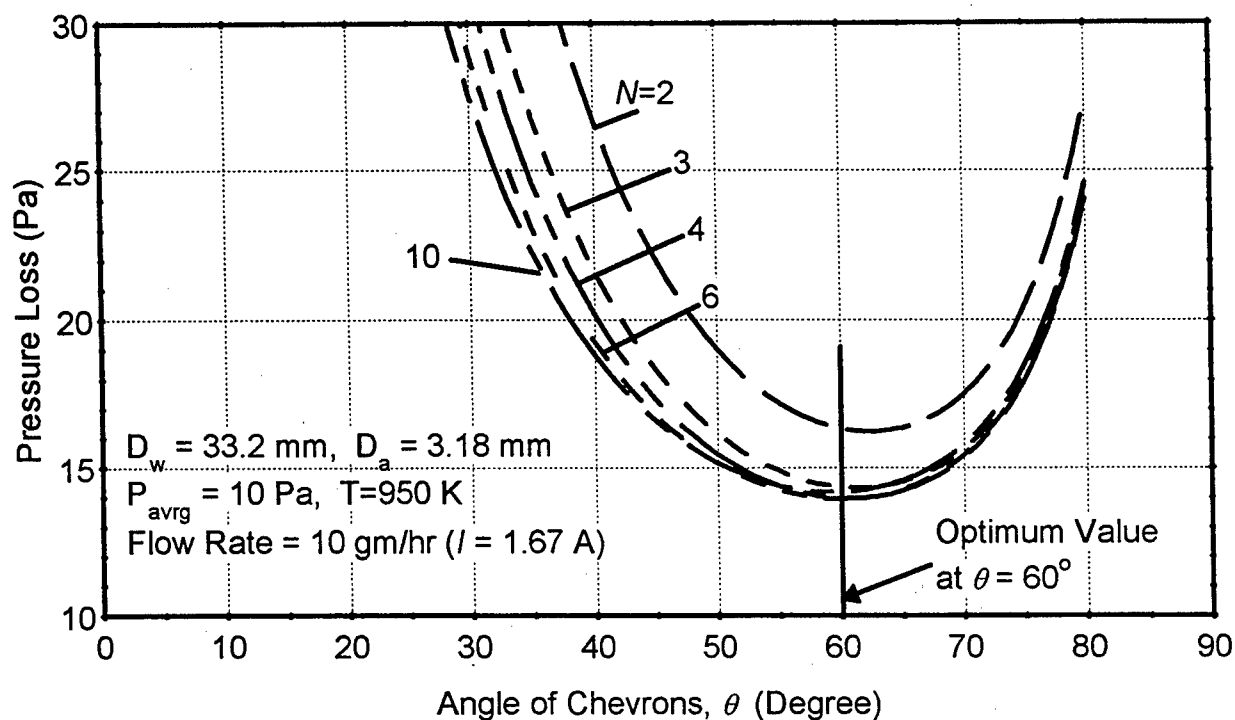


Figure 3.9. Pressure Loss Through Unseparated Radiation Shield as a Function of Angle  $\theta$  and Number of Chevrons  $N$  ( $\alpha=0$ ).

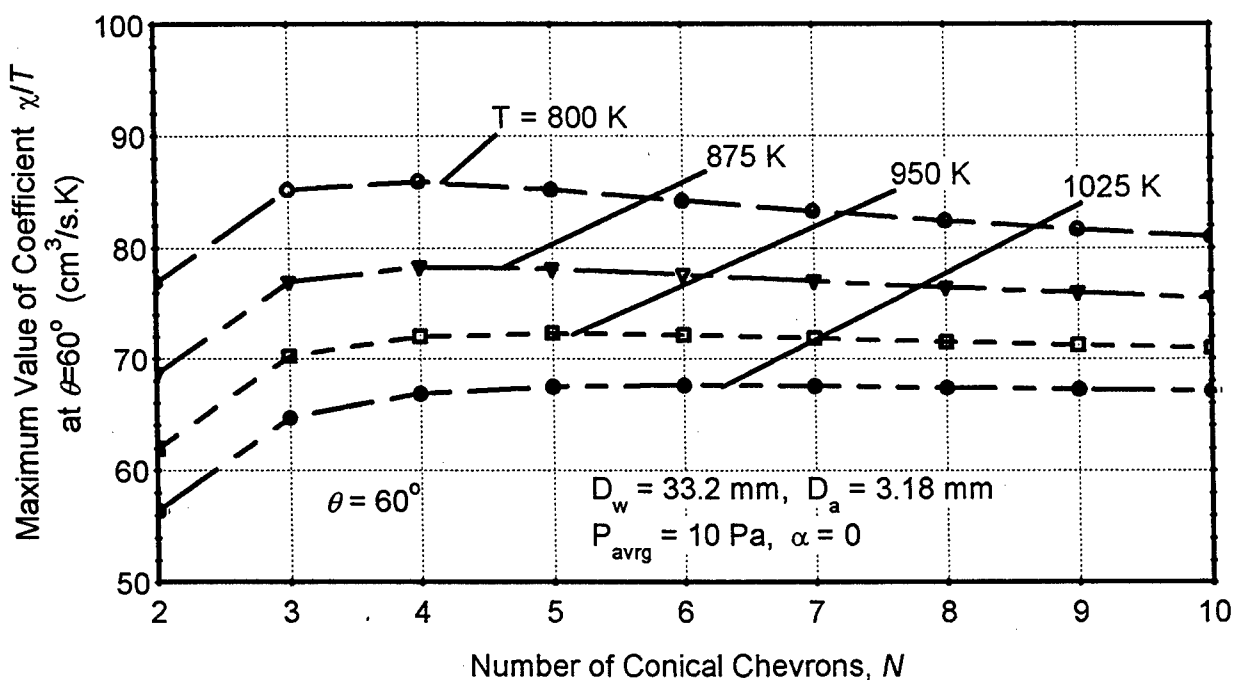


Figure 3.10. Effects of Temperature and Number of Chevrons on the Pressure Loss Through Radiation Shield ( $\alpha=0$ ,  $\theta=60^\circ$ ).

### Pressure Losses through Separated Conical Chevrons

Another shield geometry of interest is that of separated conical chevrons. In this geometry, the backward and forward halves of the chevrons are not welded together, but are separated some distance from each other. The vapor loss model developed in this work is used to evaluate the pressure losses in this geometry, with only minor changes. This configuration is equivalent to 2 chevrons shields of identical flow path ( $L/2$ ) in series. Examination of Equation (3.51) shows that the viscous flow diffusion coefficient remains unchanged, while the path length,  $L$ , appearing in the expression of the Knudsen flow diffusion coefficient, is replaced by  $L/2$ . The expression for the pressure drop, Equation (3.62), remains unchanged, because  $L$  is replaced by  $L/2$  in this equation, but the pressure drop must be multiplied by 2 to account for both sections of the shield. In the end, the only difference between separated and non-separated chevrons' geometries is the value of the path length in the expression of the Knudsen flow diffusion coefficient. Because the latter is an increasing function of path length, one expects separated chevrons to have a larger pressure drop than non-separated chevrons. The pressure drop in the annulus between the two separated portions of the shield is negligible when the separation distance is small.

The calculated vapor pressure loss through separated conical chevrons is plotted in Figure 3.13 as a function of  $\theta$  and  $N$ , at a typical sodium mass flow rate of 10 gm/hr, and temperature and pressure of 950 K and 10 Pa, respectively, and a minimum configuration ( $\alpha=0$ ). As this figure shows, the pressure loss reached a minimum at an angle of  $62^\circ$ , for a separated shield with 3 or 4 chevrons. The minimum pressure drop, 17 Pa, was 22% larger (3 Pa above) than that for non-separated chevrons. Again, a  $10^\circ$  deviation from the optimum chevron angle of  $62^\circ$  resulted in only a 1 Pa increase in pressure drop.

The effect of temperature on the pressure loss, for a separated shield with optimum  $62^\circ$ -angle chevrons, is illustrated by Figure 3.14. As for the case of unseparated chevrons, the pressure drop increased (the flow conductance  $\chi$  decreased) with temperature, and therefore with the distance between the shield and the condenser. For example, a 75 K increase in the chevrons temperature resulted in a 6% (or 1 Pa) increase in vapor pressure losses. Figure 3.14 also shows more clearly the effect of  $N$  on the flow conductance  $\chi$ . The latter reached its peak at  $N = 3$  or 4, and then decreased with increasing values of  $N$ . This decrease is more pronounced than for the case of unseparated chevrons (Figure 3.10).

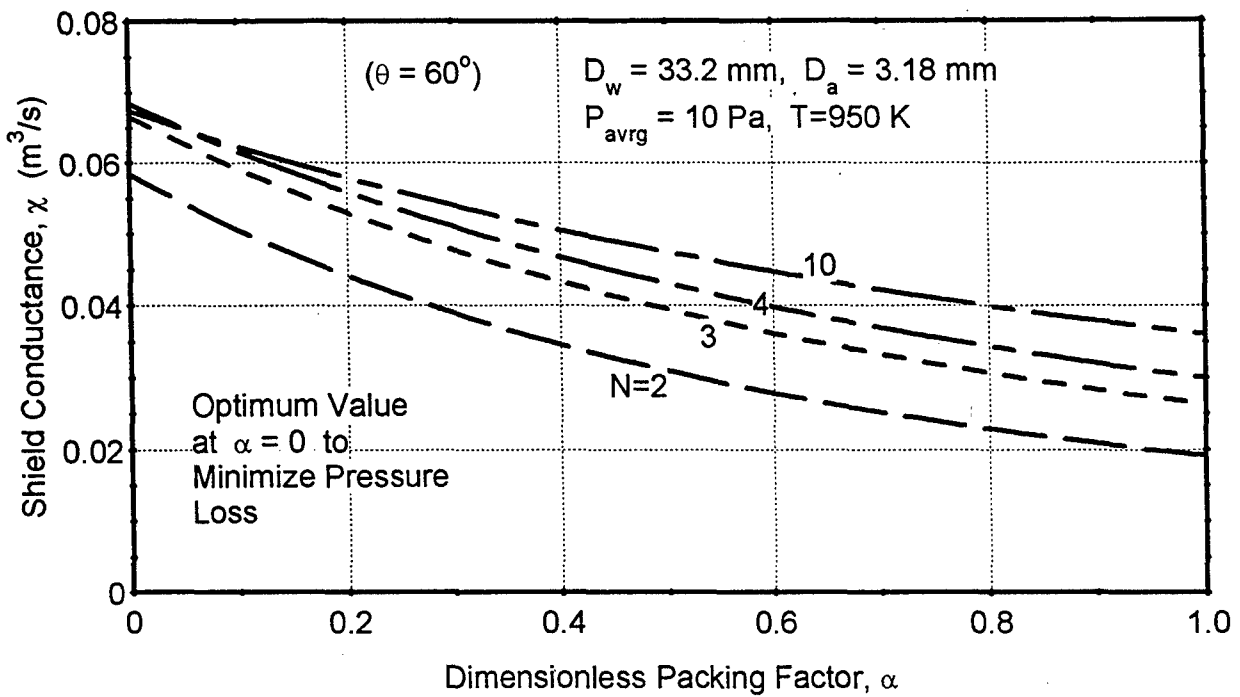


Figure 3.11. Shield Flow Conductance,  $\chi$  as a Function of Packing Factor  $\alpha$  and Number of Chevrons  $N$  ( $\theta=60^\circ$ ).

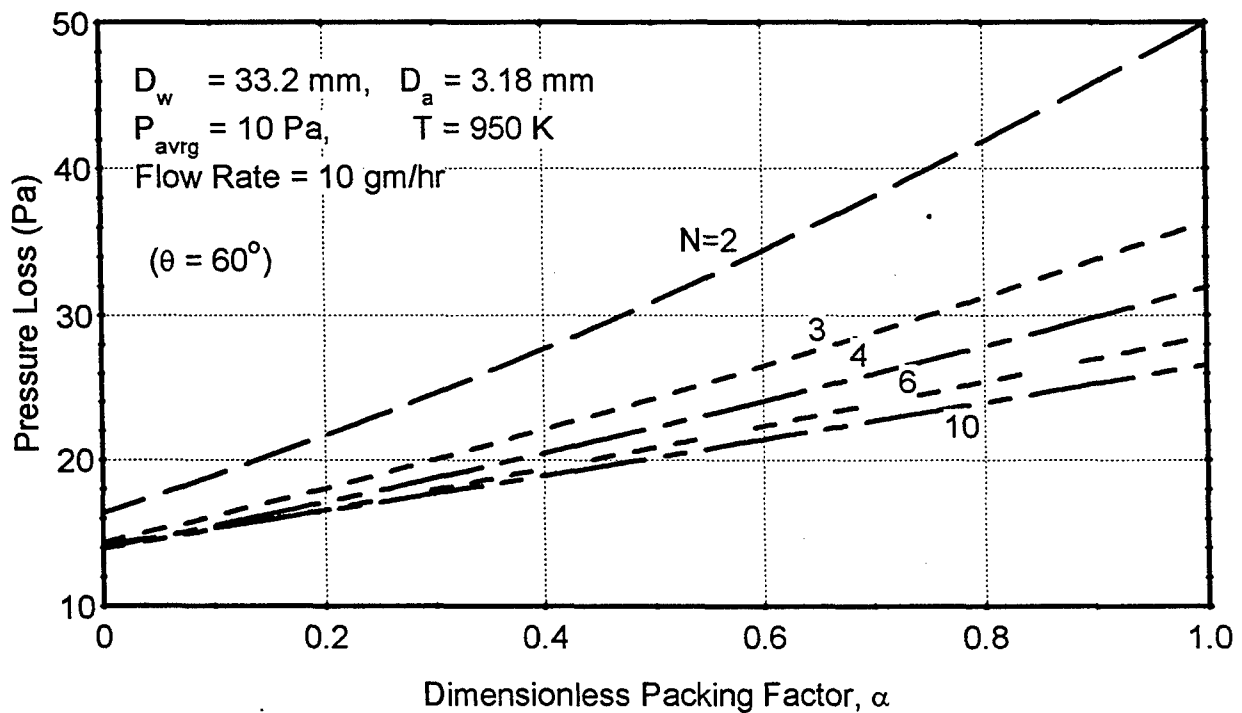


Figure 3.12. Calculated Pressure Loss Through Radiation Shield as a Function of Packing Factor  $\alpha$  and Number of Chevrons  $N$  ( $\theta=60^\circ$ ).

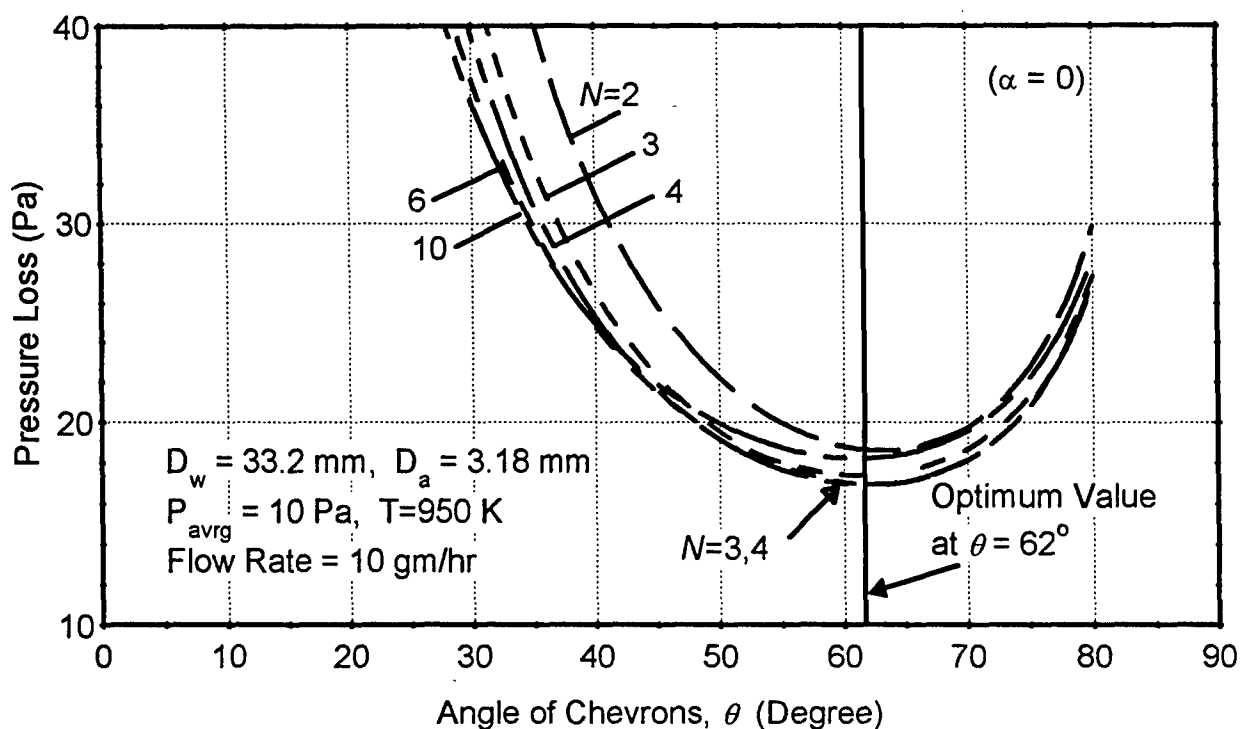


Figure 3.13. Pressure Loss Through Separated Chevron's Shield as a Function of Angle  $\theta$  and Number of Chevrons,  $N$  ( $\alpha=0$ ).

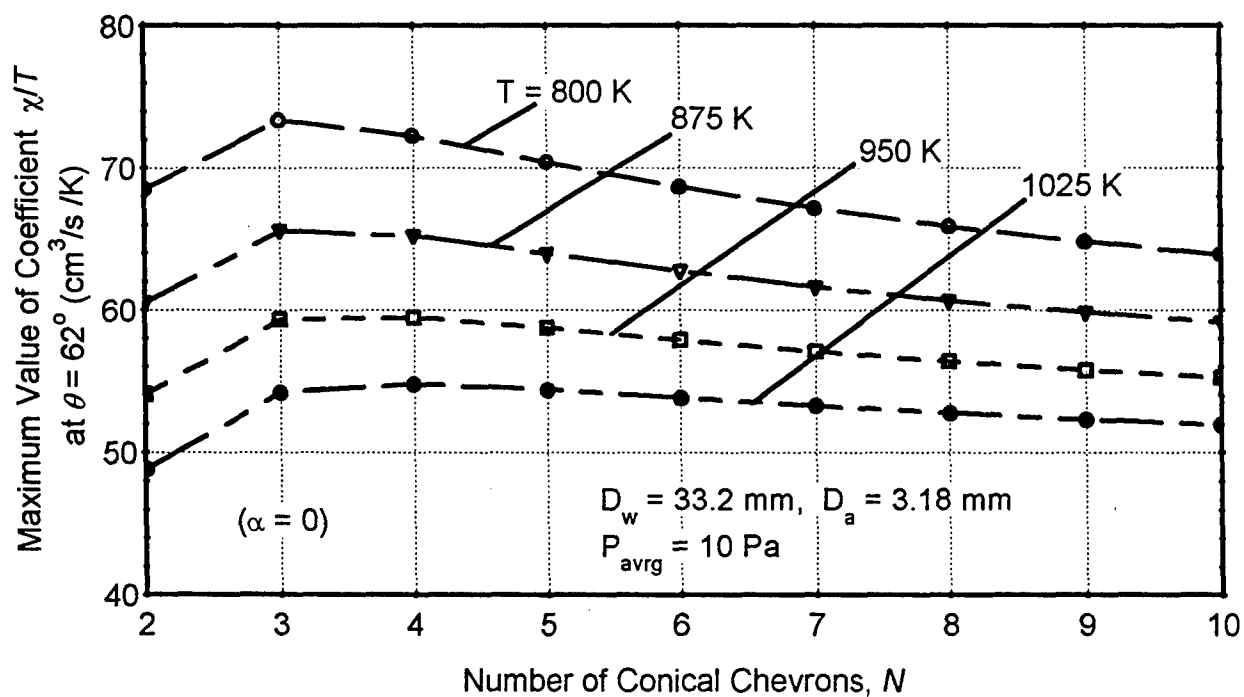


Figure 3.14. Effects of Temperature and Number of Chevrons,  $N$  on the Pressure Loss Through Separated Chevron's Shield ( $\alpha=0$ ,  $\theta=62^\circ$ ).



### 3.5 SUMMARY AND CONCLUSIONS

A detailed model was developed for calculating the vapor pressure losses and characterizing the flow regimes on the cathode side of vapor anode, multi-tube AMTEC cells. The model uses the Dusty Gas Model and predicts the vapor flow over a wide range of pressures, including the free-molecular, transition and continuum flow regimes. The model accounts for the pressure drops due to vapor flow through the cathode porous electrode, mass injection along the BASE tubes, change in flow area at the top of the BASE tubes, vapor flow in the annulus above the BASE tubes, through the conical chevron's radiation shield, and due to condensation of vapor.

To predict the performance of vapor anode, multi-tube AMTEC cells, the vapor pressure loss model was coupled to a one-dimensional AMTEC electrical model, which allowed the current density to vary axially along the BASE tubes. The resulting cell model was used to predict the electrical performance of a vapor anode, multi-tube AMTEC cell, given the temperatures of the BASE tubes, of the side wall and of the condenser. For simplicity, the axial temperature distribution along the BASE tubes was assumed uniform, and equal to the evaporator temperature. Also, the vapor temperature above the BASE tubes (on the cathode side) was assumed equal to the side wall temperature, and varied linearly between the BASE and the condenser.

Results showed that the vapor flow on the low-pressure side of the PX-1A multi-tube AMTEC cell was in the transition regime, with Knudsen numbers ranging between 0.04 and 0.4. At a cell electrical current of about 1.5 A (or sodium mass flow rate of about 9 gm/hr), the vapor axial Reynolds number was less than 10. The vapor axial Mach number peaked at 0.25 at the condenser, a value low enough to justify neglecting the vapor compressible effects in the conical chevron's shield model.

The major contributions to the vapor pressure losses between condenser and BASE tubes surface were, in order of decreasing magnitude: flow through the chevron's shield, condensation of sodium vapor on the condenser surface, and sudden expansion of flow area at the top of BASE tubes. For a radiation shield clearance of 48 mm, the AMTEC cell analyzed had an effective dimensionless factor for vapor pressure losses  $G = 143$  with chevron's shield, and  $G = 71$  without shield. The pressure loss through the chevron's radiation shield dominated, by far, all other pressure losses, contributing more than half the total pressure losses between the condenser and cathode/solid electrolyte surface. The total vapor pressure drop in the cell varied linearly with the cell electric current, which is a characteristic of the free-molecule and transition flow regimes. For these flow regimes, the flow diffusion coefficients were weak functions of the vapor mass flow rate.

The increase in vapor pressure losses on the cathode side of the vapor anode, multi-tube AMTEC cell, due to the presence of the chevron's shield, however, only resulted in a 5% decrease in cell electrical power output. This was because the concentration losses in the TiN electrodes were small compared to the charge-exchange polarization and internal ohmic losses of the cell.

The present vapor pressure loss model was also used to optimize the chevrons' geometry for minimizing the vapor pressure loss through the shield. For the shield geometry which ensured minimum blockage of all direct radiation between BASE tubes and condenser ( $\alpha=0$ ), the lowest pressure loss occurred when the chevrons angle was about  $60^\circ$ , and using 4 or 5 chevrons. The vapor pressure loss was not particularly sensitive to the chevrons angle near the optimum value, allowing some tolerance for manufacturing the shield. The pressure loss through the chevrons shield increased quickly as the packing factor,  $\alpha$ , was increased. The larger the value of  $\alpha$ , the larger the optimum number of chevrons  $N$ . In the case of separated conical chevrons, the optimum geometry had 3 or 4 chevrons, with an angle of  $62^\circ$ , for which the pressure loss was about 25% higher than that in non-separated chevrons.

In the next chapter, the two-dimensional electric model of vapor anode, multi-tube AMTEC cells used in the AMTEC Performance and Evaluation Analysis Model (APEAM) is developed and described in details.

## 4. AN ELECTRIC MODEL OF VAPOR ANODE, MULTI-TUBE AMTEC CELLS

In this chapter, the two-dimensional electric model of vapor anode, multi-tube Alkali-Metal thermal-to-Electric Conversion (AMTEC) used in the AMTEC Performance and Evaluation Analysis Model (APEAM) is developed and described in details. Each vapor anode, multi-tube PX-series AMTEC cell has between 5 and 7 Beta''-Alumina Solid Electrolyte (BASE) tubes, connected electrically in series. Each BASE tube has a total of 6 cm<sup>2</sup> of electrode surface area (Figure 4.1). The TiN anode and cathode porous electrodes are covered with molybdenum mesh current collectors, to minimize internal electric losses. More details on the PX-series cells' design and test results can be found in Chapters 2, 11 and 12.

The two-dimensional cell's electric circuit model determines the electrical resistances of the BASE, electrodes, current collectors, and conductor leads to the external load, and calculates the cell's electrical potentials, electrode current density, and the cell's total electrical current. This model is described in details in the next sections. This model is also used to evaluate the contribution of the various electrical loss processes in the PX-series cells. The results of the effects of BASE/electrode/current collector contact resistance, charge-exchange current and BASE tube leakage resistance on the PX-3G cell performance are analyzed and discussed.

### 4.1 NOMENCLATURE

$A$	Cross section area (m <sup>2</sup> )
$B$	Temperature-independent, charge-exchange coefficient (A.K <sup>1/2</sup> / Pa.m <sup>2</sup> )
$d_{bus}$	Bus wire diameter (m)
$F$	Faraday's constant ( $F = 96,485$ . C / mole)
$f_B$	Faraday's coefficient, $f_B = F / (R_g T_B)$ (C/J)
$G$	Dimensionless geometric factor for vapor pressure losses
$H$	Height of electrode axial segments (m)
$h$	Wire-screen mesh size (m)
$I$	Electrical current (A)
$J$	Electrical (radial) current density (A / m <sup>2</sup> )
$J^{ex}$	Charge-exchange current density (A / m <sup>2</sup> )
$J_{sat}^{ex}$	Saturated equilibrium, charge-exchange current density (A / m <sup>2</sup> )
$L_E$	Length of BASE electrodes (m)
$L_{rings}$	Length of helical wire per axial segment, Equation 4.11 (m)
$N$	Number of electrode axial segments
$N_p$	Number of mesh wires per half circumference of BASE tube, Equation 4.9
$N_{rings}$	Number of helical wire rings per axial segment, Equation 4. 11
$N_S$	Number of series-connected BASE tubes
$N_{wires}$	Number of mesh wires per axial segment, Equation 4.9
$P$	Pressure (Pa)
$R$	Electrical resistance ( $\Omega$ )

$R_g$	Perfect gas constant ( $R_g = 8.314 \text{ J / mole.K}$ )
$R_{int}$	Internal resistance of AMTEC cell ( $\Omega$ )
$R_L$	External load resistance ( $\Omega$ )
$R_{leak}$	Leakage resistance of BASE braze joint ( $\Omega$ )
$R_o$	Equivalent external load per BASE tube ( $\Omega$ )
$R'_B$	BASE ionic resistance ( $\Omega.m^2$ )
$R'_{cont}$	Contact resistance between BASE/electrode/current collector ( $\Omega.m^2$ )
$r$	Outer radius (m)
$T$	Temperature (K)
$t$	Thickness (m)
$V$	Electrical voltage (V)

#### Greek

$\alpha$	Electrochemical transfer coefficient, $\alpha = 1/2$
$\Delta T$	Temperature margin (temperature difference between BASE tube's cold end and evaporator)
$\varepsilon$	Volume porosity
$\zeta$	Concentration and charge-exchange polarization losses (V)
$\rho$	Electrical/ionic resistivity ( $\Omega.m$ )

#### Subscript / Superscript

$a$	Anode
$B$	Beta"-Alumina Solid Electrolyte (BASE)
$bus$	Axial bus wire
$c$	Cathode
$cc$	Closed-circuit
$cd$	Cell's cold end (condenser)
$conn$	BASE tubes connector lead
$E$	Porous cathode electrode
$ex$	Charge-exchange
$hot$	Cell's hot end
$lead$	Connector lead
$mesh$	Wire screen mesh
$o$	Effective electromotive force
$oc$	Open-circuit
$r$	Radial
$sat$	Liquid-vapor saturation line
$sheet$	Electrode sheet
$sp$	Metal sponge
$w$	Wire
$wire$	Tie wire
$z$	Axial
$\theta$	Circumferential

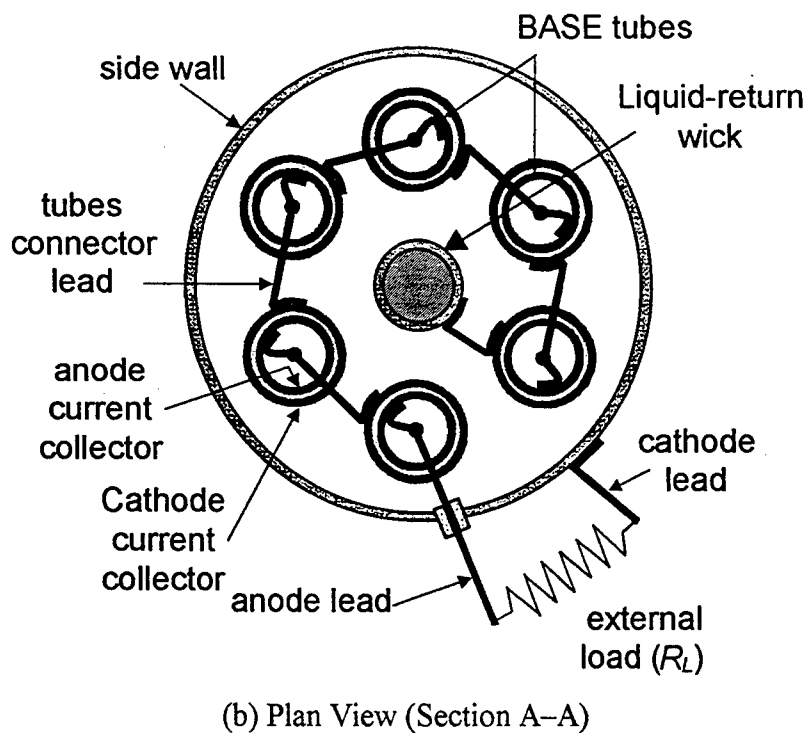
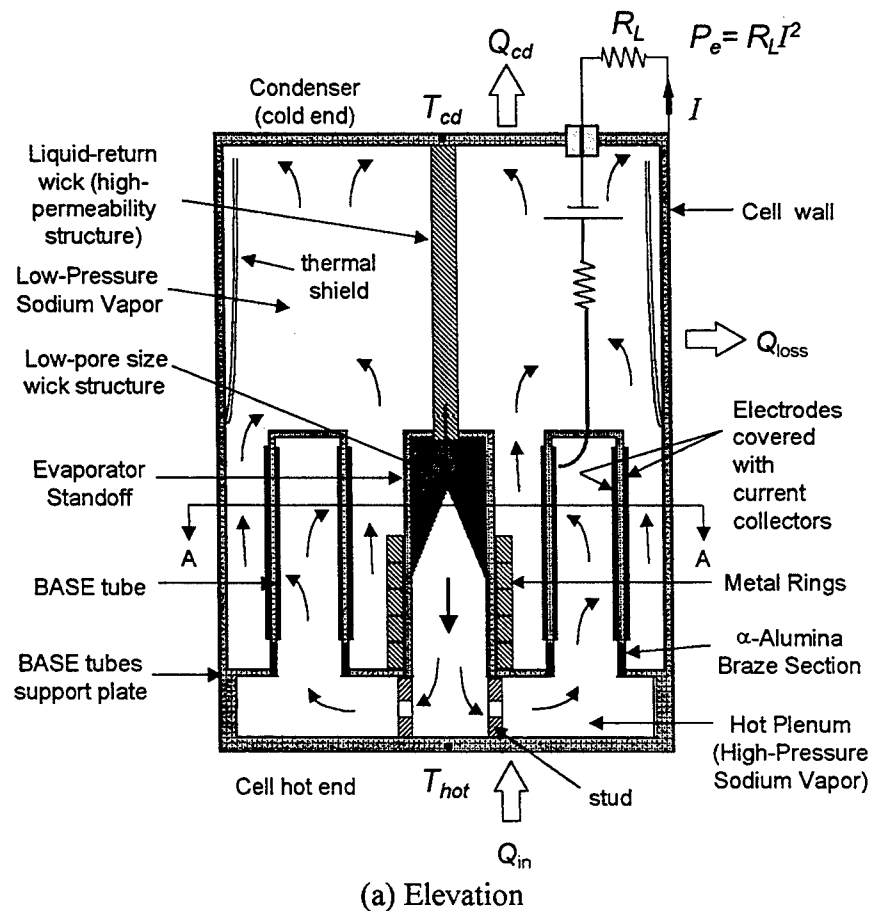


Figure 4.1. Cross Sections of a PX-Series, Multi-Tube AMTEC Cell (Not to Scale).

## 4.2 MODEL DESCRIPTION

The two-dimensional electric model of vapor anode, multi-tube AMTEC cells includes four options of current collector configurations (Figure 4.2), and accounts for the effects of non-uniform axial temperature and sodium vapor pressure profiles along the BASE tubes/cathode electrodes, and for the radial and axial electrical losses in the current collector networks. This model, when coupled to the other submodels in APEAM, was used to evaluate the contributions of the various components of the internal electric losses in the cell. The internal electric losses are those due to: (a) concentration and charge-exchange polarization losses at the BASE/electrodes interfaces; (b) BASE ionic resistance; (c) contact resistance between BASE/electrodes and electrodes/current collectors; (d) sheet resistance of the electrodes; (e) resistances of current collectors, bus wires, and conductor leads to the external load; and (f) resistance to leakage current between the anode and cathode electrodes through the BASE metal-ceramic braze joints. These joints link the BASE tubes to the cell's metal support plate and must be highly conductive to heat but highly resistive to electric current. These electric losses in a typical AMTEC cell are all accounted for in the present model and are discussed separately in the following subsections.

### 4.2.1 Open-Circuit Voltage and Polarization Losses

Neglecting the Seebeck voltage generated by the radial temperature gradient across the BASE, the effective electromotive force of the cell is:

$$V_o^{cc} = V^{oc} - \zeta_a - (-\zeta_c) . \quad (4.1)$$

The open-circuit voltage,  $V^{oc}$ , is proportional to the isothermal expansion work of sodium ions in the BASE tubes, and is given by the Nernst equation (Cole 1983):

$$V^{oc} = \frac{R_g T_B}{F} \ln \left[ P_a^{oc} / P_c^{oc} \right] = \frac{1}{f_B} \ln \left[ P_a^{oc} / P_c^{oc} \right] . \quad (4.2)$$

The concentration and charge-exchange polarization overpotentials at the anode and cathode are given by the Butler-Volmer equation (Williams et al. 1990a, Underwood et al. 1992):

$$\frac{J_i}{J_i^{ex}} = \exp[-\alpha f_B \zeta_i] - \frac{P_i^{cc}}{P_i^{oc}} \exp[(1-\alpha) f_B \zeta_i] . \quad (4.3a)$$

The subscript 'i' in Eq. (4.3a) stands for either 'a' (anode) or 'c' (cathode). For a symmetric barrier, the electrochemical transfer coefficient  $\alpha = 1/2$ , and Eq. (4.3a) can be inverted to give the polarization overpotential explicitly in terms of the cell's current density. Two different expressions can be obtained, which are equivalent. Introducing

$$X = \exp\left[-\frac{1}{2} f_B \zeta_i\right] ,$$

Equation (4.3a) can be rewritten

$$X^2 - \frac{J_i}{J_i^{ex}} X - \frac{P_i^{cc}}{P_i^{oc}} = 0.$$

The positive root of this second-degree polynomial is

$$X = \frac{1}{2} \left( \sqrt{\Delta} + \frac{J_i}{J_i^{ex}} \right),$$

where

$$\Delta = \left( \frac{J_i}{J_i^{ex}} \right)^2 + 4 \frac{P_i^{cc}}{P_i^{oc}},$$

so that the polarization overpotential has the final expression:

$$\zeta_i = -\frac{2R_g T_B}{F} \ln \left\{ \frac{1}{2} \left[ \left( \frac{J_i}{J_i^{ex}} \right)^2 + 4 \frac{P_i^{cc}}{P_i^{oc}} \right]^{1/2} + \frac{1}{2} \frac{J_i}{J_i^{ex}} \right\}. \quad (4.3b)$$

Alternatively, if we introduce

$$Y = \exp\left[+\frac{1}{2} f_B \zeta_i\right],$$

Equation (4.3a) can also be written

$$\frac{P_i^{cc}}{P_i^{oc}} Y^2 + \frac{J_i}{J_i^{ex}} Y - 1 = 0.$$

The positive root of this second-degree polynomial is

$$Y = \frac{1}{2} \frac{P_i^{oc}}{P_i^{cc}} \left( \sqrt{\Delta} - \frac{J_i}{J_i^{ex}} \right),$$

so that the polarization overpotential can also be expressed as (Williams et al. 1990a):

$$\zeta_i = + \frac{2R_g T_B}{F} \ln \left\{ \frac{1}{2} \frac{P_i^{oc}}{P_i^{cc}} \left\{ \left[ \left( \frac{J_i}{J_i^{ex}} \right)^2 + 4 \frac{P_i^{cc}}{P_i^{oc}} \right]^{1/2} - \frac{J_i}{J_i^{ex}} \right\} \right\}. \quad (4.3c)$$

It can be easily shown that Equations (4.3b) and (4.3c) are equivalent. Making use of the identity

$$-\ln[X] = \ln \left[ \frac{1}{X} \right],$$

one can write

$$(4.3b) \Leftrightarrow (4.3c)$$

$$\Leftrightarrow \frac{1}{2} \sqrt{\Delta} + \frac{1}{2} \frac{J_i}{J_i^{ex}} \equiv \frac{2P_i^{cc} / P_i^{oc}}{\sqrt{\Delta} - \frac{J_i}{J_i^{ex}}},$$

$$\Leftrightarrow \left( \sqrt{\Delta} + \frac{J_i}{J_i^{ex}} \right) \times \left( \sqrt{\Delta} - \frac{J_i}{J_i^{ex}} \right) \equiv 4 \frac{P_i^{cc}}{P_i^{oc}},$$

$$\Leftrightarrow \Delta \equiv \left( \frac{J_i}{J_i^{ex}} \right)^2 + 4 \frac{P_i^{cc}}{P_i^{oc}},$$

which is true by definition of  $\Delta$ . Therefore, Equations (4.3b) and (4.3c) are equivalent. In the present work, we prefer to use Equation (4.3b) as it is more elegant and more amenable to physical interpretation.



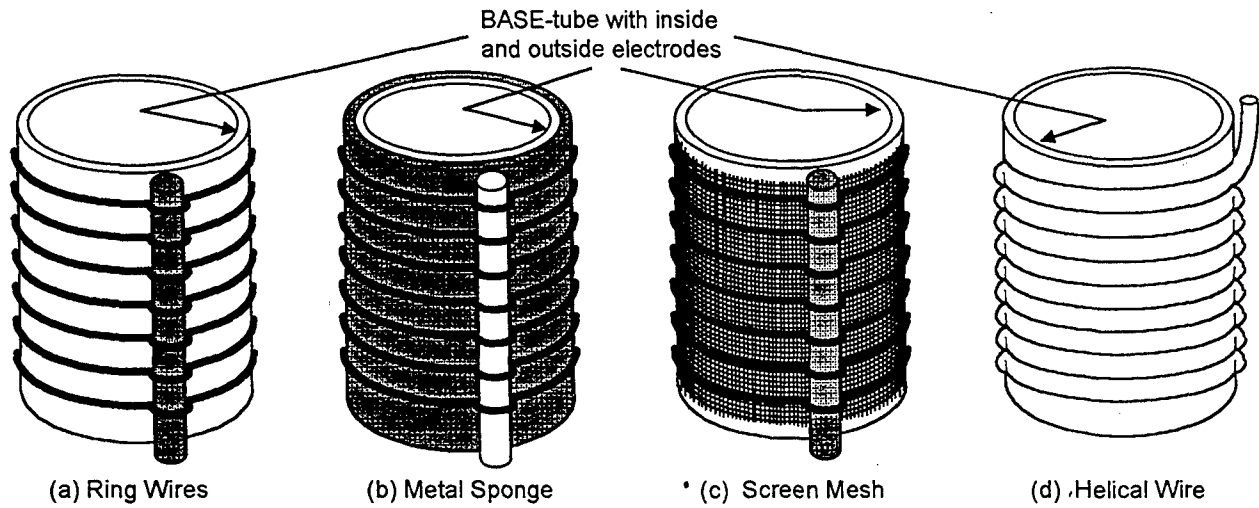


Figure 4.2. Current Collector Designs in Vapor Anode, Multi-Tube AMTEC Cell.

The overpotential,  $\zeta_i$ , increases logarithmically with the cell current, reducing the voltage potential across the BASE. In Eq. (4.3b),  $\zeta_c < 0$ ,  $\zeta_a > 0$ , and  $J_c = -J_a$  for a thin BASE membrane. The charge-exchange current densities,  $J_i^{ex}$ , a measure of the effective local conductance at the BASE/sodium ions/electrode grains triple points, are related to the saturated equilibrium exchange-current density,  $J_{sat}^{ex}$ , as (Williams et al. 1990a and 1990b):

$$J_i^{ex} = J_{sat}^{ex} \left[ \frac{P_i^{oc}}{P_{sat}(T_B)} \right]^\alpha \quad (4.4a)$$

Since the sodium vapor pressure at the cathode ( $P_c^{cc} < 50$  Pa) is several orders of magnitude smaller than that at the anode ( $P_a^{cc} \sim 15 - 60$  kPa), the anode exchange-current density is much larger than the cathode exchange-current density, hence the polarization overpotential on the anode side,  $\zeta_a$ , is negligible. Experimental investigations have shown that the saturated equilibrium exchange-current density,  $J_{sat}^{ex}$ , is essentially a function of the BASE temperature and of the type of electrodes. It can be expressed as (Williams et al. 1990a, Underwood et al. 1992):

$$J_{sat}^{ex} = B \times \frac{P_{sat}(T_B)}{\sqrt{T_B}}, \quad (4.4b)$$

where  $B$  is the temperature-independent charge-exchange coefficient, expressed in units of  $A.K^{1/2}/Pa.m^2$ . As a result:

$$J_i^{ex} = B \times \left[ P_i^{oc} P_{sat}(T_B) / T_B \right]^{1/2} \quad (4.4c)$$

As shown in Equation (4.3b), the concentration losses, or the effect of increased pressure at the BASE/cathode electrode interface (due to sodium vapor pressure losses in the low pressure cavity of the cell, Fig. 1a), increase with cell current or sodium flow rate. The pressure drop across the cathode electrode is expressed in terms of an empirical dimensionless factor  $G_E$ . Both  $B$  and  $G_E$  are characteristic of the type of electrodes used, and are determined experimentally. Typical TiN electrodes have  $B \sim 80$  SI and  $G_E \sim 50$  (Ryan et al. 1998).

When the charge-exchange polarization losses are negligible (i.e.  $B$  is infinite), the Nernst electromotive force of the AMTEC cell is reduced only by the concentration losses, and is proportional to the expansion work by sodium ions through the BASE, under load:

$$V_o^{cc} = \frac{1}{f_B} \ln \left[ P_a^{cc} / P_c^{cc} \right] . \quad (4.5)$$

#### 4.2.2 BASE Ionic Resistance

The BASE ionic resistance is given by:

$$R'_B = \rho_B \times r_B \ln[r_B / (r_B - t_B)] , \quad (4.6)$$

and reduces to  $R'_B = \rho_B \times t_B$ , when  $t_B \ll r_B$ . This ionic resistance is directly proportional to the BASE tube thickness. The PX-series cells use cylindrical BASE tubes having an outer radius,  $r_B = 3.81$  mm, and a thickness,  $t_B = 0.508$  mm. This thickness is a compromise between performance (requiring a thinner wall) and structure strength (requiring a thicker wall) of the ceramic BASE tubes.

#### 4.2.3 Current Collector Losses

For large electrodes area, current collection while maintaining high electrode performance is a design and modeling challenge. The electronic sheet resistance of the metal electrode could be significant and must be compensated for with the use of highly conductive current collector networks. High-conductivity thin porous electrodes can be fabricated by decreasing their volume porosity or increasing their thickness, but at the expense of increased flow resistance to the sodium vapor (i.e. higher  $G_E$ ). Current collectors which properly contact the BASE electrodes, without significantly reducing the electrodes surface area, must be designed to minimize the ohmic losses, by providing the shortest current flow path from any point on the BASE electrode surface to the cell's electric leads. This is accomplished through the use of a metal sponge or a metal-wire grid that provides both current pick-up points from the electrode and axial current transport at low ohmic losses (Sievers et al. 1988).

To calculate the electrodes sheet resistance, and the resistances of the current collectors and the buses, a two-dimensional electric model was developed. This model can handle any of four different current collector configurations typically used in vapor anode, multi-tube AMTEC cells (Sievers et al. 1988, and Tanaka et al. 1992). The first configuration (Figure 4.2a) consists of tie wires wrapped around the BASE tube's cathode electrode, and connected to a larger axial bus. The second is a metal sponge wrapped around the BASE tube's cathode electrode and held in place by tie wires connected to an axial bus (Figure 4.2b). The third consists of one layer of wire screen mesh wrapped around the BASE tube's cathode electrode and held in place by tie wires connected to an axial bus (Figure 4.2c). The fourth is a single wire wrapped around the BASE tube's cathode electrode as a helix (Figure 4.2d).

The two-dimensional electric model of these current collector networks discretized the BASE tube/electrodes/current collectors system into  $N$  axial segments of equal height,  $H$  (Figure 4.3). Every axial segment  $k$  provides an effective electromotive force  $V_k^o$  (Equation 4.1), and its resistance,  $R_k$ , includes the BASE ionic resistance, contact resistances between the current collectors and electrodes, sheet resistances of the electrodes, and radial/circumferential resistances of the current collectors. The ohmic resistances  $R_k^a$  and  $R_k^c$  are the axial resistances of the anode and cathode current collectors, respectively. The resistance  $R_o$  in segment  $k = 0$  (Figure 4.3) is the equivalent external load per BASE tube. Finally,  $R_{leak}$  is the leakage resistance between the anode and cathode electrodes, through the BASE metal-to-ceramic braze joint (Figure 4.1a). This leakage path is treated as segment number  $(N+1)$  in the model.

The problem of current collection is truly three-dimensional and calculations of local current density and electric potential can be carried out using finite elements techniques and integrating over the electrode surface and the current collector grid elements (Tanaka et al. 1992). A current collection path was assumed, from the BASE surface through the electrode and the collector network components. The corresponding ohmic resistances  $R_k$ ,  $R_k^a$  and  $R_k^c$  were obtained by integrating the Joule losses along the conduction path (Sievers et al. 1988). Since electrons travel along the path of least resistance, the approach of selecting a given, probable conduction path is conservative. Calculations results obtained for the resistances of each current collector type in Figure 4.2 are given next.

### Ring Wires in Contact with Axial Bus

In this configuration (Figure 4.2a), it is assumed that electrons travel axially through the electrode (sheet resistance) to the nearest wire of the current collector, then travel circumferentially through the ring to the contact point with the axial bus. The latter collects current at the different contact points with the tie wires, which are separated by a distance  $H$ . For this collection path, we obtain:

$$R_k = \frac{R_B' + R_{cont}^a + R_{cont}^c}{[2\pi r_B H]} + R_{sheet}^{E,z} + R_{wire}^{\theta}, \quad (4.7a)$$

where

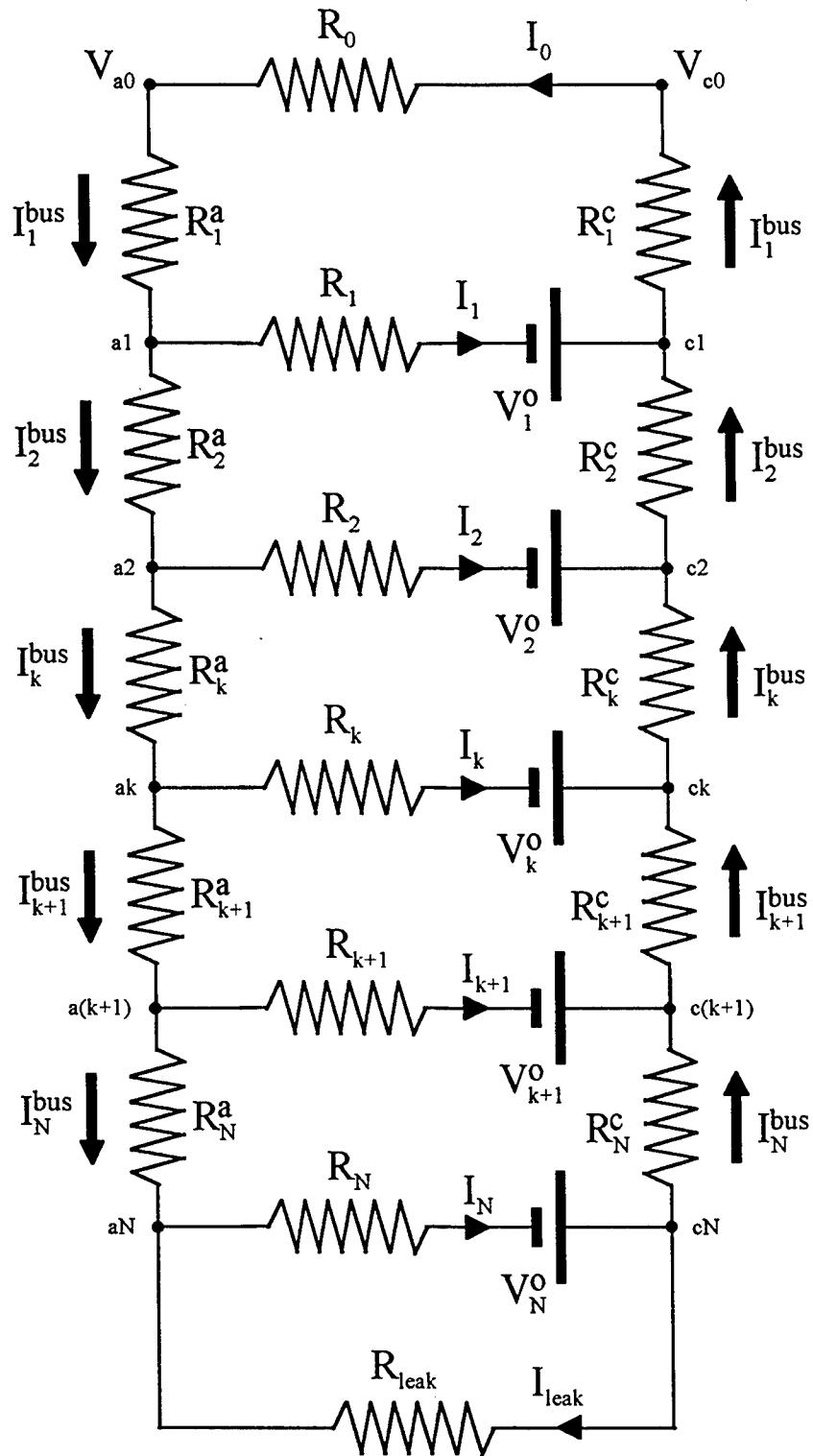


Figure 4.3. Electric Circuit Model of BASE Tube's Current Collectors.

$$R_{sheet}^{E,z} = \frac{H^2}{12} \frac{\rho_E}{t_E(1-\epsilon_E)} \times \frac{1}{[2\pi r_B H]}, \quad (4.7b)$$

and

$$R_{wire}^{\theta} = \frac{\rho_w}{A_w} \left[ \frac{2\pi(r_B + r_w)}{12} \right]. \quad (4.7c)$$

The axial resistance of a bus section of height  $H$  is simply:

$$R_k^{bus} = \frac{\rho_{bus}}{A_{bus}} H. \quad (4.7d)$$

### Metal Sponge in Contact with Axial Bus

In this configuration (Figure 4.2b), it is assumed that electrons travel radially through the electrode to the metal sponge, then travel circumferentially through the sponge to the nearest contact point with the axial bus. In this case:

$$R_k = \frac{R_B' + R_{cont}^{a'} + R_{cont}^{c'}}{[2\pi r_B H]} + R_{sheet}^{E,r} + R_{sponge}^r + R_{sponge}^{\theta}, \quad (4.8a)$$

where

$$R_{sheet}^{E,r} = \frac{\rho_E t_E}{(1-\epsilon_E)} \times \frac{1}{[2\pi r_B H]}, \quad (4.8b)$$

$$R_{sponge}^r = \frac{\rho_{sp} t_{sp} / 2}{(1-\epsilon_{sp})} \times \frac{1}{[2\pi r_B H]}, \quad (4.8c)$$

and

$$R_{sponge}^{\theta} = \frac{\rho_{sp}}{t_{sp}(1-\epsilon_{sp})H} \times \frac{2\pi(r_B + t_{sp}/2)}{12}. \quad (4.8d)$$

The axial bus continuously collects electrons along its length, and the resistance of a segment  $k$  of the bus is given as:

$$R_k^{bus} = \frac{\rho_{bus} H}{A_{bus}} \left[ \frac{I_{k+1}^{bus}}{I_k^{bus}} + \frac{1}{3} \left( 1 - \frac{I_{k+1}^{bus}}{I_k^{bus}} \right)^2 \right]. \quad (4.8d)$$

With a large number of axial sections ( $N > 20$ ), only a few iterations were needed for the convergence of the solution (to resolve the dependence of  $R_k^{bus}$  on the currents).

### Screen Mesh in Contact with Axial Bus

In this more involved configuration (Figure 4.2c), electrons flow axially and circumferentially through the electrode to the nearest mesh grid segment of the current collector, then travel to the nearest horizontal grid segment, which conducts them to the nearest contact point with the axial bus (Figure 4.4). Since the screen mesh is a good conducting structure, the conduction through the tie wires was neglected in this analysis. Resulting equations were integrated over  $H \gg h$  ( $h$  is the mesh size). Introducing  $N_{wires}$  and  $N_p$  such that:

$$H = h \times N_{wires}, \quad \text{and} \quad \frac{2\pi r_B}{h} = 2(N_p + 1), \quad (4.9)$$

we obtained:

$$R_k = \frac{R'_B + R_{cont}^{a'} + R_{cont}^{c'}}{[2\pi r_B H]} + R_{sheet}^E + R_{mesh}^z + R_{mesh}^\theta, \quad (4.10a)$$

where

$$R_{sheet}^E = \frac{h^2}{24} \frac{\rho_E}{t_E(1 - \epsilon_E)} \times \frac{1}{[2\pi r_B H]}, \quad (4.10b)$$

$$R_{mesh}^z + R_{mesh}^\theta = \frac{h^3}{30} \frac{\rho_w^{mesh}}{A_w^{mesh}} (1 + \alpha) \times \frac{1}{[2\pi r_B H]}, \quad (4.10c)$$

and

$$\alpha = \frac{1}{N_p + 1} [10N_p^3 + 30N_p^2 + 31N_p + 11]. \quad (4.10d)$$

The axial bus collects current at the contact points with the grid mesh (Figure 4.4), and its resistance is given as:

$$R_k^{bus} = \frac{\rho_{bus} H}{A_{bus}} \left[ \frac{I_{k+1}^{bus}}{I_k^{bus}} + \frac{1}{3} \left( 1 + \frac{1}{2N_{wires}^2} \right) \left( 1 - \frac{I_{k+1}^{bus}}{I_k^{bus}} \right)^2 \right]. \quad (4.10e)$$

### Wrapped Helical Wire

In this configuration (Figure 4.2d), a bus wire of radius  $r_{bus}$  is tightly wrapped around the BASE tube. The angle of the helix is assumed small. Electrons travel axially through the electrode to the nearest wire contact line of the current collector, then circumferentially through the helical wire. Resulting equations were integrated over  $H > r_{bus}$ . Introducing  $N_{rings}$ ,  $L_{rings}$  and  $A_{bus}$  such that:

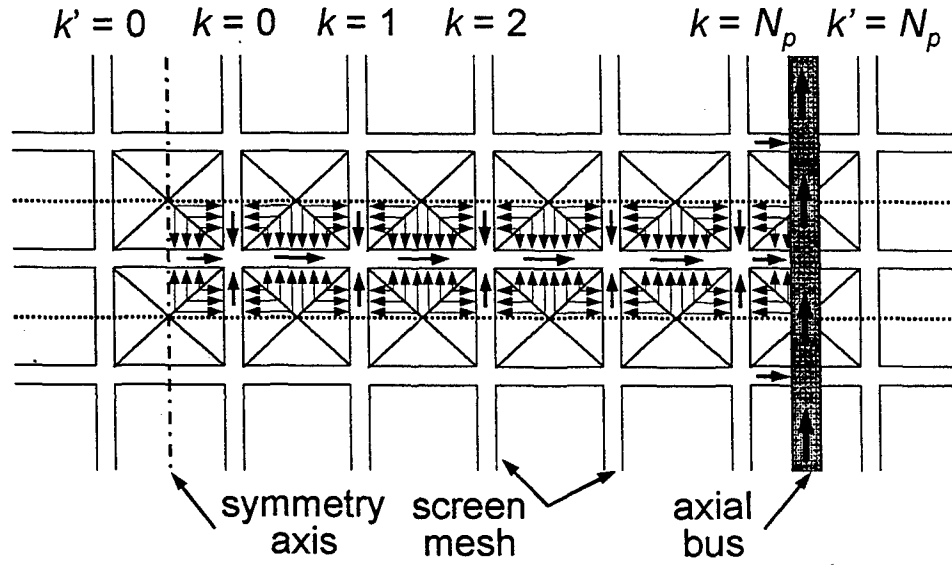


Figure 4.4. Electrons' Conduction Path in a Screen Mesh Current Collector.

$$H = 2r_{bus} \times N_{rings}, L_{rings} = 2\pi(r_B + r_{bus}) \times N_{rings}, \text{ and } A_{bus} = \pi r_{bus}^2, \quad (4.11)$$

we obtained:

$$R_k = \frac{R'_B + R_{cont}^{a'} + R_{cont}^{c'}}{[2\pi r_B H]} + R_{sheet}^{E,z}, \quad (4.12a)$$

where

$$R_{sheet}^{E,z} = \frac{r_{bus}^2}{3} \frac{\rho_E}{t_E(1 - \epsilon_E)} \times \frac{1}{[2\pi r_B H]}, \quad (4.12b)$$

and

$$R_k^{bus} = \frac{\rho_{bus} L_{rings}}{A_{bus}} \left[ \frac{I_{k+1}^{bus}}{I_k^{bus}} + \frac{1}{3} \left( 1 - \frac{I_{k+1}^{bus}}{I_k^{bus}} \right)^2 \right]. \quad (4.12c)$$

#### 4.2.4 Calculation of Electric Current and Voltage

The conservation of current at the nodes of the electric circuit of the BASE/electrodes/current collectors system in Figure 4.3 shows that the current travelling down the anode collector is equal to that travelling up the cathode collector. The electric currents at the nodes of the electric circuit

in Figure 4.3 were determined from Kirchhoff's law. The electrons leakage path is treated as an additional branch ( $N+1$ ) with:

$$R_{N+1} = R_{leak}, R_{N+1}^a = R_{N+1}^c = 0, \text{ and } V_{N+1}^o = 0. \quad (4.13)$$

When applied to the closed circuit between the load and the  $k$ th branch, Kirchhoff's law is written as:

$$V_k^o = R_o I_o + R_k I_k + \sum_{i=1}^k (R_i^c + R_i^a) \times I_i^{bus}. \quad (4.14)$$

Since  $I_o = I_1^{bus}$  and  $I_k = I_k^{bus} - I_{k+1}^{bus}$ , one obtains:

$$V_k^o = R_o I_1^{bus} + R_k (I_k^{bus} - I_{k+1}^{bus}) + \sum_{i=1}^k (R_i^c + R_i^a) \times I_i^{bus}, \text{ for } k = 1 \text{ to } (N+1). \quad (4.15)$$

Note that  $I_{N+2}^{bus} = 0$ .

Equations (4.15) represent a linear system of  $(N+1) \times (N+1)$  relations that were solved for the unknowns  $\{I_k^{bus}\}$ ,  $k=1$  to  $N+1$ , using a simple Gauss elimination algorithm. To improve the convergence of the iterative solution, the concentration and charge-exchange overpotentials that appear in the effective electromotive forces  $V_k^o$  (Equation 4.1) were linearized in terms of branch current  $I_k = I_k^{bus} - I_{k+1}^{bus}$ , using Equation (4.3b).

#### 4.2.5 Equivalent External Load Resistance

Because of the symmetry in the AMTEC cell, the BASE tubes have identical temperature, sodium vapor pressure and current density axial distributions. Since the  $N_s$  BASE tubes in the cell are connected electrically in series, every tube contributes an equal voltage to the load. Figures 4.5 and 4.6 show schematics of the equivalent electrical circuit in the cell. The cathode end of BASE tube #  $k$  is connected to the anode of the next tube #  $(k+1)$  through a connector lead of resistance  $R_{lead}^{conn}$ . The anode of the first tube and cathode of the last tube are connected to the external load through leads of resistances  $R_{lead}^a$  and  $R_{lead}^c$ , respectively. Since

$$V_1^c - V_1^a = \dots = V_k^c - V_k^a = \dots = V_{N_s}^c - V_{N_s}^a = V^c - V^a, \quad (4.16)$$

Kirchhoff's law applied to the circuit in Fig. 6 gives:

$$N_s (V^c - V^a) = \{(N_s - 1)R_{lead}^{conn} + R_{lead}^a + R_{lead}^c + R_L\} I_o. \quad (4.17)$$



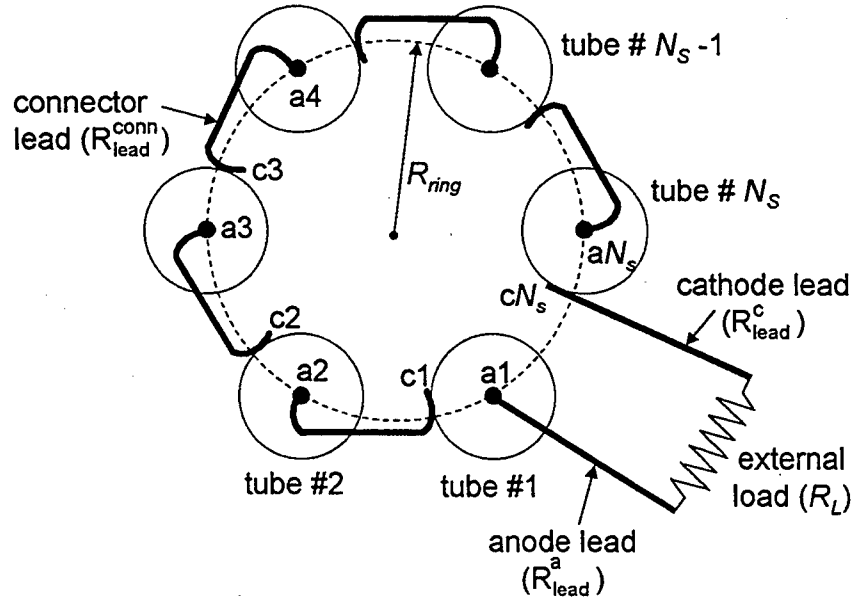


Figure 4.5. Electrical Connection of BASE Tubes and External Load in PX-Series Cell.

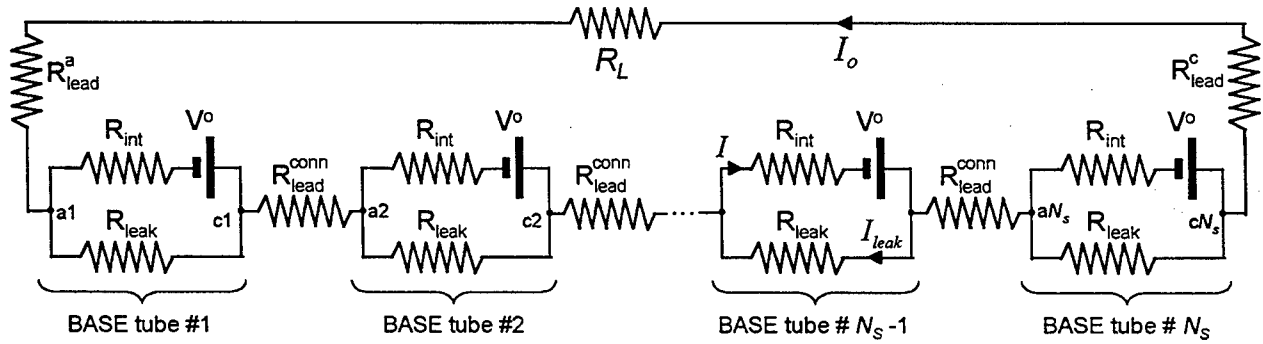


Figure 4.6. Electric Circuit Model of BASE Tubes and External Load in PX-Series Cell.

Since  $V^c - V^a = R_o I_o$  by definition (Figure 4.3), the effective external load resistance per BASE tube can be expressed as:

$$R_o = \{(N_s - 1)R_{lead}^{conn} + R_{lead}^a + R_{lead}^c + R_L\} / N_s . \quad (4.18)$$

In the present electric model, the electrical resistances of the electrodes and current collectors were taken to be temperature-dependent. The ionic resistivity of the Na-BASE,  $\rho_B$ , was calculated using the following relation (Steinbruck et al. 1993):

$$\rho_B = T_B \times \left( 1.62 \times 10^{-5} \times \exp[-45.5/T_B] + 1.55 \times 10^{-7} \times \exp[3,722./T_B] \right) . \quad (4.19)$$

### 4.3 RESULTS AND DISCUSSION

The present electric model was integrated into the full cell model, APEAM, and an efficient numerical procedure was developed to resolve the couplings between the various models of the different physical processes in the cell (see Chapter 5, Section 5.4). The axial distributions of the sodium vapor pressure along the electrodes and of the BASE temperature were obtained from the sodium vapor pressure loss model and heat transfer model, respectively. Analysis of the results showed that, except for a thick sponge collector, all current collectors investigated performed extremely well, with insignificant internal losses. These current collectors provide enough contact points with the electrodes, reducing the sheet resistances in the electrodes.

The fully-integrated cell model (APEAM) has been extensively benchmarked with experimental data of the cells tested at AFRL (see Chapters 11 and 12). The design parameters for a number of cells, and those relevant to the cell electric model, such as current collector designs, are given in Table 4.1. All the PX-series cells listed in Table 4.1 have been tested in vacuum at AFRL. This table also lists the values of the estimated cathode electrode geometric factor for pressure drop,  $G_E$ , contact resistance between electrode and current collector,  $R'_{cont} = R_{cont}^{a'} = R_{cont}^{c'}$ , charge-exchange coefficient,  $B$ , and leakage resistance of the metal-ceramic braze joint between BASE tube and SS support plate,  $R_{leak}$ , that were used in the model for best comparison with test data. To compare the electric losses in the cell, the corresponding voltage losses are expressed as a fraction of the theoretical Nernst (theoretical) electrical power of the cell:

$$P_{Nernst} = N_S \times (2\pi r_B) \int_{z=0}^{L_E} V^{oc}(z) \cdot J(z) dz \approx N_S \times \sum_{k=1}^N V_k^{oc} I_k. \quad (4.20)$$

This electric power equals that delivered to the external load plus the sum of all internal and lead losses. The main contributors to the internal electrical losses in the cells, in an order of decreasing importance, were found to be: (a) concentration/charge-exchange polarization losses on the cathode side; (b) contact losses between current collectors and metal electrodes; (c) BASE ionic resistance; and (d) electrons leakage between anode and cathode electrodes. In all cases, the Joule losses in the current collector networks and in the connecting leads between the BASE tubes amounted to less than 6% of the Nernst power of the cell (Table 4.1). The polarization/concentration losses of the TiN electrodes were major, amounting to 25–50% of the Nernst power. The contact losses were a far second, amounting to less than 9%. When combined together with the BASE ionic resistance losses, they amounted to less than 16% of the Nernst power in all cells in Table 4.1.

The effect of changing the external load resistance (or the cell electrical current) on the weighting of the different electrical losses in the cell is illustrated in Figure 4.7. This figure shows that for the PX-3G cell, which operated at hot side and cold side temperatures of 1123 K and 553 K, respectively, the charge-exchange/concentration losses increased logarithmically with cell current (also, see Figure 4.13c). However, the internal ohmic losses (contact losses, ionic losses in BASE tube, current collectors and connecting leads losses) increased linearly with the cell electrical current (Figure 4.7). The leakage losses were large at low electrical current (high voltage), but

Table 4.1. Electrical Losses in PX-Series Cells near their Peak Electric Power.

Parameters:	PX-2C	PX-4C	PX-5A	PX-3G <sup>a</sup>	PX-3A
<b>Cell Design:</b>					
Number of BASE tubes	7	6	6	6	5
Cathode electrode / tube (mm <sup>2</sup> )	600	600	600	600	600
Current collectors	100-mesh Cu	50-mesh Mo	50-mesh Mo	60-mesh Mo	60-mesh Mo
Mesh wire diameter	110 $\mu$ m	210 $\mu$ m	210 $\mu$ m	163 $\mu$ m	178 $\mu$ m
Bus wire cross section area (mm <sup>2</sup> )	0.503 (Cu)	0.503 (Mo)	0.503 (Mo)	0.806 (Ta)	0.503 (Mo)
Electrode geometric factor, $G_E$	12	50	50	50	50
Contact resistance, $R'_{cont}$ ( $\Omega$ .cm <sup>2</sup> )	0.08	0.06	0.06	0.06	0.06
Exchange current, $B$ (A.K <sup>1/2</sup> /Pa.m <sup>2</sup> )	120	120	120	75	120
Leakage resistance, $R_{leak}$ ( $\Omega$ )	$+\infty$	$+\infty$	$+\infty$	3.0	5.0
<b>Cell Performance:</b>					
External load ( $\Omega$ )	2.0	1.2	1.2	1.14	0.65
Cell current (A)	1.47	1.763	1.759	1.798	2.67
Load electric power ( $W_e$ )	4.39	3.73	3.71	3.69	4.64
Cell conversion efficiency	11.2%	10.7%	11.8%	12.8%	14.2%
Leakage current, $I_{leak}$ (A)	0.0	0.0	0.0	0.121	0.079
Cell heat input ( $W_{th}$ )	39.0	34.9	31.5	28.90	32.7
Wall heat losses ( $W_{th}$ )	6.5	6.7	7.1	1.95	6.1
Open-circuit voltage (V)	6.33	4.57	3.58	5.10	3.61
Concentr./polarization losses (V)	2.84	1.87	0.89	2.45	1.11
Cell internal resistance ( $\Omega$ )	0.348	0.285	0.285	0.274	0.240
Anode pressure (kPa)	14.7	12.7	13.2	17.2	33.2
Cathode pressure (Pa)	16.2	24.3	30.4	26.7	48.0
Cell's Nernst electrical power ( $W_e$ )	9.42	8.09	6.33	9.76	9.97
<b>Nernst Electrical Power Fractions:</b>					
External load resistance (%)	46.5	46.1	58.7	37.7	46.6
Concentration / polarization (%)	45.0	41.1	25.0	48.4	30.8
Contact resistance (%)	4.6	4.9	6.2	4.8	8.1
BASE ionic resistance (%)	3.2	4.5	5.8	4.4	7.5
Electrons leakage (%)	0.0	0.0	0.0	2.7	1.5
Current collectors (%)	0.4	2.0	2.5	1.2	3.3
BASE tubes connecting leads (%)	0.3	1.4	1.8	0.8	2.2
<b>Temperatures (K):</b>					
Hot end, $T_{hot}$	1127	1130	1123	1123	1173
BASE brazes (maximum)	1097	1092	1089	1094	1140
Hot end of electrodes	1037	1036	1042	1051	1123
Cold end of electrodes	1002	988	1000	1012	1060
Cold end of BASE tubes	1000	986	997	1010	1055
Evaporator, $T_{ev}$	979	966	969	990	1044
Margin, $\Delta T$	+21 K	+20 K	+28 K	+20 K	+11 K
Cold end, $T_{cd}$	529	565	623	553	623
Initial test date	12/24/96	3/1/97	5/1/97	11/4/97	7/9/97
Operation (hrs)	600	1800	672	3000	4500

(<sup>a</sup>) PX-3G cell #1 in 8-cell ground-demo system.

decreased very fast with increasing current, since they are proportional to the square root of the electrolyte's voltage differential (Figure 4.12b).

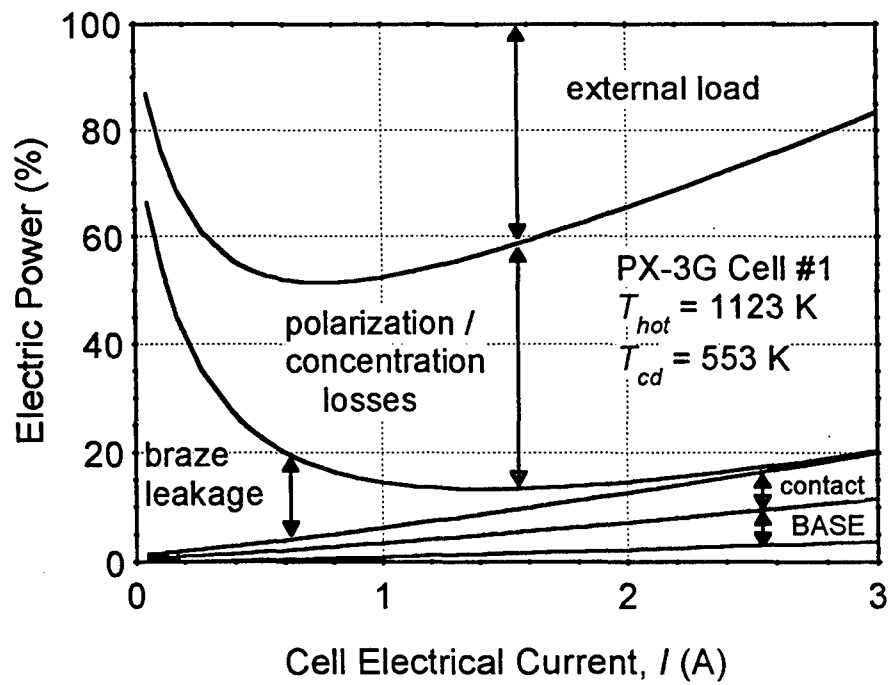


Figure 4.7. Fraction of Electrical Loss Processes in PX-3G Cell.

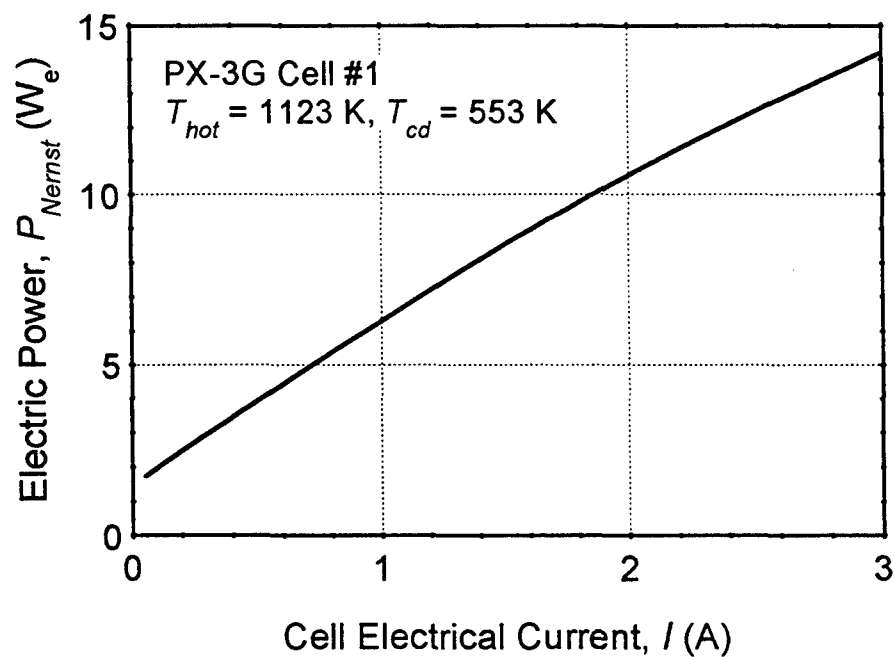


Figure 4.8. Theoretical Nernst Power in PX-3G Cell.

When the cell current,  $I = 0.7$  A, the fraction of the cell's Nernst electric power delivered to the external load peaked at 48% (Figure 4.7). However, since the theoretical Nernst power increases with increasing cell current (Equation (4.20), and Figure 4.8), the absolute value of the load electrical power peaked at a higher cell current  $I = 1.8$  A (Figure 4.11a). The load peak electric power amounted to only 36% of the Nernst power of the cell. Note that the open-circuit theoretical Nernst power does not equal zero (when the electrical current through the load,  $I = 0$ ), because of the leakage current through the brazes of the BASE tubes. When  $I = 0$  (open-circuit),  $I_{leak} = 0.27$  A (Figure 4.12c, for  $R_{leak} = 3 \Omega$ ) and the theoretical Nernst power of the cell equals the electrical power losses in the leakage resistances:  $P_{Nernst} = N_S \times R_{leak} I_{leak}^2 = 1.3 \text{ W}_e$  (Figure 4.8).

### 4.3.1 Sodium Vapor Pressure and Current Density in PX-3G

Figure 4.9 shows the calculated vapor pressure distribution on the cathode (low-pressure) side of the PX-3G cell. The pressure profile along the BASE tubes is typically parabolic, due to the continuous vapor addition along the BASE outer surface. As expected, the sodium vapor pressure drop on the cathode side increases with increasing cell current, or vapor mass flow rate. At a cell current of 1.8 A, the sodium vapor pressure along the BASE/cathode electrode interface varied between 24 Pa and 30 Pa. There was a 6.7 Pa pressure drop across the cathode electrode, and a 5.3 Pa pressure drop at the BASE/cathode electrode interface due to evaporation of sodium vapor.

The calculated current density in PX-3G at an external load resistance  $R_L = 1.14 \Omega$  ( $I = 1.8$  A) is shown in Figure 4.10, along with the predicted axial temperature distribution along the BASE tubes. The current density,  $J_c$ , along the cathode electrode only changed by up to 12%, and had a minimum of  $0.307 \text{ A/cm}^2$  near the mid-plane of the electrode. This axial distribution of  $J_c$  resulted from the combined effects of the axial distributions of sodium vapor pressure on the cathode side and of the BASE temperature. The temperature of the electrode varied between 1012 K and 1051 K (Figure 4.10, Table 4.1). The Mo current collection grids on the inside and outside surfaces of the BASE tubes increased the effective axial conductance of the solid electrolyte membrane by 2 orders of magnitude, limiting the temperature drop along the electrode portion of the BASE tubes to only 39 K. Figure 4.10, however, indicates a larger temperature drop of about 43 K along the braze section of the BASE tubes, which is not covered by the current collectors. The calculated maximum temperature of the braze in the PX-3G cell was 1094 K when operated at the peak electrical power (Figure 4.10, and Table 4.1).

Parametric analyses were performed to investigate the effects of the contact losses, leakage current, and charge-exchange/concentration losses on the performance of the PX-3G cell (Figure 4.1). The analyses were performed at fixed  $T_{hot} = 1123$  K and condenser temperature,  $T_{cd} = 553$  K. The values of  $R'_{cont}$ ,  $R_{leak}$  and  $B$  were varied independently, to quantify their individual effect on the I-V characteristic and electrical power output of the PX-3G cell. Results are presented and discussed next.

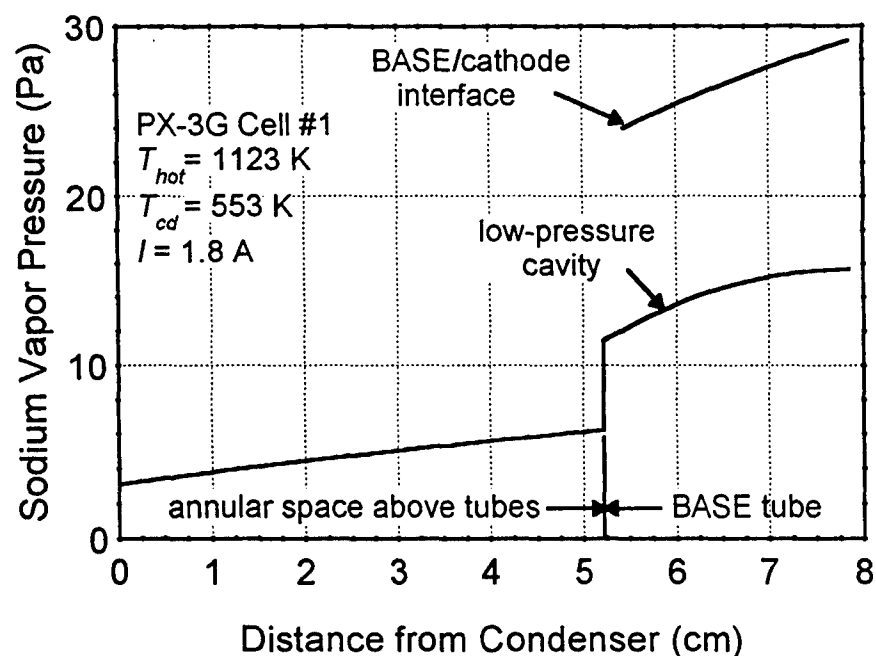


Figure 4.9. Sodium Vapor Pressure on Low-Pressure Side of PX-3G Cell.

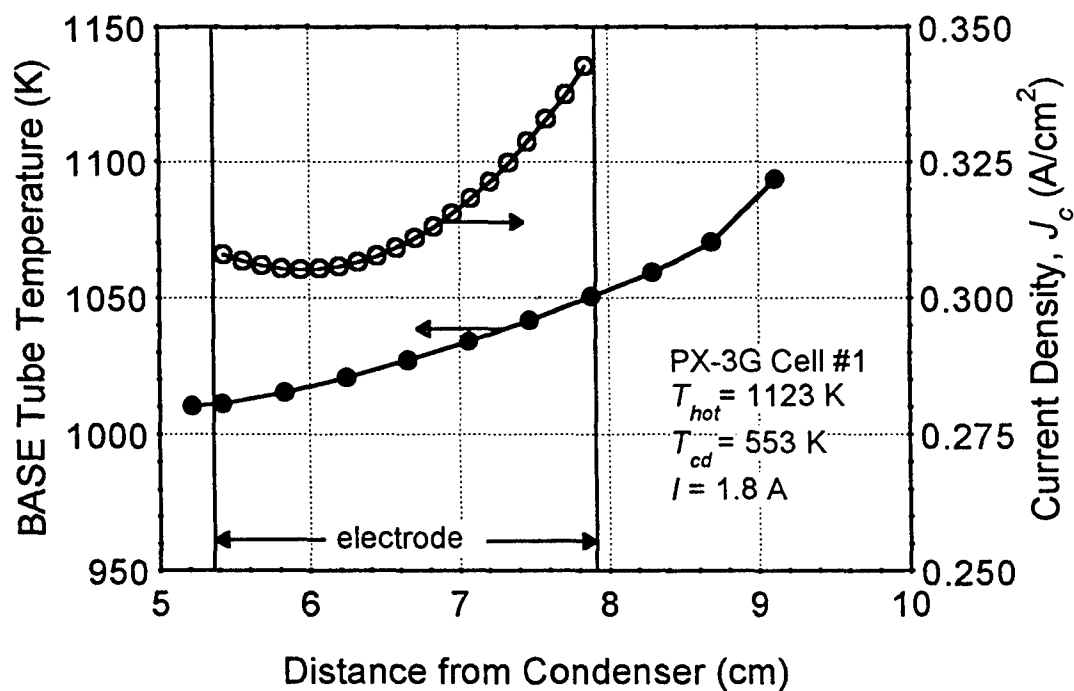


Figure 4.10. BASE Tubes' Temperature and Current Density in PX-3G Cell.

### 4.3.2 Effect of Internal Ohmic Losses

Figure 4.11 shows the effect of decreasing the contact resistance on the performance parameters of the PX-3G cell. Since ohmic losses increase with cell current, the effect of  $R'_{cont}$  is most noticeable in the low voltage region of the I-V characteristic. Higher values of  $R'_{cont}$  reduce the peak electric power of the cell and shift it to lower cell current (or higher cell terminal voltage), and vice versa (Figure 4.11a). Doubling  $R'_{cont}$  (from  $0.06 \Omega \cdot \text{cm}^2$  to  $0.12 \Omega \cdot \text{cm}^2$ ) increases the cell internal resistance by 46% (from  $0.274 \Omega$  to  $0.40 \Omega$ ), and decreases the cell peak electric power by 10%, to 3.32 W<sub>e</sub>.

The internal electric losses of the cell increased linearly with  $R'_{cont}$  (Figure 4.11c). The PX-3G cell, which has six 0.508 mm-thick BASE tubes, and 25.4 mm-long TiN electrodes, had a predicted internal resistance of  $0.274 \Omega$  (Figure 4.11c). The components of the cell internal resistance were: (a) the ionic resistance of the BASE, which is proportional to the  $\beta''$ -alumina solid electrolyte thickness (39.3% of  $R_{int}$ ); (b) the contact resistances between the BASE and the metallic electrodes, and between the electrodes and the current collectors (42.9% of  $R_{int}$ ); (c) the ohmic losses in the 60-mesh, molybdenum current collectors (10.7% of  $R_{int}$ ); and (d) the ohmic losses in the connecting leads (7.1% of  $R_{int}$ ) (Table 4.1).

### 4.3.3 Effect of Leakage Losses

Figure 4.12 shows the predicted leakage current  $I_{leak}$  through the metal-ceramic braze in the PX-3G cell #1 as a function of cell current,  $I$ . At the peak electric power of the cell,  $I = 1.8 \text{ A}$  and  $I_{leak} = 0.12 \text{ A}$  per BASE tube. When the external load resistance,  $R_L$  increased, the cell electric current,  $I$  decreased, and the increased voltage drop between the anode and cathode electrodes (Figure 4.12b) stimulated larger leakage current (or leakage losses) through the metal-ceramic braze joint, between the BASE tubes and the SS support plate. When  $R_L$  decreased,  $I$  increased and the voltage difference between the anode and cathode electrodes decreased, causing  $I_{leak}$ , and hence, leakage losses, to decrease (Figure 4.12c).

Figure 4.12 also shows the effect of  $R_{leak}$  on the performance of the PX-3G cell and on the leakage current through the BASE brazes. Again, the influence of  $R_{leak}$  is more noticeable in the high voltage region of the I-V characteristic. The leakage losses lower the cell's electrical power output, but insignificantly affects the cell current corresponding to the peak electric power (Figure 4.12a). The latter is a clear and accurate indicator of the existence of leakage losses in the cells.

### 4.3.4 Effect of Concentration and Charge-Exchange Polarization Losses

The charge-exchange coefficient,  $B$ , was varied between  $50 \text{ A} \cdot \text{K}^{1/2} / \text{Pa} \cdot \text{m}^2$  and  $+\infty$  (theoretical limit), and the corresponding load electrical power and voltage were calculated and plotted in Figures 4.13a and 4.13b. As shown in these figures, the exchange current coefficient,  $B$  affects

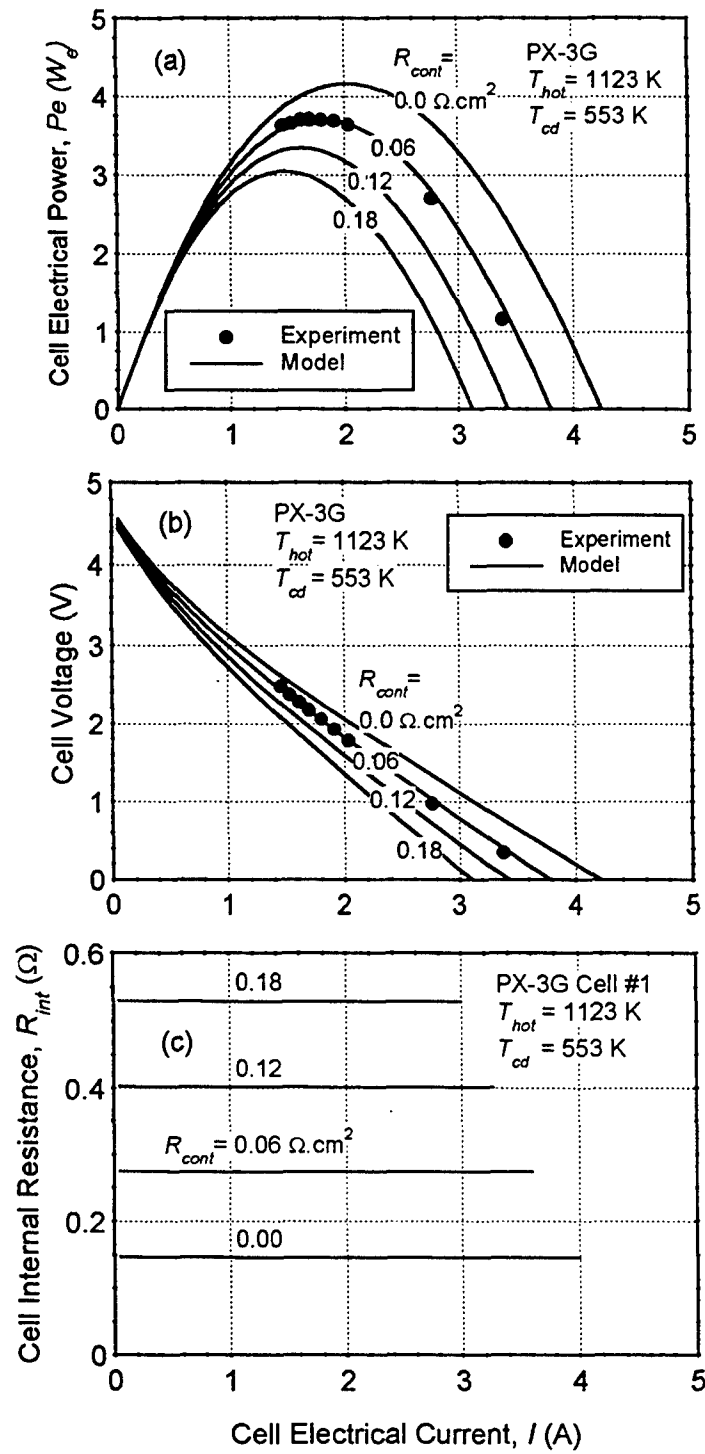


Figure 4.11. Effect of Contact Resistance on Performance of PX-3G Cell.



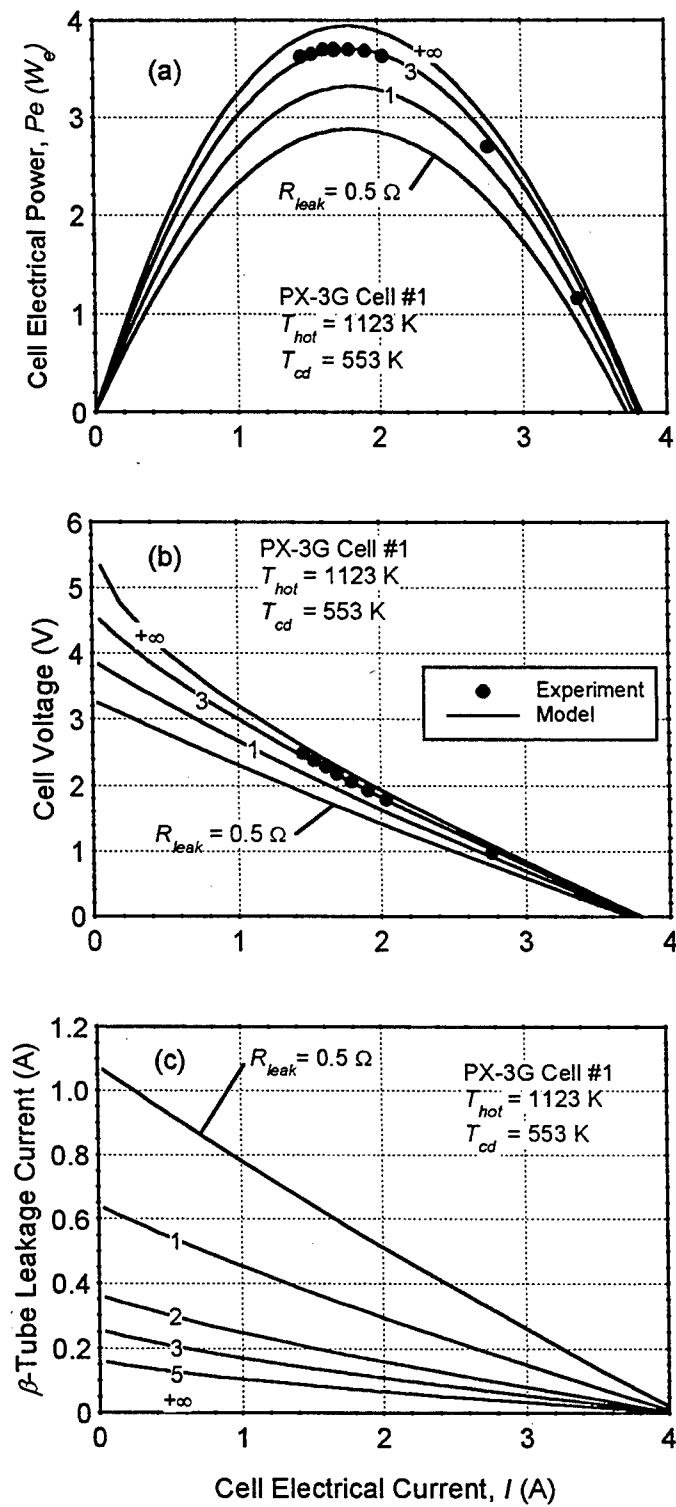


Figure 4.12. Effect of Braze Leakage Current on Performance of PX-3G Cell.

the entire I-V characteristic of the cell. Higher  $B$  values shift the I-V characteristic in parallel fashion to the upper right (i.e. toward higher current and voltage) and vice versa.

As shown in Figure 4.13a, the PX-3G cell delivered a peak load power of 3.7  $W_e$  when operated at hot and cold side temperatures of 1123 K and 553 K, respectively. Model results matched the experimental data when  $B = 75 \text{ A.K}^{1/2}/\text{Pa.m}^2$  was used. This value is typical of that of TiN electrodes used in the PX-3G cell (Ryan et al. 1998). Values in the range 120 – 200  $\text{A.K}^{1/2}/\text{Pa.m}^2$  have, however, been measured for uncontaminated  $\text{Rh}_2\text{W}$  electrodes (Ryan et al. 1992).

Figures 4.13a and 4.13b show the effect of increasing  $B$  on the cell peak power output and voltage. A PX-3G cell with  $\text{Rh}_2\text{W}$  electrodes could have delivered a peak load power in the range 4.2 – 4.6  $W_e$  (14% to 25% more than the PX-3G cell with TiN electrodes). Even higher cell performance could be obtained with  $B$  values as high as 400  $\text{A.K}^{1/2}/\text{Pa.m}^2$ , using oxide-enhanced Mo electrodes or possibly new refractory materials such as  $\text{TiB}_2$  (Fang and Knödler 1998): a peak power of 5.0  $W_e$ , which is 35% higher than that of the PX-3G cell with TiN electrodes. In addition to demonstrating high performance, the electrodes must also demonstrate structural stability of operation at high temperatures, for long period of times, commensurate with the expected mission lifetime (14 years for the Pluto/Express, and 6 years for the Europa mission).

Figure 4.13c shows that increasing  $B$  from 75 to 400  $\text{A.K}^{1/2}/\text{Pa.m}^2$  reduces the polarization/concentration overpotential in the cell by about 30%, resulting in a 35% increase in the cell peak electric power (from 3.7 to 5.0  $W_e$ ). However, even if a perfect electrode was used (i.e.  $B = +\infty$ ), the overpotential would not be zero (1.74 V at the peak power, corresponding to  $I = 2.5 \text{ A}$ ), because of the concentration losses (or effect of vapor pressure losses in the low pressure cavity; Equation 4.3b, Figure 4.13c). The PX-3G cell has a predicted total geometric factor  $G = 192$  on the low-pressure side (see Chapter 3). The total vapor pressure losses comprise those due to evaporation of sodium at the BASE/electrode interface ( $G_{ev} = 40$ ), vapor transpiration through TiN cathode electrode ( $G_E = 50$ ), vapor flow between electrode surface and cell condenser ( $G_{\eta} = 82$ ), and condensation of sodium vapor ( $G_{cd} = 20$ ). Therefore, the pressure drop through the electrode contributed only  $(50 / 192) = 26\%$  of the total vapor pressure losses in the low-pressure cavity.

#### 4.4 SUMMARY AND CONCLUSION

To quantify the contribution of the various electric losses in vapor anode, multi-tube AMTEC cells, a two-dimensional electric model was developed, which included four options of current collector configurations: tie wires wrapped around the BASE tube, a metal sponge or a wire screen mesh held in place by tie wires, or a single helical wire. The current collector resistances were calculated using a conservative approach, by assuming a current collection path, and integrating the Joule losses along the path.

The present model accounted for non-uniform axial temperature and vapor pressure profiles along the BASE tubes/electrodes; concentration and charge-exchange polarization losses at the BASE/electrode interfaces; ionic losses of the BASE; contact losses between electrodes and

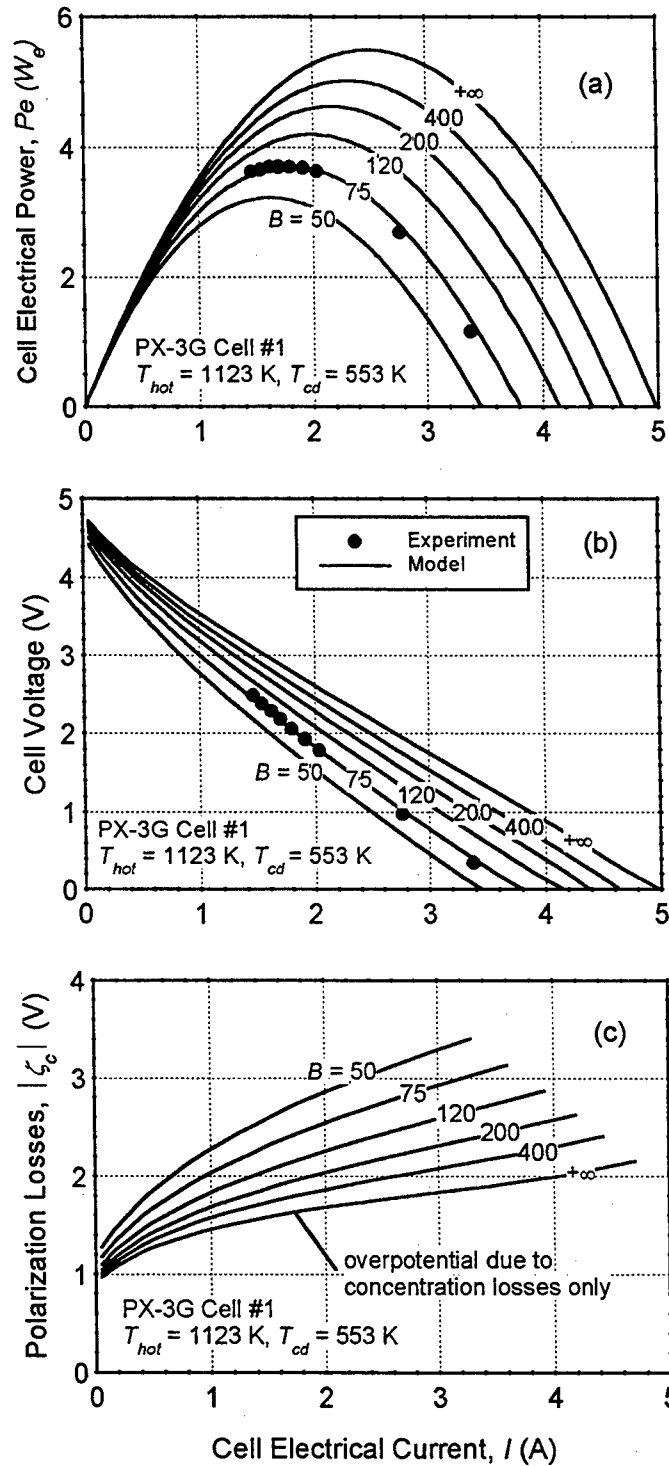


Figure 4.13. Effect of Charge-Exchange Coefficient,  $B$ , on Performance of PX-3G Cell.

current collectors; leakage losses between anode and cathode electrodes through the BASE braze joint; sheet losses in the plane of the electrodes; and radial and axial electrical losses in the current collector networks, including those in the bus wires and the conductor leads to the load. The

model was successfully integrated into APEAM, a full cell model. Results of several PX-series cells which have been tested at AFRL showed that the electrical losses in the current collector networks and the connecting leads were negligible. However, the polarization/concentration losses in the TiN electrodes were the largest, amounting to 25–50% of the theoretical Nernst electric power. Contact losses, combined with BASE ionic losses, amounted to less than 16% of the theoretical Nernst power.

The cell model results matched the experimental data of the PX-3G cell when  $B = 75 \text{ A.K}^{1/2}/\text{Pa.m}^2$ ,  $R'_{cont} = 0.06 \text{ } \Omega.\text{cm}^2$  and  $R_{leak} = 3 \text{ } \Omega$ . The PX-3G cell delivered a peak power of  $3.7 W_e$  at  $I = 1.8 \text{ A}$  and overpotential of  $2.4 \text{ V}$ , when operated at  $T_{hot} = 1123 \text{ K}$  and  $T_{cd} = 553 \text{ K}$ . This cell had six  $0.508 \text{ mm}$ -thick BASE tubes, and  $25.4 \text{ mm}$ -long TiN electrodes, and a predicted internal resistance,  $R_{int} = 0.274 \text{ } \Omega$ . The ionic resistance of the BASE contributed 39.3% of  $R_{int}$ , while the contact resistances between the BASE and the metallic electrodes, and between the electrodes and the current collectors contributed 42.9% of  $R_{int}$ . The ohmic losses in the current collectors and leads constituted the remaining of  $R_{int}$ .

Results also showed that a PX-3G cell with  $\text{Rh}_2\text{W}$  or other advanced electrodes, exhibiting  $B$  values in the range  $120\text{--}200 \text{ A.K}^{1/2}/\text{Pa.m}^2$ , could have delivered a peak load electrical power in the range  $4.2\text{--}4.6 W_e$  (which is 14% to 25% more than the PX-3G cell with TiN electrodes). However, even if a perfect electrode were used (i.e.  $B = +\infty$ ), the overpotential would not reduce to zero, because of the concentration losses or the effect of sodium vapor pressure on the cathode side of the BASE tube. The PX-3G cell had a predicted total geometric factor  $G = 192$  for vapor pressure losses. The pressure drop through the TiN electrode contributed only 26% of the total vapor pressure losses in the low-pressure cavity.

The next chapter describes the radiation/conduction heat transfer model used in APEAM to predict the heat flows and temperatures throughout the PX-series, multi-tube AMTEC cell.

## 5. RADIATION/CONDUCTION HEAT TRANSFER MODEL OF PX-SERIES CELLS

This chapter describes in details the radiation/conduction heat flow model which calculates internal parasitic heat losses and temperatures within the PX-series, multi-tube AMTEC cell cavity. The model accounts for the presence of an internal circumferential radiation shield, and a conduction stud between the hot end of the cell and the BASE tubes support plate. In the present radiation/ conduction model, all surfaces exchanging radiant energy within the cell cavity are assumed gray and diffuse. The model calculates radiation and conduction heat fluxes between the different elements of the cell. The input file allows the user to specify the type of boundary condition at the side wall of the AMTEC cell, such as adiabatic, or thermally coupled to the surrounding insulation through a radiation gap. The radiative emissivities and all thermophysical properties are calculated as functions of temperature.

The radiation view factors are calculated using either closed-form algebraic solutions or approximate relations. The AMTEC cell is divided into several elemental cavities, which are radiatively coupled: the hot plenum baffle, the evaporator standoff, the inside of BASE Tubes, the BASE tubes/standoff bundle, the coaxial cylindrical cavity above the BASE tubes, and the annular space between the circumferential shield and the cell wall (Figure 5.1). The radiation view factors database was checked for various baseline cavities to confirm the accuracy of the radiation flux relations obtained from configuration-factor algebra. Also, all reciprocity and enclosure relations were satisfied, a necessary condition to insure balance of radiant energy in the cell. A routine was developed and tested to inverse the radiation matrix using the Gauss-Jordan elimination algorithm. An efficient iterative solution procedure was developed to couple the radiation/conduction heat flow model to the other physical submodels in the fully-integrated model.

Finally, the fully-integrated cell model is used to simulate the experimental setup of AMTEC PX-series cells at AFRL. Model results are compared with experimental results of PX-4C, PX-5A and PX-3A cells, that were tested in vacuum at AFRL. Results illustrate the effects of using a CREARE condenser and a conduction stud, reducing the number of BASE tubes, and changing the size of the cell diameter, on the heat flow and temperatures in the cell, as well as the cell electrical performance parameters.

### 5.1 NOMENCLATURE

#### English

$A_{bk}$	Radiative back face of solid element $k$
$A_{fk}$	Radiative front face of solid element $k$
$F_{kp}$	Radiation view factor between surfaces $A_k$ and $A_p$
$I$	Total cell electrical current (A)
$N$	Number of axial sections along BASE tubes
$N_c$	Number of axial sections along standoff

$N_R$	Total number of radiant surface areas
$N_S$	Total number of solid elements (nodes)
$N_{sh}$	Number of axial sections along shield
$N_w$	Number of axial sections along artery
$P_e$	Cell electrical power output (W <sub>e</sub> )
$q$	Heat flux (W / m <sup>2</sup> )
$Q$	Heat flow (W)
$R_L$	External load resistance (Ω)
$R_w$	Inner radius of cell wall (m)
$T$	Temperature (K)
$T'$	Temperature correction vector (K)
$T^*$	Best estimate of temperatures in the cell at the time of computation (K)

### Greek

$\alpha_k$	Total (hemispherical) absorptivity of surface $A_k$
$\beta_k$	Flag, $\beta_k = 1$ if element $k$ possesses a radiative back face, $\beta_k = 0$ otherwise
$\delta_{kp}$	Kronecker delta, $\delta_{kp} = 1$ if $k=p$ , $\delta_{kp} = 0$ otherwise
$\varepsilon_k$	Total (hemispherical) emissivity of surface $A_k$
$\eta$	Cell overall conversion efficiency (%)
$\rho_k$	Total (hemispherical) reflectivity of surface $A_k$
$\sigma$	Stefan-Boltzmann constant, $\sigma = 5.67 \times 10^{-8}$ W / m <sup>2</sup> .K <sup>4</sup>
$\varphi_k$	Flag, $\varphi_k = 1$ if element $k$ possesses a radiative front face, $\varphi_k = 0$ otherwise

### Subscript / Superscript

air	Air calorimeter
cond	Condenser
hot	Cell's hot end
in	Incident radiant / Input
loss	Net radiant energy loss
out	Outgoing radiant
rods	Alumina rods supporting the cell's cold plate

## 5.2 INTRODUCTION

The PX-series cells manufactured by Advanced Modular Power Systems (AMPS) and tested in vacuum at AFRL, have 5, 6 or 7 BASE tubes brazed to a stainless steel support plate and a central felt-metal wick for returning the liquid sodium working fluid to the evaporator (Figure 1). The low-pressure (cathode) and high-pressure (anode) sides of the  $\beta''$ -Alumina Solid Electrolyte (BASE) are covered with TiN porous electrodes and molybdenum mesh current collectors. The BASE tubes in the AMTEC cell are electrically connected in series. The heat input,  $Q_{in}$ , is transported by conduction and radiation from the cell's hot plate to the BASE tubes and to the evaporator structure. The circumferential radiation shield, placed in the cavity above the BASE

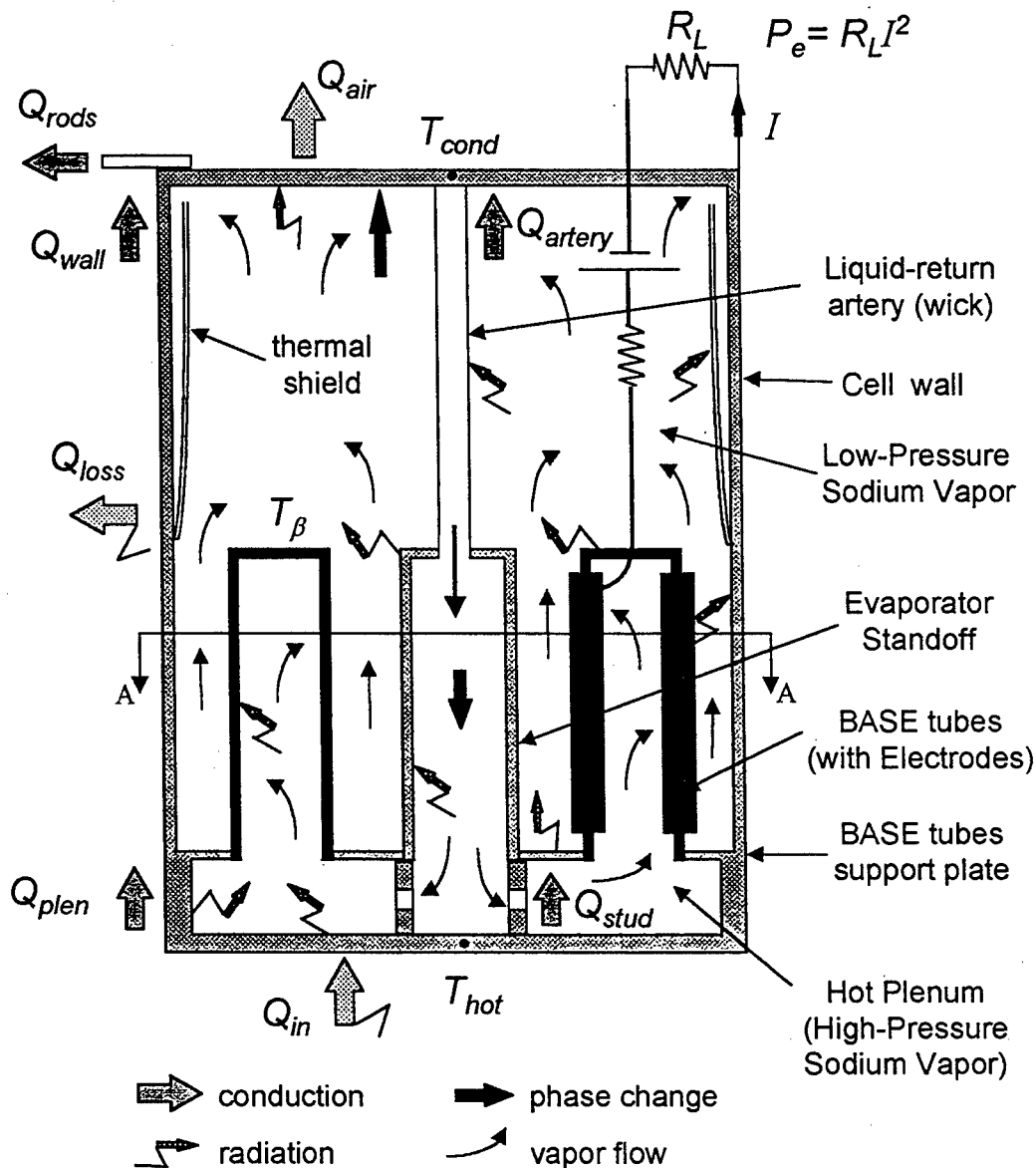


Figure 5.1a. A Schematic of Vapor Anode, Multi-Tube AMTEC Cell and Heat Transfer Processes (Not to Scale).

tubes, reduces parasitic heat losses to the side wall. The metal stud improves heat conduction from the hot end to the support plate, which helps achieve higher evaporator and BASE temperatures (Figure 5.1). To prevent condensation of sodium vapor and electrical shorting of the BASE tubes in the cell, the BASE temperature is kept slightly higher (20 – 50 K) than that of the evaporator (Figure 5.1). Some of these cells also have a conical evaporator, which provides a larger surface area for evaporation of liquid sodium.

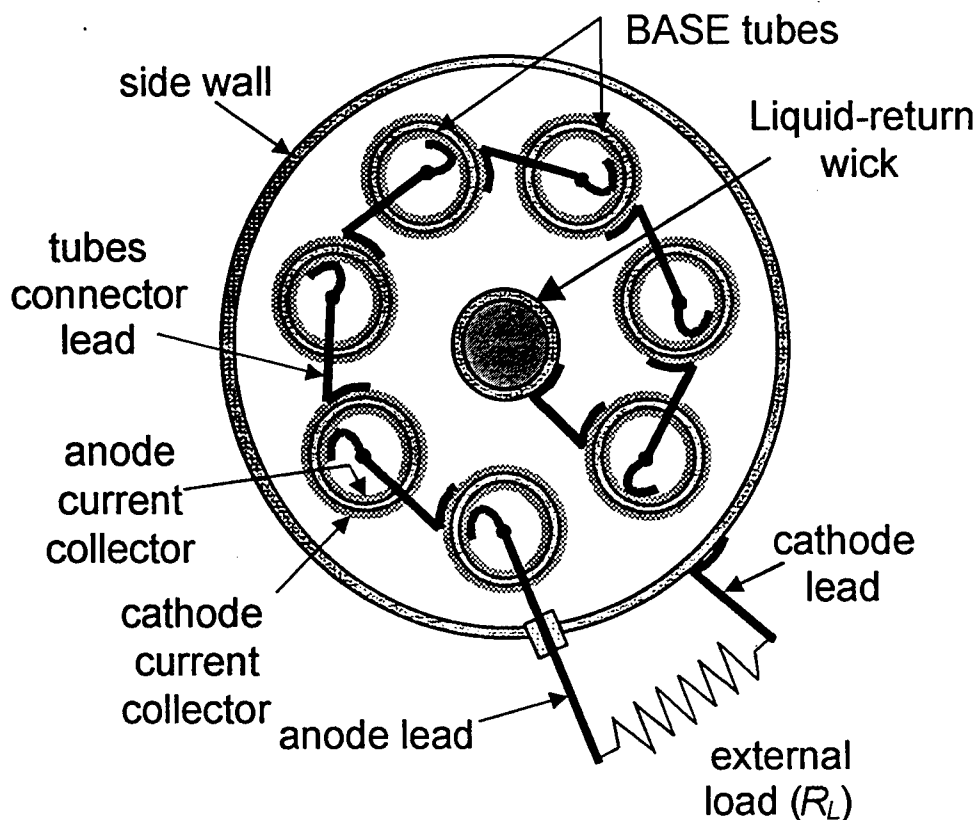


Figure 5.1b. A Schematic of Vapor Anode, Multi-Tube AMTEC Cell (Section A-A).

Modeling radiation heat transfer in the enclosure of an AMTEC cell is a challenging task because of its complex geometry. Only a few investigators have attempted to tackle this difficult problem. Ivanenok and Sievers (1996) have developed a vapor anode, multi-tube AMTEC cell model by coupling a one-node electrical model with a slip-flow vapor pressure loss model, and a 20-node thermal model of the cell. The thermal model accounted for both radiation and conduction in the cell. Their calculated wall temperatures and parasitic heat losses compared well with experimental data, for the case of near adiabatic cell wall. Schock and Or (1997), Schock et al. (1997) and Hendricks et al. (1998) have developed comprehensive thermal models for PX-type cells, based on the SINDA Thermal Analyzer software. Shock and Or (1997) used the ITAS Radiation Interchange package to calculate all radiation view factors within the cell cavity. Unfortunately, these authors have not compared their model predictions with actual experimental data. Hendricks et al. (1998) used the RadCAD thermal radiation analysis software, based on Monte-Carlo ray-tracing, to evaluate all radiation view factors in the cell. They reported their calculations of PX-type cells using 170 temperature nodes and assuming an adiabatic cell wall. Only 12 and 5 nodes were used along the cell wall and BASE tubes, respectively. By contrast, the evaporator standoff, BASE tubes support plate, conduction stud and thermal heat shields were finely discretized. Results of their model compared well with experimental data. However, calculating the radiation view factors using numerical contour integration or Monte Carlo calculation methods is very CPU intensive. Furthermore, large thermal analyzer codes such as



SINDA/FLUINT are not particularly suitable or easily amenable to handling the strong couplings between the many physical processes occurring in an AMTEC cell, resulting in a relatively slow convergence.

In this chapter, a comprehensive radiation/conduction thermal model is developed to calculate internal parasitic heat losses and temperatures in the PX-series, vapor anode, multi-tube AMTEC cells. This model is coupled to the vapor pressure loss model and electrochemical and electrical circuit models described in Chapters 3 and 4, using an efficient iterative solution procedure. Finally, results of the integrated cell model are compared with experimental measurements for PX-4C, PX-5A and PX-3A cells, tested in vacuum at AFRL. Results of the integrated cell model illustrate the effects of using a CREARE condenser, a conduction stud, and of reducing the number of BASE tubes and the size of the cell diameter, on the heat transport and temperatures fields in the cell cavity, and on the cell electrical performance.

### 5.3 MODEL DESCRIPTION

The present radiation/conduction thermal model was developed to calculate internal parasitic heat losses and temperatures within the cell enclosure (Figure 5.1). All surfaces that exchange radiant energy in the interior of the cell were assumed gray and diffuse. The hemispherical total absorptivity and emissivity of the surfaces were assumed equal, and depended only on temperature (Siegel and Howell 1981). Even though this condition is achieved only by a limited number of real materials, it is often the most reasonable approach, for two reasons. First, the radiative properties are usually not known to high accuracy, especially their dependence on wavelength and direction. Second, in many cases of practical interest, the gray-diffuse approach is accurate enough, even in enclosures involving specular surfaces, or surfaces with both diffuse and specular components (Schornhorst and Viskanta 1968). Two additional assumptions were made: (a) the reflected energy is diffuse, and (b) the reflected energy is uniform over each surface element.

The model can easily handle 100 – 200 temperature nodes in the cell and the surrounding insulation package. The cell wall thickness, and the volume porosity of the liquid sodium return artery and evaporator wick are allowed to vary axially. This thermal model can perform both transient and steady-state calculations. The input file specifies the type of boundary condition at the side wall of the AMTEC cell, such as adiabatic, or thermally coupled to the surrounding insulation through a radiation gap. The surface emissivities and all thermophysical properties of structural materials and sodium are temperature dependent. At the temperatures of interest ( $< 1200$  K), the low pressure ( $< 1$  atm), monoatomic sodium vapor is essentially transparent to radiation. Because of the very small density and thermal capacity of sodium vapor, heat transport by convection is negligible compared to that due to radiation and conduction.

### 5.3.1 Modeling of Radiation Heat Transfer

This subsection describes the radiation heat exchange between surfaces. The special situation in which all the surfaces involved are black is dealt with first. Black surfaces are perfect absorbers, and the energy exchange process is greatly simplified because there is no reflected energy to be considered. Also, black surfaces emit in a perfectly diffuse fashion, such that the radiation intensity leaving a surface is independent of the direction of emission. This simplifies the computation of how much of this radiation will reach another surface.

The fraction of radiant energy leaving one surface and reaching another is defined as the radiation view factor, which only depends on the geometric orientation of the two surfaces with respect to each other. The geometric dependence is discussed here for black surfaces, but the results have a wider generality as they will apply for any uniform diffuse radiation leaving a surface. This geometric dependence leads to some algebraic relations between the factors. After the relations for radiation exchange between two surfaces are developed, they can be applied to any number of surfaces arranged to form an enclosure of black surfaces each at a different temperature. In following sections, the concepts developed for black surfaces are extended for systems with diffuse-gray surfaces.

#### Configuration Factors between Two Black Surfaces of Finite Areas

Consider the configuration factor for radiation emitted from an isothermal surface  $A_1$  shown in Figure 5.2 and reaching  $A_2$ . By definition,  $F_{12}$  is the fraction of radiant energy leaving  $A_1$  that arrives at  $A_2$ . The total radiant energy leaving the black surface  $A_1$  is  $\sigma T_1^4 A_1$  since  $A_1$  is isothermal at  $T_1$ . The radiant energy leaving an element  $dA_1$  that reaches  $dA_2$  is given as (Siegel and Howell 1981):

$$d^2 Q_{dA_1 \rightarrow dA_2} = \sigma T_1^4 \frac{\cos \theta_1 \cos \theta_2}{\pi R^2} dA_1 dA_2 \quad (5.1)$$

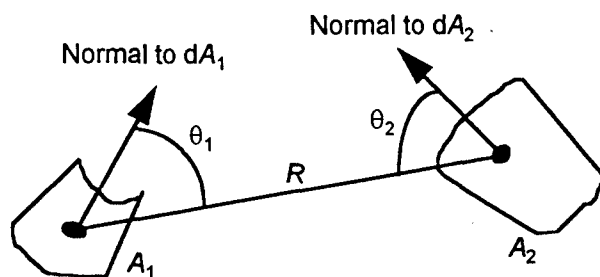


Figure 5.2. Geometry for Radiant Energy Exchange between Finite Areas.

Integrating Equation (5.1) over both  $A_1$  and  $A_2$  will give the radiant energy leaving  $A_1$  that reaches  $A_2$ . The configuration factor has then the expression:

$$F_{12} = \frac{1}{A_1} \int_{A_1} \int_{A_2} \frac{\cos\theta_1 \cos\theta_2}{\pi R^2} dA_2 dA_1 . \quad (5.2)$$

In a manner similar to the derivation of Equation (5.2), the configuration factor from  $A_2$  to  $A_1$  is found to be:

$$F_{21} = \frac{1}{A_2} \int_{A_1} \int_{A_2} \frac{\cos\theta_1 \cos\theta_2}{\pi R^2} dA_2 dA_1 . \quad (5.3)$$

The double integrals in Equations (5.2) and (5.3) are identical, resulting in the following reciprocity relation:

$$A_1 F_{12} = A_2 F_{21} . \quad (5.4)$$

Note that Equations (5.1) to (5.4) were derived based on the assumption of a diffuse and uniform intensity leaving the surfaces (black surfaces). The energy radiated from  $A_1$  that reaches  $A_2$  is then  $Q_{12} = \sigma T_1^4 A_1 F_{12}$ . Similarly, that radiated from  $A_2$  and reaching  $A_1$  is  $Q_{21} = \sigma T_2^4 A_2 F_{21}$ , and the net radiation transfer from  $A_1$  to  $A_2$  is given by  $Q_{12} - Q_{21} = \sigma(T_1^4 - T_2^4) A_1 F_{12}$ .

Because of the difficulty involved in directly computing configuration factors from the integral definition Equation (5.2) for many geometries, it is desirable to utilize shortcut methods whenever possible. Such shortcuts can be obtained by using the definition of view factors in terms of fractional intercepted radiant energy and the reciprocal relations. The interrelation between view factors is termed configuration-factor algebra (Siegel and Howell 1981, Chapter 7), and is used intensively in Appendix C to compute the view factors in the multi-tube AMTEC cells.

Additional useful relations can be derived for the case where the view factors are between surfaces that form a complete enclosure. For an enclosure of  $N$  surfaces, the total radiant energy leaving any surface inside the enclosure, for example surface  $A_p$ , must be incident on all the surfaces making up the enclosure. Thus the sum of all fractions of energy leaving one surface and reaching the surfaces of the enclosure must be equal to one; that is:

$$F_{p1} + F_{p2} + F_{p3} + \cdots + F_{pp} + \cdots + F_{pN} = \sum_{k=1}^N F_{pk} = 1 . \quad (5.5)$$

The factor  $F_{pp}$  is included because when  $A_p$  is concave (for example, if  $A_p$  were the internal surface of a cylinder), it will intercept a portion of its own emitted energy.

### 5.3.2 Radiation View Factors in Vapor-Anode, Multi-Tube, AMTEC Cells

The chief difficulties in radiant interchange problems are in the geometrical complexities and algebraic manipulations, and the multidimensional integrations that must be carried out to determine the view factors for the specific geometries. CPU intensive numerical codes, which use numerical contour integration or Monte Carlo calculation methods, could be used to calculate the radiation view factors. Another approach is to take advantage of the extensive tabulations of view factor formulas available in the literature for simple geometries (Siegel and Howell 1981, Howell 1982). The second approach was used herein to ensure a faster, more efficient running model on PC compatible machines, thus suitable for performing design and parametric analyses.

In this work, a radiation view factors database was developed for the various surface elements in the complex cavity of PX-series cells (Figure 5.1). Figure 5.3 shows the numerical mesh used to calculate the heat transfer in a cell without a thermal shield nor a conduction metal stud. The cell consists of a stainless-steel cylindrical, pressure-tight container, made up of a hot circular plate, a cold condenser plate, and a thin annular side wall. Inside the cell, a circular stainless-steel plate supports the BASE tubes and the annular casing of the evaporator standoff. The latter is connected to the wick of the condenser plate through a circular liquid-return artery. The support plate, BASE tubes, and evaporator standoff provide a physical boundary between the sodium high-pressure and low-pressure cavities.

The mesh generator discretized the BASE tubes bundle into  $N$  sections of identical height, and the coaxial cylindrical cavity above the BASE tubes into  $N_w$  identical axial sections. The evaporator standoff was discretized into  $N_e$  identical axial sections, while the wick of the evaporator was discretized into  $N_{ew} = (N - N_e)$  axial sections of equal height. The model assumes a flat evaporator surface for convenience. However, in order to match the evaporation rate in the conical evaporator, the flat evaporator area was multiplied by a factor that is equal to the effective evaporation area ratio of the two evaporators. Only one axial node was used in the hot plenum wall, since the height of the plenum was very small, typically  $< 2$  mm.

As shown in Figure 5.3, there are 2 separate enclosures for radiation heat transfer within the cell, the high and the low vapor pressure cavities. For the purpose of calculating the radiation view factors, the cell cavity was divided into several, radiatively coupled, elementary or sub-cavities (Figure 5.3): (a) the hot plenum baffle; (b) the evaporator standoff; (c) the inside of BASE tubes; (d) the BASE tubes/standoff bundle; (e) the coaxial cylindrical cavity above the BASE tubes; and (f) the annular space between the circumferential shield and the cell wall. The surfaces  $\bar{\beta}_o$ ,  $\bar{C}_o$ ,  $top$ , and  $ceil$  are fictitious boundaries through which radiative coupling between sub-cavities occurs (Figure 5.3). The radiation view factors for each of the sub-cavities were calculated using an approximate analytical approach. In the artery cylindrical sub-cavity, the  $N_b$  BASE tube tops were approximated by an equivalent thick-circular ring of identical surface area (Figure 5.1). Similarly, in the hot plenum sub-cavity, the  $N_b$  BASE tube openings were approximated by an equivalent thick-circular ring. Using these approximations, all view factors in the sub-cavities (a), (b), (c), (e) and (f) were determined analytically using closed-form algebraic relations and

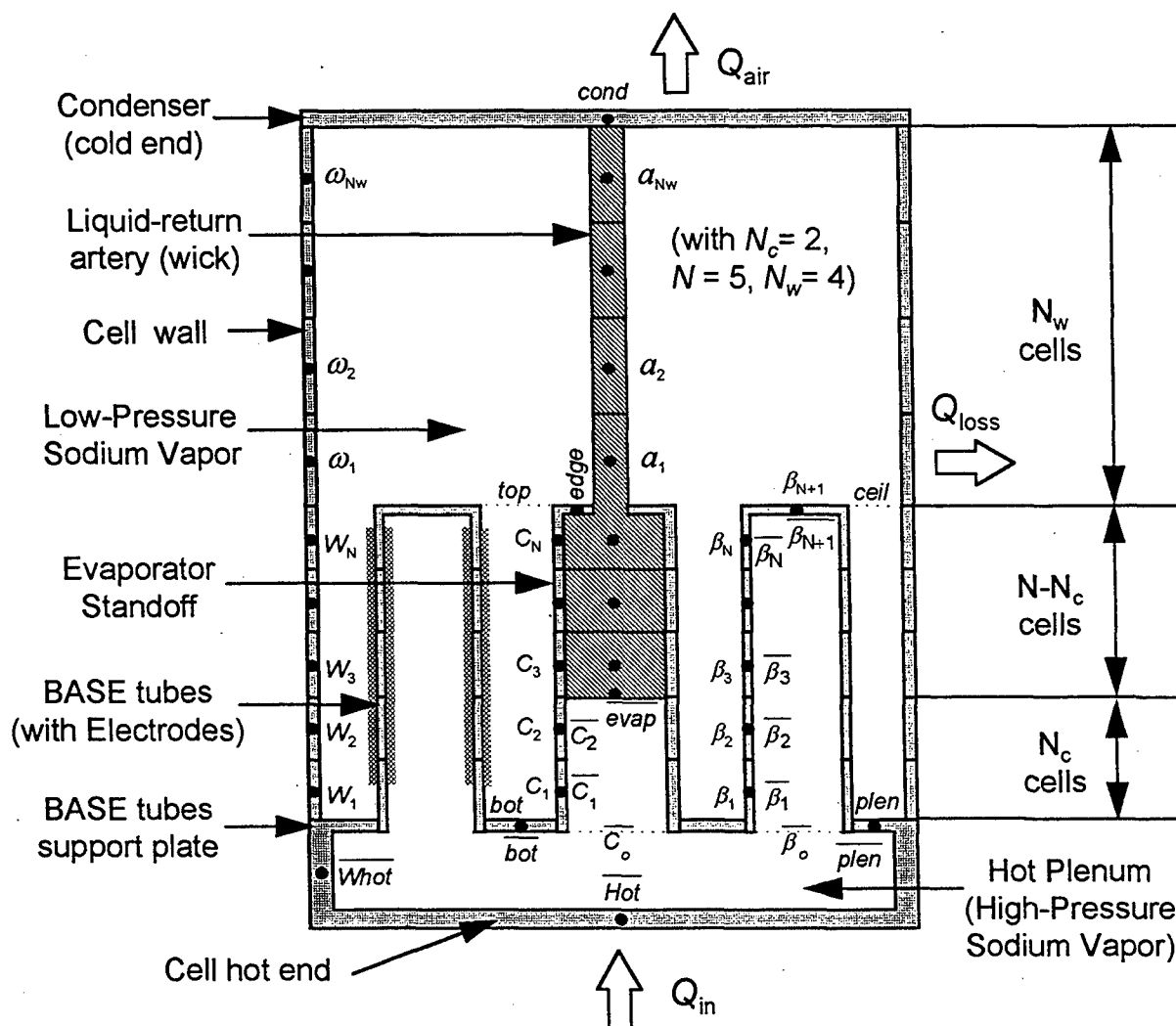


Figure 5.3. Numerical Grid Layout of Multi-Tube AMTEC Cell, without Thermal Shield nor Conduction Stud.

elementary flux algebra (Siegel and Howell 1981, Howell 1982, Appendix C). The factors for the coaxial cylindrical cavities required single numerical integration using Simpson's rule.

Because of the complex geometry of the BASE tubes/standoff bundle cavity, approximate relations of the view factors were derived, that ensured that all reciprocity ( $A_k F_{kp} = A_p F_{pk}$ ) and

enclosure relations ( $\sum_{k=1}^{N_R} F_{pk} = 1$ ) were satisfied. The reciprocity and enclosure relations were accounted for explicitly when computing the view factors in all the cell sub-cavities. The complete set of linear view factor relationships was solved using Gauss elimination. A complete description of the view factor relations developed in this work can be found in Appendix C. A few examples and the major features of the derivation, however, are given below.

Hottel's crossed-string analytical method (Siegel and Howell 1981) was used, in conjunction with the approximate cavity model of Juul (1982), to estimate the view factors between the evaporator standoff and the BASE tubes, and between the different BASE tubes, that were partially obstructed by the evaporator standoff or by another BASE tube (Figure 5.1b). Using the crossed-string method, the view factor between infinite, vertical cylinders 1 and 2 was obtained as (Figure 5.4a):

$$F_{12}^{\infty} = \frac{1}{2\pi R} \left\{ (1+R) \sin^{-1} \frac{1+R}{X} - (1-R) \sin^{-1} \frac{1-R}{X} + \sqrt{X^2 - (1+R)^2} - \sqrt{X^2 - (1-R)^2} \right\}, \quad (5.6)$$

where  $R = \frac{R_1}{R_2}$  and  $X = \frac{a}{R_2}$ .

When the cylinders have identical radii ( $R=1$ ), Equation (5.6) reduces to:

$$F_{12}^{\infty} = F_{21}^{\infty} = \frac{1}{\pi} \left\{ \sin^{-1} \frac{1}{H} + \sqrt{H^2 - 1} - H \right\}, \quad (5.7)$$

where  $H = \frac{X}{2} = \frac{a}{2R_1}$ , which is identical to that given by Siegel and Howell (1981).

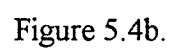
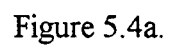
The view factor between two infinitely-long, vertical cylinders  $A_1$  and  $A_1'$  of radii  $R_1$ , partially obstructed by another vertical cylinder  $A_2$  of radius  $R_2$ , was also calculated using the crossed-string method. For small obstruction,  $\beta < \phi$  (Figure 5.4b), one obtained:

$$F_{A_1 \rightarrow A_1'} = \frac{1}{\pi} \left\{ \sin^{-1} \frac{1}{X} + \sqrt{X^2 - 1} - X \right\} + \frac{1}{2\pi} \left\{ (\sigma - \theta) - R\beta + X - \sqrt{X^2 + (H+R)^2 - (1-R)^2} \right\},$$

where  $\sigma = \tan^{-1} \frac{H+R}{X}$ ,  $\theta = \sin^{-1} \frac{1+R}{\sqrt{X^2 + (H+R)^2}}$ ,  $\omega = \tan^{-1} \frac{X}{H+R}$ ,

$$R = \frac{R_2}{R_1}, X = \frac{a}{2R_1}, H = \frac{d-R_2}{R_1} = \frac{h}{R_1}, \text{ and } \beta = \omega + \theta - \frac{\pi}{2} \quad (\beta < \phi, 0 < H < 1). \quad (5.8)$$

When  $h=R_1$ , then  $H=1$ ,  $\beta=0$ ,  $\gamma=\phi$  and  $\sigma=\theta$ . In that case, the second bracket in Equation (5.8) equals zero and the view factor reduces to that between two unobstructed vertical cylinders of identical radii, Equation (5.7). For large obstruction, ( $\beta > \phi$ ), the view factor between  $A_1$  and  $A_1'$  has the expression (Figure 5.4c):



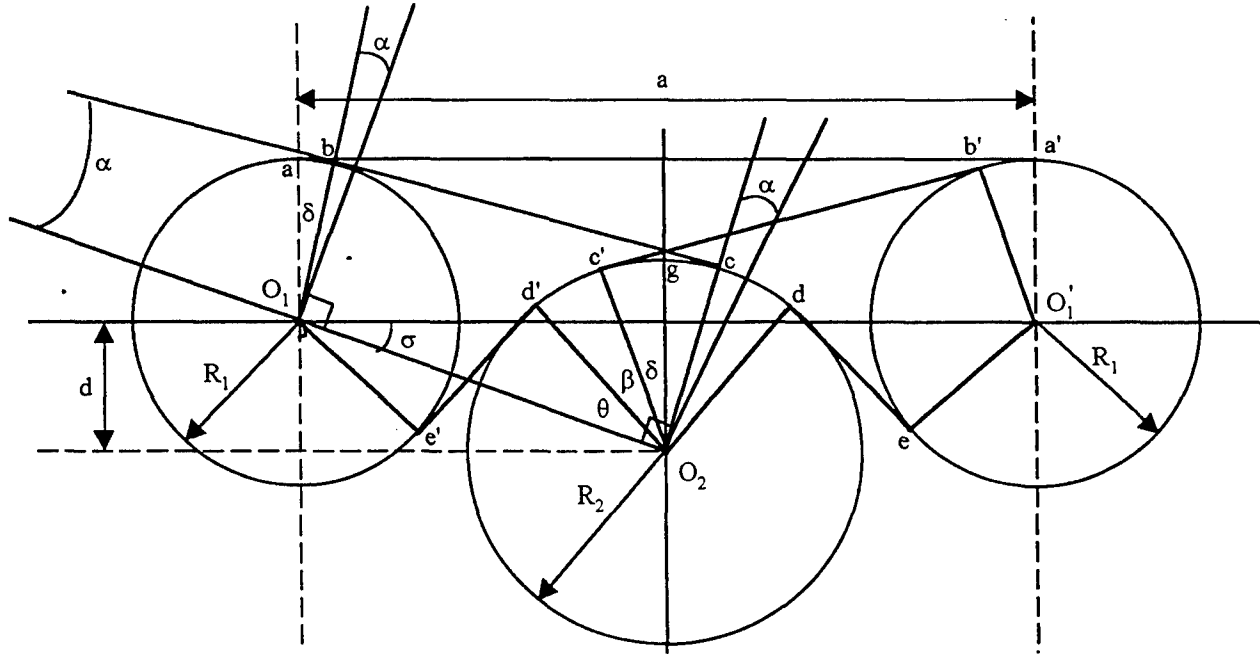


Figure 5.4c.

Figure 5.4. Calculation of View Factor Between Infinitely-Long Parallel Cylinders Partially Obstructed by Another Parallel Cylinder, Using Hottel's Crossed-String Method; (a) No Obstruction; (b) Small, Partial Obstruction ( $\beta \leq \varphi$ ,  $H \leq 1$ ); (c) Large, Partial Obstruction ( $\beta \geq \varphi$ ,  $H \geq -1$ ,  $X > R + 1$ ).

$$F_{A_1 \rightarrow A_1'} = \frac{1}{2\pi} \left\{ (1-R)(\sigma - \alpha) + \sqrt{X^2(H+R)^2 - (1-R)^2} - X \right\}, \text{ where} \quad (5.9)$$

$$\sigma = \tan^{-1} \frac{H+R}{X} \quad \text{and} \quad \alpha = \sin^{-1} \frac{R-1}{\sqrt{X^2 + (H+R)^2}} \quad (H < 0)$$

When  $d = R_2 - R_1$ , then  $H = -1$ , and consideration of the rectangular triangle of sides  $X$  and  $|R-1|$  shows that  $F_{A_1 \rightarrow A_1'}$  reduces to zero; the view between cylinders  $A_1$  and  $A_1'$  is completely obstructed by cylinder  $A_2$ . Although it is not directly apparent, both Equations (5.8) and (5.9) give identical results when  $\beta = \varphi$ , that is when the cylinder  $A_2$  is in contact with the cross-strings  $\overline{bd}$  and  $\overline{d'b'}$  between the 2 identical cylinders ( $\gamma = 0$ , and  $\delta = \varphi$ , see Figures 5.4b and 5.4c). This is because, for these view factors derived from the crossed-string method, the length of the strings used in the two equations is identical when  $\beta = \varphi$ .

Juul (1982) has developed an approximate analytical expression for the view factor between two opposed (vertical) cylinders of finite and equal length. In the arrangement where cylinder 1 is completely surrounded by  $n$  identical (vertical) cylinders of radius  $R_2$ , and whose axes lie on a



concentric circle having a radius equal to the spacing  $a$  between cylinders 1 and 2, the view factor between cylinders 1 and 2 can be approximated by (Juul 1982):

$$F_{12} \cong F_{12}^{\infty} (1 - 2F_{13'}) = F_{12}^{\infty} \times F_{10}, \quad (5.10)$$

where  $F_{12}^{\infty}$  is the view factor between infinitely-long cylinders 1 and 2, given by Equation (5.6).  $F_{10}$  is the view factor between cylinder 1 and the inner surface of an opposed and concentric cylinder having a radius  $R_o$  given by:

$$\left(\frac{R_o}{R_2}\right)^2 = 1 + \left[ \sqrt{\left(\frac{a}{R_2}\right)^2 - 1} - \frac{\pi}{2} \right] \times \left[ \sin^{-1} \frac{R_2}{a} \right]. \quad (5.11)$$

Juul (1982) has compared the results of this approximate method with that obtained by numerical integration and showed Equation (5.10) to be very accurate; the difference was less than 1% when  $R_1 \leq R_2$  and  $3 < h/R_2 < 10$ . For all cases of practical interest, the error in the view factor calculated using Equation (5.10) was less than 3%. The approximate method of Juul was extended to the case where the finite cylinders 1 and 2 are separated by a height  $c$ :

$F_{12} \cong F_{12}^{\infty} \times F_{10}$ , where  $A_o$  is the inner surface of a cylinder having a radius  $R_o$ , concentric with the cylinder 1, and at the level of cylinder 2 with a height  $h_2$ .

The present model has made extensive use of reciprocity, symmetry and fractional analysis to reduce the number of approximate factor relationships to a strict minimum and insure satisfaction of all reciprocity and enclosure relations. For example, the view factors between the bottom ring and BASE tube sections are simply obtained by symmetry:  $F_{bot \rightarrow \beta_k} = F_{top \rightarrow \beta_{N+1-k}}$ . The view factors between the first evaporator standoff section  $C_1$  and the surfaces  $W_k$ , *ceil* and *plen*, were calculated using fractional analysis, assuming that the fractions of rays emitted by  $C_1$  and reaching these other surfaces are unchanged, with or without the BASE tubes present (Figures 5.1 and 5.3). These fractions are obtained using the calculated view factors  $G$  in the annular cavity obtained when the BASE tubes were removed. The fraction of rays leaking through the open spacings between BASE tubes (Figure 5.1) was then calculated as:

$$F_{C_1 \rightarrow leak} = 1 - F_{C_1 \rightarrow top} - F_{C_1 \rightarrow bot} - \sum_{k=1}^N F_{C_1 \rightarrow \beta_k} \quad (5.12)$$

If we define:

$$G_{C_1 \rightarrow leak} = G_{C_1 \rightarrow ceil} + G_{C_1 \rightarrow plen} + \sum_{k=1}^N G_{C_1 \rightarrow W_k}, \quad (5.13)$$

then

$$\begin{aligned}
F_{C_1 \rightarrow \text{ceil}} &= \frac{G_{C_1 \rightarrow \text{ceil}}}{G_{C_1 \rightarrow \text{leak}}} \times F_{C_1 \rightarrow \text{leak}} , \\
F_{C_1 \rightarrow \text{plen}} &= \frac{G_{C_1 \rightarrow \text{plen}}}{G_{C_1 \rightarrow \text{leak}}} \times F_{C_1 \rightarrow \text{leak}} , \text{ and} \\
F_{C_1 \rightarrow W_k} &= \frac{G_{C_1 \rightarrow W_k}}{G_{C_1 \rightarrow \text{leak}}} \times F_{C_1 \rightarrow \text{leak}} , \quad k = 1 \text{ to } N .
\end{aligned} \tag{5.14}$$

Note that the use of fractional view factors insures that the enclosure relation is satisfied for  $C_1$ . The factors  $F_{C_1 \rightarrow W_k}$  can then be used to deduce all factors  $F_{C_p \rightarrow W_k}$ . By symmetry:

$$F_{C_p \rightarrow W_k} = F_{C_1 \rightarrow W_{|p-k|+1}} . \tag{5.15}$$

The calculated view factors of the cell's sub-cavities were modified to account for the radiative coupling between them, through the fictitious boundaries  $\overline{\beta_o}$ ,  $\overline{C_o}$ ,  $\overline{top}$ , and  $\overline{ceil}$ , which were eliminated. As an illustration, let us consider the simpler case of the radiative coupling between the hot baffle and evaporator standoff. Since the inside height of the hot baffle is much smaller than both its diameter and the height of the first standoff axial section  $\overline{C_1}$ , all radiation emitted by the surface  $\overline{Whot}$ , streaming through surface  $\overline{C_o}$ , will end into surface  $\overline{C_1}$  (Figure 5.3). Therefore:

$$\begin{aligned}
F_{\overline{Whot} \rightarrow \overline{C_1}} &= F_{\overline{Whot} \rightarrow \overline{C_o}} , \quad F_{\overline{Whot} \rightarrow \overline{C_k}} = 0 \quad \text{for } k > 1, \text{ and} \\
F_{\overline{Whot} \rightarrow \overline{evap}} &= 0 .
\end{aligned} \tag{5.16}$$

$F_{\overline{C_1} \rightarrow \overline{Whot}}$  is calculated by reciprocity, and since surface  $\overline{C_1}$  sees only  $\overline{Whot}$  and  $\overline{Hot}$  through  $\overline{C_o}$ , we have:  $F_{\overline{C_1} \rightarrow \overline{Hot}} = F_{\overline{C_1} \rightarrow \overline{C_o}} - F_{\overline{C_1} \rightarrow \overline{Whot}}$ . Finally, all other surfaces inside the evaporator casing see only the hot plate through  $\overline{C_o}$ , so that:

$$\begin{aligned}
F_{\overline{C_k} \rightarrow \overline{Hot}} &= F_{\overline{C_k} \rightarrow \overline{C_o}} \quad \text{for } k > 1, \text{ and} \\
F_{\overline{evap} \rightarrow \overline{Hot}} &= F_{\overline{evap} \rightarrow \overline{C_o}} .
\end{aligned} \tag{5.17}$$

All other factors between the hot baffle and evaporator standoff casing can be obtained by reciprocity, or are nul.

A similar treatment is applied to the radiative coupling between the inside surfaces of the BASE tubes and surfaces  $\overline{Whot}$  and  $\overline{Hot}$  of the high-pressure baffle. The only difference from the previous treatment is that the surface areas inside a BASE tube must be multiplied by the number

of tubes in the cell,  $N_p$ , before performing the radiative coupling treatment. In the end, all view factors involving surfaces  $\overline{C_o}$  and  $\overline{\beta_o}$  were set equal to zero.

The coupling between the tubes bundle's sub-cavity and the artery cylindrical sub-cavity above was the most challenging. Because of their complex geometry, in addition to the reciprocity and enclosure relations, it was necessary to develop other approximate relations to calculate all the radiation view factors in the cell. Again, the present model made extensive use of reciprocity, symmetry and fractional analysis to reduce the number of unknown factors to a strict minimum and insure satisfaction of all reciprocity and enclosure relations. More details on the calculation of the radiation view factors in the PX-series cell cavity can be found in Appendix C. The radiation view factors data base was checked for various baseline configurations to confirm the accuracy of the radiation flux relations; all reciprocity and enclosure relations in the cell cavities were satisfied, to ensure radiant energy balance in the cell (Appendix C).

### 5.3.3 Circumferential Radiation Heat Shield in AMTEC Cell

Some multi-tube AMTEC cell designs included a circumferential heat shield above the BASE tubes, to reduce the internal radiation losses to the cell wall (Figure 5.1). The heat shield (Figure 5.1a) was modeled as a thin cylindrical metallic shell of radius  $R_{sh}$ , placed close to the cell wall,  $(R_w - R_{sh}) \ll R_w$ . It was divided into  $N_{sh}$  identical axial sections. Because of the proximity of the shield to the cell wall, the view factors calculated in the low-pressure cavity of the cell were unchanged. The upper wall shells  $k = N_w - N_{sh} + 1$  to  $N_w$  actually became the inner cylindrical shells of the heat shield. The view factors for the annulus between the cell wall and the radiation shield were easily calculated using closed-form algebraic relations. The top and bottom rings of this annular cavity were assumed to be perfect reflectors, so as not to disturb the radiant energy exchanges within the cell enclosure. This assumption is realistic, since the bottom ring was actually closed at the weld between the thermal shield and the cell wall. Also, the top ring saw a portion of the condenser surface, which was typically highly reflective. When a Creare condenser was used, the effective reflectivity of the condenser surface was close to that of a liquid sodium film, 0.95 (Crowley and Izenson 1993).

### 5.3.4 Conduction Stud in Hot Plenum of AMTEC Cell

Numerical analyses and experimental results have shown that the performance of earlier multi-tube AMTEC cell designs was limited by their ability to supply the required heat for sodium vaporization in the evaporator (Merrill et al. 1998). To enhance the heat conduction path to the evaporator wick, new cell designs included a thick metallic stud between the cell hot plate and the evaporator standoff/BASE tubes support plate (Figure 5.1a). The addition of this stud would require modifying the view factors in the hot plenum cavity. However, the analyses conducted in this work have shown that the heat transport on the hot side of the cell was essentially by conduction to the BASE tubes/evaporator standoff support plate, with a relatively small temperature drop. Radiative transport in the hot plenum cavity was negligible, compared to the thermal conduction. This was because of the relatively large cross section areas of the stud and of

the hot plenum side wall, and since the hot plenum of the cell was very narrow. Radiation transport between the cell's hot end and the inside of the BASE tubes and the evaporator standoff were correctly accounted for by the original view factors, for the plenum cavity without a conduction stud. Therefore, no special radiation treatment was used when a conduction stud was placed in the hot plenum cavity of the cell.

### 5.3.5 Radiation Exchange between Diffuse-Gray Surfaces

For practical radiation computations, the assumption of black surfaces is quite restrictive. The black computation theory, nevertheless, serves the very important function of providing a foundation for more general exchange and enclosure theories. In this work, all structural surfaces are assumed to be gray and diffuse. The directional spectral emissivity and absorptivity of a diffuse-gray surface do not depend on the angle (diffuse) nor the wavelength (gray), but depend on the surface temperature (Siegel and Howell 1981). As a result, the hemispherical total absorptivity and emissivity of a diffuse-gray surface are equal, and depend only on the surface temperature:  $\alpha(T) = \epsilon(T) = 1 - \rho(T)$ , where  $\rho$  is the reflectivity. Even though this condition is achieved only by a limited number of real materials, the diffuse-gray approximation greatly simplifies the radiation exchange problem. This is often the most reasonable approach for two reasons. First, the radiative properties are usually not known to high accuracy, especially with regard to their dependence on wavelength and direction. Therefore, performing a refined computation would be fruitless when only crude property data are available. Second, the gray-diffuse approach is accurate enough for many cases of practical interest (but not for solar concentrators and furnaces), even in enclosures involving specular surfaces, or surfaces with both diffuse and specular components. Schornhorst and Viskanta (1968) compared experimental and numerical results for radiant exchange between several types of surfaces and found that, regardless of the presence of specular surfaces, the diffuse-surface analysis agreed best with experimental results. This is because in enclosures, the many reflections and re-reflections taking place between surfaces tend to average out the radiative and directional nonuniformities. For example, the radiation leaving (emitted plus reflected) a directionally emitting surface may be fairly diffuse, if it consists mostly of reflected energy arising from radiation incident from all directions.

Note that the individual surface areas that form an enclosure are selected on the basis of geometry and imposed thermal boundary conditions. A further consideration is the accuracy of the solution. If too few areas are used, temperature gradients will be large, and the assumption of quasi-isothermal surfaces would be invalid, causing poor accuracy; on the other hand, too many areas would require excessive computational time. Thus some engineering judgement is required in selecting both the shape of the surfaces and their number.

It is a restriction in the present analysis that, whatever thermal boundary conditions are imposed on the surfaces, each separate surface of the enclosure must be at a uniform temperature. If the imposed heating conditions are such that the temperature would vary markedly over an area, the area should be subdivided into smaller, more nearly isothermal portions. As a consequence of this

isothermal area requirement, the emitted radiant energy is uniform over each surface of the enclosure.

Because a gray surface is not a perfect absorber (its absorptivity is less than unity rather than unity as for the black surface), part of the radiant energy incident upon it is reflected. With regard to the reflected energy, two assumptions are made: (a) the reflected energy is diffuse, that is, the reflected intensity at any location on the surface is uniform for all directions; and (b) the reflected energy is uniform over each surface in the enclosure. With these assumptions reasonably met, the reflected energy for each surface has the same diffuse and uniformly distributed characteristics as the emitted energy. Hence, the reflected and emitted energies can be combined into a single energy quantity leaving the surface.

Consider an enclosure composed of  $N_R$  discrete, gray-diffuse (opaque) surfaces. A complex radiative exchange occurs inside the enclosure as radiation leaves a surface, travels to the other surfaces, is partially reflected, and is then re-reflected many times within the enclosure with partial absorption at each contact with a surface. Clearly, it would be very complicated to follow the rays as they undergo this process. Fortunately, it is not necessary to do this. An analysis can be formulated in a convenient manner by using the net-radiation method. Consider the  $k$ th surface area  $A_k$  of the enclosure (Figure 5.5). A fraction  $\alpha_k = \epsilon_k$  of the radiant energy incident upon  $A_k$  is absorbed by the surface, while the remaining is diffusively reflected. Note that the absorptivity and reflectivity of an opaque gray surface are simply expressed in terms of the hemispherical total emissivity ( $\rho_k = 1 - \alpha_k = 1 - \epsilon_k$ ), which is only a function of surface temperature. The rate of outgoing radiant energy from  $A_k$  (per unit area) is the sum of directly emitted plus reflected energy:

$$q_k^{out} = \rho_k q_k^{in} + \epsilon_k \sigma T_k^4 = (1 - \epsilon_k) q_k^{in} + \epsilon_k \sigma T_k^4 \quad (5.18)$$

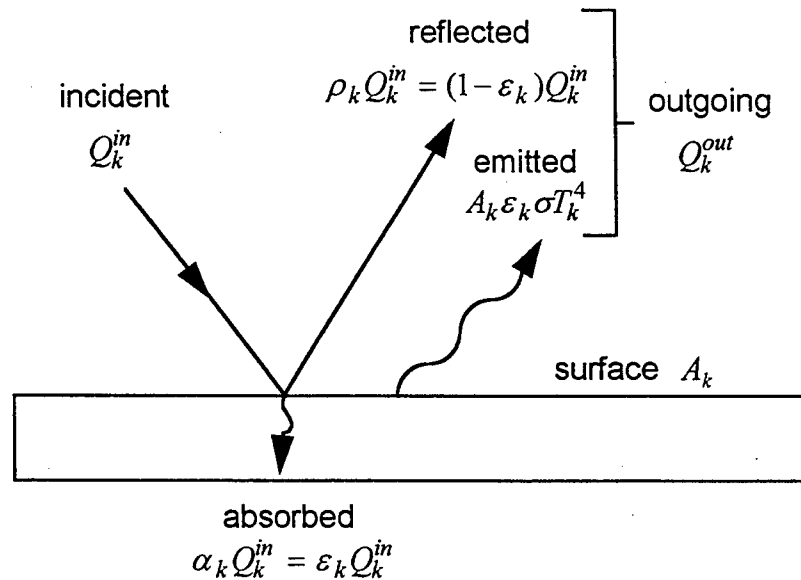


Figure 5.5. Radiant Energies Incident Upon and Leaving a Gray-Diffuse Surface.

The incident flux  $q_k^{in}$ , the rate of incoming radiant energy to the area  $A_k$ , is derived from the fractions of the radiant energies leaving the surfaces in the enclosure that arrive at the  $k$ th surface:

$$Q_k^{in} \equiv A_k q_k^{in} = \sum_{p=1}^{N_R} F_{pk} Q_p^{out} = \sum_{p=1}^{N_R} A_p F_{pk} q_p^{out} . \quad (5.19)$$

After making use of reciprocity, Equation (5.4), one obtains:

$$q_k^{in} = \sum_{p=1}^{N_R} F_{kp} q_p^{out} . \quad (5.20)$$

Substituting Equation (5.20) into Equation (5.18) yields the following radiant energy balance for the surface  $A_k$ :

$$q_k^{out} - (1 - \varepsilon_k) \sum_{p=1}^{N_R} F_{kp} q_p^{out} = \varepsilon_k \sigma T_k^4 . \quad (5.21)$$

Equations (5.21) form a  $N_R \times N_R$  linear system which relates the rates of outgoing radiant energy in the enclosure,  $\{q_k^{out}\}_{k=1, NR}$  to the surface temperatures,  $\{T_k\}_{k=1, NR}$ .

The net radiant energy loss at the surface  $A_k$  is easily obtained as:

$$Q_k^{loss} = Q_k^{out} - Q_k^{in} = A_k (q_k^{out} - q_k^{in}) . \quad (5.22)$$

This quantity must appear in the energy balance equation for the solid element with surface  $A_k$ , as a net loss term.

### 5.3.6 Radiant Energy Balance in Enclosure

The total incident radiant energy onto the surface areas of the enclosure can be obtained by summing Equations (5.19), as:

$$\sum_{k=1}^{N_R} Q_k^{in} = \sum_{p=1}^{N_R} \left( \sum_{k=1}^{N_R} F_{pk} \right) Q_p^{out} = \sum_{p=1}^{N_R} Q_p^{out} , \quad (5.23)$$

where we made use of the enclosure relation, Equation (5.5). We find that the total incident radiant energy in an enclosure is equal to the total radiant energy leaving the surfaces of the enclosure. As a result:

$$\sum_{k=1}^{N_R} Q_k^{loss} = \sum_{k=1}^{N_R} Q_k^{out} - \sum_{k=1}^{N_R} Q_k^{in} = 0. \quad (5.24)$$

We find that, in an enclosure, radiant energy transfer does not contribute any absolute heat sink or heat source to the surfaces involved, but merely redistributes the radiant energy between the surfaces. Clearly, it is necessary that all reciprocity and enclosure relations (Equations 5.4 and 5.5) be satisfied in the model, in order to insure proper conservation of radiant energy in the enclosure.

Another relation that can be used to verify that the radiative heat transfer problem in the enclosure was solved accurately can be obtained by multiplying Equation (5.18) by  $A_k$  and summing over  $k$ :

$$\sum_{k=1}^{N_R} [Q_k^{out} - (1 - \varepsilon_k) Q_k^{in}] = \sum_{k=1}^{N_R} \varepsilon_k Q_k^{in} = \sum_{k=1}^{N_R} A_k \varepsilon_k \sigma T_k^4. \quad (5.25)$$

Equation (5.25) simply states the fact that the total radiant energy emitted in the enclosure must be equal to the total energy absorbed by the surfaces.

### 5.3.7 Energy Balance for Solid Elements of the AMTEC Cell

The energy balance and associated boundary conditions were discretized on a staggered grid using the well-known control-volume approach proposed by Patankar (1980). The solution obtained using this approach satisfies global conservation, even on a non-uniform grid. The multi-tube AMTEC cell was discretized into  $N_S$  ( $N_S = 4N + 2N_w - N_c + 8$ ) solid elements (Figure 5.3). There were  $N+N_w+1$  wall sections,  $N+1$  BASE tube elements,  $N$  evaporator tube sections,  $N_w+N-N_c$  artery and evaporator wick sections, one each for the hot end plate, condenser, standoff annular edge, and the evaporator surface, and 2 ring elements for the support plate.

Most solid elements  $k$  exchanged radiant energy through their front area  $A_{fk}$ , only ( $fk=1$  to  $N_S$ ). Some elements  $k$  exchanged radiant energy in both the high-pressure, hot plenum cavity, and the low-pressure enclosure above the BASE tubes, through both their front face,  $A_{fk}$ , and back face,  $A_{bk}$  ( $bk=N_S+1$  to  $N_R$ ). These elements were the BASE tubes support plate nodes, *bot* and *plen*, the BASE tubes nodes,  $\beta_1$  to  $\beta_{N+1}$ , and the evaporator standoff nodes,  $C_1$  to  $C_{N_c}$  (Figure 5.3). There were a total of  $N_R$  ( $N_R = N_S + 2N_c + 3$ ) surface elements, which exchanged radiant energy within the cell cavities.  $N_R$  is equal to the number of solid elements,  $N_S$ , minus the number of elements that did not communicate with the vapor space, and therefore, did not exchange heat by radiation ( $N-N_c$  evaporator wick nodes), plus the number of solid elements which also have a back face in contact with sodium vapor ( $N+1$  BASE tube elements,  $N_c$  evaporator standoff sections, and 2 ring elements for the support plate). The energy balance for an element  $k$  was written as:

$$\sum_{p=1}^{N_s} \Lambda_{kp} T_p - S_k = -\varphi_k Q_{fk}^{loss} - \beta_k Q_{bk}^{loss} \quad (5.26)$$

In Equation (5.26),  $\varphi_k = 1$ , when the element  $k$  possesses a radiating front face, and  $\varphi_k = 0$  otherwise. Also,  $\beta_k = 1$ , when the element  $k$  possesses a radiative back face, and  $\beta_k = 0$  otherwise.

The terms on the left hand side of Equation (5.26), arose from the well-known control-volume discretization method (Patankar 1980), and include heat storage enthalpies, heat conduction between node  $k$  and adjacent elements, convection due to liquid sodium flow in the wicks of the artery and the evaporator, and source/sink terms due to condensation and evaporation of sodium at the condenser and evaporator nodes, respectively. These terms also include the fraction of heat converted to electrical energy in the BASE tube nodes, and heat input and losses at the outer boundaries of the cell (hot end, side wall, and condenser). Since the Peclet number of the liquid sodium flow was small ( $< 0.08$ ), the conductive mode of heat transfer dominated the convective one in the liquid-return wick; therefore, a centered scheme was used for the discretization of the convection heat fluxes (Patankar 1980).

The electric current density along the BASE TiN electrodes and the total electrical current, calculated by the cell electrical model (see Chapter 4), were used in the input to the present radiation/conduction model. All radiant heat exchange terms were collected on the right hand side of Equation (5.26). When the temperature of the hot end or of the condenser was specified, Equation (5.26) for that particular node was replaced with:

$$T_k = T_{specified} \quad (5.27)$$

After the temperatures of all nodes in the cell were obtained, Equation (5.26) was used to evaluate the heat input at the hot end and the heat removed at the cold end of the cell (condenser). In Equation (5.26), the matrix coefficients,  $\Lambda_{kp}$ , the source terms,  $S_k$ , and the net radiant energy loss terms,  $Q^{loss}$ , were all functions of temperature, through the temperature-dependent properties (thermal conductivities, density of sodium liquid, specific heat capacities and latent heat of vaporization). The same is true of the net radiant energy loss terms  $Q^{loss}$ , since the radiative emissivities are also functions of temperature. Because these thermal properties vary only slowly with temperature, they were treated explicitly in the present model.

In the AMTEC cell, the mass flow rate of sodium is proportional to the cell electrical current. However, since the heat of vaporization/condensation constitutes a large fraction of the total heat input to the cell, it significantly affects the evaporator and condenser temperatures. Therefore, the partial derivatives of the cell current in terms of the evaporator, BASE tubes and condenser temperatures were obtained from the cell electrical model (Chapter 4). These derivatives were used to linearize the dependence of the sodium flow rate on temperature in the energy balance equations of the condenser and evaporator nodes. Results from numerical experiments performed in this work showed that this linearization was a key to obtaining an efficient, fast-converging solution algorithm.



To solve the energy balance, Equation (5.26), for the solid node temperatures, the net radiant energy loss terms,  $Q^{loss}$ , were expressed as functions of temperatures. First, the net radiant energy losses were expressed in terms of the rates of outgoing radiant energy, by combining Equations (5.20) and (5.22), as:

$$q_k^{loss} = q_k^{out} - \sum_{p=1}^{N_R} F_{kp} q_p^{out}, \text{ for } k = 1 \text{ to } N_R, \quad (5.28a)$$

or in matrix notation:

$$[q^{loss}] = \{\mathfrak{I} - F\}[q^{out}]. \quad (5.28b)$$

The radiant energy balance for surface  $A_k$ , Equation (5.21), reproduced here for convenience:

$$q_k^{out} - (1 - \varepsilon_k) \sum_{p=1}^{N_R} F_{kp} q_p^{out} = \varepsilon_k \sigma T_k^4, \quad (5.21)$$

represents an  $N_R \times N_R$  linear system of equations, which relates the rates of outgoing radiant energy in the cell enclosure to the surface temperatures, as:

$$\begin{aligned} \{R\}[q^{out}] &= [\varepsilon_k \sigma T_k^4], \text{ where} \\ R_{kp} &= \delta_{kp} - (1 - \varepsilon_k) F_{kp}, \quad k, p = 1 \text{ to } N_R. \end{aligned} \quad (5.29)$$

A solution routine was developed and tested to inverse the radiation matrix  $\{R\}$  using the Gauss-Jordan elimination algorithm. It was found that computing the inverse matrix once before the internal iterations (necessary to resolve the couplings in the radiation/conduction model), rather than solving the linearized system at every iteration by a faster Gauss elimination algorithm, was more efficient in terms of CPU time. Once the radiation matrix was inverted, the net radiant energy loss terms were expressed explicitly in terms of the node temperatures, as:

$$\begin{aligned} [q^{loss}] &= \{\mathfrak{I} - F\}[q^{out}] = \{\mathfrak{I} - F\}\{R\}^{-1}[\varepsilon_k \sigma T_k^4], \text{ or} \\ [Q^{loss}] &= \{M\}[\sigma T_k^4], \text{ where} \\ M_{kp} &= A_k \varepsilon_p \left( R_{kp}^{-1} - \sum_{m=1}^{N_R} F_{km} R_{mp}^{-1} \right), \quad k, p = 1 \text{ to } N_R. \end{aligned} \quad (5.30)$$

The energy balance for the solid element  $k$  in the cell could then be written as:

$$\sum_{p=1}^{N_S} \Lambda_{kp} T_p - S_k + \sigma \sum_{m=1}^{N_R} (\varphi_k M_{fk,m} + \beta_k M_{bk,m}) T_m^4 = 0, \quad k=1 \text{ to } N_S. \quad (5.31)$$

The temperatures of the back faces of the solid nodes (exchanging radiant energy through both their front and back faces) were taken equal to that of the front faces of the elements:

$$T_{bk} = T_{fk}, \quad bk = N_S + 1 \text{ to } N_R. \quad (5.32)$$

The matrices  $\{A\}$  and  $\{M\}$ , and source term  $[S]$  in Equation (5.31) were evaluated explicitly using the best estimate of the temperatures  $[T^*]$  in the cell, at the time of the computation (they depend on the values of the temperature-dependent, thermophysical and radiative properties). One seeks a temperature correction vector  $[T']$ , such that the vector  $[T] = [T^*] + [T']$  satisfies the energy balance Equations (5.31) – (5.32). To resolve the strong nonlinearity of radiant energy fluxes, the fourth power of the temperature was linearized using the first two terms of the Taylor series, as:

$$T_m^4 = (T_m^* + T_m')^4 \cong (T_m^*)^4 + 4(T_m^*)^3 T_m' = (T_m^*)^3 [T_m^* + 4T_m'] . \quad (5.33)$$

The linearized energy balance Equation (5.31) had the final form:

$$\sum_{p=1}^{N_S} \Lambda_{kp}^* T_p' + 4\sigma \sum_{m=1}^{N_R} (\varphi_k M_{fk,m}^* + \beta_k M_{bk,m}^*) (T_m^*)^3 T_m' = \hat{S}_k, \quad \text{where} \quad (5.34)$$

$$\hat{S}_k = S_k^* - \sum_{p=1}^{N_S} \Lambda_{kp}^* T_p^* - \varphi_k (Q_{fk}^{loss})^* - \beta_k (Q_{bk}^{loss})^*, \quad k = 1 \text{ to } N_S .$$

Since all temperatures were assumed uniform initially, the equations for the back face temperatures were easily linearized as:

$$T_{bk}' = T_{fk}', \quad bk = N_S + 1 \text{ to } N_R. \quad (5.35)$$

When the temperature of either the hot end or of the condenser was specified, Equation (5.34) for that particular node was replaced with the linearized form of Equation (5.27):

$$T_k' = T_{specified} - T_k^*. \quad (5.36)$$

The linearized energy balance Equations (5.34) – (5.36) were solved for the temperature corrections  $[T']$ , using Gauss elimination method with row normalization and partial pivoting. Then the temperatures in the cell were corrected as:

$$T_k^* = T_k^* + T_k', \quad \text{for } k = 1 \text{ to } N_R. \quad (5.37)$$

After the temperatures in the cell cavity were corrected, an energy balance for the cell was performed again. The solution was iterated until temperatures satisfied the convergence criterion (when the magnitude of the temperature correction vector  $< 0.2$  K) and the cell energy balance

was satisfied (within  $< 0.1\%$ ). In practice, only 2 to 3 iterations were necessary to resolve the strong non-linearity of the radiant energy fluxes.

## 5.4 METHOD OF SOLUTION IN APEAM

The three major building blocks in the AMTEC Performance and Evaluation Analysis Model (APEAM) were described in Chapters 3, 4 and previous Section 5.3: (a) the *sodium vapor pressure loss model*, which calculates the sodium vapor pressure at the interface between the cathode electrode and the BASE (Chapter 3); (b) the *cell electrochemical and electric model*, which calculates the effective potential developed across the BASE due to the isothermal expansion of sodium ions, determines the resistances of the BASE, electrodes, current collectors and conductor leads to the external load, and calculates the cell's electrical potentials, electrode current density, and the cell's total electric current (Chapter 4); and (c) the *radiation/conduction heat transfer model*, which accounts for all heat exchanges between the different components of the cell and calculates the temperatures throughout the cell (Chapter 5, Section 5.3). Some of the major characteristics of these submodels are summarized below. The efficient iterative solution procedure developed in this work and used in APEAM, which ensured good couplings between the different submodels, is described in the following section.

### 5.4.1 Sodium Vapor Pressure Loss Model

At an evaporator temperature above 900 K, the vapor pressure losses on the anode side of a PX-type cell are negligible, compared to the sodium vapor pressure ( $> 5$  kPa). By contrast, the sodium vapor pressure on the cathode side is 2 to 3 orders of magnitude lower than on the anode side ( $< 100$  Pa), at a typical condenser temperature below 650 K. The actual pressure of sodium vapor at the interface between the BASE and the cathode electrode depends on the Na saturation pressure at the condenser temperature,  $T_{cond}$ , and the pressure losses due to sodium vapor flow between the BASE and the condenser. The pressure losses due to sodium vapor flow through the cathode porous electrode; along the BASE tubes (with axial mass addition and vapor compressible effects); due to the change in flow area at the top of the BASE tubes; in the region above the BASE tubes (annular space with centerline artery); and due to condensation at the cold end of the cell (Figure 2.2a), are all accounted for in the model. The vapor diffusion coefficients in the free-molecular flow regime are calculated using the Knudsen and Dushman formulas, while those for the continuum regime are obtained from an analytical solution (when available), or by using the equivalent hydraulic diameter approximation. The Dusty-Gas-Model (DGM) is used to determine the flow diffusion coefficients for the different vapor flow regimes: free-molecule, transition, and continuum. All necessary temperatures in the cell are calculated by the radiation/conduction heat transfer model. The sodium vapor flow rate, which is proportional to the cell electric current, is obtained from the cell electrical model.

### 5.4.2 Cell Electrochemical and Electric Model

The cell electric model is comprised of: (a) an *electrochemical model*, which calculates the effective potential developed across the BASE due to the isothermal expansion of sodium ions;

(b) a *resistance model*, which determines the electric resistances of the BASE, electrodes, current collectors, bus wires and the conductor leads to the external load; and (c) an *electrical circuit model*, which calculates the electrical potentials, electrode current density, and the cell total electrical current. The one-dimensional electrochemical model accounts for the axial variation of the current density along the BASE tube. The concentration and charge-exchange polarization losses are calculated using the Butler-Volmer Equation (2.8). The cell electric model accounts for the effects on the current density of non-uniform axial temperature and vapor pressure profiles along the BASE tubes. It also accounts for radial and axial electrical losses in the current collector network. The electric model incorporates various current collector configurations, such as helical wire, circumferential wires, and metallic sponge or wire-screened mesh held in place with circumferential wires in combination with an axial bus collector. The sodium vapor pressure on the cathode side of the BASE is obtained from the vapor pressure loss model.

#### 5.4.3 Radiation/Conduction Heat Transfer Model

The cell thermal model calculates internal parasitic heat losses and temperatures throughout the AMTEC cell. The model discretizes the cell components into many elements and accounts for conduction, radiation, convection and phase change heat transfers between them (Figure 5.1a). All surfaces that exchange radiant energy in the interior of the cell are assumed gray and diffuse. The radiation/conduction model can easily handle between 100 and 200 temperature nodes in the cell and the surrounding insulation package. The cell wall thickness, and the volume porosities of the liquid-return artery and the evaporator wick, are allowed to vary axially. The model can handle both transient and steady-state calculations. The input file allows the user to specify the type of boundary conditions at the hot and cold end of the cell, and at the side wall of the cell, such as adiabatic, or thermally coupled to the surrounding insulation through a radiation gap. The radiative emissivities and thermophysical properties of all structure materials, BASE tubes and sodium working fluid are calculated as functions of temperature. The heats of vaporization and condensation in the cell, and the sensible heats of the liquid sodium flowing in the artery and the evaporator wick, are calculated based on the cell current given by the electric model.

#### 5.4.4 Method of Solution

An efficient iterative solution procedure was developed to solve the governing and constituent equations. The major couplings between the different physical processes and submodels in the PX-series cells are summarized in Figure 5.6.

The solution procedure was performed in the following sequential order from (a) to (m):

- (a) calculate all geometric parameters and radiation view factors.
- (b) initialize cell electrical current and all node temperatures in the cell (assumed uniform).
- (c) update thermophysical and radiation properties in the cell.
- (d) inverse the matrix for thermal radiation exchange using Gauss-Jordan elimination.
- (e) perform energy balance for every element and linearize the net radiant energy losses in terms of temperature corrections using the inverse radiation matrix obtained in step (d).

The matrices coefficients and source terms were evaluated explicitly using the best estimate of the temperatures  $[T^*]$  in the cell, at the time of the computation (they depended on thermophysical and radiative properties, which are function of temperatures). One seeks a temperature correction vector  $[T']$ , such that the vector  $[T] = [T^*] + [T']$  satisfies the energy balance equations. To resolve the strong nonlinearity of the radiant energy fluxes with temperatures, the fourth power of the temperature was linearized using the first two terms of the Taylor series. The linearized energy balance equations were solved for the temperature corrections  $[T']$ , using Gauss elimination with row normalization and partial pivoting. Then the temperatures in the cell were corrected.

- (f) iterate to (e) until temperatures converged (the temperature correction vector goes to zero). In practice, only 2 to 3 iterations were necessary to resolve the strong non-linearity of the radiant energy fluxes. Note that (d) and (e) were the most CPU intensive steps of the algorithm.
- (g) calculate sodium vapor pressure losses and determine sodium vapor pressures at the BASE membrane/electrodes interfaces, using the vapor pressure drop model [17].
- (h) obtain cell open-circuit voltages and concentration/polarization losses from the electrochemical model.
- (i) calculate all electrical resistivities and resistances in the cell.
- (j) calculate the electrical current in the cell using Gauss elimination.
- (k) iterate to step (g) until the electrical current converges. Only 2 to 7 iterations were needed in practice (steps (g) to (j) were not very CPU intensive).
- (l) calculate partial derivatives of current in terms of evaporator, BASE tubes and condenser temperatures. These derivatives were used in step (e) of the algorithm, to assess the effect of temperatures on cell current. This linearization was the key to an efficient, fast-converging solution algorithm.
- (m) Finally, iterate to step (c) until both cell current and temperatures converge. In practice, less than 6 iterations were necessary to insure that the temperatures converged to within 0.1 K.

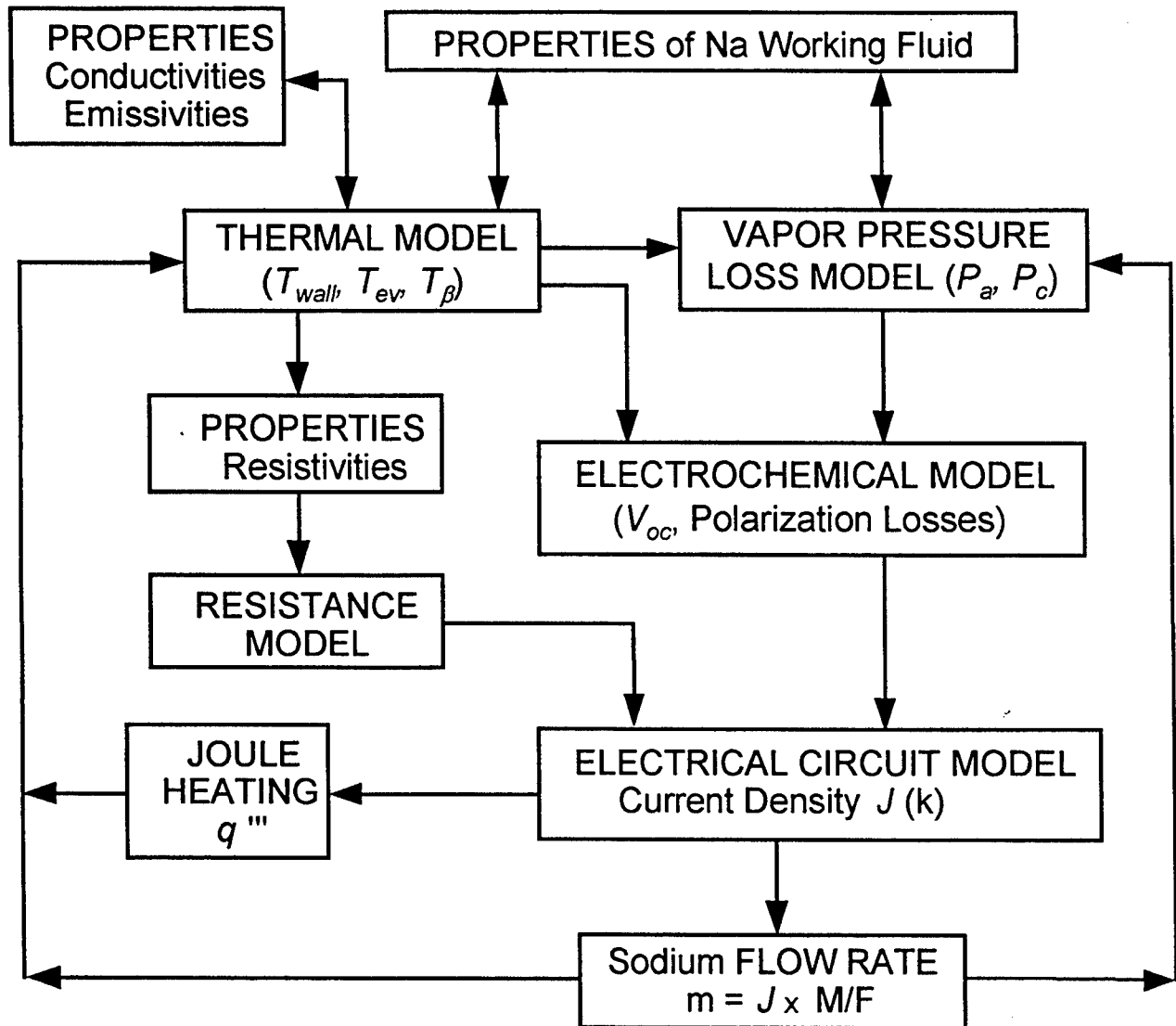


Figure 5.6. Schematic of APEAM Model's Architecture.

## 5.5 PREDICTION OF THERMAL AND PERFORMANCE DATA OF PX-4C, PX-5A AND PX-3A CELLS

The present radiation/conduction thermal model was coupled to the vapor pressure loss model (see Chapter 3) and electrochemical and electrical circuit models (see Chapter 4) of the PX-series cell, using the iterative solution procedure described above in Section 5.4, to resolve the strong couplings between various physical processes in the cell, and to construct an integrated cell model. The fully-integrated cell model (APEAM) was used to simulate the experimental setup of PX-series AMTEC cells at AFRL. The model results were compared with experimental measurements of PX-4C, PX-5A and PX-3A cells. In the experiments, a boron nitride block,

which held a small electrical heater, was fitted to the cell's hot plate. The heater was radiatively coupled to the hot plate. Heat was removed from the condenser plate using an air calorimeter. The air inlet and outlet temperatures and flow rate were measured in the tests. The PX-cell tests were performed in vacuum at  $5 \times 10^{-6}$  torr (0.7 mPa) (Merrill et al. 1997). The radiation/conduction thermal model in APEAM was modified to account for axial and radial conduction in the Min-K insulation surrounding the cell in the vacuum tests. The cell wall was thermally coupled to the surrounding Min-K through a radiation gap, and heat was dissipated at the insulation surface by radiation to the vacuum chamber. The test data were obtained at fixed hot and cold end temperatures, by controlling the heater electrical power and air mass flow rate in the experiment. The AMTEC cells used 25.4 mm-long TiN electrodes, covered with molybdenum current collectors. The temperature-independent exchange current and the contact resistance between electrodes and BASE were taken equal to  $120 \text{ A.K}^{1/2}/\text{Pa.m}^2$  and  $0.08 \text{ } \Omega.\text{cm}^2$ , respectively, in the model. In the experiments, the external load resistance was varied in steps, and the cell was allowed to reach equilibrium between steps, before recording the performance data. More details on the experimental setup and test conduct can be found in Chapter 8.

Calculations were performed with  $N_c = 4$ ,  $N = 10$ ,  $N_w = 12$ , and  $N_{sh} = 11$ . The resulting mesh had 79 temperature nodes and 100 surfaces exchanging radiant energy within the cell cavity. An additional 48 temperature nodes were used in the surrounding insulation in the test. Each calculation took about 60 s on a 486/33 MHz Personal Computer, and less than 10 s on a Pentium/200 MHz PC. About a fourth of this time was used to calculate the view factors in the cell.

The calculated heat removal at the condenser end, temperatures of the hot end, BASE tubes cold end, and condenser, as well as the cell electrical power and voltage, were in good agreement with experimental data (see Chapter 11, Sections 11.7 – 11.10). Such good agreement gave confidence in the soundness of the modeling approach and the accuracy of the radiation/conduction model. In the following sections, the predicted heat transfer and temperatures in PX-4C, PX-5A and PX-3A, near the cell's peak conversion efficiency, are presented.

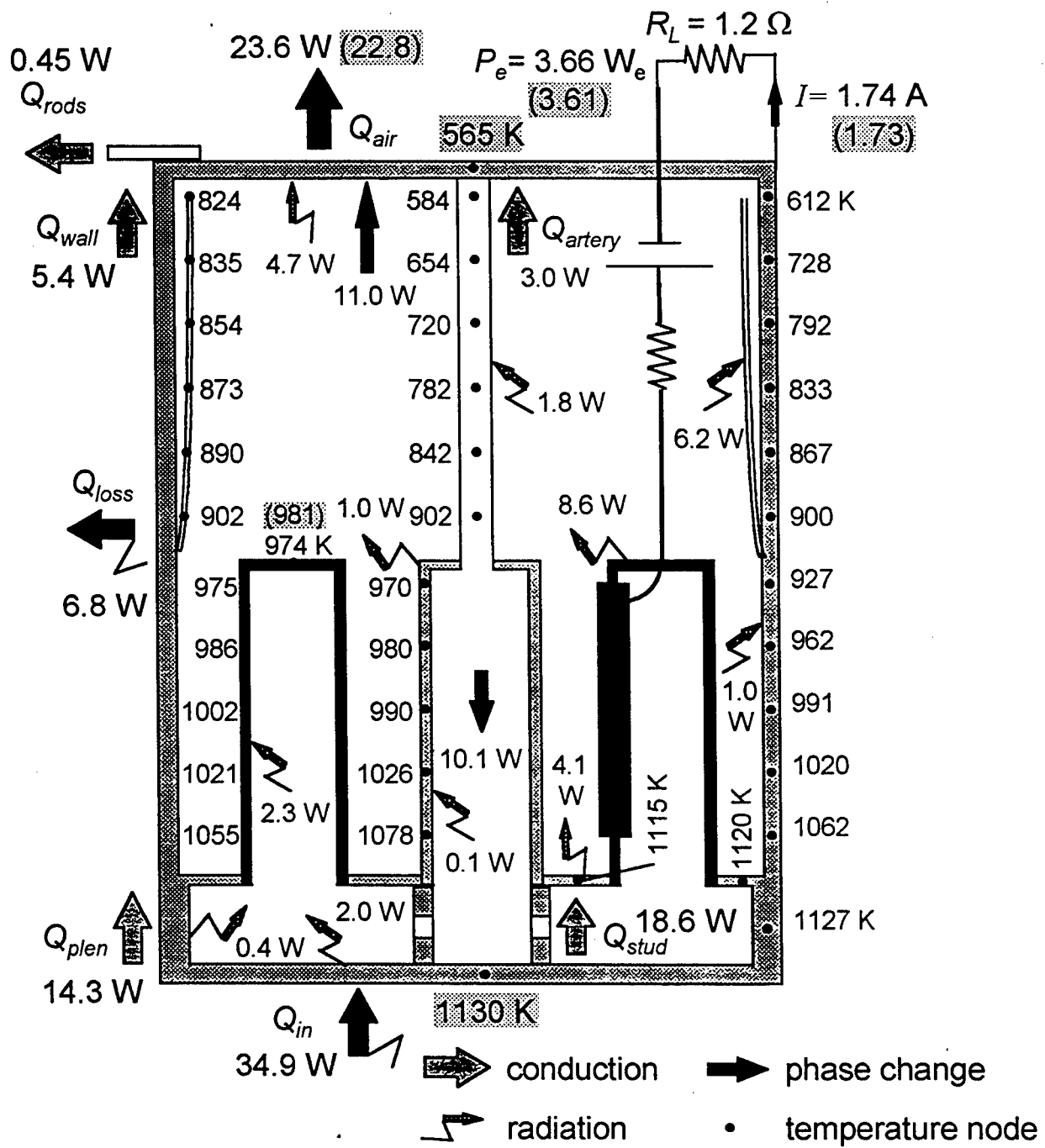


Figure 5.7. Predicted Heat Transfer and Temperatures in PX-4C AMTEC Cell, at the Peak Conversion Efficiency.



### 5.5.1 Heat Transfer and Temperatures in PX-4C Cell

The PX-4C cell was 38 mm in diameter, and made entirely of stainless steel. It had six 40 mm-long BASE tubes, that were connected electrically in series, a conical evaporator, a circumferential shield above the BASE tubes, a conduction stud, 100 mm<sup>2</sup> in cross section area, and four 2.5 mm-thick stainless steel rings around the evaporator standoff. Experimental data were obtained at fixed hot and cold end temperatures of 1130 K and 565 K, respectively. The effective radiative emissivity of the stainless steel screen wick covering the condenser surface was taken equal to 0.15 in the model.

Figure 5.7 shows the calculated heat transport and the predicted thermal energy exchange in the PX-4C cell. The predicted structure temperatures at some of the nodes are also shown in this figure. The heat input to the cell, 34.9 W, was essentially transported by conduction to the BASE tubes/evaporator standoff support plate. The conduction stud transported 18.6 W (about 53% of  $Q_{in}$ ), and the plenum wall conducted 14.3 W (about 41% of  $Q_{in}$ ) to the support plate. Only 2.0 W were radiated out from the hot end (6% of  $Q_{in}$ ). About 54% of the heat transported through the conduction stud was used to evaporate the sodium liquid in the evaporator (10.1 W). The temperature of the support plate was only 15 K lower than the cell hot end temperature, due to the thick metal stud and plenum wall. In the high sodium pressure cavity, the hot end of the cell and the hot plenum wall lost 2.0 W and 0.4 W by radiation, respectively. Most of this radiant energy was absorbed inside the 6 BASE tubes (2.3 W), and 0.1 W was absorbed inside the evaporator standoff.

A total of 24 W was removed at the cold end of the cell. Most of this energy was removed by the air calorimeter, while a small fraction (0.45 W) was lost by conduction through the alumina rods supporting the cell cold plate. The total heat removed at the cold end was comprised of: (a) the latent heat of condensation of sodium vapor (11.0 W); (b) heat conduction up the side wall of the cell (5.4 W); (c) parasitic radiation losses to the condenser surface (4.7 W); and (d) heat conduction up the liquid-Na return artery (3.0 W).

In the low sodium pressure cavity, the hot support plate lost 4.1 W by radiation, and the 7 BASE tubes radiated 8.6 W to the cooler surfaces of the cell. The cold end of the BASE tubes was 140 K cooler than the support plate. A temperature drop of about 75 K occurred along the  $\alpha$ -alumina insulator/braze section of the BASE tubes. The temperature gradient along the electrodes was much smaller than along the insulator, due to the large conductance of the 40-mesh Mo current collectors. The axial temperature profiles along the evaporator standoff, the side wall, and the BASE tubes were similar, hence, little heat was exchanged by radiation between these components. The temperature of the stainless steel (SS) radiation shield varied between 824 K and 902 K, while the cell wall temperature near the condenser was 565 K. As a result, the radiation shield significantly reduced the parasitic heat losses to the cell wall. PX-4C delivered 3.66 We at a predicted peak conversion efficiency of 10.5%. The predicted heat losses through the cell wall were 6.8 W, or about 20% of the heat input to the cell (Figure 5.7).

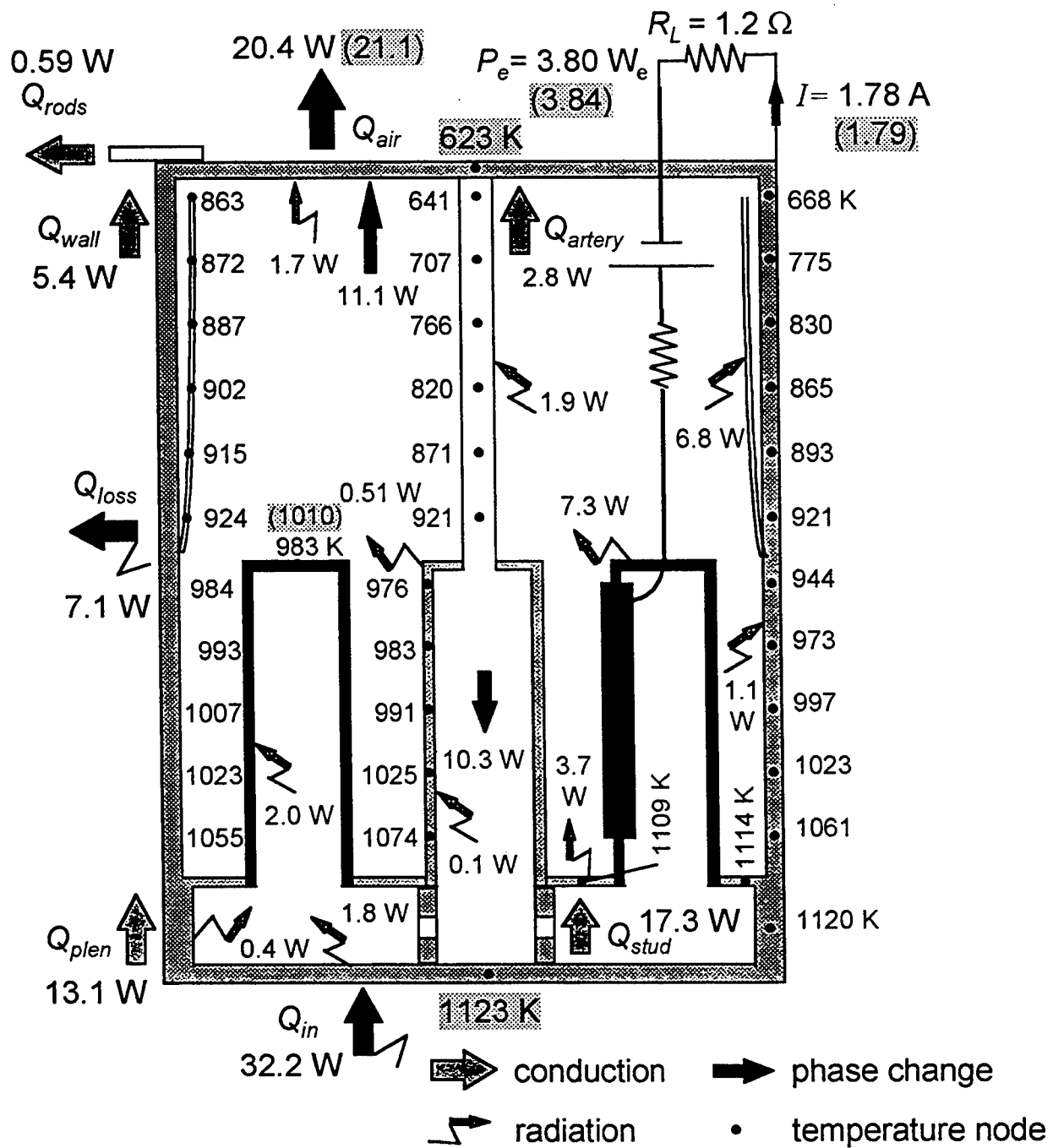


Figure 5.8. Predicted Heat Transfer and Temperatures in PX-5A AMTEC Cell, at the Peak Conversion Efficiency.

### 5.5.2 Heat Transfer and Temperatures in PX-5A Cell

The PX-5A cell was identical to PX-4C, except that the mesh pad condenser was replaced with a Creare condenser (Crowley and Izenzon 1993, also Chapter 2, Section 2.3), to ensure the formation of a continuous film of liquid sodium on its surface; hence reducing the radiative heat losses to the condenser. The effective radiative emissivity of the CREARE condenser surface was taken equal to 0.05 in the model. Results are presented in Figure 5.8. The substitution of the stainless steel screen condenser with a CREARE type condenser, and increasing the condenser temperature (from 565 K to 623 K), caused a significant (3.0 W) reduction in parasitic radiation losses to the condenser (4.7 W versus 1.7 W). The BASE tubes only lost 7.3 W by radiation to the cooler surfaces of the low pressure cavity, and the cold end temperature of the BASE tubes increased by 9 K. The hot side temperature of PX-5A was also 7 K lower than that in PX-4C. The cell electrical power output increased by 0.14 We, and the peak conversion efficiency increased by 1.3 points (from 10.5% to 11.8%). The energy reflected by the CREARE condenser fell onto the surfaces of the radiation shield, the artery, and the surfaces of the BASE tubes and of the evaporator standoff. As a result, the radiation shield and the artery in PX-5A received an additional 0.6 W and 0.1 W, respectively, while the outer surfaces of the BASE tubes and the evaporator standoff lost 1.3 W and 0.5 W less by radiation, respectively.

### 5.5.3 Heat Transfer and Temperatures in PX-3A Cell

The PX-3A cell was smaller in size (29 mm in diameter) than PX-4C and PX-5A, and used five, shorter (32 mm-long) BASE tubes. It used a CREARE condenser, a conical evaporator, a SS circumferential shield, a conduction stud that was 38 mm<sup>2</sup> in cross section area, and five 1.1 mm-thick nickel (Ni) rings around the evaporator standoff. These rings had the same conductance as those in the PX-4C and PX-5A. The use of Ni instead of SS made it possible to reduce the thickness of the evaporator standoff rings, and to reduce the outer diameter of the PX-3A cell. Results are presented in Figure 5.9 for the case of hot and cold end temperatures of 1123 K and 623 K, respectively.

The radiation view factors between the BASE tubes bundle and the cooler surfaces in the low-pressure cavity were smaller than for PX-4C and PX-5A, which reduced the parasitic heat losses in the cell. As shown in Figure 5.9, the 5 BASE tubes in PX-3A only lost 3.7 W by radiation in the low pressure cavity. Also, the view factors between the BASE tubes support plate and the cooler surfaces of the low-pressure cavity decreased. As a result, the support plate only lost 0.5 W by radiation, 3.2 W less than in PX-5A. The heat losses through the side wall decreased by 1.4 W. The decrease in the cell wall cross section area also decreased the heat conduction up the side wall from 5.4 W to 3.8 W (Figures 5.8 and 5.9), and only 0.84 W were lost by radiation to the condenser surface.

The reduction in cell parasitic heat losses increased the temperatures of the BASE tubes and of the evaporator standoff. The cold end temperature of the BASE tubes increased by 40 K, to 1022 K, and the BASE tubes' braze temperature increased by 20 K. Because the  $\alpha$ -alumina insulator



pressure cavity of the PX-3A cell, the hot end lost only 1.1 W by radiation to the inside of the BASE tubes. The reduction in the radiant energy transfer within the cell was due to the decrease in the number of BASE tubes, and to the higher temperature of the BASE tubes. Owing to the lower parasitic heat losses in PX-3A, the predicted cell peak conversion efficiency increased by 1.2 points, to 13.0%. The reduction of the number of BASE tubes, by one (from 6 to 5), decreased the cell electrical power output by 0.42 We. However, the average electrodes power density in PX-3A ( $0.111 \text{ We} / \text{cm}^2$ ) was 7% higher than that in PX-5A. This is because the BASE tubes and evaporator in PX-3A were hotter than in PX-5A.

## 5.6 SUMMARY AND CONCLUSIONS

A detailed radiation/conduction thermal model was developed for calculating internal parasitic heat losses and temperatures in vapor anode, multi-tube AMTEC cells. The model accounted for the presence of an internal circumferential shield and a conduction stud between the cell's hot end and BASE tubes support plate. The model calculated all radiation view factors using closed-form algebraic solutions or approximate relations, and satisfied all reciprocity and enclosure relations. The radiation/conduction model was integrated into a full AMTEC cell model developed at UNM-ISNPS.

The predicted heat removal at the condenser end, temperatures of the hot end, BASE tubes cold end, and condenser, and the cell electrical power and voltage outputs, were in good agreement with experimental results of PX-4C, PX-5A and PX-3A cells. Such good agreement confirmed the soundness of the modeling approach and the accuracy of the radiation/conduction model.

The calculated heat transfer and performance parameters in PX-4C, PX-5A and PX-3A, near the predicted peak conversion efficiencies, are shown in Table 5.1. The use of a CREARE condenser in PX-5A, in lieu of the mesh pad condenser of PX-4C, and increasing the condenser temperature (from 565 K to 623 K), caused a 3 W reduction in parasitic radiation losses to the condenser (from 4.7 W to 1.7 W). Also, the BASE tubes in PX-5A only lost 7.3 W by radiation to the cooler surfaces of the low pressure cavity (Table 5.1). The cell electrical power output increased by 0.14 We, and the predicted peak efficiency increased by 1.3 points, from 10.5% to 11.8%.

Reducing the length and the number of BASE tubes, and the cell diameter in PX-3A reduced the radiation view factors between the BASE tubes bundle and the cooler surfaces in the low-pressure cavity, reducing the parasitic heat losses in the cell. The heat losses through the side wall decreased by 1.4 W (from 7.1 W to 5.7 W).

The decrease in the cell wall cross section area also decreased the heat conduction up the side wall by 1.6 W, from 5.4 W to 3.8 W (Table 5.1). The 5 BASE tubes in PX-3A only lost 3.7 W by radiation in the low-pressure cavity, and only 0.84 W were lost by radiation to the condenser surface. As a result, PX-3A reached a peak conversion efficiency of 13.0%, which was 1.2 points higher than in PX-5A (Table 5.1). The reduction of the number of BASE tubes, from 6 to 5, decreased the cell electrical power output by 0.42 We. However, the average electrodes power

density in PX-3A ( $0.111 \text{ We} / \text{cm}^2$ ) was 7% higher than in PX-5A, because the BASE tubes and evaporator in PX-3A were hotter than in PX-5A.

Table 5.1. Predicted Heat Transfer and Performance Parameters for PX-Series Cells.

Parameters	PX-4C	PX-5A	PX-3A
<u>Cell design:</u>			
Cell diameter (mm)	38	38	29
Conduction stud area ( $\text{mm}^2$ )	100	100	38
Standoff rings material/thickness (mm)	SS / 2.5	SS / 2.5	Ni / 1.1
Condenser type	SS mesh pad	CREARE	CREARE
BASE tubes length (mm)	40	40	32
Number of BASE tubes	6	6	5
Cell hot end temperature (K)	1130	1123	1123
Cell condenser temperature (K)	565	623	623
Cell wall heat losses (W)	6.8	7.1	5.7
<u>Cell performance:</u>			
Cell current (A)	1.74	1.78	1.68
Cell electrical power output (We)	3.66	3.80	3.38
Electrodes power density ( $\text{We} / \text{cm}^2$ )	0.100	0.104	0.111
Overall cell conversion efficiency	10.5%	11.8%	13.0%
<u>Heat conduction (W):</u>			
Hot plenum side wall	14.3	13.1	13.3
Conduction stud	18.6	17.3	11.6
Loss through artery	3.0	2.8	3.2
Loss through side wall	5.4	5.4	3.8
<u>Radiation in low-pressure cavity (W):</u>			
from BASE tubes support plate	4.1	3.7	0.5
from wall facing BASE tubes	-1.0	-1.1	+1.2
from outside of BASE tubes	8.6	7.3	3.7
to evaporator standoff	-1.0	-0.5	+0.36
to outside of artery	1.8	1.9	1.9
to inner shield surface	6.2	6.8	2.3
to condenser	4.7	1.7	0.84

The next chapter describes the thermal-hydraulic model which was developed to calculate the pressure losses and determine the capillary limit of the liquid-sodium return wick in the PX-series, vapor anode, multi-tube AMTEC cell, examines the effects of the wick parameters and evaporator temperature on the liquid sodium circulation, and presents some optimization analysis results.

## 6. PRESSURE LOSSES AND CAPILLARY LIMIT IN LIQUID-RETURN ARTERY OF PX-SERIES, MULTI-TUBE AMTEC CELL

In this chapter, a thermal-hydraulic model is developed to calculate the pressure losses and determine the capillary limit of the liquid-sodium return wick in the PX-2C, vapor anode, multi-tube AMTEC cell. The model is used to examine the effects of the wick parameters and evaporator temperature on the liquid sodium circulation. Results showed that, for a wick porosity of 0.2 and a sodium mass flow rate of 7.2 gm/hr, the calculated pressure losses in the wick were 3.5 kPa, 6.1 kPa, and 14.4 kPa, at effective pore radii of 20  $\mu\text{m}$ , 15  $\mu\text{m}$ , and 10  $\mu\text{m}$ , respectively. To operate a PX-type AMTEC cell at evaporator temperatures of 950 K, 1025 K and 1100 K, maximum wick pore radii of 27  $\mu\text{m}$ , 10  $\mu\text{m}$ , and 4  $\mu\text{m}$ , respectively, are needed, to overcome the evaporator saturation pressure (10 kPa, 27 kPa and 61 kPa, respectively). At evaporator temperatures  $> 1050$  K, the liquid pressure losses in a single pore size, homogeneous wick would be prohibitively high. Therefore, a wick that is comprised of two sections, a long section with a large permeability, to reduce the liquid pressure losses, and a short evaporator section, with a much smaller pore size, to provide a high capillary pressure head, is recommended.

### 6.1 NOMENCLATURE

#### English

$A$	Cross section area of liquid-return wick ( $\text{m}^2$ )
$d$	Average diameter of sintered particles (m)
$F$	Faraday's constant, $F = 96,485$ Coulomb / mole
$I$	Total cell electrical current (A)
$K$	Wick permeability ( $\text{m}^2$ )
$L$	Length of liquid-return wick (m)
$M$	Molecular weight of sodium, $M = 23$ gm/mole
$\dot{m}$	Sodium mass flow rate (kg/s)
$N_B$	Number of BASE tubes in cell (electrically connected in series)
$P$	Sodium pressure (Pa)
$P_e$	Cell electrical power output (We)
$Q$	Heat flow (W)
$R_c$	Radius of curvature of liquid-vapor interface (m)
$R_p$	Effective pore radius of wick (m)
$T$	Temperature (K)
$z$	Axial coordinate (m)

#### Greek

$\Delta P_{loss}$	Sodium liquid pressure losses in wick (Pa)
$\Delta P_{cap}$	Wick capillary pressure head (Pa)

$\varepsilon$	Wick volume porosity
$\nu$	Kinematic viscosity of liquid sodium ( $\text{m}^2/\text{s}$ )
$\sigma$	Surface tension of liquid sodium ( $\text{N} / \text{m}$ )

### Subscript / Superscript

air	Air calorimeter at condenser end
cd	Condenser
ev	Evaporator
in	Input at hot end of cell
loss	Side wall losses
sat	Saturation

## 6.2 INTRODUCTION

In a vapor anode, Alkali-Metal Thermal-to-Electric Converter (AMTEC), the liquid sodium at the condenser is at 550-700 K and 1-100 Pa. The liquid sodium is circulated back to the high-temperature (950-1100 K), high-pressure (10-60 kPa) evaporator. The vapor anode, multi-tube PX-series AMTEC cells utilize a centrally-located capillary wick structure, such as sintered, felt metals or cable arteries, to circulate the liquid sodium from the condenser to the evaporator. The amount of liquid working fluid returned to the evaporator is self-regulating. As liquid sodium evaporates, the increase in capillary forces at the liquid-vapor interface pulls more fluid to the evaporative surface.

Recent experiments and preliminary analyses have uncovered a number of critical issues. One of these issues is to optimize the wick structure for circulating the liquid sodium in the cell, at a rate commensurate with the load electrical current, without compromising the cell performance. The wick design should minimize the pressure losses of liquid sodium flow and provide the needed vapor mass flow rate at high enough evaporator temperature. Furthermore, the diameter as well as the effective thermal conductivity of the wick structure, which is saturated with liquid sodium, should not promote large heat conduction losses from the evaporator to the condenser of the cell. These competing effects should be accounted for in optimizing the liquid sodium return wick.

In this chapter, a thermal-hydraulic model is developed to optimize the liquid-sodium return wick in the PX-series AMTEC cells. This model calculates the pressure losses in the wick and determines its capillary limit. An optimization analysis is performed to determine the circulation capability of the wick, as a function of its porous properties and length. Charts of the recommended wick design parameters for optimum operation, such as volume porosity and effective pore size, as functions of sodium mass flow rate and evaporator temperature, are developed.



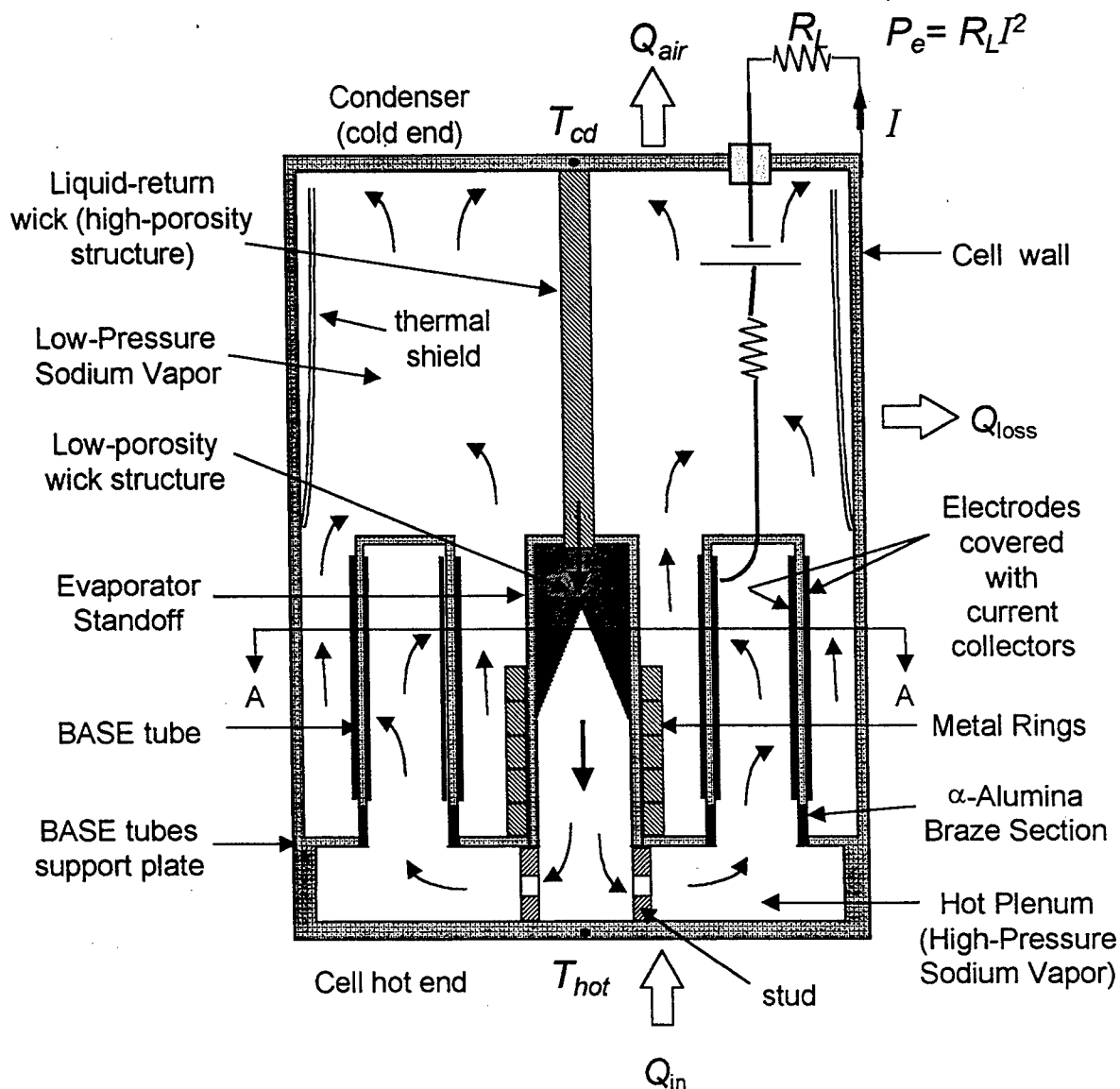


Figure 6.1. A Schematic of Vapor Anode, Multi-Tube AMTEC Cell (Not to Scale).

The PX-series AMTEC cells currently under investigation at AFRL have between 5 and 7 tubes each. These tubes are made of  $\beta''$ -Alumina Solid Electrolyte (BASE), and brazed to a common stainless steel support plate. A felt-metal wick, for returning the liquid sodium from the remotely-located condenser to the evaporator, is centrally located in the cell (Figure 6.1). The sodium vapor pressure on the anode side of the BASE tubes is approximately equal to its saturation pressure at the evaporator temperature,  $T_{ev}$ . For typical evaporator temperatures of 950 K and 1100 K, the sodium vapor pressures are 10 kPa and 60 kPa, respectively. By contrast, the sodium vapor pressure on the cathode side of the BASE tubes is 2 to 3 orders of magnitude lower ( $< 100$  Pa) than at the anode side. The liquid-return wick is made of felt metal, and has a small diameter to reduce the parasitic conduction losses to the condenser.

As liquid sodium flows from the condenser to the evaporator, it is heated by radiation from the surrounding BASE tubes. Heat is provided to the evaporator end of the wick by conduction and radiation from the hot end. Based on the rate of heat supply, the evaporator wick generates sodium vapor, at a pressure that depends on the evaporator temperature (Figure 6.1). New PX-series cells use a metal stud between the cell hot end and the BASE tube support plate, to provide more heat by conduction to the evaporator, resulting in higher evaporator and BASE tube temperatures, for enhanced cell performance (Figure 6.1). The temperature of the BASE tubes is kept slightly higher than that of the evaporator, to prevent condensation inside the tubes, and potential electric shorting of the tubes.

### 6.3 MODEL DESCRIPTION

In the present liquid-sodium return wick model, the thermophysical properties of liquid sodium, such as vapor pressure, kinematic viscosity, and surface tension, are temperature dependent. These properties were obtained from Vargaftik (1975) and Ohse (1985). The liquid sodium flow in the porous wick structure can be described by the well-known Darcy equation (Chi 1976):

$$\frac{dP}{dz} = -v \frac{\dot{m}}{KA} \quad (6.1)$$

The permeability of the wick structure,  $K$ , was calculated from the Blake-Kozeny equation (Ergun 1952) as:

$$K = \frac{d^2}{150} \frac{\varepsilon^3}{(1 - \varepsilon)^2} \quad (6.2)$$

The characteristic dimension,  $d$ , in Equation (6.2), is given as (Chi 1976):

$$d = \frac{2R_p}{0.41}, \quad (6.3)$$

where  $R_p$  is the effective pore radius of the sintered wick. Integrating Equation (6.1), along the liquid-return wick, gives the following expression for the liquid pressure drop:

$$\Delta P_{loss} = \frac{\dot{m}}{KA} \int_0^L v dz = \frac{\dot{m}L}{KA} \left( \frac{1}{L} \int_0^L v dz \right) \quad (6.4)$$

The wick permeability,  $K$ , is a function of wick porosity,  $\varepsilon$ , and average pore radius,  $R_p$ . The sodium vapor mass flow rate is directly related to the AMTEC cell electrical current,  $I$ , as:

$$\dot{m} = N_B \frac{M}{F} I, \quad (6.5)$$

where  $N_B$  is the number of BASE tubes in the cell. Therefore, the pressure drop in the wick can be given as:

$$\Delta P_{loss} = N_B \frac{MI}{F} \frac{L}{KA} \left( \frac{1}{L} \int_0^L v dz \right). \quad (6.6)$$

The liquid sodium properties were correlated as:

$$P_{sat}(T) = 10^{9.679 - 5383.2/T} \text{ (Pa)}, \quad (6.7a)$$

$$\sigma(T) = 0.2351 - 10^{-4} \times T \text{ (N/s)}, \quad (6.7b)$$

$$\nu(T) = 1.64 \times 10^{-7} + \frac{0.173}{T^{2.13}} \text{ (m}^2/\text{s)}. \quad (6.7c)$$

The predicted sodium vapor pressure using Equation (7a) is within 4% of Ditchburn's correlation, which was based on experimental data of 11 investigators (Bomelburg and Smith 1972). The liquid sodium saturation pressure, surface tension and kinematic viscosity are shown in Figures 6.2, 6.3 and 6.4, respectively.

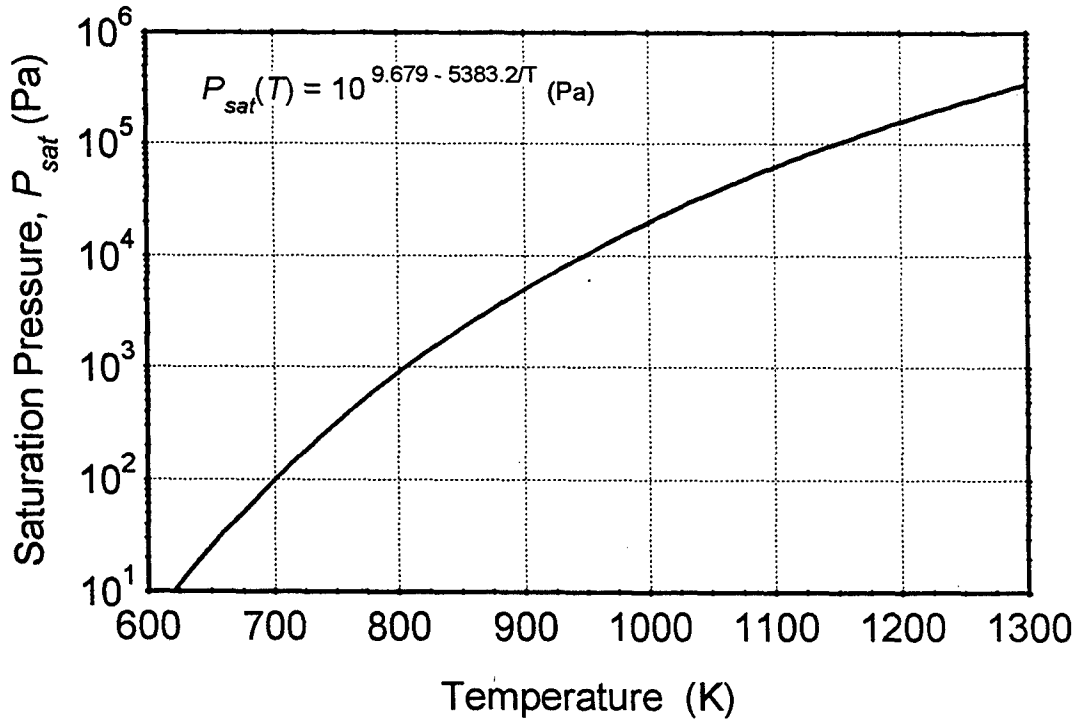


Figure 6.2. Saturation Pressure of Liquid Sodium.

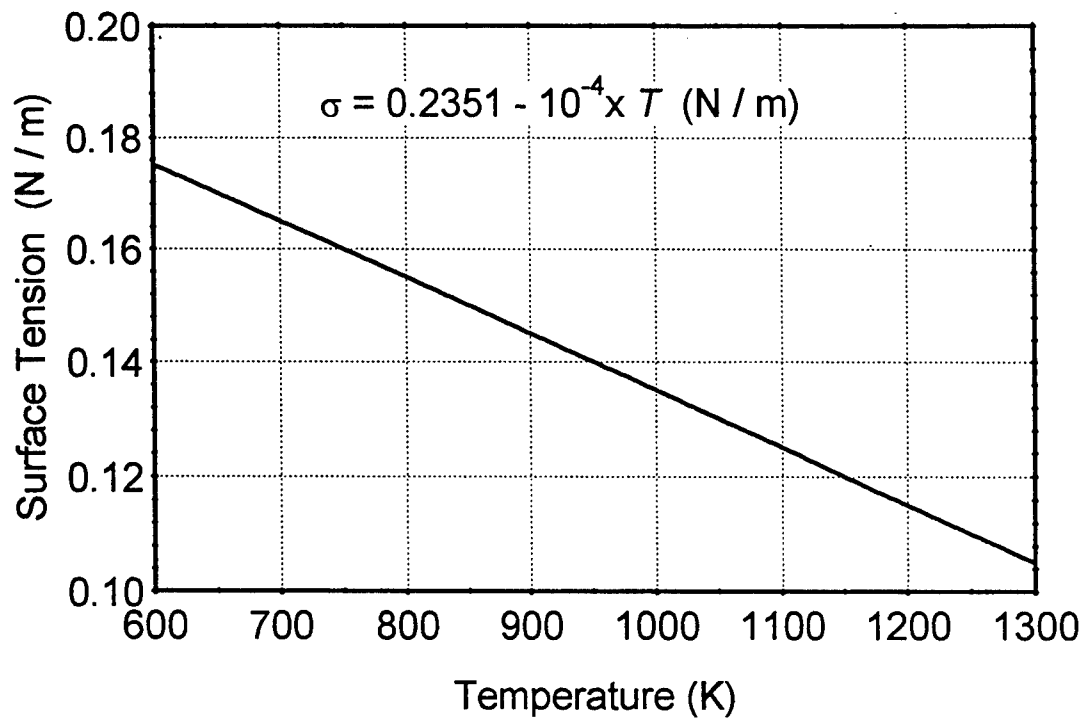


Figure 6.3. Surface Tension of Liquid Sodium.

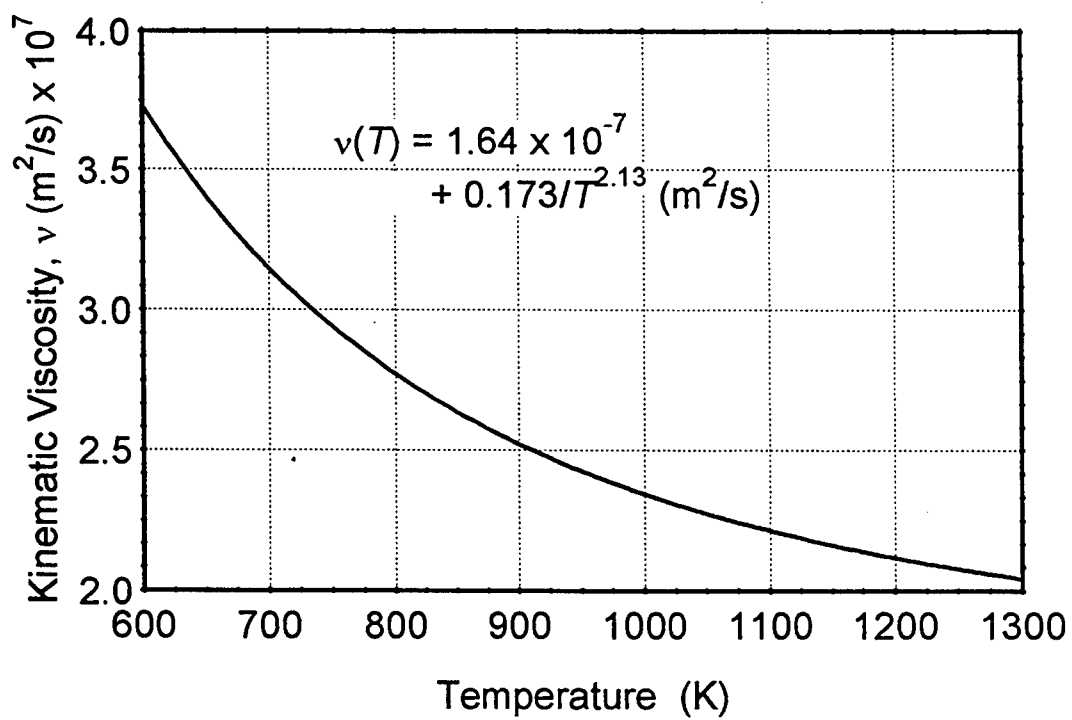


Figure 6.4. Kinematic Viscosity of Liquid Sodium.

## 6.4 RESULTS AND DISCUSSION

The pressure drop in the wick structure increased with increasing liquid sodium flow rate (or total electrical current and number of BASE tubes) and wick length, and decreased with increasing cross section flow area. For an AMTEC cell with 7 BASE tubes, operating at 1.2 A (or sodium mass flow rate of 7.2 gm/hr), the calculated pressure drop in a wick having a porosity of 0.3, average pore radius of 10  $\mu\text{m}$ , 75 mm long and 7 mm<sup>2</sup> in cross section area, was 9,000 Pa (Figure 6.5). As delineated in Figure 6.5, increasing either the average pore size or the wick porosity reduced the pressure losses in the wick.

At steady-state, the liquid sodium flow rate in the wick is directly proportional to the electric current produced by the cell. However, a high liquid sodium flow rate increases the pressure losses in the wick and reduces the evaporator temperature and pressure, lowering the voltage potential of the cell. In order to minimize the effect of high liquid sodium flow rates on the cell performance, it is important to increase the evaporator temperature in the cell. This was made possible by attaching a metallic conduction stud between the cell hot plate and the BASE tubes/evaporator standoff support plate (Figure 6.1). In addition, metal rings were installed around the evaporator standoff. Such enhancement of the heat conduction path to the evaporator raised its temperature, and at the same time reduced somewhat the pressure losses in the wick, by raising the average temperature of liquid sodium flow, hence lowering its viscosity (Equations 6.4 and 6.7c).

Figure 6.6 shows that the temperature of the returning liquid sodium in the high-porosity section of the wick increased almost linearly, from the condenser temperature. A fraction of the net radiant energy received by the outer surface of the wick heated the flowing liquid sodium, between  $T_{cd}$  and  $T_{ev}$ . The temperature in the evaporator wick region was almost uniform, except near the evaporator surface, where it dropped sharply, due to evaporation. The larger temperature gradient along the liquid-sodium return wick, typically 10 K/mm (Figure 6.6), stimulated heat conduction in the wick structure to the condenser. This heat conduction loss could be significant. For example, in the PX-2C cell, that had a 75 mm-long wick, with a 7 mm<sup>2</sup> cross section area, these conduction losses were about 5 W, at a condenser temperature of 530 K and an evaporator wick temperature of 975 K.

The calculated pressure losses in the liquid-sodium return wick of the PX-2C AMTEC cell are shown in Figure 6.7, at an evaporator temperature of 950 K ( $P_{ev} = 10.3$  kPa). At low pore size, the pressure losses in the wick increased very rapidly with decreasing pore size, because the wick permeability is proportional to the square of the effective pore size (Equations 6.2 and 6.3). For a wick porosity of 0.2 and a cell electrical current of 1.2 A (or sodium mass flow rate of 7.2 gm/hr, since  $N_B = 7$  in PX-2C), the calculated pressure losses in the wick were 3,500 Pa, 6,100 Pa, and 14,400 Pa, at effective pore radii of 20  $\mu\text{m}$ , 15  $\mu\text{m}$ , and 10  $\mu\text{m}$ , respectively (Figure 6.7).

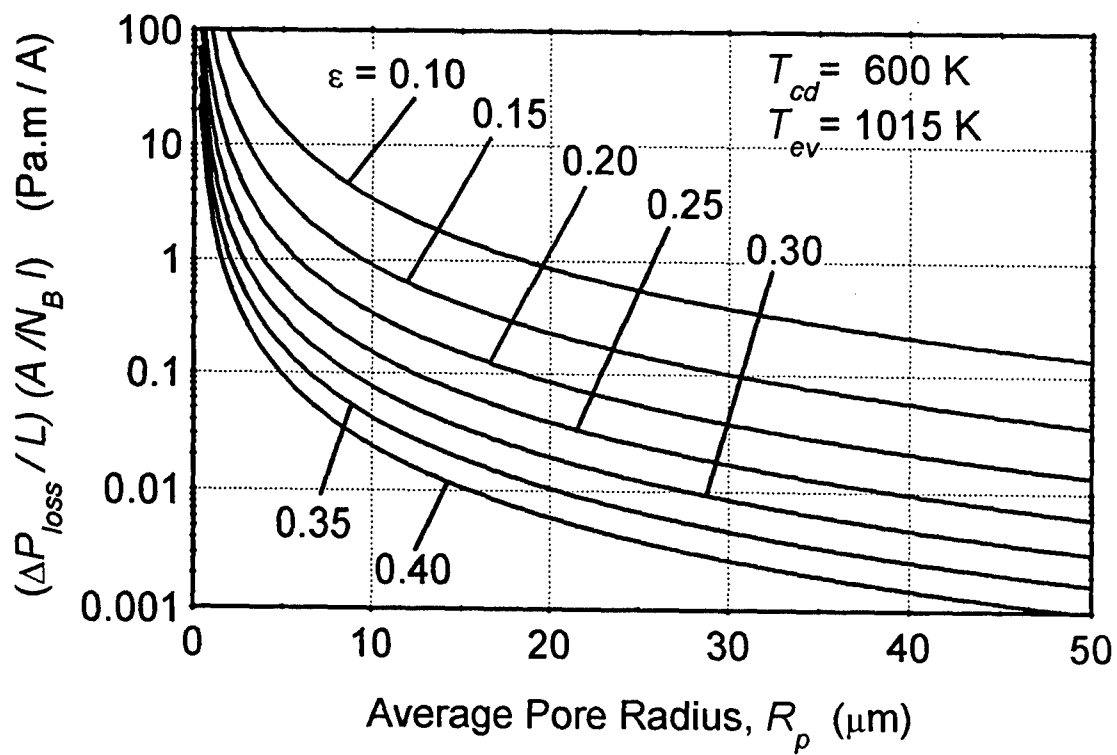


Figure 6.5. Pressure Loss as a Function of Wick Porosity and Average Pore Size.

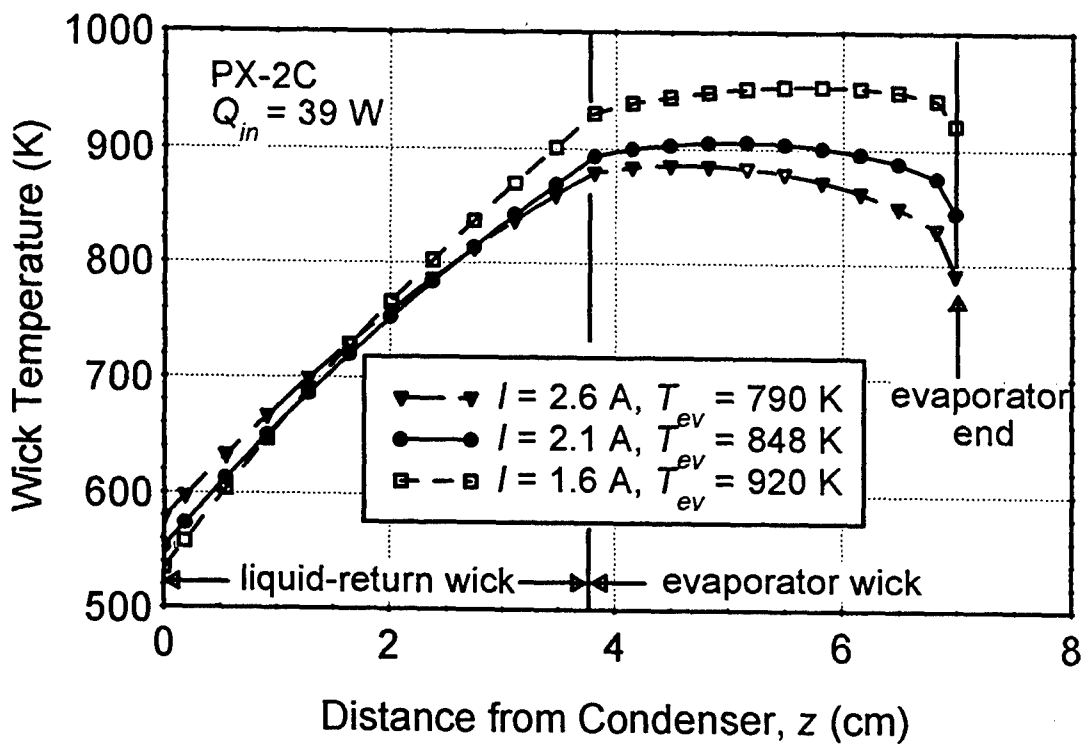


Figure 6.6. Calculated Wick Temperature Profile in PX-2C AMTEC Cell.

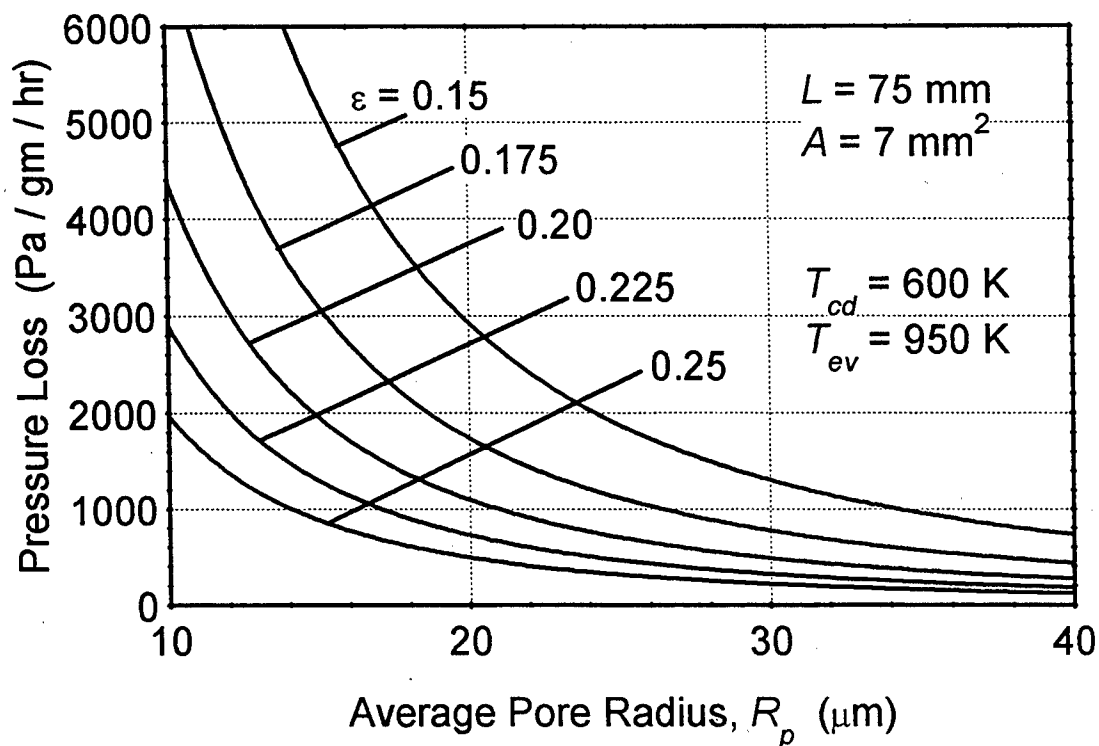


Figure 6.7. Wick Pressure Losses in PX-2C Cell.

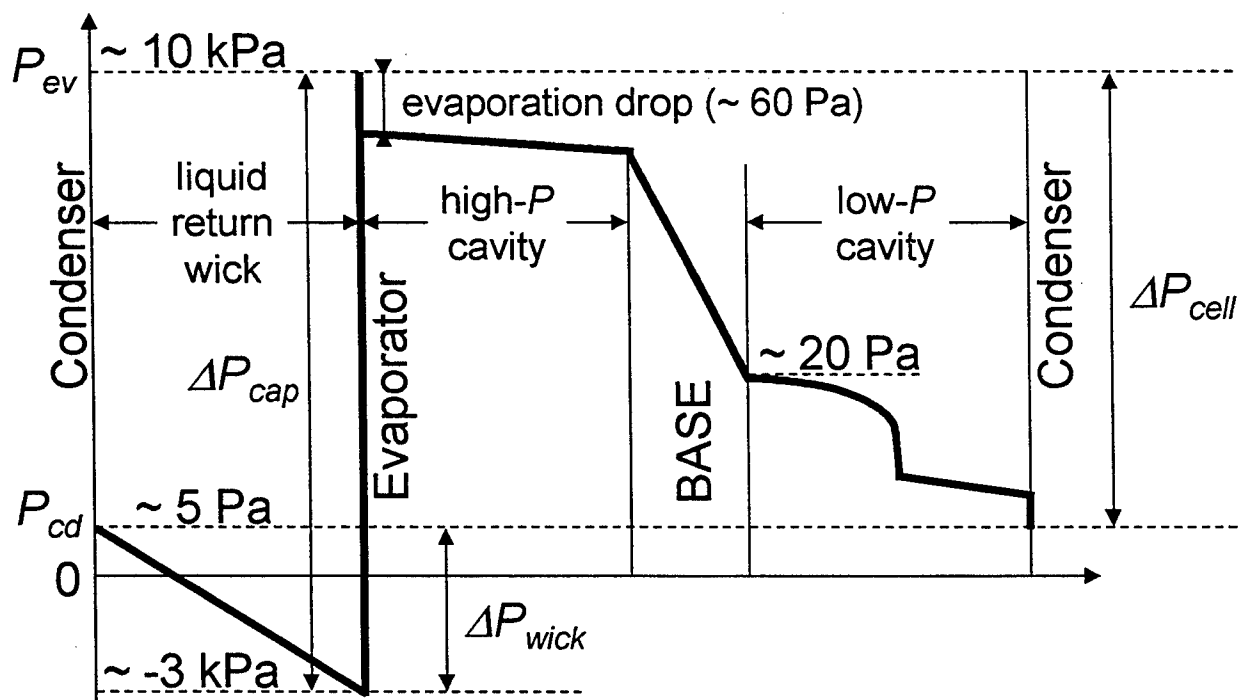


Figure 6.8. A Line Diagram of the Local Pressure in PX-2C Cell ( $Q_{in} = 39 \text{ W}$ ,  $T_{cd} = 600 \text{ K}$ ,  $T_{ev} = 950 \text{ K}$ ,  $\dot{m} = 9 \text{ gm/hr}$ ,  $P_e = 4.5 \text{ We}$ ).

### 6.4.1 Wick Capillary Limit

Dryout of the wick may occur if its pumping capability is insufficient to maintain the liquid flow from the condenser to the evaporator, or if the condenser structure is not saturated with sodium condensate. The wick capillary pressure must be equal to or larger than the sum of the pressure losses in the cell (due to liquid sodium flow in the wick, evaporation of liquid sodium at the evaporator wick surface, sodium vapor flow from the evaporator to the BASE/anode surface, isothermal expansion of sodium vapor through the BASE membrane, sodium vapor flow from the BASE/cathode interface to the condenser, and condensation of sodium vapor at the condenser surface). The capillary limit in the wick can be expressed as:

$$\Delta P_{cap} = \frac{2\sigma}{R_p} \geq P_{sat}(T_{ev}) - P_{sat}(T_{cd}) + \Delta P_{loss} . \quad (6.8)$$

The condenser saturation pressure is negligible, typically 3 to 4 orders of magnitude smaller than the evaporator saturation pressure. Figure 6.8 shows a line diagram of the local sodium pressure in the PX-2C AMTEC cell. The liquid in the condenser wick is at saturation, about 5 Pa at a condenser temperature of 600 K. The pressure losses in the wick, which are much larger than the condenser saturation pressure, cause the local liquid pressure to go negative, placing the liquid sodium in the wick under tension (Figure 6.8). A local tension in liquid sodium as low as -2,400 Pa has been observed in a wick-fed, vapor anode AMTEC cell (Anderson 1992, and Anderson et al. 1993).

An increase in pressure occurs at the liquid-vapor interface of the evaporator ( $2\sigma/R_c$ ). At an evaporator temperature of 950 K, the sodium saturation pressure is about 10 kPa (Figure 6.8). Evaporation of liquid sodium occurs at the evaporator wick surface, causing a pressure drop in the PX-2C cell of about 60 Pa, for a conical evaporator surface of 60 mm<sup>2</sup> (3 times the cross section area of the evaporator standoff), at a typical cell current  $I = 1.5$  A (a sodium mass flow rate of 9 gm/hr). The sodium vapor flows through the conduction stud, to the interior of the BASE tubes, reaching the anode side of the BASE, with negligible pressure losses ( $< 50$  Pa). The thermodynamic potential across the BASE causes ionization of the sodium atoms. The free electrons circulate through the external load, producing electric work. The sodium ions diffuse isothermally through the BASE membrane (Figure 6.8), and recombine with the returning electrons, at the interface between the BASE and the cathode electrode. The neutral sodium atoms, which emerge at a very low pressure of 20 Pa, traverse the low-pressure cavity to the cell cold end, where they condense.

In the vacuum tests at AFRL, the cell condenser was situated below the evaporator, and the liquid sodium in the wick was flowing against the gravity force. The pressure loss due to gravity was small compared to the evaporator saturation pressure, and could be neglected ( $< 600$  Pa).

In the following analyses, Equation (6.4), (6.7) and (6.8), were used to obtain the minimum volume porosity of the wick for circulating liquid sodium at different mass flow rates (Figures 6.9 and 6.10). These calculations were for a condenser temperature of 600 K, a wick length of 75



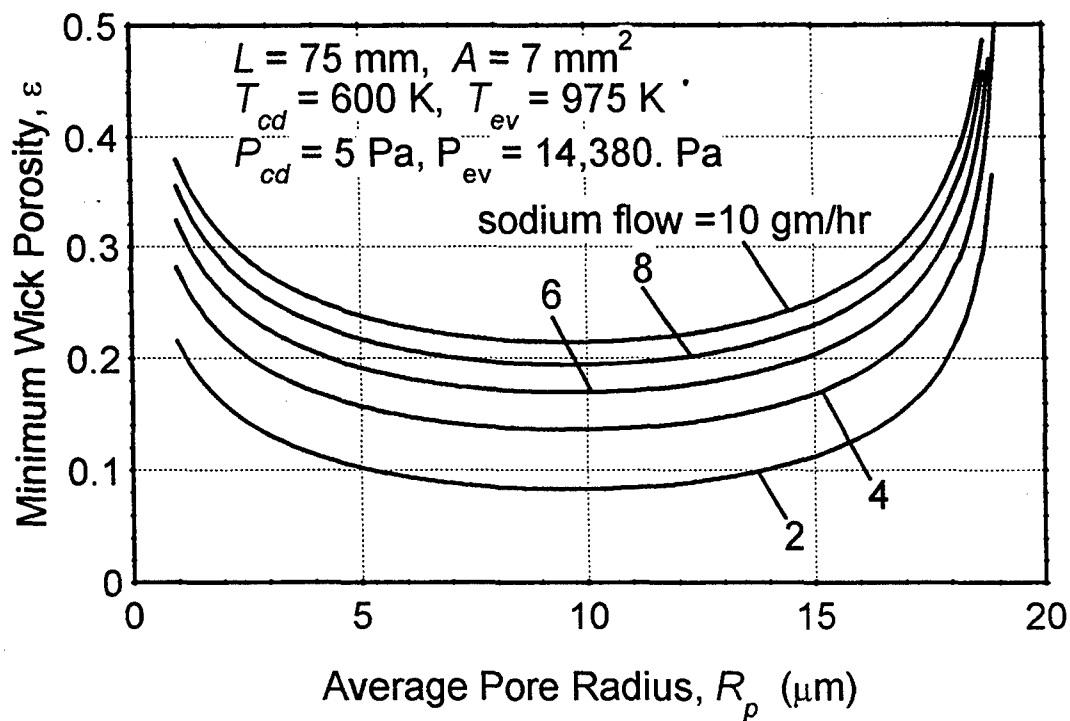


Figure 6.9. Minimum Wick Porosity at an Evaporator Temperature of 975 K.

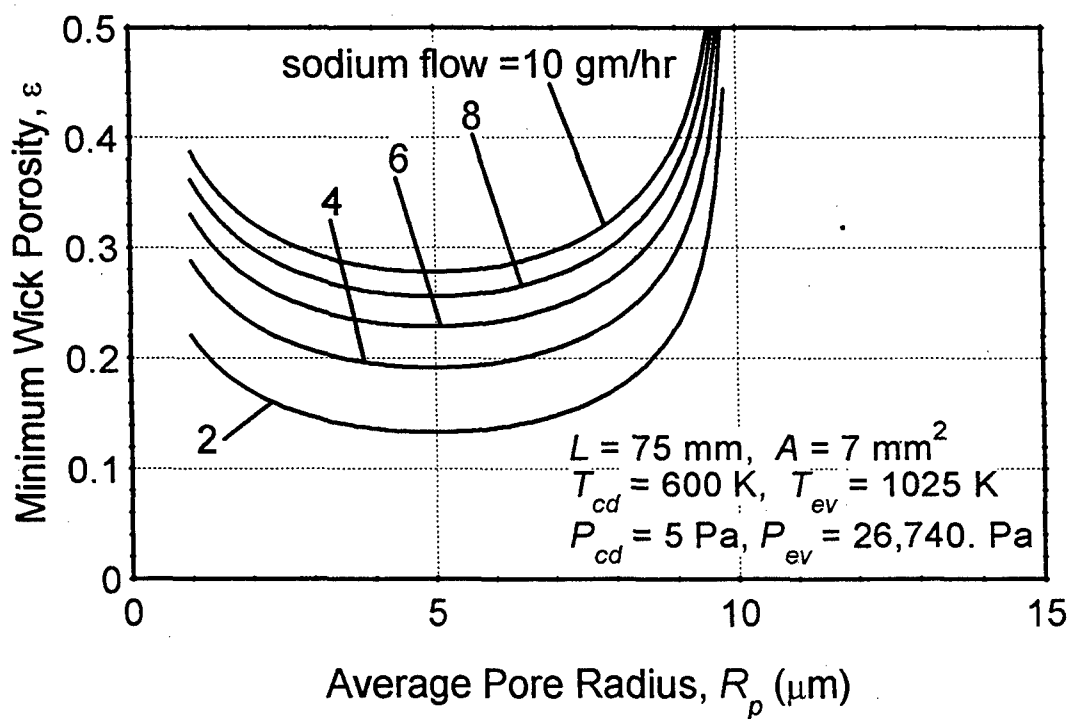


Figure 6.10. Minimum Wick Porosity at an Evaporator Temperature of 1025 K.

mm and a wick cross section area of  $7 \text{ mm}^2$ . At an evaporator temperature of 975 K, the capillary structure must at least overcome the evaporator saturation pressure of 14.4 kPa. The vertical asymptotes at pore radii of  $19 \text{ }\mu\text{m}$  and  $10 \text{ }\mu\text{m}$  in Figures 6.9 and 6.10, respectively, correspond to the pore size needed to overcome the evaporator saturation pressures (of 14.4 kPa and 26.7 kPa, respectively). As the pore size decreased, the gain in capillary pumping capability initially increased faster than the pressure losses in the wick. Eventually, the minimum allowable volume porosity of the wick reached a minimum value. As the pore size of the wick decreased further, below its optimum value of  $9 \text{ }\mu\text{m}$  and  $5 \text{ }\mu\text{m}$ , at evaporator temperatures of 975 K and 1025 K, respectively, the pressure losses in the liquid-sodium return wick became a larger fraction of the capillary pumping capability of the wick. This is because the wick permeability increases with the square of the pore size, while the capillary pressure head is only inversely proportional to the pore radius (Equation 6.8). At an evaporator temperature of 975 K and a sodium mass flow rate of 8 gm/hr, the range of suitable pore sizes is fairly wide, about 2 to  $17 \text{ }\mu\text{m}$  at a wick volume porosity of 0.30 (Figure 6.9).

At a higher evaporator temperature of 1025 K (Figure 6.10), the range of possible pore sizes is much more restricted than in Figure 6.9, between 2 and  $8 \text{ }\mu\text{m}$  at a porosity of 0.30 and a sodium mass flow rate of 8 gm/hr (Figure 6.10). At such high evaporator temperature, the pressure drop due to liquid flow through the wick is a smaller fraction of the evaporator saturation pressure, 26.7 kPa (Figure 6.11). The maximum allowable pore radius of the wick (the vertical asymptotes at larger pore radius, in Figures 6.9-6.11) decreased with increasing evaporator temperature due to the increase in evaporator pressure, and the decrease in the surface tension of the liquid. Figure 6.11 shows that the minimum allowable volume porosity of the wick increased as the evaporator temperature increased. Increasing the evaporator temperature decreased the surface tension of sodium, hence lowering the capillary pressure head of the evaporator. Also, the larger the evaporator temperature, the larger the evaporator saturation pressure that the wick must overcome, requiring a reduction in the liquid pressure losses in the wick in order to transport a specified mass flow rate. A reduction in the wick pressure loss requires higher wick permeability, and larger volume porosity.

The design requirements of the liquid-sodium return wick are a trade-off between: (a) the wick must provide large capillary pumping, hence requiring a small maximum pore size; and (b) the wick should have large permeability to minimize axial pressure losses, which requires large volume porosity. These two requirements need to be optimized. As shown in Figure 6.11, very restrictive conditions on pore size and porosity must be satisfied by the wick capillary structure in order to operate current PX-series, vapor anode, multi-tube AMTEC cells at higher electrical currents and evaporator temperatures.

#### 6.4.2 Composite Liquid-Sodium Return Wick

One obvious solution to the dilemma of decreasing wick volume porosity (or decreasing permeability) with decreasing pore size, is to use a wick composed of two sections, with different characteristics. The primary wick, whose main purpose is to transport the liquid sodium from the condenser to the evaporator, would have a large permeability to minimize the liquid sodium flow

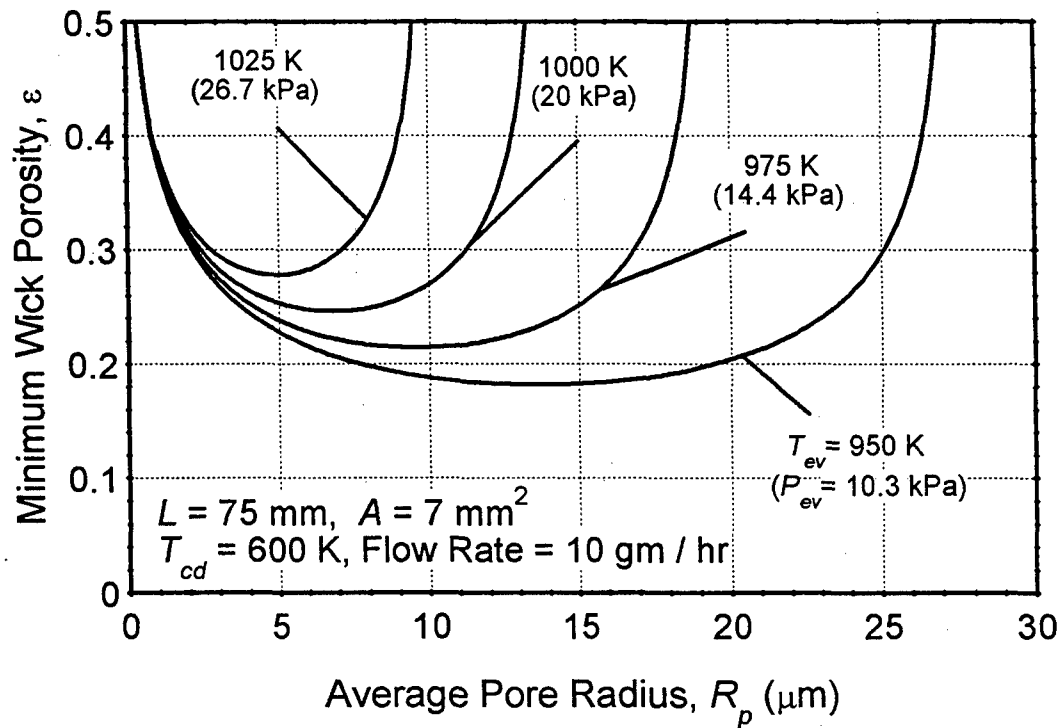


Figure 6.11. Minimum Wick Porosity at a Sodium Flow Rate of 10 gm/hr.

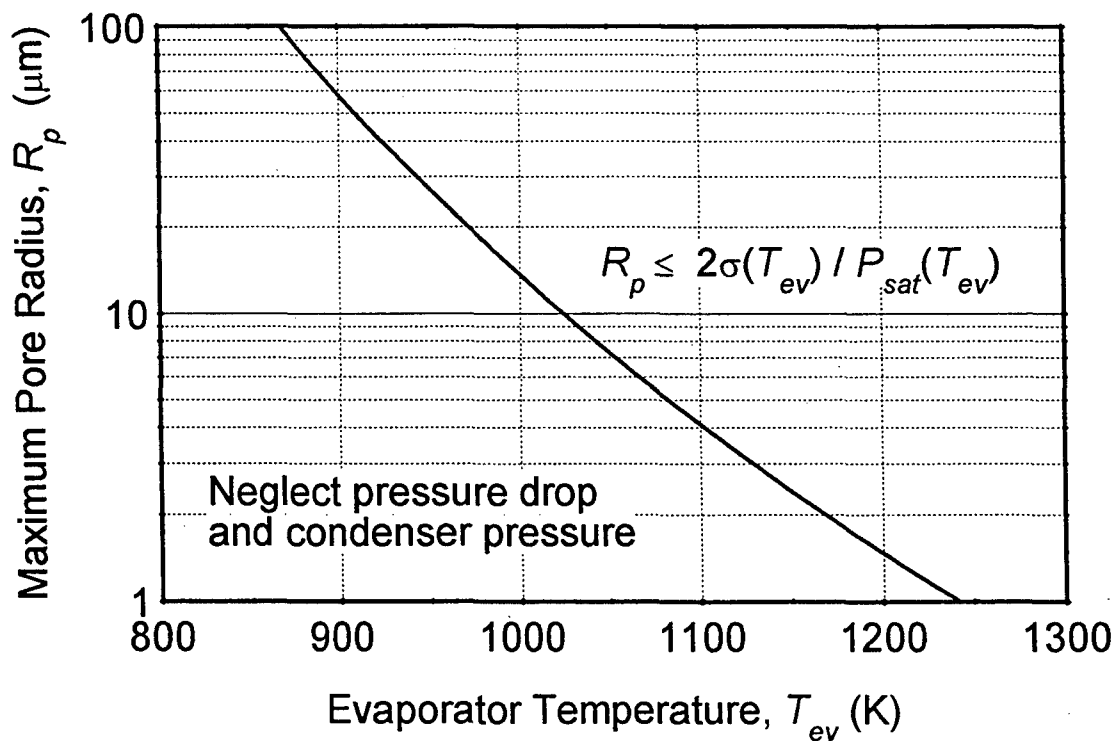


Figure 6.12. Maximum Pore Radius as a Function of Evaporator Temperature.

pressure losses, and an average or large pore size. The second section, the evaporator wick section, should have a smaller pore size to provide a high capillary pressure head, to overcome evaporator saturation pressure and wick pressure losses. The porosity of this section of wick is less important, since its length is small ( $< 20$  mm).

In PX-2C, the remotely-located condenser was coated with a sintered-powder metal wick, which was relatively coarse, and had a low capillary pumping capability, and a high permeability. The primary wick structure was made of felt metal and had a higher capillary pumping capability than the condenser wick. The wick diameter was relatively small to limit the parasitic conduction losses from the hot evaporator to the condenser. As liquid sodium approached the evaporator, it flowed through the felt-metal evaporator wick, which had a much higher capillary pumping capability (small pore size), for achieving high capillary pressure head.

The choice of the condenser wick structure, and those of the primary liquid-return wick and of the evaporator wick, required a trade-off between higher capillary pumping capability and low liquid pressure losses. Decreasing the pore size of the wick increased the capillary pumping capability, but also increased the pressure losses in the wick. The condenser wick and the primary section of the return wick must have a relatively high permeability to minimize the overall pressure losses. In a well-designed composite liquid-return wick, the pressure losses through the high-permeability section of the wick, and the pressure losses through the evaporator wick, should only be a small fraction of the evaporator saturation pressure. In such case, the maximum pore size of the evaporator wick can be approximated as:

$$R_p \leq \frac{2\sigma(T_{ev})}{P_{sat}(T_{ev})} \quad (6.9)$$

As shown in Figure 6.12, the maximum pore radius decreased at a faster rate than the sodium saturation pressure increased, since the surface tension of liquid sodium decreased with temperature. At evaporator temperatures of 950 K, 1025 K and 1100 K, the maximum pore radius of the wick evaporator should be 27  $\mu\text{m}$ , 10  $\mu\text{m}$ , and 4  $\mu\text{m}$ , respectively (Figure 6.12). The maximum pore size can be experimentally determined from the measured suction height in the wick and from the fluid properties. On the other hand, the pressure losses through the wick depend on the average pore size in the structure. The latter is experimentally determined by measuring the mass flow rate and pressure drop, and can be inferred from Equations (6.2) to (6.4).

Izenson and Crowley (1993 and 1996) have manufactured and tested new micromachined evaporators, that were coupled to a high-permeability primary liquid-return line. These composite return wicks could provide a capillary pressure head of about 60 kPa to enable continuous operation of AMTEC devices at evaporator temperatures up to 1100 K. The first design consisted of a 125  $\mu\text{m}$ -thick stainless steel plate, through which holes were laser-drilled in a square pitch of 40  $\mu\text{m}$  (Izenson and Crowley 1993). The capillary structure supported approximately 100,000 micropores with a nominal radius of 2.5  $\mu\text{m}$  and a maximum pore size of 3.4  $\mu\text{m}$ . The second wick design consisted of a micromachined evaporator made from arrays of

microscopic grooves (Izenson and Crowley 1993), approximately 50  $\mu\text{m}$  deep and 5  $\mu\text{m}$  wide at their opening.

## 6.5 SUMMARY AND CONCLUSIONS

A thermal-hydraulic model was developed to calculate the pressure losses and determine the capillary limit of the liquid-sodium return wick in vapor anode, multi-tube, PX-series AMTEC cells. The effects of the wick parameters (pore size and volume porosity) and evaporator temperature on the liquid-sodium circulation rate were examined. The capillary pressure rise in the evaporator wick must equal or exceed the sum of liquid sodium pressure losses and evaporator saturation pressure in the cell. The pressure losses in the wick decreased with increasing either the average pore size or the wick porosity. Attaining high capillary pressure rise in the evaporator, however, requires using a wick with small size pores.

Calculations were performed for the PX-2C cell, which had a 75 mm-long wick with a cross section area of 7 mm<sup>2</sup>. For a wick porosity of 0.2 and a sodium mass flow rate of 7.2 gm/hr, the calculated pressure losses in the wick were 3,500 Pa, 6,100 Pa, and 14,400 Pa, at effective pore radii of 20  $\mu\text{m}$ , 15  $\mu\text{m}$ , and 10  $\mu\text{m}$ , respectively. At an evaporator temperature of 975 K and a sodium mass flow rate of 8 gm/hr, the range of suitable pore sizes was fairly wide, about 2 to 17  $\mu\text{m}$ , for a wick volume porosity of 0.30. At a higher evaporator temperature of 1025 K, the range of suitable pore sizes was much more restricted; 2 to 8  $\mu\text{m}$ . Operating at evaporator temperatures of 950 K, 1025 K and 1100 K, required maximum wick pore radii of 27  $\mu\text{m}$ , 10  $\mu\text{m}$ , and 4  $\mu\text{m}$ , respectively, to overcome the evaporator saturation pressure (10 kPa, 27 kPa and 61 kPa, respectively). The maximum allowable pore radius for the wick decreased with increasing evaporator temperature, due to the higher vapor pressure, and due to the decrease in the surface tension of liquid sodium.

At evaporator temperatures  $> 1050$  K, the liquid pressure losses through a single pore size, homogeneous liquid-return wick would be prohibitively high, because the wick permeability varies proportionally with the square of the pore size. Therefore, it is recommended to use a wick comprised of two sections: (a) a primary wick, whose main purpose is to transport the liquid sodium from the condenser to the evaporator, with a large permeability to minimize the liquid sodium flow pressure losses; and (b) a short evaporator wick section, with a smaller pore size to provide a high capillary pressure head.

Proper modeling of AMTEC operation and correct interpretation of experimental results require that the overall momentum balance in the cell be satisfied, including the pressure losses and capillary pressure head in the wick. This would only be possible if the geometrical parameters of the liquid-sodium return wick (pore size, porosity, and permeability) are known. Therefore, these wick parameters should be determined experimentally.

The next chapter describes in details the experimental setup designed to evaluate the thermal conductivity of insulation materials used in the single-cell and multi-cell setups at AFRL, namely alumina powders of different sizes and molded Min-K (TE-1800).

## 7. MEASUREMENTS OF THERMAL CONDUCTIVITIES OF ALUMINA POWDERS AND MIN-K IN VACUUM

### 7.1 NOMENCLATURE

$A$	Cross-sectional area of the foils that is perpendicular to the heat flow [ $\text{m}^2$ ]
$a$	Fitting constant in Equation (7.1)
$b$	Fitting constant in Equation (7.1)
$k$	Thermal conductivity [ $\text{W/m.K}$ ]
$k_m$	Thermal conductivity of the foils material [ $\text{W/m.K}$ ]
$k_{mf}^{\text{ax}}$	Thermal conductance of the multi-foils insulation in axial direction [ $\text{W/K}$ ]
$k_{mf}^{\perp}$	Thermal conductance of the multi-foils insulation in perpendicular direction [ $\text{W/K}$ ]
$L_{\text{eff}}$	Effective length of heater which produces heat [ $\text{m}$ ]
$L_x$	Axial length of the multi-foils insulation [ $\text{m}$ ]
$n$	Number of multi-foils
$Q$	Total heat generated by the electric heater [ $\text{W}$ ]
$r$	Radial distance from the centerline, [ $\text{m}$ ]
$T$	Temperature [ $\text{K}$ ]
$T_h$	Temperature at the hot side of the multi-foils insulation [ $\text{K}$ ]
$T_c$	Temperature at the cold side of the multi-foils insulation [ $\text{K}$ ]
$w$	Width of the multi-foils insulation [ $\text{m}$ ]

### GREEK

$\delta_f$	Thickness of foils [ $\text{m}$ ]
$\delta_x$	Spacing between foils [ $\text{m}$ ]
$\epsilon_{\text{eff}}$	Effective radiative emissivity of the foils
$\sigma$	Stefan-Boltzmann constant, $\sigma = 5.6697 \times 10^{-8} \text{ W/m}^2 \text{ K}^4$

### 7.2 INTRODUCTION

Low thermal conductivity, high temperature, lightweight insulation materials are being investigated for use with Alkali-Metal Thermal-to-Electric Conversion cells (AMTECs). AMTECs are being considered, in conjunction with a Small General Purpose Heat Source (GPHS), to power the spacecraft for the NASA's year 2003 launch of the Pluto Express (PX) mission. AMTECs are passive and promise a relatively high conversion efficiency of 15 - 25%, at a hot side temperatures of  $\sim 1100 \text{ K}$  and a radiator temperature of  $\sim 600 \text{ K}$ .

The PX-series cells designed and manufactured by Advanced Modular Power Systems, Inc. (AMPS), are currently being tested in vacuum at AFRL (Schuller et al. 1996). A major

consideration for improving the conversion efficiency of AMTECs in laboratory tests and after deployment in space is to use a low thermal conductivity, lightweight, and high temperature insulation material. In addition to increasing the cell efficiency, such an insulation material would minimally impact the total mass of the power system.

Multi-foils insulation has been favored and performed well in space applications when heat losses occur in the perpendicular direction to the metal foils, and the wall temperature is quite uniform. This insulation consists of thin stainless steel or molybdenum foils (5 - 25  $\mu\text{m}$  thick) separated by small gaps ( $\sim 100$   $\mu\text{m}$  wide). Small size zirconia or alumina particles are deposited onto the surface of the foils to prevent conduction losses due to metal-metal contact.

In the presence of a large axial temperature gradient in the wall, however, multi-foils insulation does not perform as well because of the axial conduction in the metal foils. This condition is encountered in AMTECs near the condenser, where the axial temperature gradient in the cell wall could be as high as 20-30 K/m (Schock et al. 1997a). In order to minimize axial conduction in the multi-foils insulation near the condenser of an AMTEC cell Schock et al. (1997b) proposed changing the rectangular arrangements of the multi-foils shown in Figure 7.1a, to the tapered arrangement in Figure 7.1b. The tapered metal foils near the condenser of the AMTEC cell reduced the heat losses by axial conduction in the foils along the cell wall, but at the expense of increasing the heat losses from the cell wall in the perpendicular direction.

Alumina powders have been suggested as a potential insulation material. The advantages of the alumina powder are its lightweight, chemical and thermal stability up to very high temperatures, and the ease by which it could be backed around the cell. However, the alumina powders must be contained in a metal container, which would add to the overall weight of the cell and may complicate the power system integration. A solid material, which possesses similar properties as the alumina powder, would be therefore, preferred.

There are no thermal conductivity data available for alumina powders as functions of temperature in vacuum. Blackwell et al. (1996) have measured the thermal conductivity of  $\text{Al}_2\text{O}_3$  powder (no particle size was specified), with and without a binder (a 3% of a 50/50 mixture of methylcellulose and hydroxypropylcellulose), at atmospheric conditions. They reported a thermal conductivity for  $\text{Al}_2\text{O}_3$  at 793 K, without a binder, of 0.182 W/m.K, which is very high for the AMTECs applications.

In order to minimize heat losses from the AMTECs near the condenser, two homogenous, high temperature insulation materials are being investigated at AFRL. These materials are alumina powders having average particle sizes of 1.0  $\mu\text{m}$  and 0.01  $\mu\text{m}$  and porosities of 91.4% and 96.2%, respectively, and molded Min-K (TE1800). The Min-K is the commercial name of a thermal insulation material, which is a mixture of titanium oxide and silica, fabricated in the form of solid disks. The Min-K is very light (has a density of 320  $\text{kg/m}^3$ ) and is recommended by the manufacturer for use at high temperatures up to  $\sim 1250$  K, even for load bearing applications.

The objectives of this work were to: (a) experimentally measure the thermal conductivity of the alumina powders and of molded Min-K (TE1800) in vacuum; (b) correlate and compare the

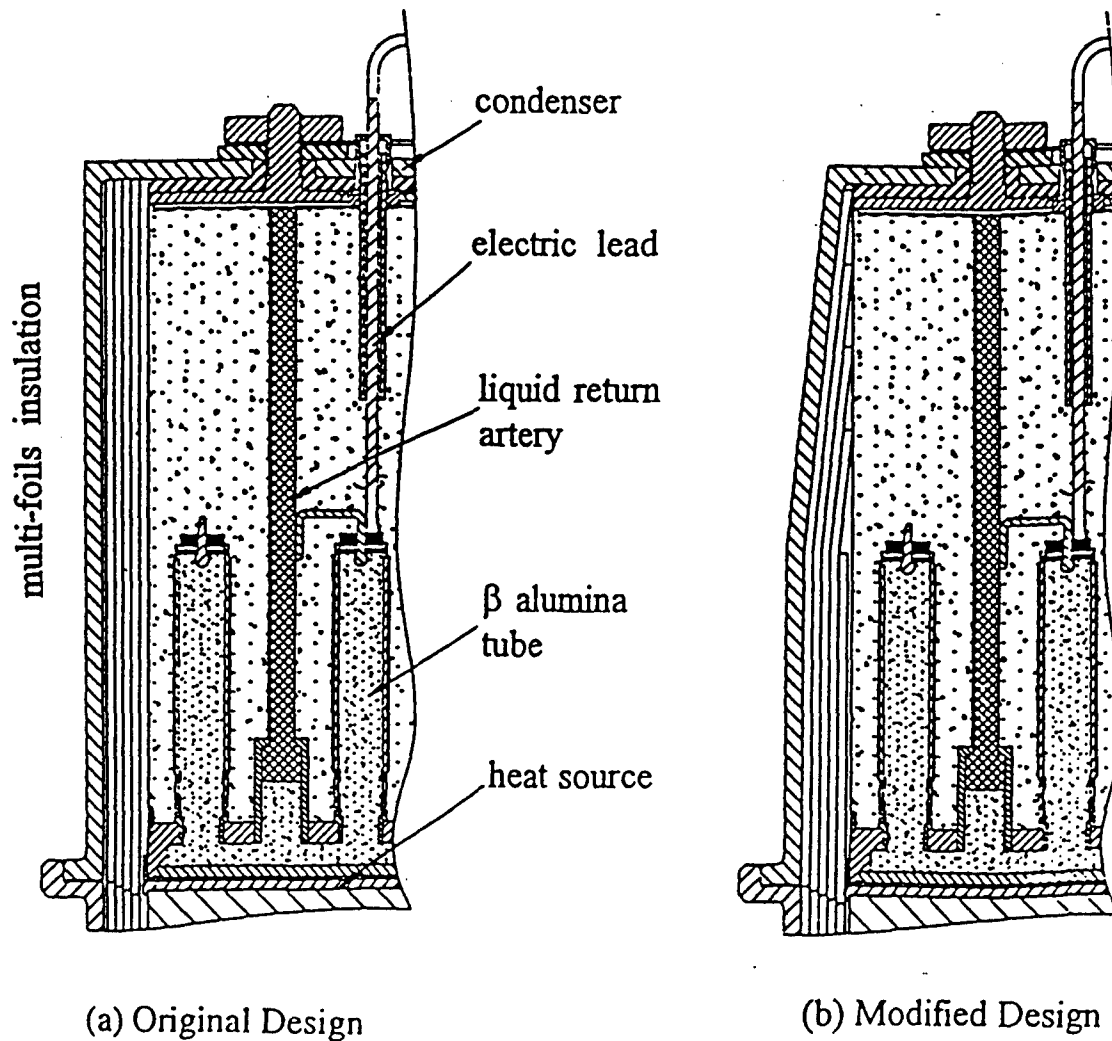


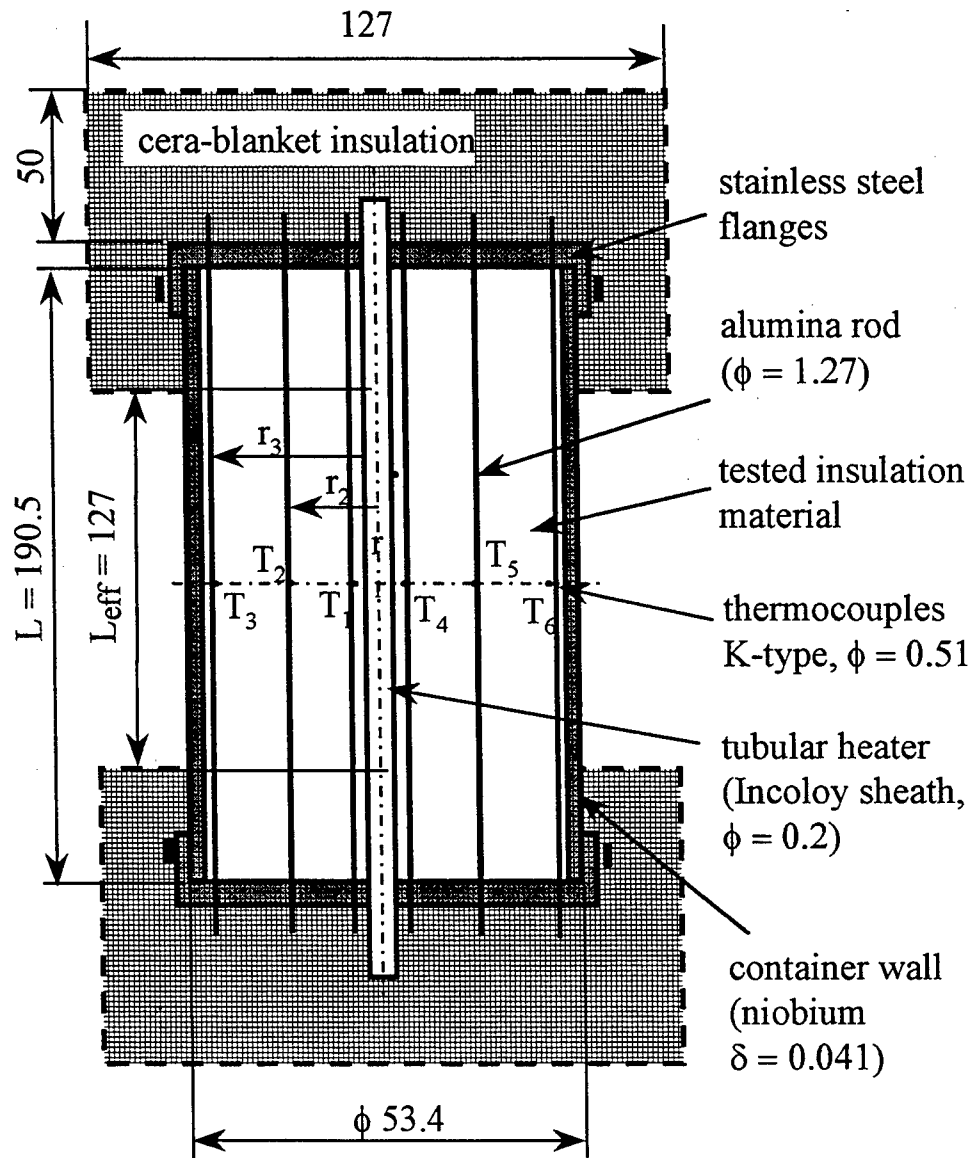
Figure 7.1. Multi-Foil Insulation for a PX-Series AMTEC Cell (Shock et al. 1997b).

thermal conductivity data for these materials as functions of temperature; and (c) compare the thermal conductance of the Min-K with those of 60 and 240 multi-foils insulations as functions of temperature, for the same thickness and hot and cold side temperatures, both in the axial and perpendicular directions.

### 7.3 EXPERIMENTAL SETUP

Two different experiment setups were used for measuring the thermal conductivity of the alumina powders and the molded Min-K, respectively. Both setups utilized a cylindrical test section, with a long, thin tubular electric heater placed at the centerline, as shown in Figures 7.2 and 7.3. The test section had a length-to-diameter ratio of 5.75. All experiments were conducted in vacuum at  $10^{-5}$  to  $10^{-7}$  torr. The steady-state temperatures at different radial locations in the insulation material were measured at different input powers to the electric heater. These data were then processed to determine the thermal conductivity of the insulation material as a function of temperature (see Appendix D).



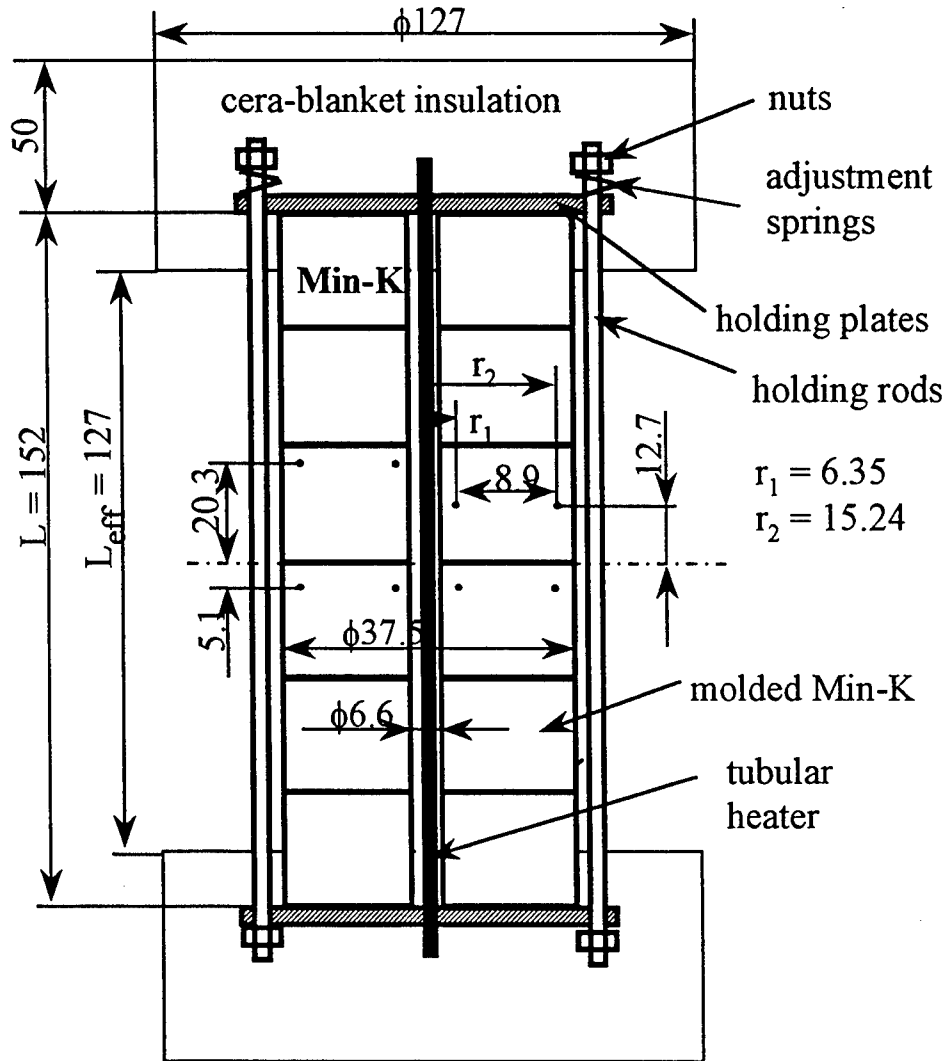


All dimensions are in mm.

Figure 7.2. Test Section for Alumina Powder Thermal Conductivity.

### 7.3.1 Setup of Alumina Powder Experiments

The setup for the alumina powder experiments consisted of a cylindrical stainless-steel container, 53.8 mm in diameter and 190.5 mm high, filled with the alumina powder, and a tubular electric heater, 5.05 mm in diameter and 190.5 mm in effective length,  $L_{\text{eff}}$ , see Figure 7.2. The tubular heater was placed along the centerline of the container. The effective porosity of the powder was



All dimensions are in mm.

Figure 7.3. Test Section for Min-K Thermal Conductivity Experiments.

determined from the measured mass of the powder used to fill the test container. Six alumina rods, 1.27 mm in diameter, were placed parallel to the central heater at 5.18, 12.7, and 22.86 mm from the centerline of the test container, respectively. Six, K-type, Inconel-shielded thermocouples, three on each side of the electric heater (Figure 7.2), were attached to the alumina rods to measure the radial temperature distribution at the mid-plane of the test sample. The measured temperatures of the alumina powder in the experiments ranged from 350 to 900 K. To reduce axial conduction losses, the top and bottom ends of the stainless-steel container were thermally insulated using thick ceramic blankets.

The estimated uncertainty in the measured temperatures was  $\pm 0.4$  K and in the electric power input to the heater was less than  $\pm 0.5\%$ . The uncertainty in the radial location of the thermocouples was about  $\pm 5.25\%$ . The total uncertainty in the measured thermal conductivity was determined using the uncertainty analysis method by Holman (1984), and was estimated at  $\pm 5.4\%$ .

### 7.3.2 Setup of Molded Min-K Experiments

The setup for the molded Min-K thermal conductivity experiments was similar to that for the alumina powder, except that no container was needed for the later, since the Min-K was solid, see Figure 7.3. Six Min-K disks, 2.54 cm thick each, were machined into annuli having inner and outer diameters of 6.6 mm and 37.5 mm, respectively. These solid annuli were stacked forming a 152 mm-high hollow cylinder, with the tubular electric heater placed vertically along the centerline (Figure 7.3). Two holding plates were used at the top and bottom of the Min-K test section and held it tightly using four steel rods to eliminate any gaps between the Min-K disks. The holding plates were covered by 5.08 cm-thick Cera-blanket insulation to minimize axial heat losses from the test section. Four spring washers were used with the holding rod (Figure 7.3) to accommodate the difference in thermal expansion between the Min-K and the holding rods, hence, maintaining the test material tightly stacked during the experiments. The thermal conductivity experiments were conducted in vacuum at  $10^{-5}$  to  $10^{-7}$  torr.

## 7.4 EXPERIMENTAL RESULTS AND ANALYSIS

The experimental data, including the measured radial temperature distribution and the heat flow through the test section, were taken at steady state. The measured radial temperature distributions in the alumina powders as well as in the Min-K were circumferentially symmetric (Figure 7.4), confirming the soundness of the experiment setup. The experimental radial temperature distributions in the insulation materials (Figure 7.4) were correlated as:

$$T(r) = a [b - \ln(r)]^{0.5}, \quad (7.1)$$

where  $r$  is the radial location of the thermocouples from the centerline of the heater in mm, and  $T$  is the measured temperature in K. The values of the coefficients  $a$  and  $b$  depend on the type of test material and the heater power used in the experiment (Figure 7.4). The measured temperature distributions in the insulation materials at different heat flow values were used to determine their thermal conductivity as functions of temperature using the methodology presented in the following section.

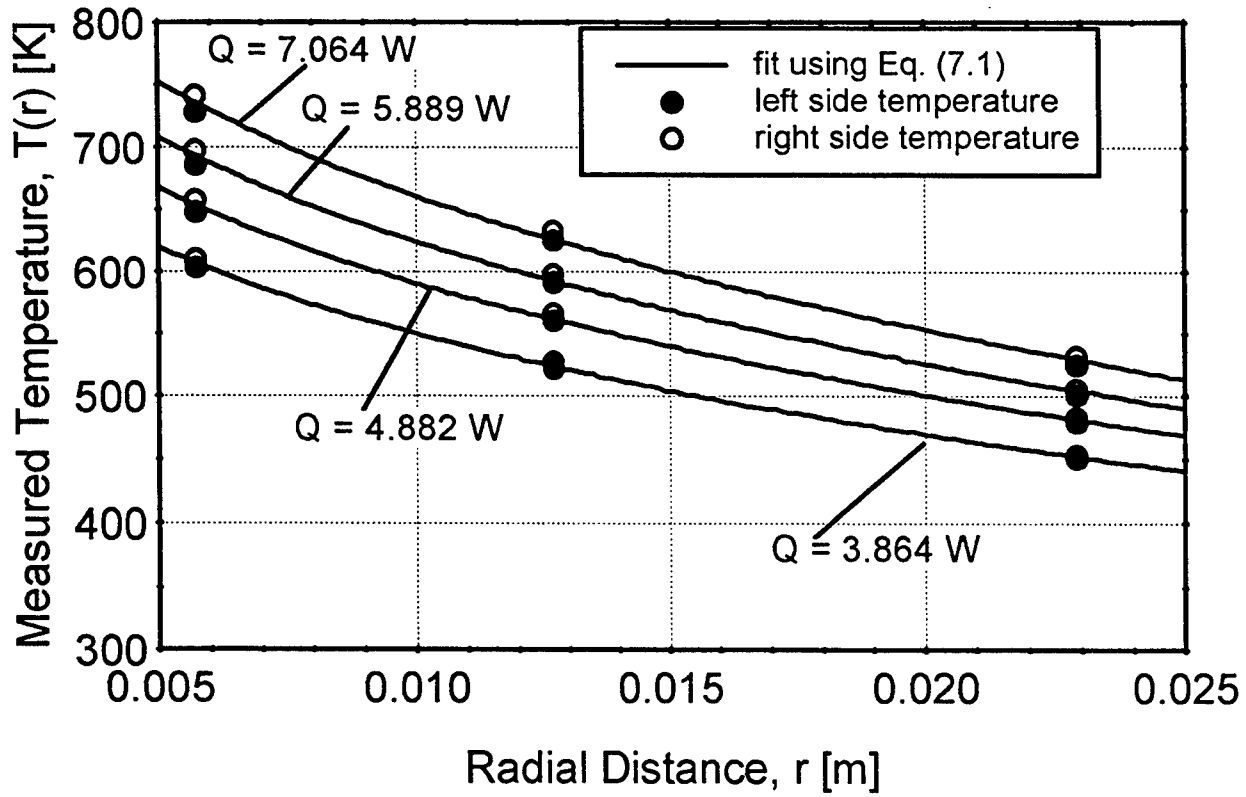


Figure 7.4. Measured Radial Temperature Distribution in 1  $\mu\text{m}$  Alumina Powders.

#### 7.4.1 Determination of Material Thermal Conductivity

Thermal conductivities of the insulation materials were determined from the measured radial temperature distributions, through the use of the integral solution of the one-dimensional, steady-state heat conduction equation in cylindrical coordinates:

$$\frac{1}{r} \frac{d}{dr} \left[ kr \frac{dT}{dr} \right] = 0, \quad (7.2)$$

The integral form of this equation can be written as:

$$\int k dT = (Q/2\pi L_{\text{eff}}) \int \frac{dr}{r} \quad (7.3)$$

The radial coordinate was divided into a number of small sectors of equal width,  $\Delta r = 1.0 \text{ mm}$ . In each sector, the thermal conductivity of the insulation material was assumed constant and equal to that at the average temperature of the sector. Thus, for a sector that extends from a radial location  $r_i$  to  $r_{i+1}$ , where  $\Delta r = (r_{i+1} - r_i)$ , Equation (7.3) can be written as:

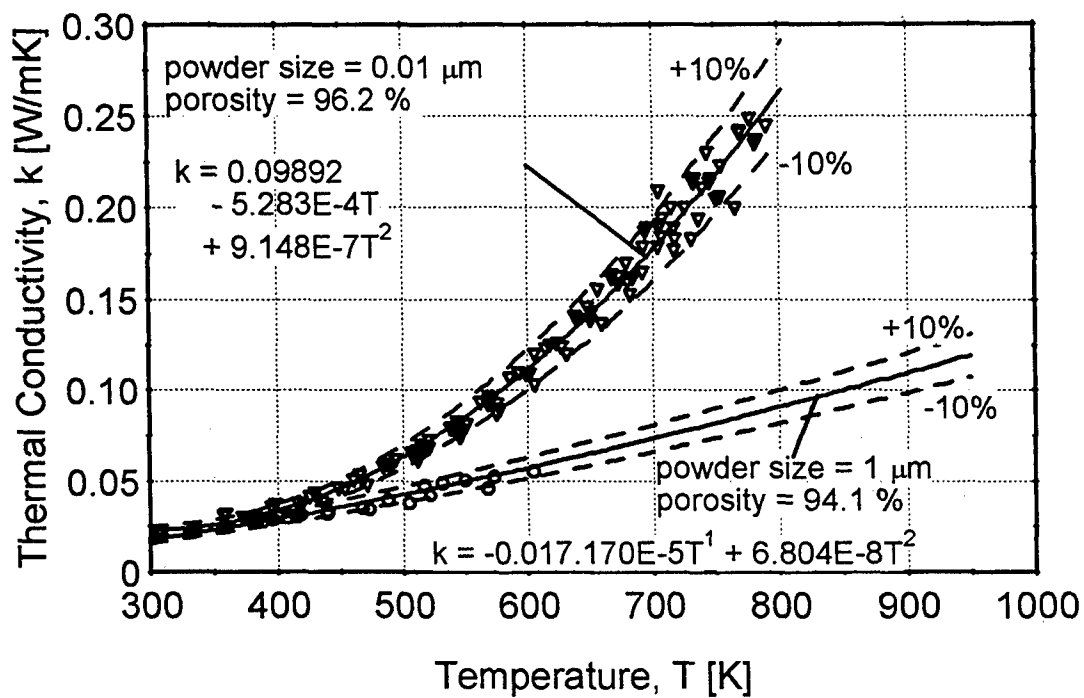


Figure 7.5. Measured Thermal Conductivities of Alumina Powders in Vacuum.

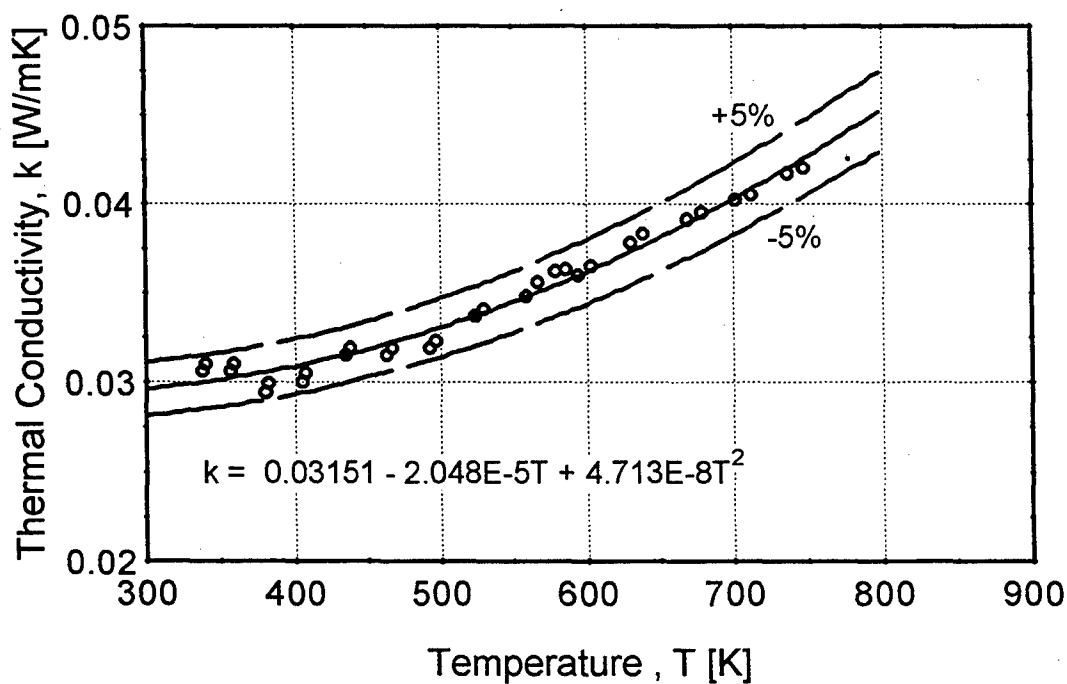


Figure 7.6. Measured Thermal Conductivities of Molded Min-K.

$$k_{i,i+1} = \frac{Q \ln(r_{i+1}/r_i)}{2\pi L_{\text{eff}}(T_i - T_{i+1})}, \quad (7.4)$$

where  $k_{i,i+1}$  is the average thermal conductivity of the material at a temperature  $T_{i,i+1} = (T_i + T_{i+1})/2$ ; and  $Q$  is the total heat generated by the electric heater along its effective length,  $L_{\text{eff}}$ . These temperatures were obtained from the measured radial temperature distributions in the test materials (Equation 7.1 and Figure 7.4). The determined values of the thermal conductivity of the alumina powders and of the Min-K are presented and correlated in the following section.

#### 7.4.2 Thermal Conductivity Values and Correlations

The results presented in Figure 7.5 show that the thermal conductivities of the alumina powders are strong functions of temperature. The thermal conductivity of the smaller particle powder is higher and increases more rapidly with increasing temperature. For example, at 500 K, the thermal conductivities for the 0.01  $\mu\text{m}$  and 1  $\mu\text{m}$  powders are 0.0423 and 0.0635 W/m.K, increasing to 0.0723 and 0.178 W/m.K, at 750 K, respectively.

The thermal conductivity of the molded Min-K in vacuum also depends on temperature (Figure 7.6). It increases with increased temperature, but is lower than those of the alumina powders, particularly at high temperatures (Figure 7.5). In the temperature range from 340 K to 740 K, the thermal conductivity of molded Min-K increases from 0.03 W/m.K to 0.041 W/m.K. The low-temperature-value is almost the same as that of the 1  $\mu\text{m}$  alumina powder (0.025 W/m.K), but the high-temperature value is about one fifth of that of the 1  $\mu\text{m}$  alumina powder (0.205 W/m.K). The thermal conductivity values of molded Min-K are even lower than those of still air. At 400 K and 700 K, the thermal conductivities of molded Min-K are 0.0310 W/m.K and 0.04 W/m.K, respectively. These values are comparable to that of air at 400 K (0.0338 W/m.K), but about 24% lower than that of air at 700 K (0.0524 W/m.K).

The determined thermal conductivities of the three insulation materials tested in vacuum were correlated as functions of temperature, as:

##### (a) Alumina powder (1 $\mu\text{m}$ particle size):

$$k \text{ (W/m.K)} = 0.099 - 5.28 \times 10^{-4} T + 9.15 \times 10^{-7} T^2, \quad \text{for } 340 < T < 760 \text{ K}; \quad (7.5)$$

##### (b) Alumina powder (0.01 $\mu\text{m}$ particle size):

$$k \text{ (W/m.K)} = -0.01 + 7.17 \times 10^{-5} T + 6.8 \times 10^{-8} T^2 \quad \text{for } 350 < T < 900 \text{ K}; \quad (7.6)$$

##### (c) Molded Min-K:

$$k \text{ (W/m.K)} = 0.032 - 2.0 \times 10^{-5} T + 4.71 \times 10^{-8} T^2, \quad \text{for } 340 < T < 740 \text{ K}. \quad (7.7)$$

As shown in Figures 7.5 and 7.6, these correlations are in good agreement with the data. Equations (7.5) and (7.6) are within  $\pm 10\%$  of the alumina powders data, and Equation (7.7) is within  $\pm 5\%$  of the Min-K data.

The thermal conductivities of the alumina powders are compared with that of the molded Min-K in Figure 7.7. As delineated in this figure, at temperatures  $> 400$  K, the thermal conductivity of Min-K is 22% and 55% of those of the  $1\ \mu\text{m}$  and  $0.01\ \mu\text{m}$  alumina powders, respectively. Below 400 K, the thermal conductivity values for all three insulation materials are almost the same,  $\sim 0.028$  W/m.K. The thermal conductivity of molded Min-K is the least dependent on temperature.

### 7.4.3 Comparison of Conductances of Min-K and Multi-Foils

The thermal conductance of multi-foils insulation consisting of 60 and 240 molybdenum foils,  $7.62\ \mu\text{m}$  thick, separated by  $125\ \mu\text{m}$  gaps, are calculated and compared with those the Min-K as functions of the hot side temperature. The multi-foil insulation perpendicular conductance is expressed as:

$$k_{mf}^{\perp} = A h_r, \quad (7.8a)$$

where

$$h_r = \left( \sigma \epsilon_{\text{eff}} / (n+1) \right) (T_h^2 + T_c^2) (T_h + T_c). \quad (7.8b)$$

In this equation, the radiation view factor for the foils was taken as unity.

In the axial direction, the conductance of the multi-foils insulation is given as:

$$k_{mf}^{\text{ax}} = k_m \left[ (n+1) \delta_f + n \delta_x \right] [w/L_x], \quad (7.9)$$

where  $\delta_x$  and  $\delta_f$  are the spacing between foils and the metal foil thickness (m), respectively,  $n$  is the number of multi-foils,  $\epsilon_{\text{eff}}$  is the effective emissivity of the foils as a function of temperature,  $\sigma$  is the Stefan-Boltzmann constant ( $5.6697 \times 10^{-8}$  W/m<sup>2</sup>.K<sup>4</sup>),  $k_m$  is the thermal conductivity of the foils material,  $T_h$  and  $T_c$  are the temperature at the hot and cold sides of the multi-foils insulation, respectively,  $A$  is the cross-sectional area of the foils that is perpendicular to the heat flow, and  $w$  and  $L_x$  are the width and the axial length of the multi-foils insulation, respectively.

The calculated conductance for the 60 and 240 multi-foils insulations, both in the perpendicular and axial directions, are compared with those of the Min-K for a cold side temperature of 320 K and hot side temperatures from 320 K to 1000 K, in Figures 7.8a and 7.8b. In these figures,  $L_n$  indicates the thickness of the Min-K that is equal to that of an "n" multi-foils insulation. As

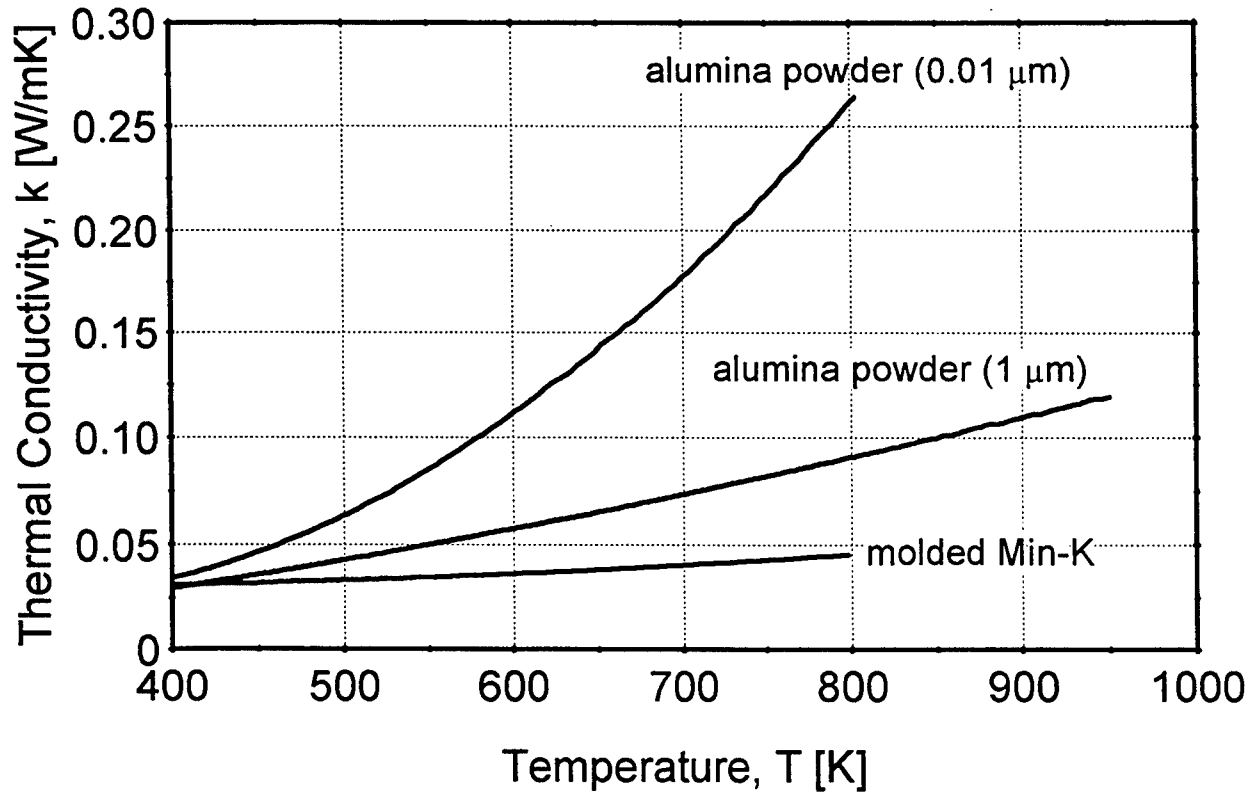


Figure 7.7. Comparison of Thermal Conductivity Correlations.

Figure 7.8a shows, the thermal conductance of the 60 and 240 multi-foils insulation in the perpendicular direction are about three orders of magnitude lower than that of the Min-K, for the same thickness. Conversely, in the axial direction, since the thermal conductivity of the molybdenum foils is higher than that of the Min-K at the same temperature, the axial conductance of the 60 and 240 Molybdenum multi-foils are an order of magnitude higher than that of the Min-K (Figure 7.8b).

Based on these results, it is concluded that the multi-foils insulation is far superior to the Min-K when the wall temperature is uniform, and the heat flow is in the perpendicular direction to both the wall and the foils. However, when there is a steep temperature gradient in the wall, as near the condenser of PX-series AMTEC cells, the multi-foils are inferior to the Min-K.

## 7.5 SUMMARY AND CONCLUSIONS

The thermal conductivities of two particle-size alumina powders and molded Min-K insulation materials were determined experimentally in vacuum, as functions of temperature in the range from 340 to 900 K. The developed thermal conductivity correlations for the alumina powders were in agreement with the experimental data to within  $\pm 10\%$ , while that for the Min-K was within  $\pm 5\%$  of the data. The thermal conductivities of all three materials are strong functions of



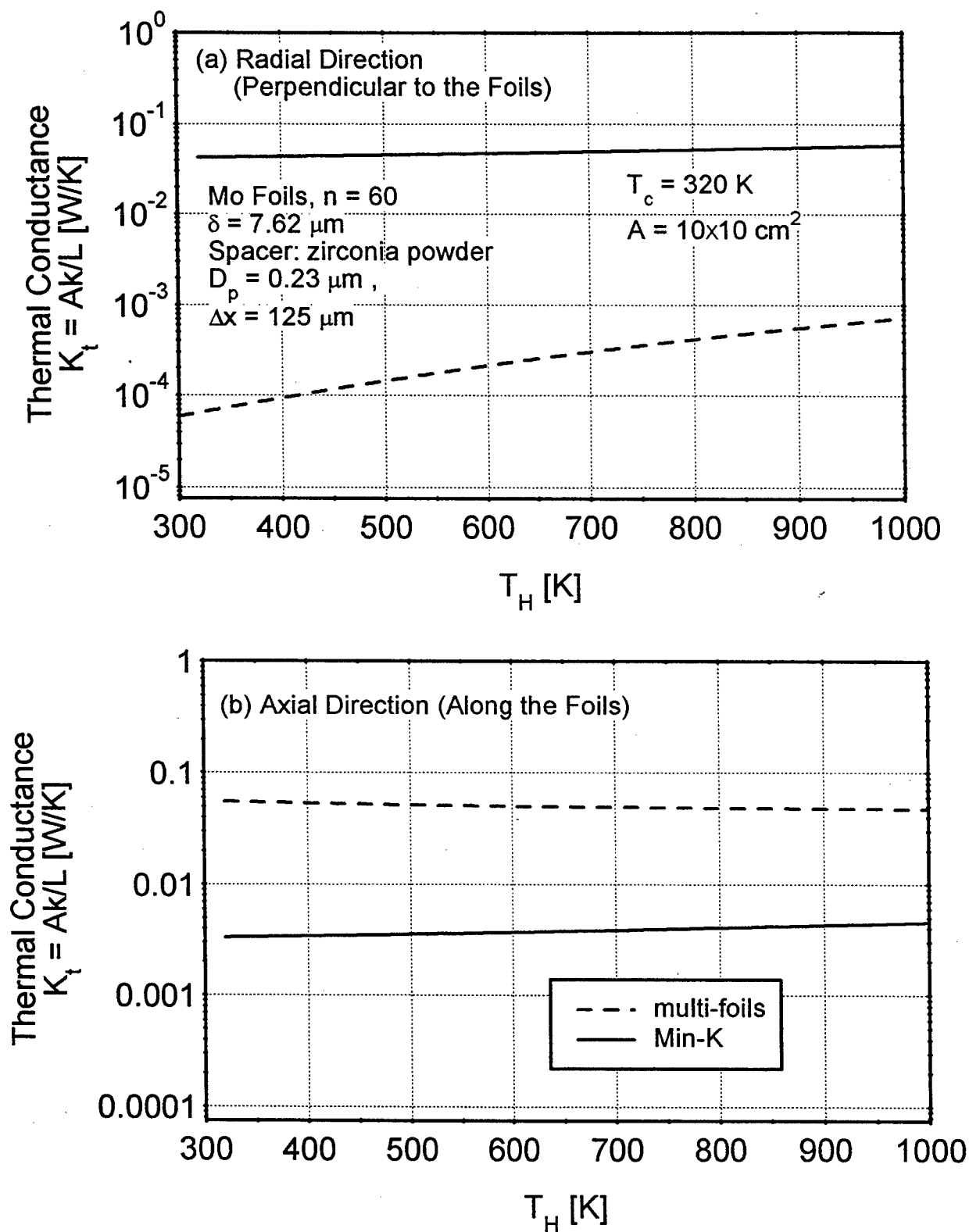


Figure 7.8. Comparison of Thermal Conductance of Multi-Foils Insulation and Min-K. (a) in Perpendicular Direction; (b) in Axial Direction.

temperature, increasing with increased temperature above 400 K. Below 400 K, all three materials have similar thermal conductivity. The thermal conductivity of the alumina powder having a particle size of 0.01  $\mu\text{m}$  increased faster with increased temperature, followed by the 1  $\mu\text{m}$  alumina powder, then the molded Min-K. The Min-K has the lowest thermal conductivity of all three materials above 400 K.

The low thermal conductivity and density of the Min-K make it a good insulation material for AMTEC cells near the condenser, where there is a large temperature gradient along the cell wall. In the portion of the cell near the heat source, however, where the wall temperature is almost uniform, the multi-foils insulation should be used. The thermal conductance of the latter could be three orders of magnitude lower than that of the Min-K, for the same thickness and hot and cold side temperatures.

In the next chapter, the single-cell and multi-cell experimental setups designed at AFRL and the data acquisition procedure used in the test are described in details.

## 8. EXPERIMENTAL SETUP AND PROCEDURES

In this chapter, the single-cell and multi-cell experimental setups designed at AFRL and the data acquisition procedure used in the test are described in details.

The experimental setup for single-cell tests at the Air Force Research Laboratory consisted of test setup, cell electric circuit, vacuum system, air cooling system, and data acquisition system (Figure 8.1). The whole experimental setup is monitored and controlled by a computer-controlled data acquisition system, using the software LabView. Two test procedures were used in the experiments: constant electric power and constant hot and cold end temperatures.

### 8.1 NOMENCLATURE

$I$	Measured cell current (A)
$Pe$	Measured cell electric power output, $Pe = IV$ ( $W_e$ )
$Q_{in}$	electric heater power (W)
$R_A$	Shunt resistor ( $\Omega$ )
$R_{ext}$	total external load resistance ( $\Omega$ )
$R_{int}$	Internal cell impedance ( $\Omega$ )
$R_L$	Multi-resistor box resistance ( $\Omega$ )
$T_{cond}$	Cell's cold end temperature (K)
$T_{ev}$	Cell's evaporator temperature (K)
$T_{hot}$	Cell's hot end temperature (K)
$T_{high,i}$	Cell's condenser high temperature limits for watch dog (K)
$T_{low,i}$	Cell's condenser low temperature limits for watch dog (K)
$T_\beta$	Measure BASE tube temperature (K)
$T_{\beta,1}$	Cell's BASE tube high temperature limit for watch dog (K)
$V$	Measured cell voltage (V)
$V_{ac,1}$	Vacuum limit for watch dog (torrs)

### 8.2 SINGLE-CELL TEST SETUP

The test setup comprised a cell and its heating, cooling, and insulating components, which included: a cell heater, a heater support, a copper cold plate, a cooling air loop, an insulation package, a structure support plate, and distributed thermocouples, see Figures 8.2a and 8.2b.

Surrounded by thick insulation, the cell was heated by the cell (Boroelectric) heater sitting on the heater support. The heater support, made of solid Boron Nitride, sit on the top of the cell, see Figures 8.3a and 8.3b. It held the cell heater at the exact top center of the cell with a 3.2 mm gap between the cell and the heater. The heater support electrically isolates the cell from the heater.

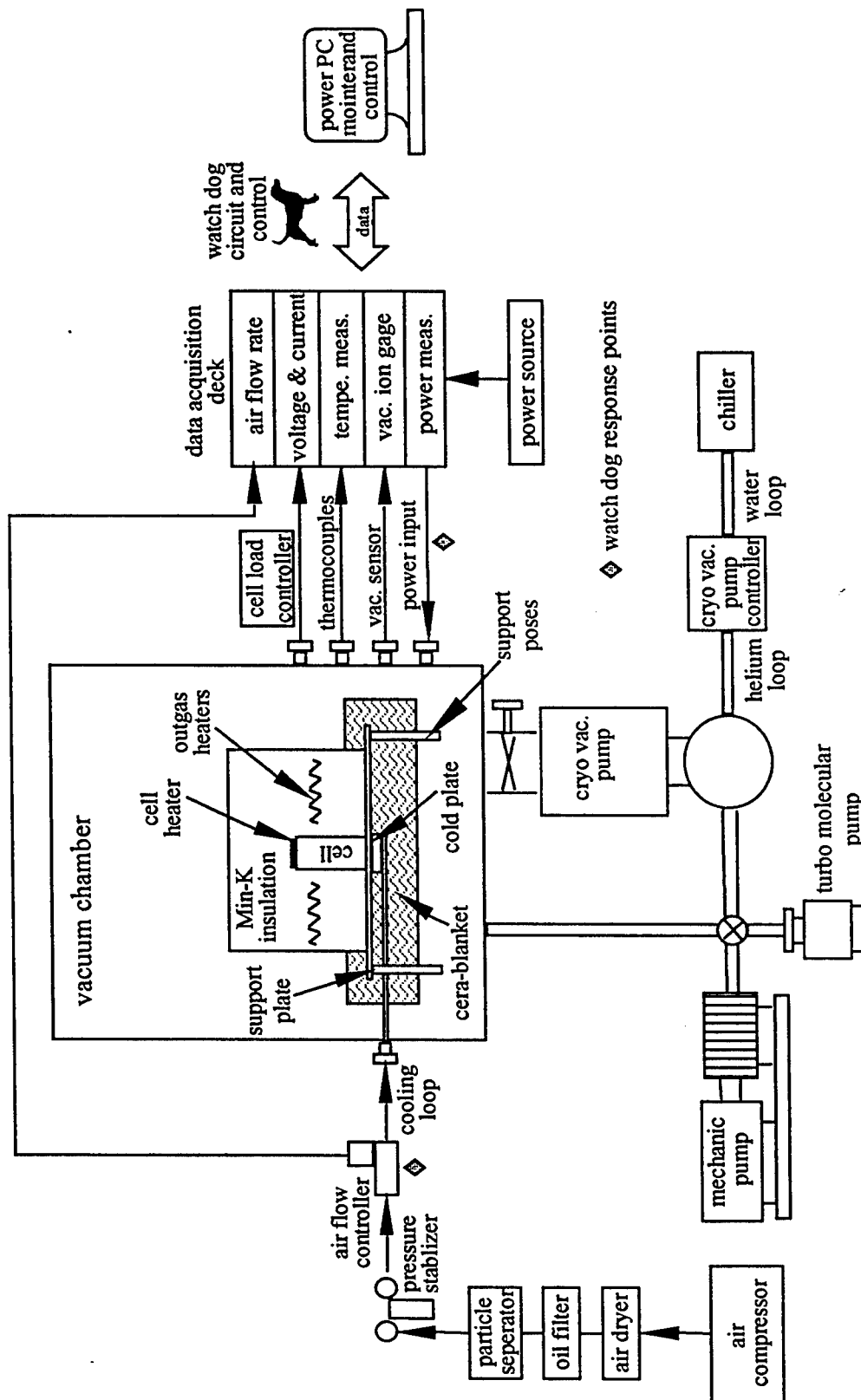


Figure 8.1. Experimental Flow Chart for Single-Cell Tests at AFRL.



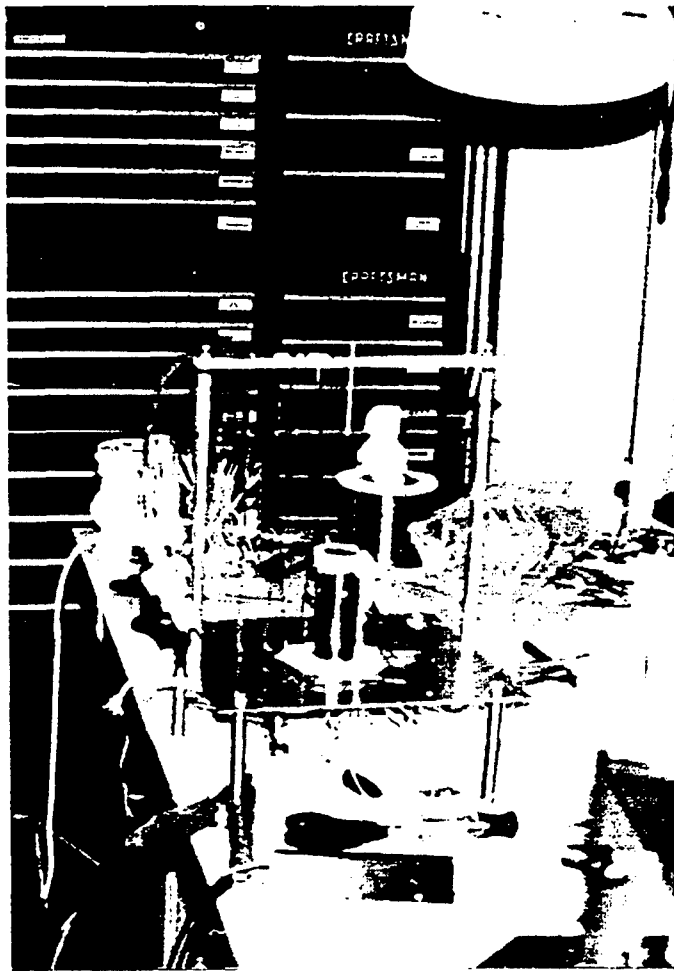
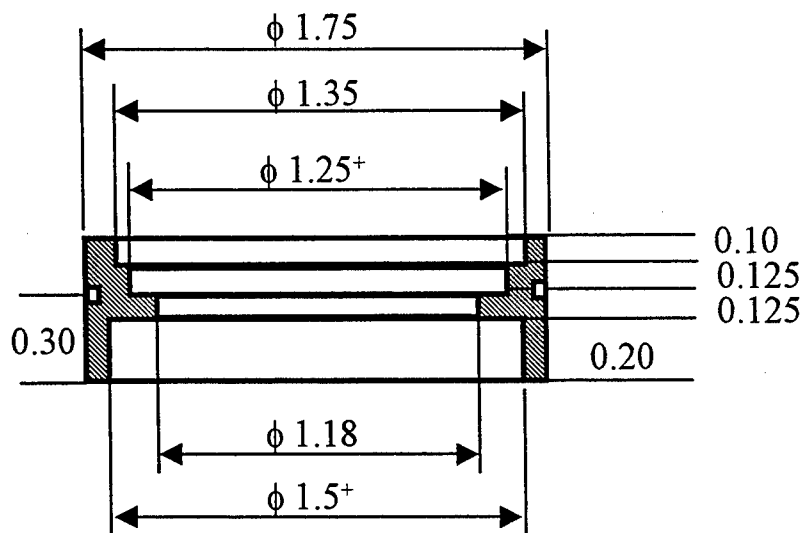


Figure 8.2b. Photograph of Single-Cell Test Setup.

The cell heater is coupled with the cell top either radiatively (gap between them) or conductively (Boron Nitride powder paste).

Heat was removed from the cell condenser by an air calorimeter. The cooling air ran through a copper tube that was brazed onto the cold plate, Figure 8.3c. The cold plate was conductively coupled to the cold end of the cell, the gap between them was filled with the Boron Nitride powder. The air inlet and outlet temperatures and flow rate in the calorimeter were measured in the tests, to allow for the calculation of the heat rejected at the cold end of the cell.

The whole test setup was supported by the structural support plate made of stainless steel, Figure 8.3d. It held the cold plate (therefore the cell) through four alumina standoffs or rods. The standoffs electrically (and thermally) isolated the cold plate, which acted as the negative electrode of the cell, from the structural support plate. The structural support plate has four poses on the bottom to stand on the vacuum chamber and to allow sufficient space for the air loop and bottom insulation, Figure 8.3d. The solid insulation package sit on the top of the structural support plate.



All dimensions are in inches.  
Material: Boron nitride

Figure 8.3a. Boroelectric Heater Block.

To minimize thermal heat losses, and maximize the conversion efficiency of the cell, the tested cell was surrounded by a large volume of insulation material, Figure 8.3e. Several insulation materials and configurations were tested during the early cell tests, which culminated in the selection of molded Min-K as the insulation material of choice for the cell test. The insulation consists of three disks of Molded Min-K, with a diameter of 203 mm and thickness of 76.2 mm each, Figure 8.3f. The interfaces between the disks were grooved to create an interlocking surface to block the direct radiation path through the interface. The central hole, 50 – 76 mm in diameter depending on the cell dimension, was machined through the bottom and middle disks to accommodate the cell. The gap between the hole and cell wall was filled with 1  $\mu\text{m}$  alumina powder to have a tight fit around the cell, and prevent radiative heat from traveling vertically along the cell wall/insulation interface, see Figure 8.2a. In order to reduce the outgassing period, two home-made outgassing heaters with Kanthal wires, were laid on the interface of Min-K disks. The three Min-K disks were held tightly by two threaded poses on the structural support plate.

In some of the early single-cell tests, more-than thirty K-type thermocouples were distributed along the cell wall and in the surrounding insulation, to obtain the temperature profiles in the setup, see Figure 8.2a. Three (or four) platinum-shielded thermocouples, which can withstand high temperature, were used for the cell-function-temperature measurement through the cell top; one (or two) were inserted into the thermocouple well(s) for the cell evaporator; another one inserted into the well for one of the BASE tubes; and one located at the center of the cell hot end. One stainless-steel-shielded thermocouple was located at the cold end surface to measure another cell-function-temperature, the condenser temperature. About ten stainless-steel-shielded thermo-

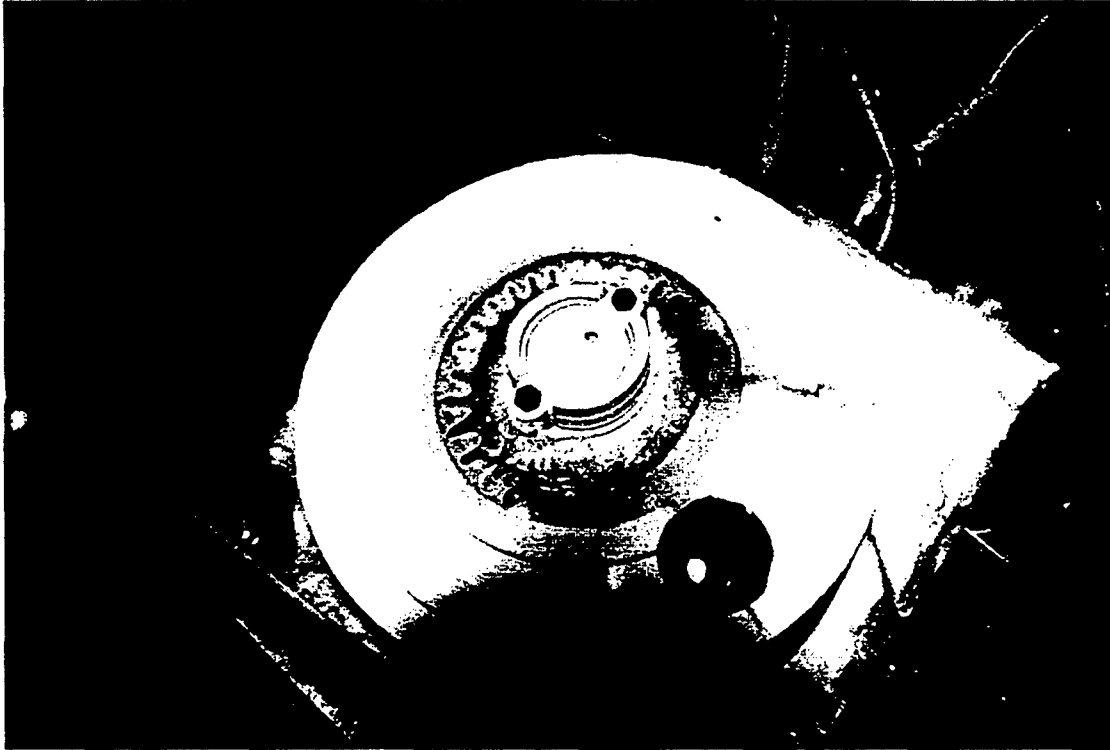


Figure 8.3b. Photograph of Cell's Heater Block.

couples (depending on the length of the cell) were tightened on the cell side wall, using gauge 30 stainless steel wires, to measure the temperature gradient along the side wall.

In some of the early single-cell tests, over fifteen home-made fiber-glass-shielded thermocouples were arranged on the top, side, and bottom surfaces of the insulation (practically 3.2 mm deep from the surface) to measure the insulation temperature profile, see Figure 8.2a. The measured temperature profiles can be used to calculate the heat losses through the insulation package and evaluate the insulation performance, using a two-dimensional conduction heat flow model developed in this work (see Chapter 10, Section 10.2 – 10.4).

### 8.3 VACUUM SYSTEM

The vacuum system for the single-cell test consists of a vacuum chamber (Figure 8.3g), a roughing (turbo) vacuum pump, a cryogenic pump with helium loop, and a water chiller (Figure 8.1). A water/ethylene glycol chiller is used to cool the cryogenic pump compressors and the turbomolecular pumps. There are four vacuum systems available in the lab, and all four can be put into operation at the same time. Every vacuum chamber had its vacuum pump system and had about over ten feed-through flange for power and instrumentation lead going through. One vacuum system has a horizontal stainless steel chamber with a inner diameter of 44.5 cm inch and a length of 61 cm. The second is a vertical stainless steel chamber with an inner diameter of 53





Figure 8.3c. Photograph of Cell's Cold Plate and Air Calorimeter Loop.

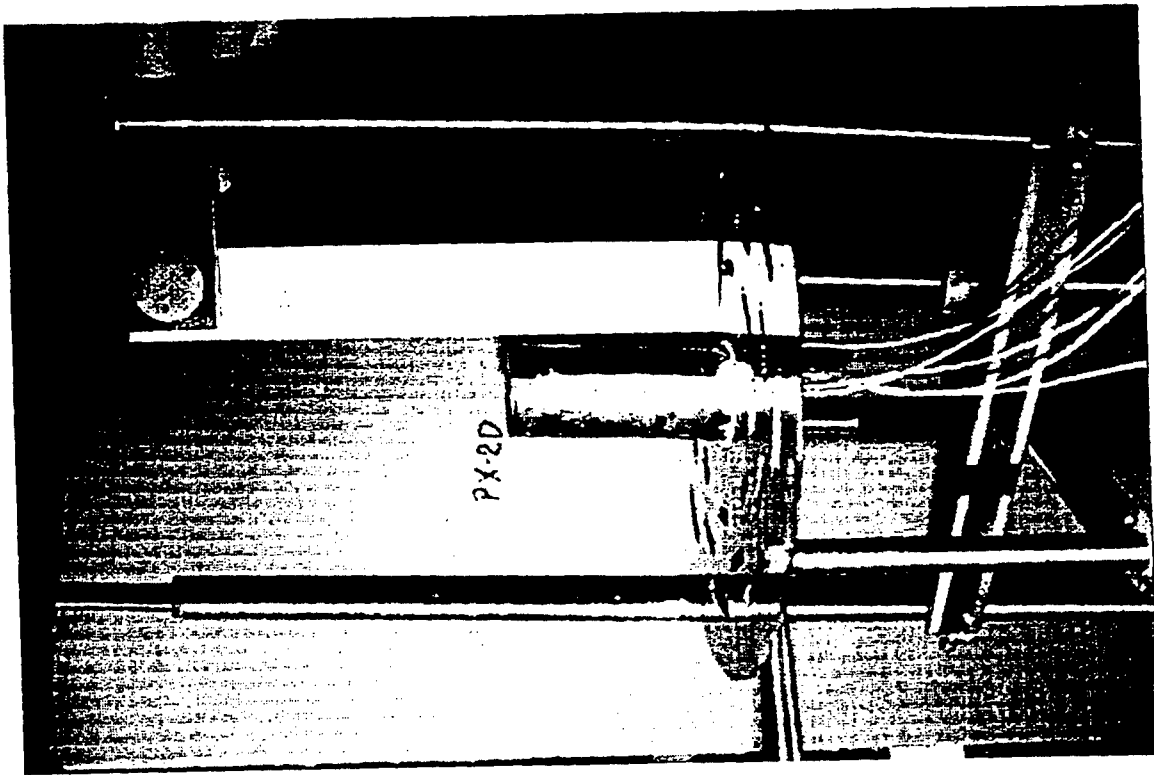


Figure 8.3d. Photograph of Test Setup Support Structure.

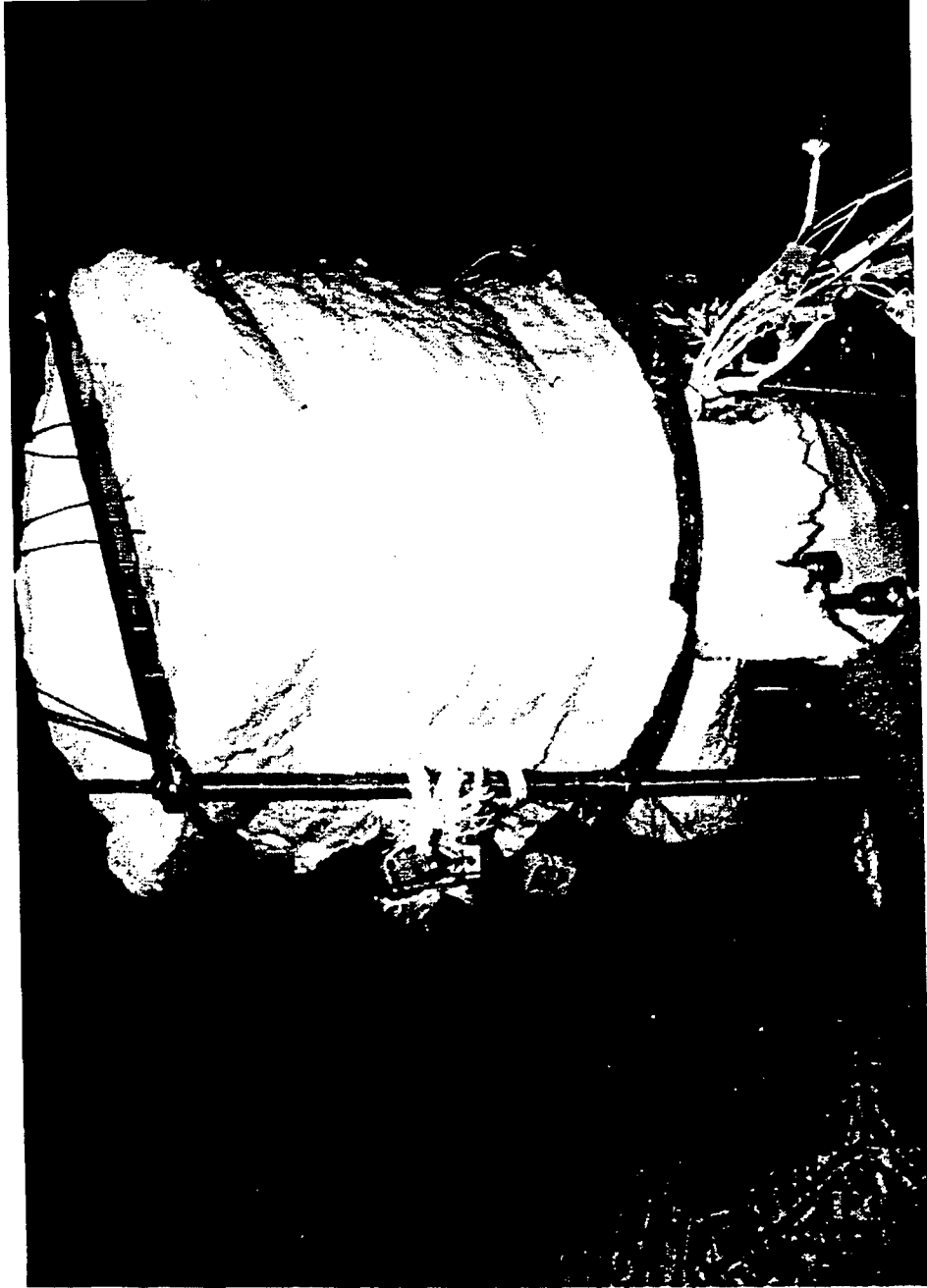


Figure 8.3e. Photograph of Cell's Insulation Package.

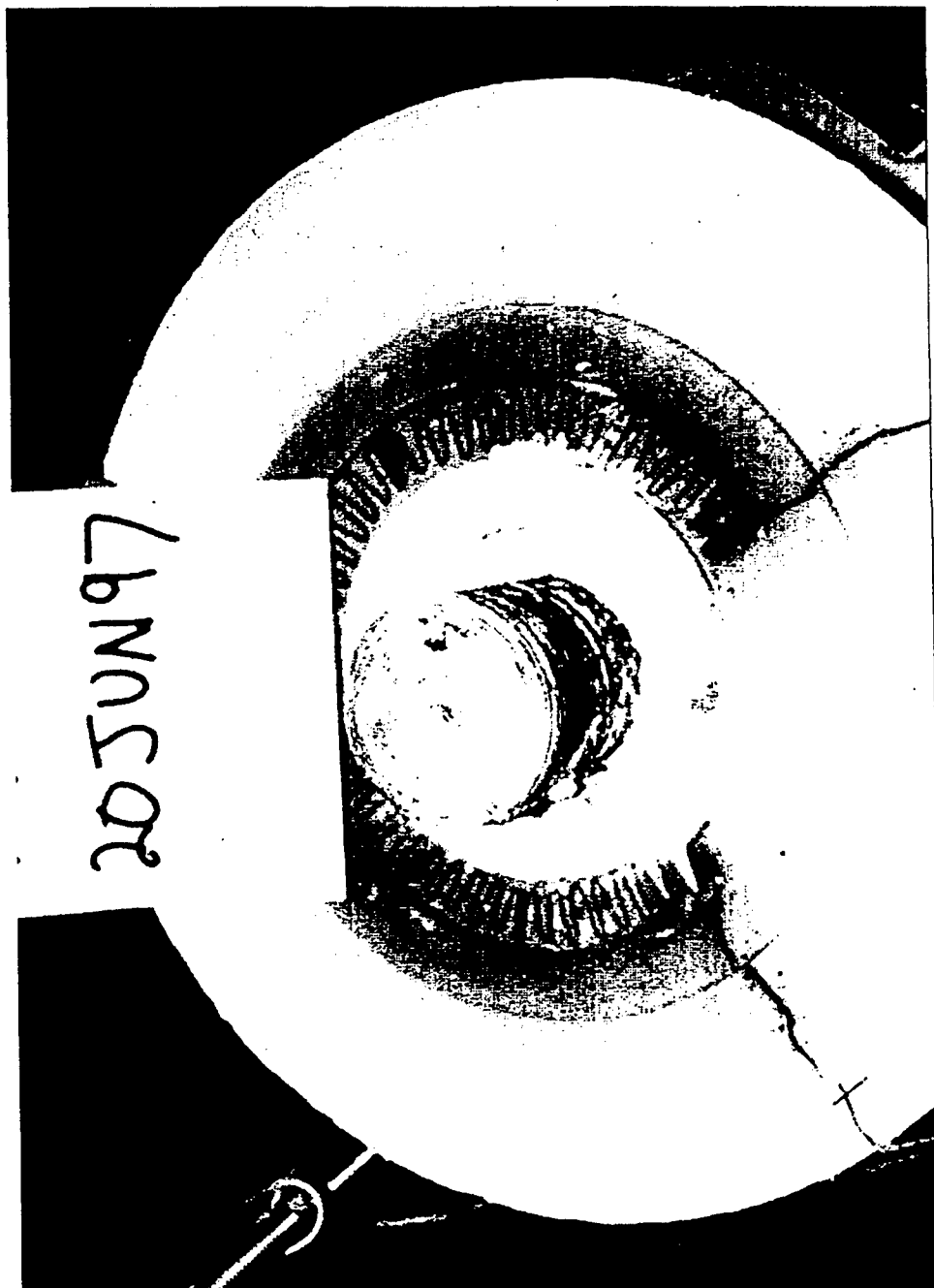


Figure 8.3f. Photograph of Cell's Min-K Insulation Disks.

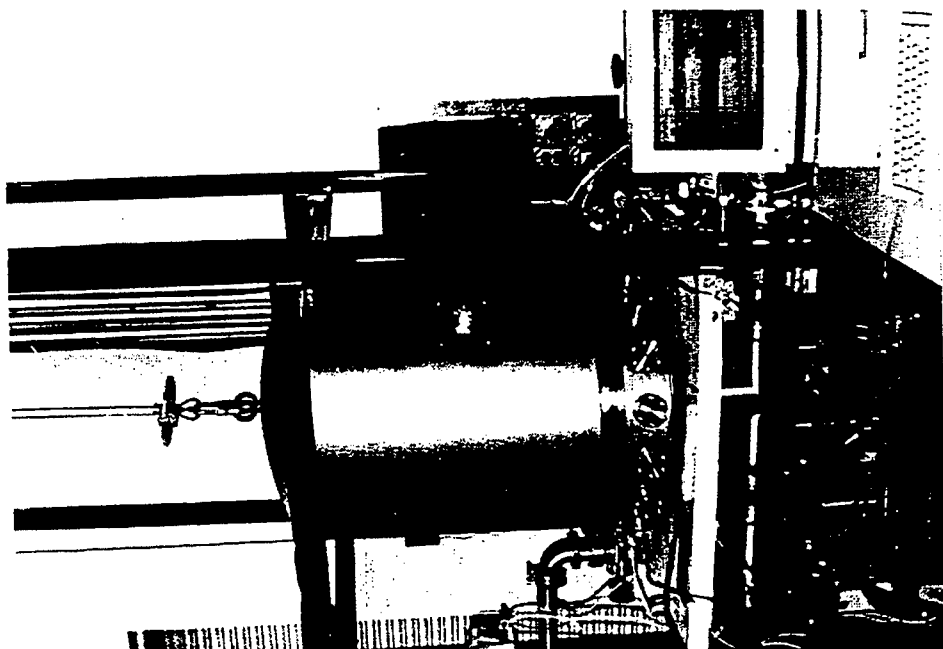


Figure 8.3g. Photograph of Vacuum Chamber.

cm and a height of 84 cm. The other systems are two vertical glass chambers with an inner diameter of 44 cm and height of 88 cm. The roughing pump can provide a vacuum up to the order of  $10^{-3}$  torrs, and the turbomolecular pump and cryo-vacuum pump can provide a hard vacuum  $< 10^{-7}$  torrs. The former is used in outgassing, and the later is used for maintaining high vacuum level during tests. The cryogenic pumps need to be regenerated at least once a month during continuous testing. Two ion vacuum sensors are used to measure the vacuum level. A Pirani gauge is used for low vacuum ( $>10^{-4}$ ), and an ion gauge is used for high vacuum.

## 8.4 COOLING SYSTEM

The cooling system consists of an air compressor, three filters/dryers, a pressure stabilizer, an air flow sensor/controller, flow tubing on the cold plate, and thermocouple locators (T-connector). The pressurized air from the compressor passes through three filters to remove the water vapor, oil, and micro-particles contained in the air line. The air pressure is controlled and stabilized by a pressure stabilizer at about 40 psi. Air flow rate is measured and controlled (0 to ~20 liter/min) by an electronic flow meter/controller. The controller measures the mass flow rate, which is converted into volumetric flow rate at the standard condition by the data acquisition software. The inlet air temperature is measured at a location far from the cold plate, while the outlet temperature is measured just about two inches from the cold plate. The temperature difference between outlet and inlet and the air flow rate allow the prediction of the heat carried by the cooling air in the experiment. Air lines from the cold plate are connected to the vacuum chamber feed-through using Cajun VCR type fitting to ensure vacuum integrity during thermal cycling.

## 8.5 CELL ELECTRIC CIRCUIT

The electric performance of a cell was measured using the circuit shown in Figure 8.4. The electric power output of the cell under test was determined from the measured cell voltage,  $V$ , and current,  $I$ . The voltage was measured at the power leads of the cell, while the current was determined from the measured voltage across a shunt resistor,  $R_A = 0.01 \Omega$  (Figures 8.4 and 8.5).

In the tests, the load resistance,  $R_L$  was varied by changing the combination of precision resistors in a multi-resistor box. As shown in Figure 8.5,  $R_L$  did not include the resistance of the connecting wires and contact points, which are difficult to determine accurately. To simplify the circuit and process experimental data, the total resistance in the circuit was divided into internal resistance,  $R_{int}$ , and external resistance,  $R_{ext}$ .

$R_{int}$  is the total internal impedance of the AMTEC cell that includes the internal cell's resistance, leakage current losses, and charge-exchange and polarization losses.  $R_{ext}$  includes all resistances outside the cell (including load resistance,  $R_L$  and contact/lead resistances).  $R_{ext}$  is easily obtained by dividing the cell output voltage,  $V$  by the measured current,  $I$ :

$$R_{ext} = \frac{V}{I}. \quad (8.1)$$

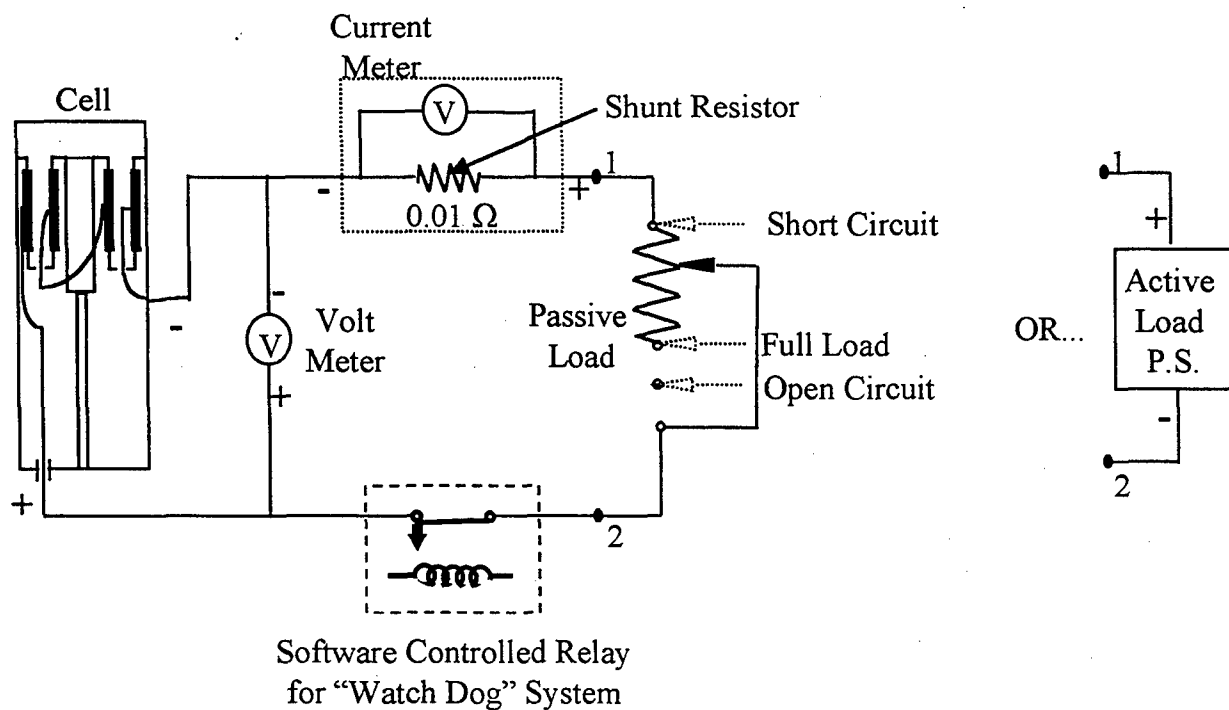


Figure 8.4. Electric Circuit Measurement for Single-Cell Test.

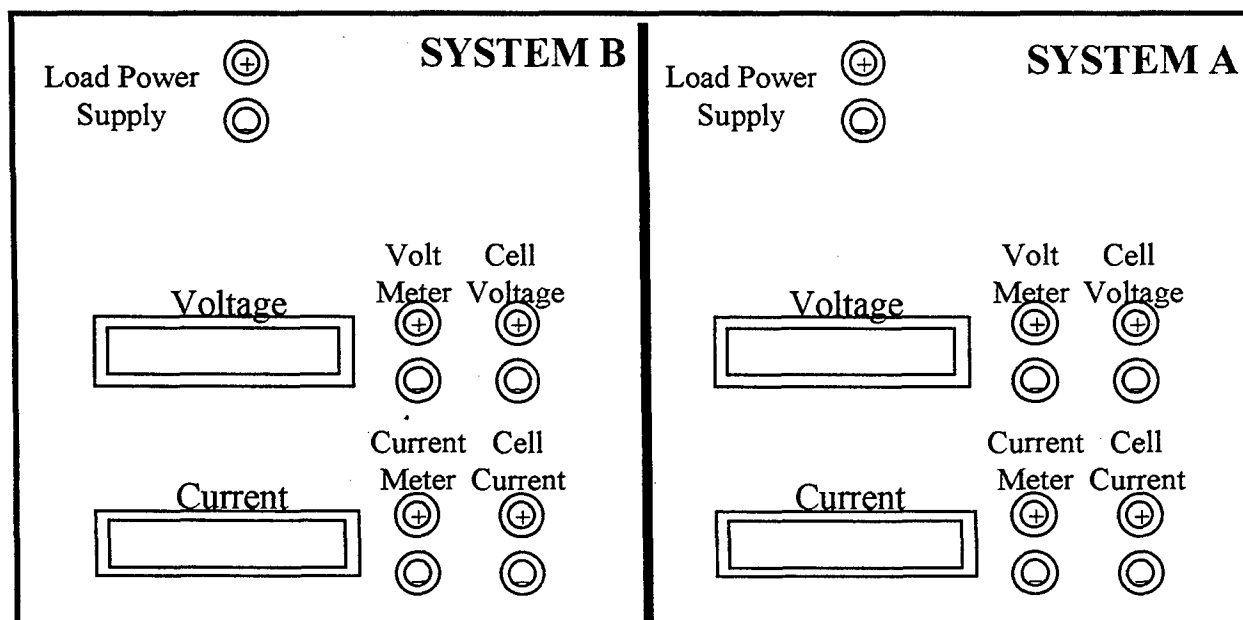


Figure 8.5. Power Measurement Control Panel.

## 8.6 DATA ACQUISITION SYSTEM AND WATCH DOG

The data acquisition system reads the measured parameters (current, voltage, temperature, air flow rate, and vacuum level) from the sensors (through data acquisition equipment) and controls the power input to heaters and the cooling air flow rate. The data acquisition system uses an HP3352 Data Acquisition controller configured with voltage multiplexer cards, thermocouple multiplexer cards, voltage/current DAC cards, and general purpose switch cards. Voltage signals from measurement sensors were read by the HP3852, which allowed determination of thermocouple reading, heater and cell current and voltage, and cooling air flow rate. The system was controlled by a power PC, using the Labview software.

In addition, the vacuum level is read through a GPIB interface (from an Infocon controller). The HP3852 uses a voltage DAC card to output a voltage which controls the air flow rate. A "watch dog" system (described below) uses general purpose switches in the HP3852 to control the heater power, cell circuit, and an autodialer. The HP3852 is interfaced to a PowerMac which converts voltages to their respective units and logs the data to a data file. Data is updated on the screen every 2 seconds and can be written to the hard disk every 5 seconds to 15 minutes (user selectable). A new data file is started at 00:00 hours each day and is written into a directory with a name convention for the date recorded. The recorded data is backed up daily to an Iomega Zip drive.

A data acquisition software was developed using Labview to monitor all temperatures, electric power, air flow rate, and chamber vacuum level, see Figure 8.1. All measured parameters are shown on the computer screen. The cooling air flow rate was controlled from the computer. The measured experimental data was automatically recorded into the data file every minute to track the experimental status. One such data file is produced every day with the date mark.

To prevent the cell from being overheated or overcooled (the sodium working fluid must remain molten) accidentally, a "watch dog" circuit was designed and built in the lab based on the analysis of possible accidents causes (Figure 8.4). The circuit consisted of relays and an autodialer, controlled by the data acquisition software (Figures 8.6 and 8.7). A "watch dog" circuit shuts down the system in a safe manner if automated recovery is not possible.

First, the condenser temperature,  $T_{cond}$ , is monitored, since too low a temperature causes freezing of sodium in the condenser, and too high a temperature might cause brazing or material problem at the condenser, see Figures 8.6a and 8.7a. Two low condenser temperature limits,  $T_{low,1}$  and  $T_{low,2}$ , and two high condenser temperature limits,  $T_{high,1}$  and  $T_{high,2}$ , were set, where  $T_{low,1} < T_{low,2}$  and  $T_{high,2} > T_{high,1}$ . If the condenser temperature goes to  $T_{low,2} < T_{cond} < T_{low,1}$ , the relay responses to cut cooling air flow to let the condenser temperature rise. If  $T_{cond}$  continues to decrease,  $T_{cond} < T_{low,2}$ , the cell circuit is shorted to allow more vapor flow to the cell condenser, see Figure 8.6a (control flow chart). On the other hand, if  $T_{cond}$  is too high,  $T_{high,1} < T_{cond} < T_{high,2}$ , the relay for cooling air flow sets the flow controller to have the maximum flow rate, and also the cell circuit is disconnected. If the condenser temperature continues to increase to  $T_{cond} > T_{high,2}$ , the electric power to the cell heater is disconnected to let the cell cool down, Figures 8.6c and 8.7b.



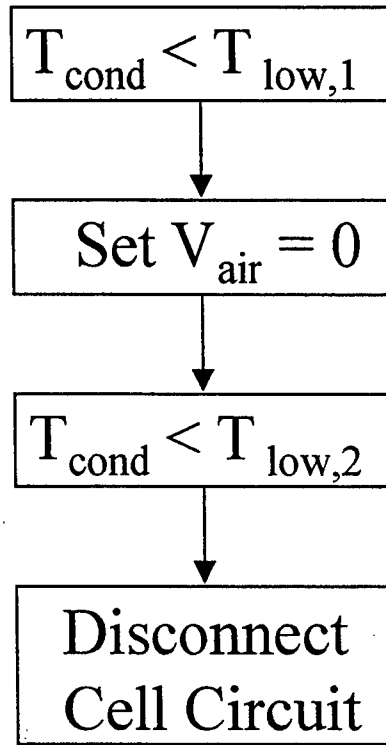


Figure 8.6a. Safety Chart for Condenser Temperature Control,  $T_{\text{low},1} > T_{\text{low},2}$ .

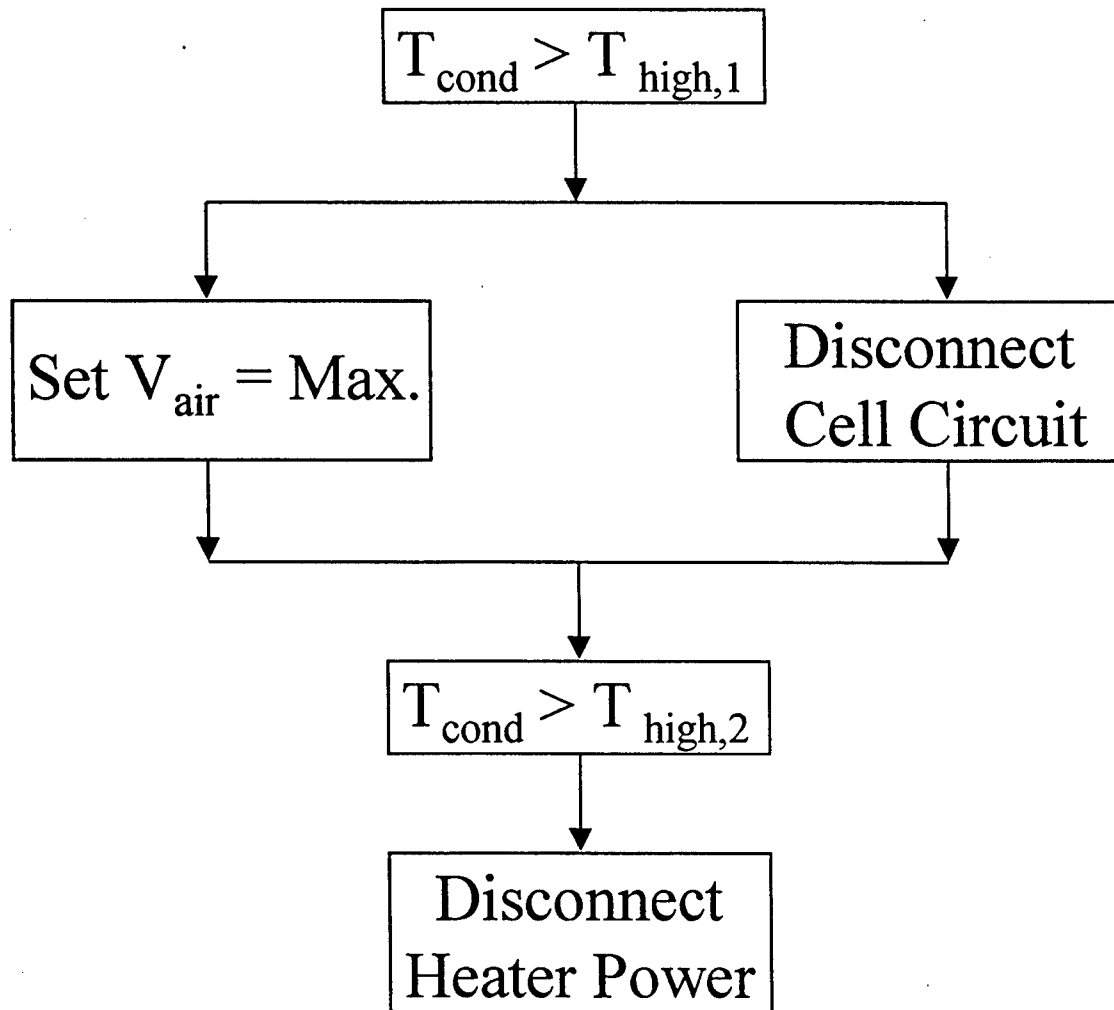


Figure 8.6b. Safety Chart for Condenser Temperature Control,  $T_{\text{high},2} > T_{\text{high},1}$ .

## Safety Control When BASE Temperature Is Lower Than Set Value

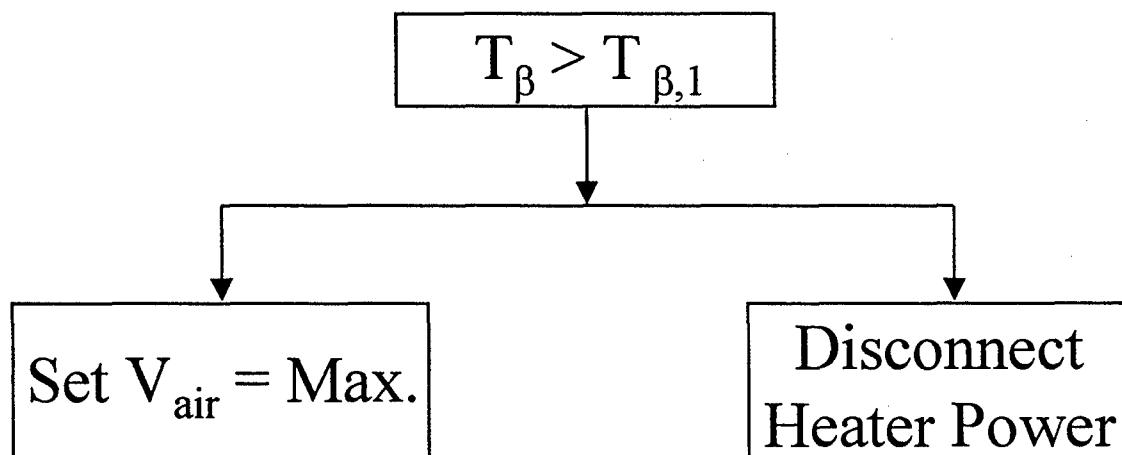


Figure 8.6c. Safety Chart for BASE Tube Temperature Control,  $T_{\beta} > T_{\beta,1}$ .

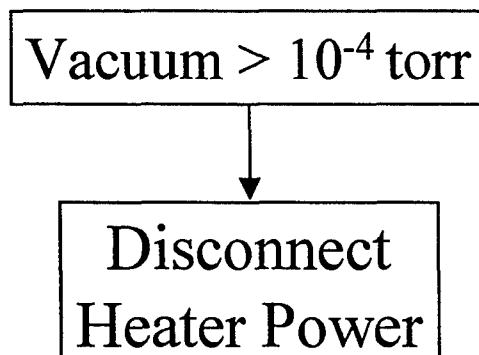


Figure 8.6d. Safety Chart for Vacuum Level  $> 10^{-4}$  torr.

In the mean time, the BASE temperature,  $T_\beta$ , is being monitored not to exceed the allowed maximum temperature,  $T_{\beta,1}$ , to prevent failure of the braze between the BASE tube and support plate. When  $T_\beta > T_{\beta,1}$ , the software sends a signal to the relays to set the cooling air flow to the maximum rate and disconnect the heater power to force the BASE temperature to come down.

The vacuum level was also monitored since a low vacuum level destroys the assumption of the simulation of the space environment and also causes serious oxidation of the heaters and insulation materials. When the vacuum level is lower than  $10^{-4}$  torr, the heater power is disconnected, see Figure 8.6d. Occurrence of any event mentioned above will close the relay for autodialer circuit to let the watch dog warn the person responsible for handling the event.

## 8.7 EXPERIMENTAL METHODOLOGY

In the cell tests, four parameters, heater heat input,  $Q_{in}$ , hot and cold end temperatures,  $T_{hot}$  and  $T_{cond}$ , and load (multi-resistor box) resistance,  $R_L$ , were controlled to study the thermal and electric performance outputs of the cell at specific combinations of three out of these four parameters. By controlling the power input to the heater and the cooling air flow rate, the cell could be operated at the desired  $T_{hot}$  and  $T_{cond}$ . By changing the external load resistance,  $R_{ext}$ , at fixed  $T_{hot}$  and  $T_{cond}$ , the cell I-V characteristic is measured. The electric power output of the cell under test is determined from the measured cell voltage,  $V$ , and current,  $I$ . Voltage was measured at the power leads of the cell, while the current was determined from the measured voltage across a shunt resistor,  $R_A = 0.01 \Omega$  (Figures 8.1 and 8.4).

Two categories of tests were conducted, constant heating power and constant temperature, depending on the test plan from the cell designer/manufacture and objectives of study in the lab. For the first category tests (mainly requested by designer/manufacture), the test starts from the nominal short circuit condition,  $R_L = 0$  (but  $R_{ext} \neq 0$ ). The cell is brought to the specified temperatures by varying the heating power to the cell heater and the cooling air flow at the condenser. The cell load is then increased using a passive decade resistance box or an active load (see Figure 8.4). As the load is varied, the heat input to the cell and the cooling air flow rate are held constant, while the cell temperatures change in response to the load change. For each load point, one and a half to two hours is required to reach full thermal equilibrium status.

The second category tests are mainly needed by the experimental parametric study, focusing on the effects of changing input parameters on the output performance. The tests were conducted by fixing two out of three parameters and varying the third one to examine the effect of the third parameter. The tests were divided into three groups, and the values of input parameters used in the tests were specified as following:

1) **Electrical Load Effect** under selected  $T_{hot}$  and  $T_{cond}$ , find  $R_L$  effect on I-V and  $R_{ext} \sim P_e$ :

$$R_L = 0 \sim \infty \Omega$$

$$\Delta R_L = 0.3 \Omega \text{ for } R_L \leq 1.5 \Omega,$$

$$\Delta R_L = 0.6 \Omega \text{ for } R_L \leq 3.3 \Omega,$$

$$\Delta R_L = 1.2 \Omega \text{ for } R_L \leq 5.5 \Omega$$

$$\Delta R_L = 2.0 \Omega \text{ to open circuit}$$

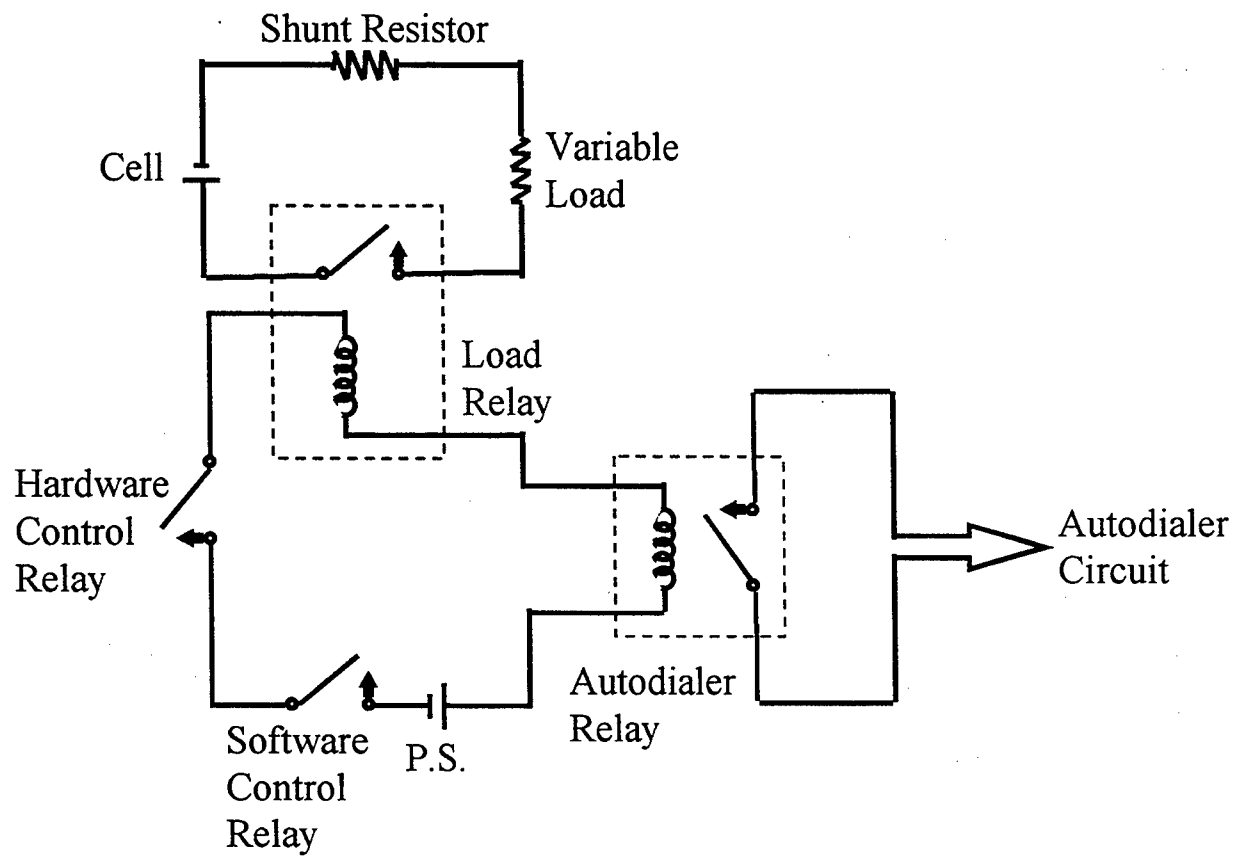


Figure 8.7a. Cell Load Safety Circuit.

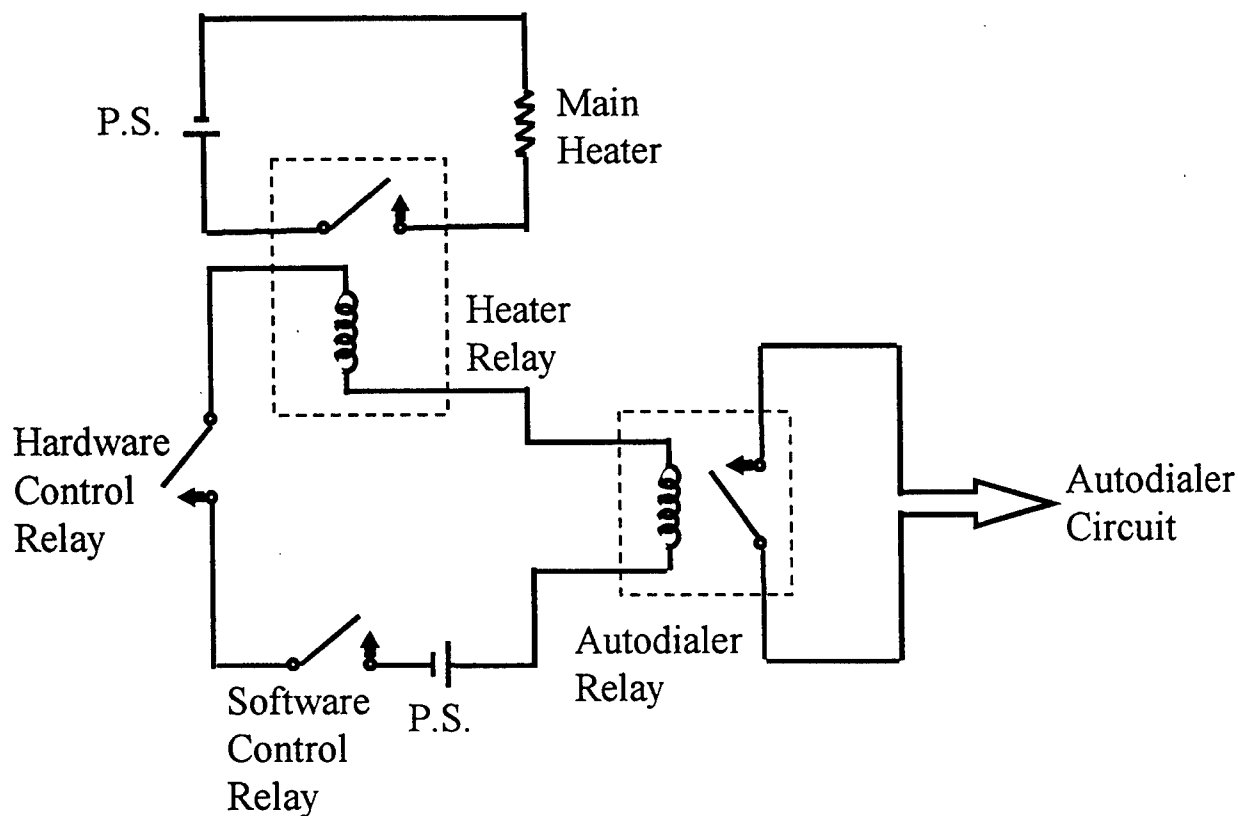


Figure 8.7b. Cell Heater Safety Circuit.

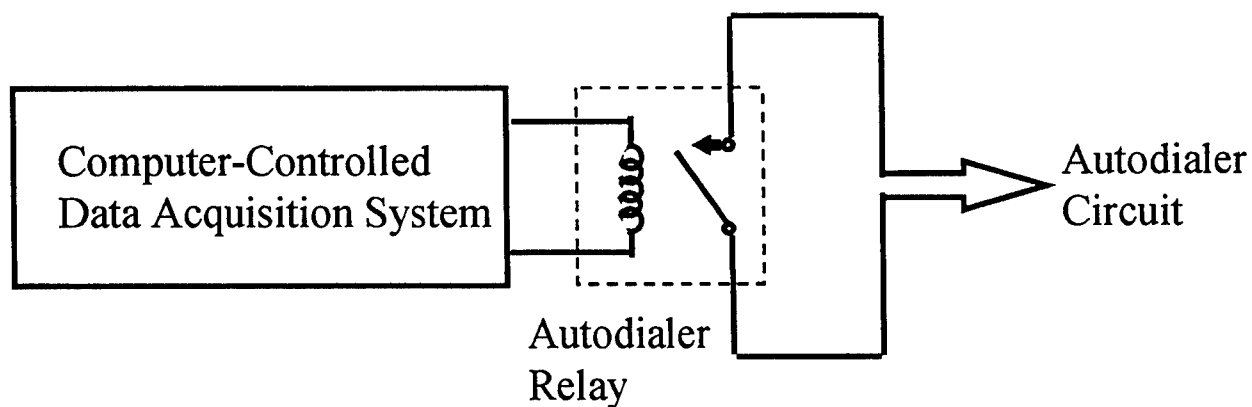


Figure 8.7c. Data Acquisition System Crash Protection Circuit.

(Note: in the tests,  $R_L$  was controlled, but  $R_{ext}$  was used in data processing.)

2) **Hot End Temperature Effect** under selected  $T_{cond}$  and  $R_{ext}$ :

$$T_{hot} = 973 \sim 1173 \text{ K}, \quad \Delta T_{hot} = 25 \text{ K}$$

3) **Condenser Temperature Effect** under selected  $T_{hot}$  and  $R_{ext}$ :

$$T_{cond} = 500 \sim 650 \text{ K}, \quad \Delta T_{cond} = 25 \text{ K}$$

As in the first category, the I-V sweep starts from the nominal short circuit conditions,  $R_L = 0$ . When the load resistance is changed, the heating power at the cell's hot end and the cooling air flow at the cell condenser were adjusted to maintain  $T_{hot}$  and  $T_{cold}$  at their selected values. Therefore, the I-V curve and  $R_{ext} \sim P_e$  curve are obtained at constant temperature conditions.

In addition to the above two categories of tests, life (degradation) tests are also conducted. Basically, the life tests are I-V curves obtained at fixed  $T_{hot}$  and  $T_{cold}$ , performed at large time interval (once or twice a month), to examine the degradation history of cell versus temperature.

## 8.8 EXPERIMENTAL PROCEDURES

### 8.8.1 Test setup Assembly

Prior to the test setup integration, the cryogenic vacuum pump was regenerated, and vacuum integrity was checked using an Alcatel Helium leak detector. The regeneration procedure consists of introducing heated argon into the cryogenic pump while the pump is cold (compressor should be turned off at the beginning of argon introduction). Heated argon will continue to flow through the pump until room temperature is reached. At this point, the pump will be evacuated and the compressor restarted. The vacuum chamber, test setup, and test article are cleaned using isopropyl alcohol. All components are handled with latex gloves during implementation. A clean environment is to be maintained in and around the vacuum chamber and test assembly area at all times.

When a AMTEC cell is received by the lab from the manufacturer, it is inspected and X-rayed to verify the cell integrity and provide a reference point for comparison during and after testing.

An insulation package, structural support plate, and cold plate with cooling air loop is then refurbished or fabricated new to accommodate the test device. The cell is attached onto the cold plate through the bolt (ground electrode) on the cell end. The gap between the cell bottom and cold plate is filled with a thin layer of Boron Nitride paste.

All thermocouples are calibrated, at temperatures of water frozen point and boiling point, before use. The cell is instrumented with thermocouples for evaporator and BASE tube temperature measurements,  $T_{ev}$  and  $T_{\beta}$ , by inserting them inside the cell through thermocouple wells designed by the manufacturer. Thermocouples are also distributed on the top,  $T_{hot}$ , bottom,  $T_{cond}$ , and in

some cases, along the wall,  $T_w$ , of the cell. Starting with the PX-2C cell, Min-K disks have been used consistently as the insulation material. The bottom disk is installed, and the gap (6.3 mm) between the central hole and the cell wall is filled with alumina powder (1  $\mu\text{m}$  in diameter). The cell top is pasted with Boron Nitride powder to enhance the conduction heat coupling between the heater and the cell top. A Boron-Electric heater sitting on the heater supporter is then assembled on the hot end of the cell. The heater leads run out of the insulation package along the interface between Min-K disks. Two outgassing heaters ( $\phi = 0.51$  mm Kanthal wires) are placed at the interfaces between the three disks to reduce the outgassing period. For the PX-4C and PX-5A cells, multi-foil insulation was also placed around the heater.

After the top Min-K disk is installed, a cross-bar compresses the Min-K disk assembly through the two long and threaded poses mounted on the support plate, to eliminate the gap between the Min-K disks. The thermocouples are then distributed on the surface of Min-K. The cold plate with the cell sitting on it is attached on the support plate with three  $\phi = 3.1$  mm alumina rods, which are electrically isolated with Mica foils. Then, the bottom of the support plate is thermally insulated with a thick Cera-blanket.

All thermocouple and power leads and measurement leads are then connected to the connectors of vacuum chamber feed-through, which bridge inside and outside of the vacuum chamber. All thermocouples and connections are checked. The cooling air loop on the cold plate is connected to the air supply line through the feed-through. After vacuum grease is coated on the vacuum sealing ring, the chamber is closed, and the vacuum pumps are connected to the chamber.

### 8.8.2 Data Acquisition System and Power Supply

All measurement leads are then connected into the HP 3852 Chassis and its component cards, which are calibrated yearly as specified by HP. However, the cell power output leads are not connected into the measurement circuit until the cell condenser temperature reaches 400 K (above the melting point of sodium, 371 K). This ensures that an external voltage, which could drive solid alumina through and break the BASE tubes, is not present. Each component card (i.e. voltage and thermocouple multiplexers) is checked against a calibrated handheld device prior to the beginning of a new test. Power supplies are calibrated yearly as specified by the manufacturer. The output of the power supply is checked against a calibrated handheld device prior to the beginning of a new test. Flow controllers and/or meters are calibrated according to the manufacturer specifications. Flow meters are set to zero before the test.

The DAS software is then initialized, and each connection through the chamber feed-through is verified and checked off on the spreadsheet to insure accuracy. The DAS instrumentation spreadsheet is added to the test log book. The diagram of tested cell is added to the log book, which shows the thermocouple layout for the test.

The monitoring parameters, BASE and condenser temperatures and vacuum level for "watch dog" system, are set to specified values. Presently, the watch dog system setting is:  $T_{\text{low1}} = 385$  K,  $T_{\text{low2}}$



= 400 K,  $T_{\text{high1}} = 650$  K,  $T_{\text{high2}} = 670$  K,  $T_{\beta,1} = 1173$  K,  $V_{\text{ac},1} = 5 \times 10^{-6}$  torrs, and  $V_{\text{ac},2} = 5 \times 10^{-5}$  torr. The circuit and autodialer are checked daily during testing.

### 8.8.3 Initialization of Tests

After sealing the vacuum chamber and checking the DAS/control system, The valves of the mechanical pumps are opened to start rough vacuuming of the system. Then, outgassing heaters are turned on with about 2 W power for each.

Once the vacuum reaches  $10^{-3}$  torrs, the valves of turbomolecular pumping stations and cryo pumps are opened, and the valves of the mechanical pumps are closed. After the vacuum reaches/is maintained between  $5 \times 10^{-5}$  and  $5 \times 10^{-4}$  torrs with turbomolecular pump, the power to the outgassing heater is increased (about 2 W/hr). The temperature measured 5 mm from the outgassing heater is kept below 900 K. When this temperature is beyond 850 K, the outgassing heater power stops increasing, and the system should remain at these conditions until vacuum reached to  $5 \times 10^{-6}$  torrs. At this point, electric power to the cell heater can be increased at a rate of 2 to 4 W per hour while maintaining at least  $1 \times 10^{-5}$  torrs vacuum. Once the cell's hot end temperature reaches the desired values, the power to the outgassing heaters is slowly reduced while the heater power is increased. After the outgassing heater power is reduced to zero, a minimum of 8 hrs steady-operation is required to reach full thermal equilibrium.

During the heating-up process, the condenser temperature is under monitoring at all time, and the cell circuit is kept open. Once the cell condenser temperature reaches 400 K (the melting point of sodium is 371 K), the cell circuit is loaded at nominal short circuit,  $R_L = 0$  (but  $R_{\text{ext}} \neq 0$ ).

At this stage, the system is ready for conducting performance tests at selected conditions. The tests are conducted in the manner described in Section 8.7.

### 8.8.5 Ending of Test

When the cell test must be ended, the temperatures throughout the whole test setup must be brought to room temperature before the vacuum chamber is allowed to come back to atmospheric pressure. First, the heater power is reduced slowly, from testing level to zero, with the cell circuit at nominal short circuit and the cooling air still running. After the condenser temperature decreases below 400 K, the cell circuit is disconnected. The vacuum chamber is not opened until all the temperature readings are near room temperature.

### 8.8.6 Response to "Watch Dog" Warning

In the event that an out-of-range parameter has caused a "watch dog" alarm (Figure 8.1), the autodialer zips out, and one of the AMTEC team member at AFRL will respond in a timely manner. If the parameter was beyond the maximum range set in the "watch dog circuit", the

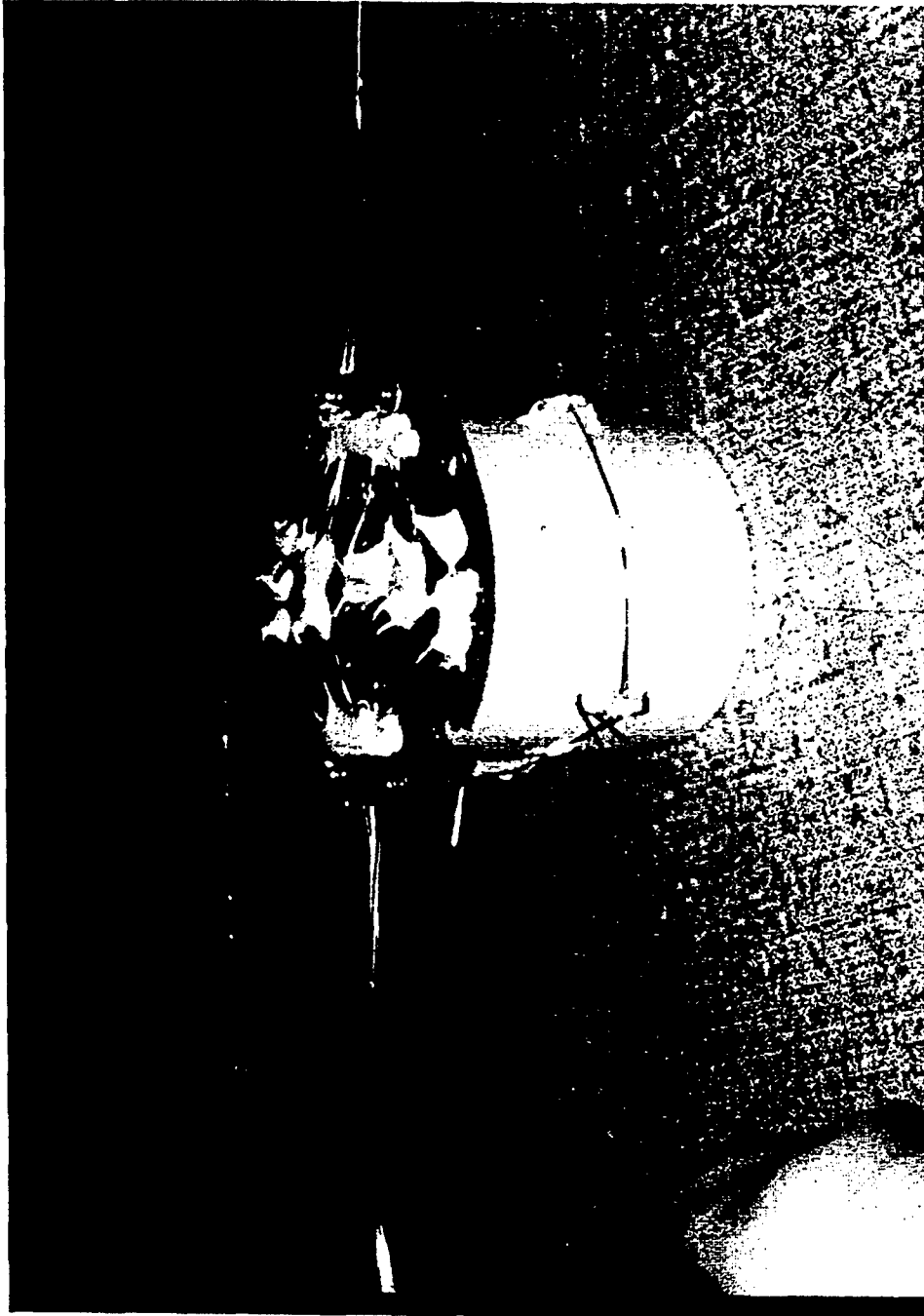


Figure 8.8a. Photograph of Boron Nitride Heater Block.

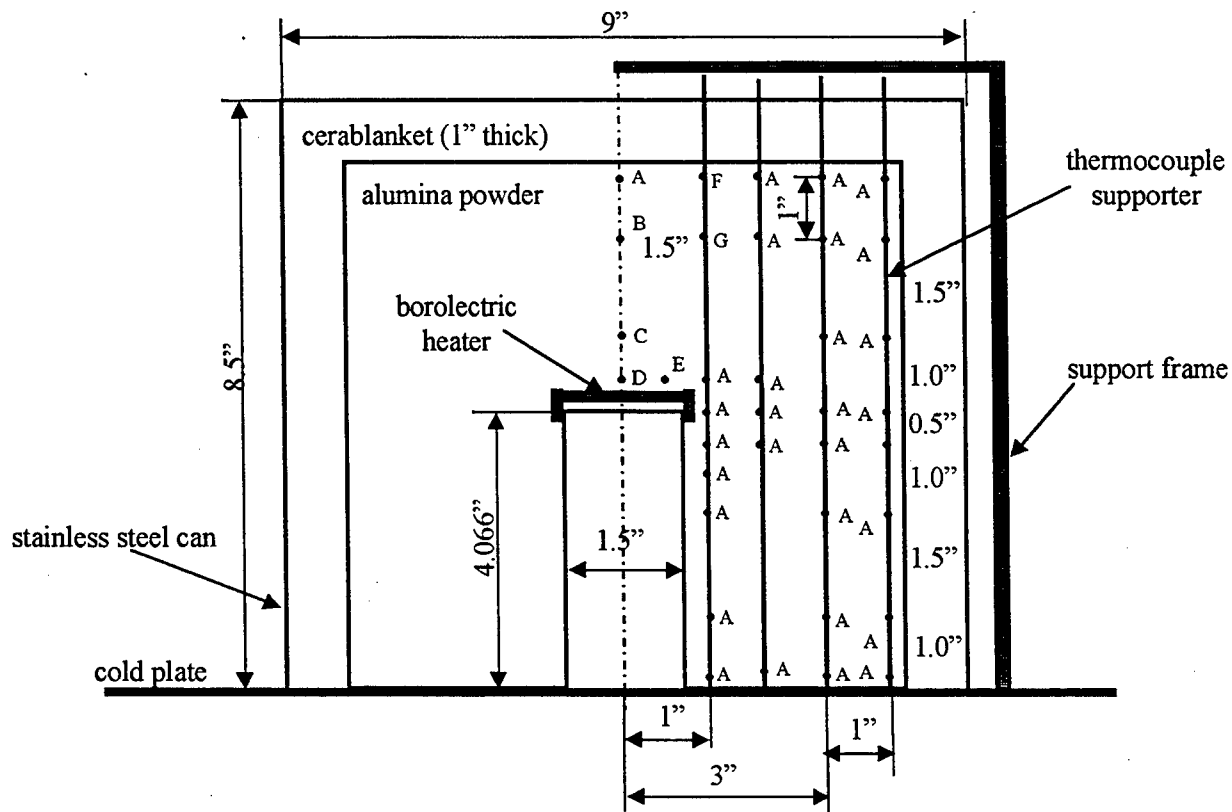


Figure 8.8b. Thermocouples Arrangement in Insulation Package of PX-1B and PX-1C Cells.

heater power will be shut down automatically. Upon arriving to the lab, the responder will assess the situation and make the appropriate correction as soon as possible. If the problem is not easy to resolve, the responder must ensure that the system is being shut down in a safe manner.

## 8.9 PARTICULARITIES OF SINGLE-CELL EXPERIMENTAL SETUPS

The design and instrumentation of the single-cell test setups were basically the same, as described above. However, a few changes were made in the test setup from cell to cell, which tended to improve the effectiveness of the thermal insulation package and/or provide better instrumentation. The next subsections describe some of these particularities.

### 8.9.1 Design of PX-1A Cell Experimental Setup

The design of the test setup of the first vapor anode, multi-tube AMTEC cell tested at the lab, PX-1A, differed markedly from that of the previously tested liquid anode, single-tube PL-9 series of cells. In particular, the multi-foil insulation package of PL-9 cells was substituted with 1- $\mu$ m alumina powder as the insulation material.

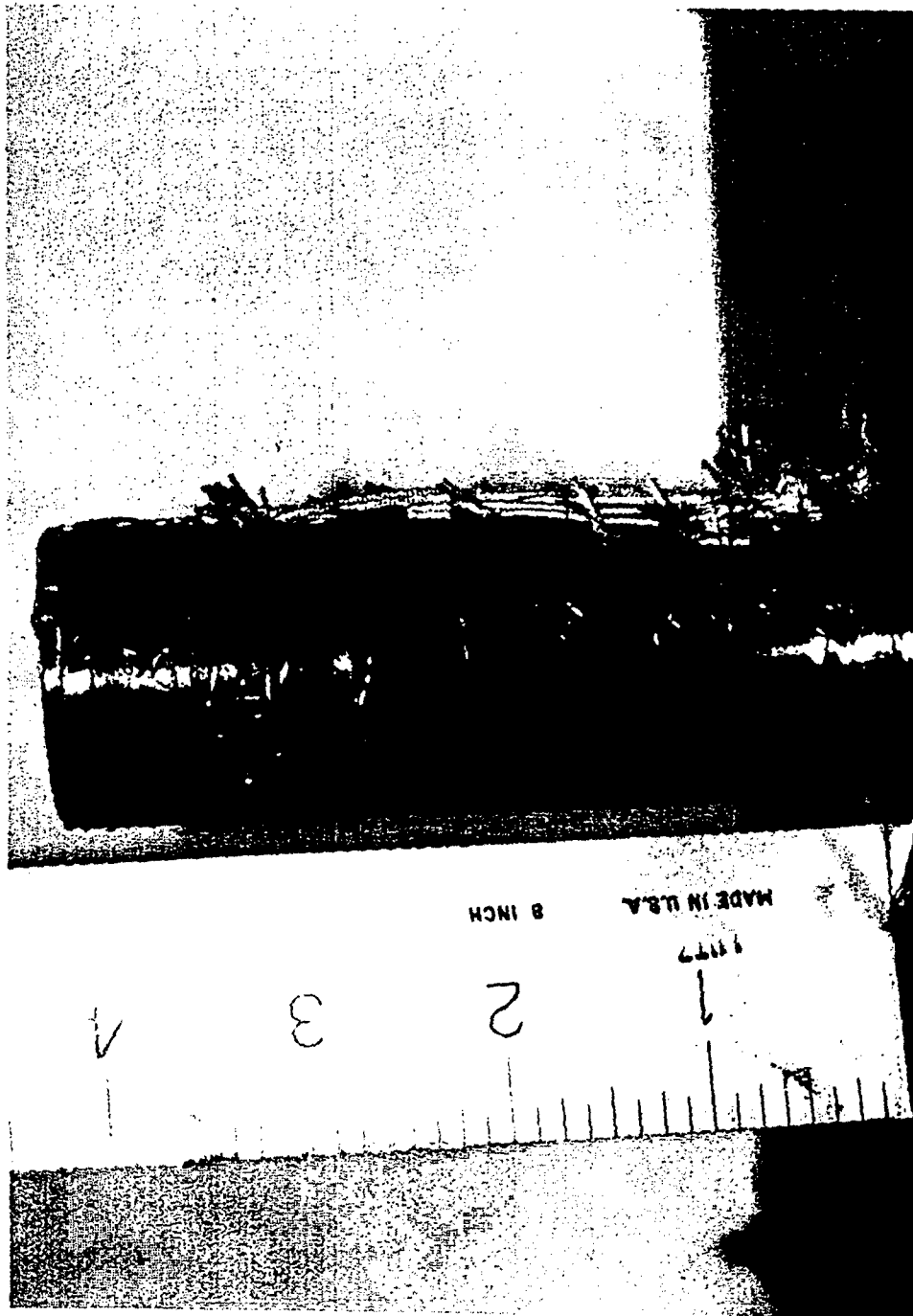


Figure 8.8c. Photograph of Thermocouples Arrangement Along Cell Wall.

Because the Boro-electric heaters used for the PL-9 series cells were too small for the PX-series cells, a heater using conventional Tungsten bulb wires was manufactured at the lab. The heater was covered with another self-made Boron Nitride block, which was instrumented with 11 K-type thermocouples, to analyze the heat losses through the heater block (Figure 8.8a). Because of the high thermal conductivity of the block material (Boron Nitride), the uncertainty in the temperature measurements, and the non-symmetric heating wire arrangement, the analysis of the heat conducted through the heater block was inconclusive. Testing of cell PX-1A was terminated because of the failure of the cell (sodium leak).

### **8.9.2 Design of PX-1B and PX-1C Cell Experimental Setups**

As in the PX-1A test setup, Alumina powder was used as the insulation material in the tests of PX-1B and PX-1C. A specially-designed thermocouple arrangement was applied onto the insulation package and the cell wall (Figures 8.8b and 8.8c). The distributed thermocouples provided temperature distributions along the boundaries of the insulation to analyze the heat losses through the insulation, and some measurements in the bulk of the insulation to verify the 2-D thermal conduction model developed in this work.

In the PX-1C test setup, the thermocouples arrangement was modified. Instead of being distributed throughout the insulation, the thermocouples were only distributed along the surface of insulation and 25 mm deep from the surface. So that the heat flux dissipated from the insulation surface could be estimated using the temperature gradient (perpendicular to the surface) measured by these thermocouples. These experimental measurements could also be used to verify the model's results.

### **8.9.3 Experimental Setup for PX-2A and PX-2C Cells with Molded Min-K Insulation**

Starting with PX-2B, the alumina powder in the thermal insulation package was replaced with molded Min-K disks. The package consisted of three pieces of molded Min-K, 20.3 cm in diameter and 7.6 cm in height each. Interfaces between the pieces were machined as concentric (male and female) grooves to block any direct radiation path between the different Min-K layers (Figure 8.2a). Nineteen thermocouples were placed in the insulation (3.2 mm from the insulation surface) in such way that the thermocouple junctions were pressed against insulation to insure good contact with insulation. With the additional thermocouples located on the cell wall, the measured temperatures along the boundaries of the insulation package would provide the boundary temperature profiles necessary for the calculation of heat losses through the insulation. Two degassing heaters (Kanthal coil) were placed at the interfaces between Min-K blocks to help in degassing from inside of the insulation package. Experimental results showed that substituting Min-K for alumina powder reduced the heat losses through the insulation package.

The Borolectric Heater support for the cell was redesigned (Figures 8.3a and 8.3b) to provide a sitting space for the shielding plate above the heater. In the previous design, this shielding plate

sat directly on top of the heater. The new design of the heater support keeps a 3.2 mm gap between the heater and the shielding plate to reduce the heat loss by thermal conduction.

#### 8.9.4 Experimental Setup for PX-4 and PX-5 Series Cells

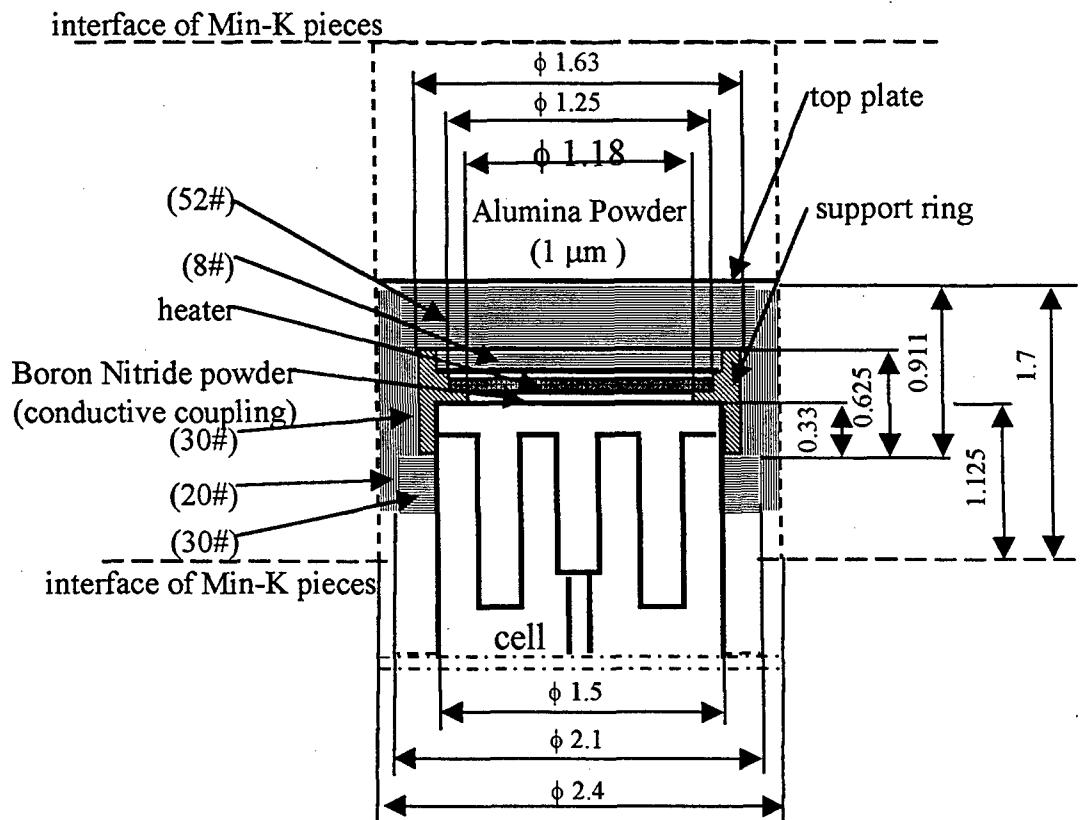
To reduce the thermal resistance between the heater and the top of the PX-series cell, conductive coupling was used in the test setups of the PX-4 and PX-5 series cells. Boron Nitride paste (1.6 mm thick) was used as the coupling material between the heater and the cell top.

The experimental setup for the PX-4 and PX-5 series of cells was basically identical to that of the PX-2 series cells, except that the cell heater was surrounded with multi-foil insulation. While Min-K significantly reduced the heat losses compared to Alumina powder, its maximum operating temperature is 1255 K. When the cells are tested at  $T_{hot} > 1100$  K, the temperature at the surface of the insulation facing the heater may be beyond this limit. Post-test examination of the Min-K insulation package has showed that the surface of Min-K facing the heater was heavily over heated (material became blue and stiff). Obviously, this would increase the thermal conductivity and reduce the insulation function of Min-K. To reduce the temperature of the insulation and reduce the heat losses, a multi-foil insulation was designed around the electric heater of new PX-series cells (Figure 9.9).

Multi-foil insulation has performed well in space applications when heat losses occur in the perpendicular direction to the metal foils. This insulation consists of thin stainless steel or molybdenum foils (5 - 25  $\mu\text{m}$  thick) separated by small gaps ( $\sim 100$   $\mu\text{m}$  wide). Small size Zirconia or alumina particles are deposited onto the surface of the foils to prevent conduction losses due to metal-metal contact. In the presence of a large axial temperature gradient in the wall, however, multi-foils insulation does not perform as well as Min-K insulation because of the axial conduction in the metal foils.

Present multi-foil shielding insulation was made of Molybdenum foils (thickness of 7.56  $\mu\text{m}$ ) and Zirconia powder (particle size of 0.23  $\mu\text{m}$ ). Zirconia powder is used as a spacer to keep the foils from touching each other. The previous method for assembling the multi-foils insulation was to paint the mixed Zirconia powder and alcohol on the foils. The problem that arose was the Zirconia coverage of the foils has higher emissivity than Molybdenum, increasing the effective emissivity of the Molybdenum multi-foils significantly.

A new spacer-depositing method was developed and tested. Instead of applying Zirconia paint, only particles of the powder are deposited on the foils, while leaving the foil surface almost bare. This method keeps the Molybdenum's low emissivity, while providing for thermal insulation between foils. However, in the new method, the Zirconia particles do not adhere well to the surface of the metal foils. If the foils are shaken hard, most particles may fall off. Further tests and development are needed to solve this problem. Present self-made multi-foils have the dimension of 0.15 mm/layer.



All dimensions are in inch

Molybdenum foils:  $\delta = 7.62 \mu\text{m}$

Spacer: Zirconia powder,  $D_p = 0.23 \mu\text{m}$

Thickness of multi-foils: 0.0055"/layer

Figure 8.9. Multi-Foil Insulation of Cell's Heater.

The multi-foil shielding insulation was configured for the PX-4C and PX-5A cells as shown in Figure 8.9. 40 layers of Molybdenum foils were stacked on the top of the heater while only five were stacked on the side of the heater-support ring. No foils were located on the bottom of the ring. Initial test results showed that the reduction in  $Q_{\text{heater}}$  was not significant in this multi-foil configuration, only about 2 watts reduction in  $Q_{\text{heater}}$  at 53 watts when compared with previous data for the case without multi-foil shielding at the same working condition.

The multi-foil insulation configuration was slightly different for the PX-4B cell. Compared to the design for PX-5A and PX-4C, the bottom of the support ring was shielded by the multi-foils (30 layers), and the side multi-foil shielding (50 layers) was extended to cover top and bottom multi-foil shielding. The number of shielding layers on the top of heater was increased to 60 layers.

While the experimental measurements for the PX-5A, PX-4C, and PX-4B cells showed a reduction in thermal heat losses when compared to the Min-K insulation packages used for previous cells, experimental results were not as good as expected. After post-experimental examination of the insulation packages, two major occurrences were found, which explain the reduction in the performance of the multifoil insulation package. The multifoils were severely oxidized (foils had turned purple), and the interface between Min-K disks, where the outgassing heaters were located, overheated. The oxidation occurred because the cell hot plate heater was turned on before the outgassing process was finished, and significantly increased the radiative emissivity of the foils, therefore reducing the shielding function. The temperature of the outgassing heaters was so high (above 1255 K, the maximum operation temperature of Min-K) that sintering and significant deformation of the Min-K occurred at the interfaces between disks; as a result, the thermal resistance of Min-K was reduced.

### **8.9.5 Experimental Setup for PX-3 Series Cells**

PX-3 series cells were smaller in diameter ( $D = 1.25$  in = 31.75 mm) than previously tested PX-series cells ( $D = 1.50$  in = 38.1 mm). Post-test examination of the insulation package showed that the 1- $\mu$ m Alumina powder filling the gap between the cell wall and the Min-K disks was sintered. This raised the question of the actual value of the thermal conductivity of this sintered powder; it might be much higher than that of the loose powder. This might increase the heat losses axially along the powder layer. To reduce this heat loss, the diameter of the central hole in the bottom Min-K disk was machined at almost the same size as the cell diameter, resulting in a gap of  $\sim 0.2$  mm. There was no alumina powder filling in the gap.

The next section describes the experimental setup at AFRL for testing multi-cell ground demo systems.

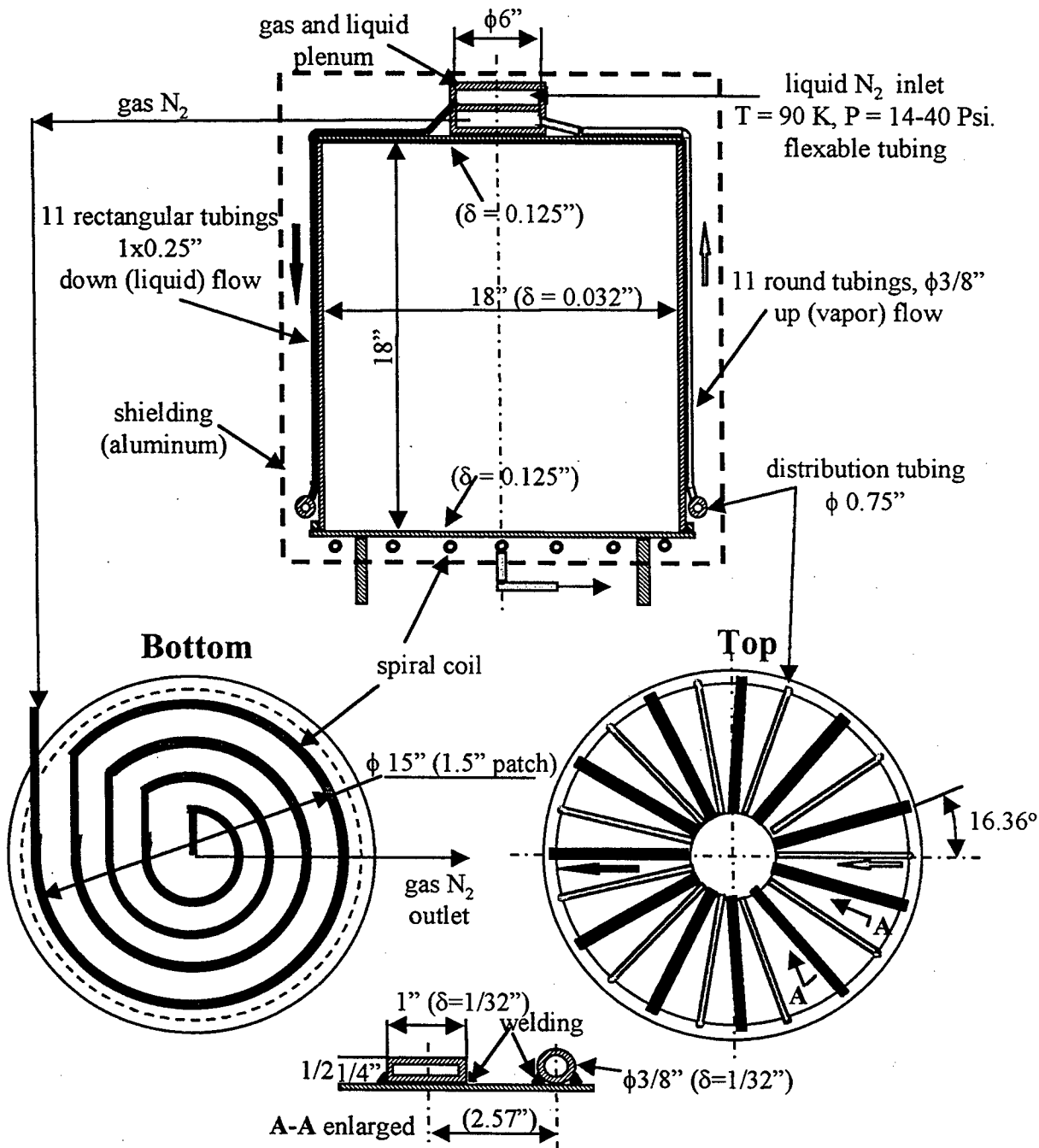
## **8.10 MULTI-CELL GROUND DEMO EXPERIMENTAL SETUP**

To demonstrate the performance of multi-cell, AMTEC generators for the Pluto/Express, Europa missions and future Air Force missions, an 8-cell ground demo, manufactured by AMPS, and a 4-cell ground demo, fabricated by OSC, were recently tested in vacuum at AFRL. The experimental setups for the ground demo systems were very similar to those designed for the single-cell tests. The major difference was in the way of removing heat from the cells' condenser. Instead of convective heat transfer by cooling air, waste heat at the cold end of the cells in the ground demo systems was dissipated by radiation to simulate space environment conditions.

In order to control the radiation environment (and the cold end temperature of the demo systems), a shroud was designed and manufactured by the AFRL mechanical shop (Figures 8.10a and 8.10b). The shroud consisted of top liquid and vapor plenums, a cylindrical shell, flow tubing on the shell, and a bottom lid with a coil. All components were made of aluminum alloy. The coolant through the shroud could be either liquid nitrogen or air, depending on the specified shroud temperature. The shroud temperature can be adjusted by selecting the type of coolant and



Heat Removal Capacity: 500 W, System Pressure: 100 Psi



Note: 1) Material for all parts aluminum. 2) All tubing are welded on to the shroud wall.  
3) Inner surface of the shroud is coated with radiation enhancement material.

Figure 8.10a. Shroud Design for Multi-Cell Ground Demo.

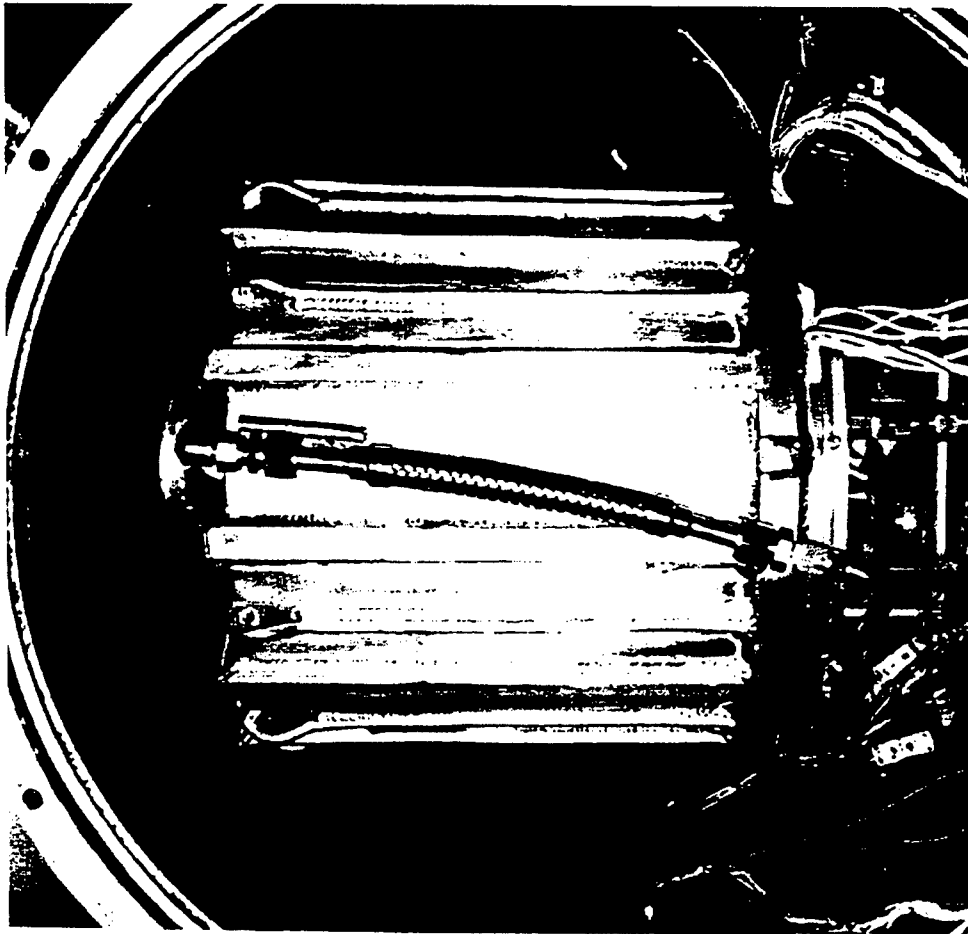


Figure 8.10b. Photograph of Shroud for Multi-Cell Ground Demo.

controlling its mass flow rate. The valve for liquid nitrogen supply is controlled by a Coming into the top liquid plenum. Liquid nitrogen flows downward into vertical tubes on the shroud wall, and evaporates along the tubes. The resulting nitrogen vapor flows from the bottom manifold back to the top vapor plenum, where it is collected and led out. In the test setup, a multi-foil insulation is used to reduce the heat losses from the shroud, so as to minimize the amount of liquid nitrogen needed. To enhance the radiation heat transfer, the inside surface of the shroud is painted with a layer of Solar Collector Coating (Thurmalox). Nine K-type thermocouples are distributed on the inner surface of the shroud to monitor its temperature.

The first shroud manufactured for the multi-cell AMTEC ground demo system was tested in vacuum chamber D. The objective of this preliminary test was to demonstrate that the shroud could remove 500 W thermal heat from the test box at a temperature at the bottom of the test box of about 600 K. Initial testing showed that the system worked well. A 4"x 4"x 6" aluminum test box with a Kanthal wire heater on the inner bottom (acting as heat source) was located at the center of the shroud to simulate the multicell ground demo system. Without cryo-pump, the vacuum could only reach as low as about  $10^{-4}$  torrs when liquid nitrogen was introduced into the shroud loop. No leakage was detected in the test.

The test showed that the shroud could remove about 450 W of heat at a simulated condenser temperature of 700 K, without black painting on the outside surface of the simulation box. The shroud was pulled out of the vacuum chamber for repainting a radiation-enhancement material on its inner surface, which was stripped off during the test.

Unlike the single cell, the ground demo systems had been insulated before they were shipped to the lab. Three thermocouples were put on the outer radiation surface of the system. The hot end temperature was controlled by the power input into the electric heater, and the condenser temperature was adjusted by the shroud temperature.

In the first multi-cell ground demo (GD) tested at AFRL, the height PX-3G cells were connected electrically in series and insulated from each other with fibrous Min-K (Carlson et al. 1998), a lightweight insulation material recommended for operation up to 1350 K, even in load-bearing application. The cell's hot end was conductively coupled to a graphite box that contained a boron-electric heater (Carlson et al. 1998). The heat source and Min-K insulation were surrounded by multifoil insulation with zirconia-particle spacers. The length of the foils was graded to reduce the axial conduction losses in the multifoil, near the cell condenser (Schock et al. 1997b). The GD was enclosed in a black anodized, 7075 aluminum alloy housing, that radiated waste heat away, and the cells were heated electrically in vacuum inside an aluminum shroud cooled with liquid nitrogen. The hot and cold side temperatures of one of the central cells in the GD were measured in the tests. Also, the electric current and the terminal voltage of each cell and of the overall power system were measured.

The 8-cell, ground demo system was instrumented and placed into the shroud vacuum chamber (Figure 8.11). After fixing the problems in the heater connection, electric connections between the cells, and thermocouple location for heater temperature, the performance tests were started, basically following AMPS test plan. Vacuum tests were performed at fixed hot side and cold side

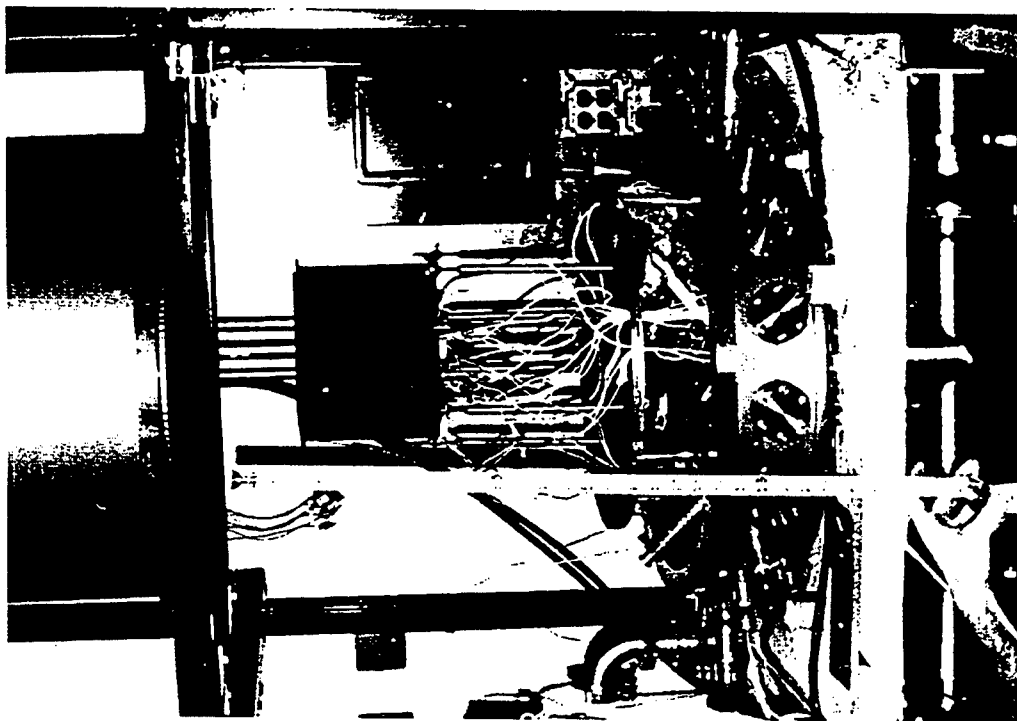


Figure 8.11. Photograph of Eight-Cell Ground Demo Test Setup.

temperatures of 1073 – 1123 K and 523 – 553 K, respectively. The first ground demo operated continuously for about 3000 hours before it was shut down.

Testing of the ground demo proceeded as expected, however test data uncovered a difficulty in effectively controlling the condenser temperature (it could not be brought up above 550 K) because of too much radiative heat transfer between the demo system box and the shroud. In an attempt to remedy this problem, a radiation shield structure of adjustable area was manufactured and placed between the demo system box and the shroud inner surface, to control the radiative heat transfer between these two components. However, this design change did not result in significant improvement.

To test the second 4-cell ground-demo system, another shroud was designed, which was basically identical to the first one, but smaller in size (it was tested in a smaller vacuum chamber). The second shroud and its support structure are shown in Figure 8.12. The 4-cell ground demo test setup is shown in Figure 8.13.

In the next chapter, the measurement uncertainties in the vacuum tests of the PX-series cells at the AFRL are calculated.



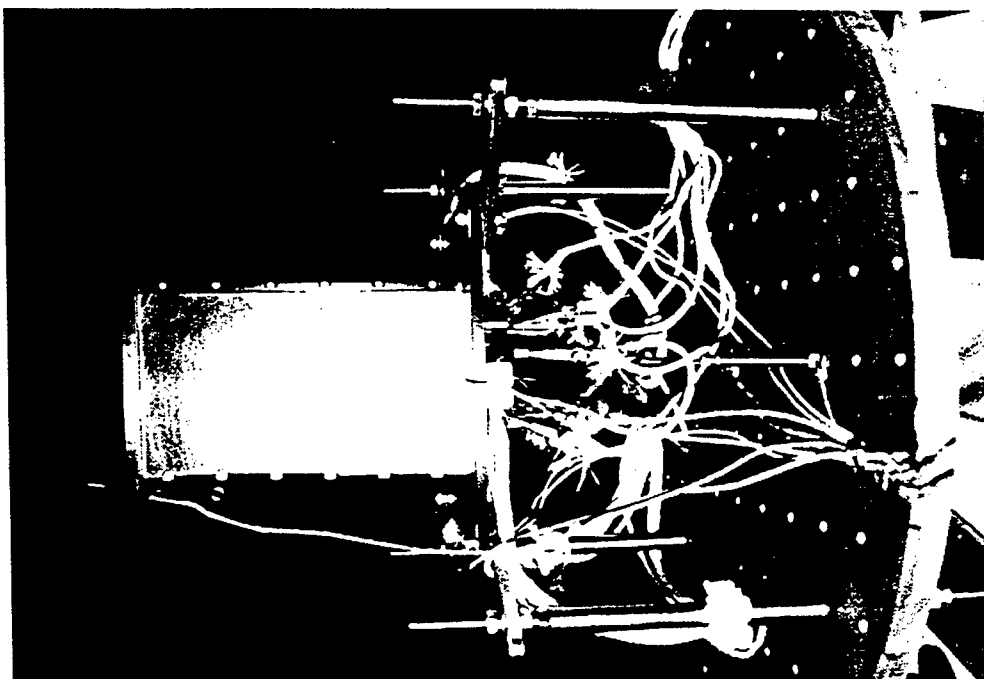


Figure 8.13. Photograph of Four-Cell Ground Demo Test Setup.

## 9. EXPERIMENTAL UNCERTAINTIES IN VACUUM TESTS OF PX-SERIES CELLS

The PX-series AMTEC cells manufactured by Advanced Modular Power System, Inc. (AMPS) are tested in vacuum at the Air Force Research Laboratory (AFRL). The experimental setups and data acquisition and test procedures were described in Chapter 8. The data from these tests is used to support model development and to assess the effects of different design changes and material choices on the overall cell performance. In order to compare the model predictions with the test results, accurate estimates of the uncertainties associated with the different experimental measurements must be determined. These uncertainties include those associated with the measurements of temperature, load electric current and voltage, and flow rate of air through the heat rejection. Other uncertainties are associated with the placement of the thermocouples (TCs) for measuring the BASE tube and evaporator temperatures (Figures 9.1 and 9.2). The leads of these TCs were inserted through thin Inconel tubes (guide tubes), with an outer diameter of 1.07 mm and an inner diameter of 0.59 mm. The TC guide tubes were welded to the hot end of the cell (Figure 9.2). These guide tubes acted as fins, conducting heat from the hot plate to the guide tube tip. The heat was also dissipated from the TC guide tube to the sodium vapor and the cavity wall by convection and radiation, respectively. The issue here is how close are the readings of these TCs to the actual temperatures of the evaporator,  $T_{ev}$ , and the BASE tube,  $T_b$ .

In this chapter, the measurement uncertainties in the vacuum tests of the PX-series AMTEC cells are calculated. In addition, a heat transfer model, called FIN, of the guide tubes of the TCs placed in the cavities of the BASE tubes and the evaporator is developed. This model is used to quantify the difference between the readings of the TCs and best estimate values of the BASE tube and evaporator temperatures in the tests. Best estimate values are obtained from the AMTEC Performance Analysis Model (APEAM), based on good predictions of the performance parameters of the cell, such as electric current and voltage, heat input and heat rejection (see Chapter 11). A parametric analysis is also performed to determine the effects caused by of the TCs' placement on their readings.

### 9.1 NOMENCLATURE

#### English

A	area ( $m^2$ )
$D_h$	hydraulic diameter (m)
$C_p$	specific heat capacity (W / kg.K)
h	heat transfer coefficient (W / $m^2$ .K)
$I_e$	cell electric current (A)
k	thermal conductivity (W / m.K)
$\dot{m}$	sodium vapor mass flow rate (kg/s)
Q	heat flow (W)
R	radius (m)
$R_{ext}$	external load resistance ( $\Omega$ )



T	temperature (K)
TC	thermocouple
$V_e$	cell electric voltage (V)
$V_{air}$	air flow rate at 1 atm and 21.1 °C ( $m^3/s$ )
x	axial distance from cell hot end (m)

#### Greek

$\varepsilon$	radiative emissivity
$\delta$	uncertainty
$\rho$	density ( $kg/m^3$ )
$\sigma$	Stefan-Boltzman Constant ( $5.67 \times 10^{-8} W/m^2K^4$ )

#### Subscript

air	of air
cav	cavity (evaporator or BASE tube cavity)
cold	cell cold end
cond	thermal conduction
e	cell electric output
ev	evaporator
hot	cell hot end
g	thermocouple guide tube
i	inner, or at <i>ith</i> control volume
in	input
o	outer
read	experimental reading
s	surface
tip	thermocouple guide tube tip
v	vapor
$\beta$	BASE tube

#### Superscript

in	incoming
out	outgoing

## 9.2 VACUUM TEST APPARATUS AT AFRL

The test setup of the PX-cell is shown in Figure 9.1. The test apparatus was placed in a vacuum chamber. Surrounded by a thick Min-K insulation, the cell was heated by a Borolectric electric heater. The heat rejected at the cell condenser was removed by the cold air flowing through a copper tube brazed to the cell cold plate. By controlling the power input to the heater,  $Q_{in}$ , and the cooling air flow rate,  $V_{air}$ , the cell could be tested at constant hot and cold end temperatures,  $T_{hot}$  and  $T_{cold}$ . Also, by changing the external load resistance,  $R_{ext}$ , the cell I-V characteristic was measured. More details on the experimental setup can be found in Chapter 8.

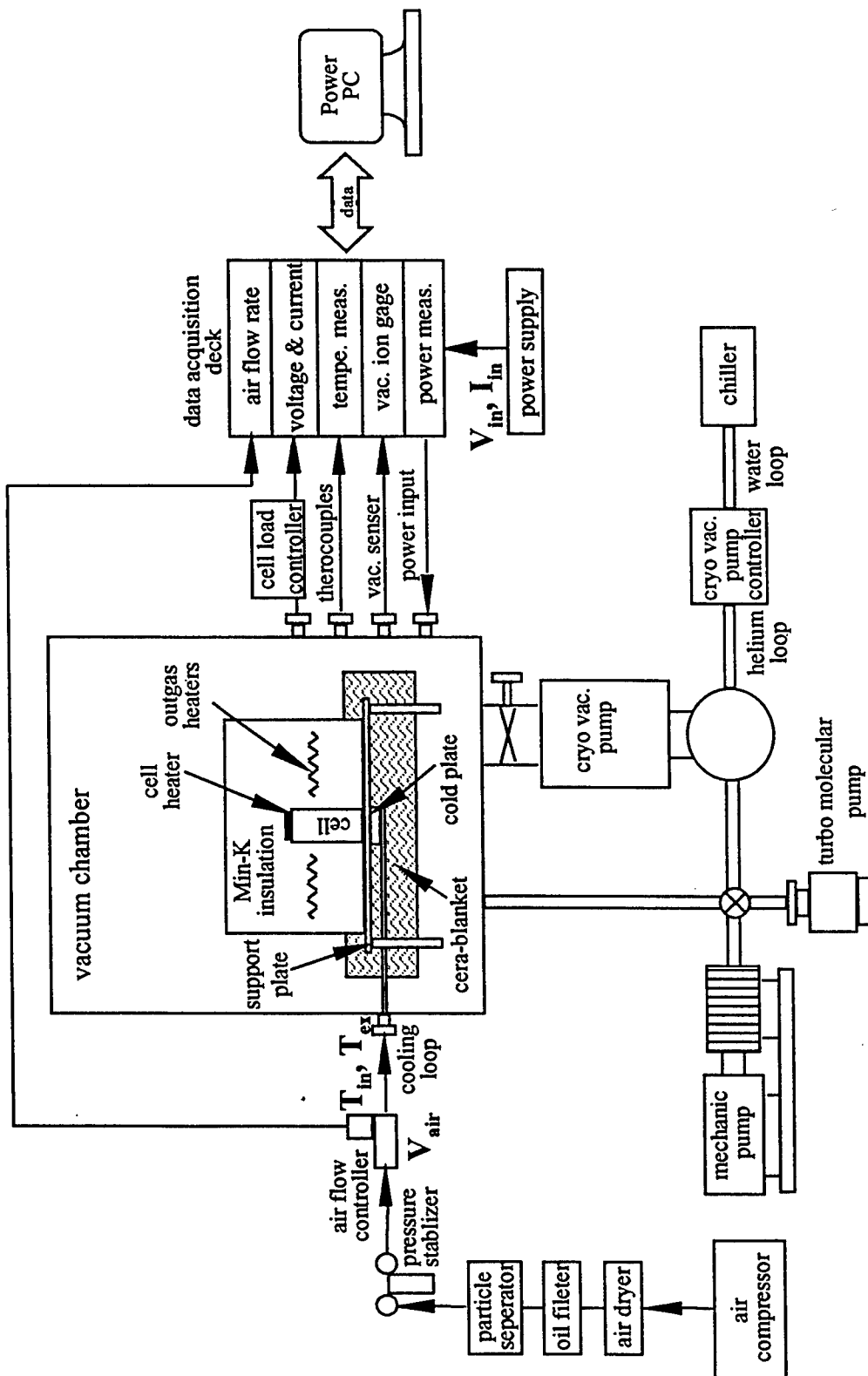


Figure 9.1. Flow Chart of Experimental Setup of Single-Cell Test at AFRL.

The measured electric current,  $I_{in}$ , and voltage,  $V_{in}$ , for the cell heater were used to calculate the heater input power. The electric power output of the PX-cell was determined from the measured cell voltage,  $V_e$ , and current,  $I_e$ . The cell voltage was measured outside the cell and the current was determined from the measured voltage across a shunt resistor,  $R_A = 0.01 \Omega$  (Figure 9.2a). The four temperature measurements that are essential to evaluating the cell performance were  $T_{hot}$ ,  $T_{ev}$ ,  $T_{\beta}$ , and  $T_{cold}$ . The inlet and outlet temperatures,  $T_{in}$  and  $T_{ex}$ , of the cooling air were also measured, along with the volumetric air flow rate,  $V_{air}$ , to calculate the heat rejection from the cell (Figure 9.1).

### 9.3 UNCERTAINTIES IN VACUUM TESTS OF PX-CELLS

Experimental uncertainty depends on whether a parameter is directly measured, or is based on measured quantities. The former is obtained directly from the calibration of the measuring devices, while the latter is determined in terms of the uncertainties of measured quantities contributing to it. When an experimental quantity,  $y$ , is expressed in terms of measured parameters,  $x_1, x_2, \dots, x_n$ , its uncertainty,  $\delta y$ , can be calculated as (Beckwith and Marangoni 1990):

$$\delta y = \sqrt{\left(\frac{\partial y}{\partial x_1} \delta x_1\right)^2 + \left(\frac{\partial y}{\partial x_2} \delta x_2\right)^2 + \dots + \left(\frac{\partial y}{\partial x_n} \delta x_n\right)^2}, \quad (9.1)$$

where  $\delta x_i$  is the uncertainty in measured quantity,  $x_i$ . All temperature and electric sensors used in the tests generated dc voltage output signals with an uncertainty of 0.02% for signals  $> 30$  mV, and 0.03% for signals  $< 30$  mV.

The uncertainties in the measured cell current and voltage were  $\pm 0.2\%$  and  $\pm 1.1\%$ , respectively. Using Equation (9.1), the calculated uncertainty in the electric power output was  $\pm 1.2\%$ . The uncertainty in the electric power input to the cell heater was  $\pm 0.7\%$ . The thermocouple had an uncertainty of  $\pm 1.1$  K or  $\pm 0.4\%$ , whichever was greater, resulting in an uncertainty of temperature measurement of  $\pm 1.7$  K, or  $\pm 1.1\%$ , whichever was greater. Details of these calculations can be found in Appendix E. The rejected heat to the air calorimeter,  $Q_{air}$ , was calculated as:

$$Q_{air} = \int_{T_{in}}^{T_{ex}} \dot{m}_{air} C_{p_{air}} dT = \int_{T_{in}}^{T_{ex}} V_{air} \rho_{air} C_{p_{air}} dT. \quad (9.2)$$

The measured air volumetric flow rate,  $V_{air}$ , had an uncertainty of 6.3% ( $\pm 1.5\%$  of full scale ( $3.33 \times 10^{-4} \text{ m}^3/\text{s}$  or 20 Standard Liter Per Minute)). The uncertainty of rejected heat,  $Q_{air}$ , was calculated as  $\pm 6.5\%$ , using Equations (9.1) and (9.2). A summary of the experimental uncertainties in the vacuum tests of the PX-series cells can be found in Table 9.1.

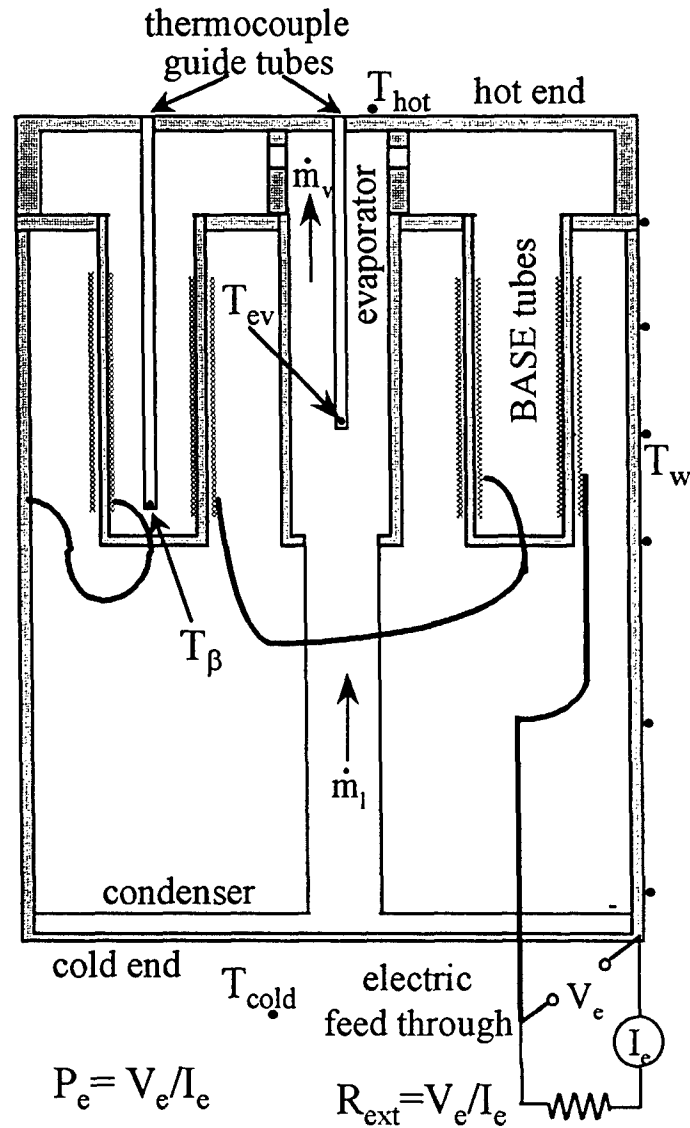


Figure 9.2a. Experimental Measurement on a PX-series Cell.

#### 9.4 FIN MODEL OF TC GUIDE TUBES IN THE BASE AND EVAPORATOR CAVITIES

Besides the uncertainties listed in Table 9.1, there was another uncertainty associated with the placement of the TCs in the cavities of the BASE and the evaporator. The issue was how close were the readings of these TCs to the actual temperatures of the evaporator and the cold end of the BASE tube. In an attempt to address this question, a heat transfer model of the guide tubes of these TCs, called FIN, was developed to predict the TCs' readings in the evaporator and the BASE cavities during the vacuum tests at AFRL.

Table 9.1. Measurement Uncertainty Analysis of PX-Series Cell Tests at AFRL.

Measured Parameters	Measurement Equipment	Test Measurement Range	Equipment Accuracy	Uncertainty $\pm$	Note
Cell Voltage, $V_e$	HP3852/44705A	0.24 ~ 5 V	Read 0.018%+0.04mV, 0.03~0.3 V Read 0.018%+0.4mV, 0.3~3 V Read 0.018%+4mV, 3~30 V	0.2%	
Cell Current, $I_e$	HP3852/44705A	0.5 ~ 5 A ( $V_A=5-60mV$ )	$V_A=0.02\%+0.02mV$ , $V_A<30mV$ $V_A=0.018\%+0.04mV$ , $V_A=30-300mV$	1.1%	$V_A=I_e R_A$ $R_A=0.01\pm 1\% \Omega$
Cell Power, $P_e$	$P_e = V_e I_e$			1.2%	
Heater Voltage, $V_{in}$	HP654A Supply HP3852/44705A	1.5 ~ 3 A	Read 0.07%+40 mV	0.05%	
Heater Current, $I_{in}$	HP654A Supply HP3852/44705A	15 ~ 30 V	Read 0.15%+4.1 *mV	0.68%	
Heater Power, $Q_{in}$	$Q_{in} = V_{in} I_{in}$			0.7%	
Temperature, T	K-Type HP3852/44705A /44708	< 177 °C 450 ~ 1300 K	max{1.1 °C, read0.4%} + 0.1 + $\delta T_v$ Note: $\delta T_v$ is the error from the reading of voltage from a thermocouples, using HP3852/44705A	1.7%	
Temperature, $(T_{out}-T_{in})_{air}$	K-Type HP3852/44705A /44708	156 ~ 300 °C		1.56	
Air Flow Rate, $V_{air}$	FMA-772-V-AIR Controller/Meter HP3852/44705A	4.8 ~ 20 SLM	1.5% of full scale (20 SLM) (0.3 + $\delta V_{air}$ )/reading Note: $\delta V_{air}$ is the error from the reading of voltage from a thermocouples, using HP3852/44705A	6.29	standard condition of meter: 1 atm and 21.1 °C
Rejected Heat, $Q_{air}$	$Q_{air} = \rho V_{air} C_p (T_{out}-T_{in})$			6.48	

These TCs, Inconel-sheathed, K-type, were inserted through Inconel guide tubes, before being placed in the respective cavities. The TC guide tubes had an inner diameter of 0.59 mm and a wall thickness of 0.24 mm. The guide tubes were inserted through and welded to the cell hot plate (Figure 9.2a). The other ends of the guide tubes that contained the sensing end of the TCs were left free standing. The TCs would measure, therefore, the equilibrium vapor temperatures of the respective cavities. Since these temperatures could be about 100 K lower than that of the hot plate, the guide tubes acted basically as cylindrical fins (Figure 9.2b). Heat is removed from the outer surface of the guide tubes by convection to the sodium vapor flow and by radiation to the cavity walls of the BASE and evaporator. The sodium vapor is heated by convection and radiation while it flowed through the evaporator cavity to the BASE cavity. The conduction stud effectively enhanced heat transfer from the hot plate to both the BASE tubes and the evaporator (Figure 9.2a). A positive temperature margin ( $T_p - T_{ev}$ ) up to 50 K is recommended to ensure that sodium condensation and run off will not occur, electrically shorting the BASE tube (Schock et al. 1997a).

The TC guide tube was modeled as a long fin, using a one-dimensional axial heat conduction approach in the guide tube wall, subject to convection and radiation on its outer surface. The inside surface of the guide tube wall was assumed adiabatic and the sensing end of the TC was assumed to be in good contact with the guide tubes at their freestanding ends. The model, FIN, was developed to predict the temperature readings of the TCs in the BASE and evaporator cavities. In addition to axial conduction in the guide tube wall, the FIN model includes (Figure 9.3): (a) heat convection from the outer surface of the guide tube wall to the sodium vapor flow in the respective cavities, and (b) thermal radiation from the outer surface of the guide tube wall to the evaporator or the BASE wall. The axial temperature distributions along the cavities wall of evaporator and the BASE tube,  $T_{cav}$ , were calculated by APEAM (see Chapters 3, 4 and 5). These temperature calculations were based on the best comparison of APEAM predictions of the cell performance parameters measured in the vacuum tests (Chapter 11). The cell PX-5A, used in the present analysis, was tested at constant hot and cold end temperatures.

The electric current produced by an AMTEC cell is directly proportional to the mass flow rate of the sodium vapor produced in the evaporator. The sodium vapor flow rate for the tested cells was below 15 gm/hr and its corresponding Reynolds number  $< 100$ . Therefore, the convective heat transfer coefficients between the sodium vapor and the TC guide tube wall,  $h_g$ , and between the vapor and the cavity wall,  $h_{cav}$ , were calculated using the following correlations (Shah and London, 1978):

$$h_g = (3.015 + 0.9969(R_o / R_i)) (k_v/D_h), \quad (9.3a)$$

and,

$$h_{cav} = 3.816 (R_o / R_i - 0.0552)^{-0.3257} (k_v/D_h). \quad (9.3b)$$

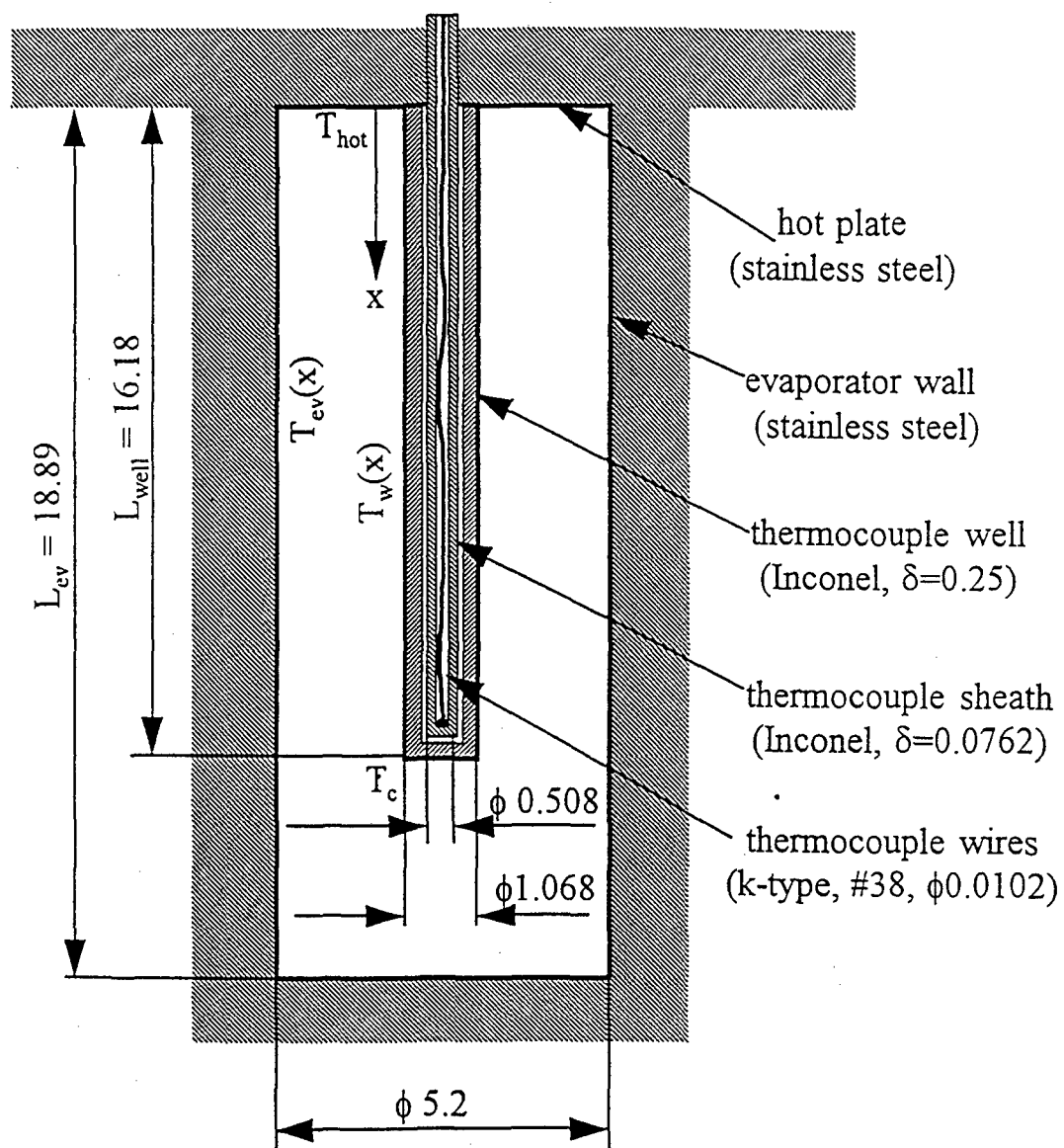


Figure 9.2b. A Schematic of Thermocouple's Guide Tube Arrangement.

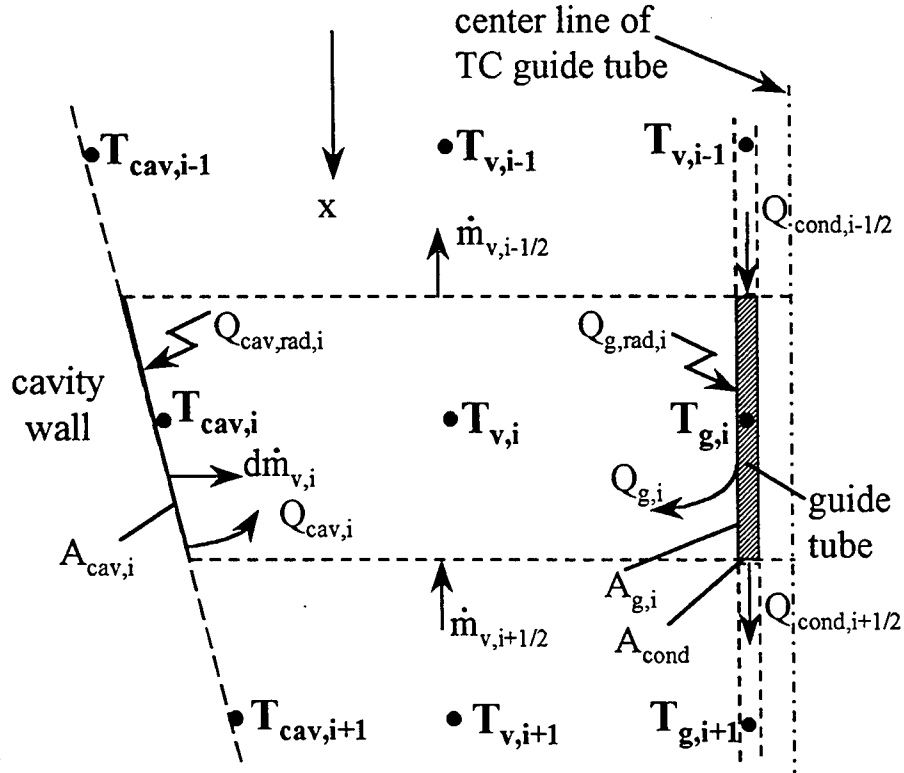


Figure 9.3. A Schematic of Thermocouple's Guide Tube "FIN" Model.

The evaporator and BASE tube cavities were divided into a number of annular control volumes in the  $x$ -direction (Figure 9.3). The local sodium vapor temperature at the center of each control volume was determined from the energy balance in the control volume. At the surface of the guide tube, heat is removed by convection to the sodium vapor flow, and by radiation to the inside surface of the cavity wall. The sodium vapor is either heated or cooled by convection at the cavity and guide tube walls. Assuming uniform evaporation along the evaporator surface, a uniform vapor diffusion through the BASE tube wall, and a constant heat capacity,  $C_p$ , in a control volume, the energy balance of the  $i$ th control volume is (Figure 9.3):

$$(T_{v,i-1/2}\dot{m}_{v,i-1/2} - T_{v,i+1/2}\dot{m}_{v,i+1/2})C_{p_i} = T_{cav,i}\Delta\dot{m}_{v,i}C_{p_i} + Q_{g,i} + Q_{cav,i}, \quad (9.4)$$

where subscripts  $-1/2$  and  $+1/2$  represent the values at the interface between the  $(i-1)$ th and  $i$ th control volumes and between  $i$ th and  $(i+1)$ th control volumes, respectively.  $Q_{g,i}$  and  $Q_{cav,i}$  are the heat transferred to the vapor by convection from the cavity and guide tube walls, respectively:



$$Q_{g,i} = h_{g,i} A_{g,i} (T_{g,i} - T_{v,i}), \quad (9.5a)$$

and

$$Q_{cav,i} = h_{cav,i} A_{cav,i} (T_{cav,i} - T_{v,i}). \quad (9.5b)$$

In Equation (9.5b),  $T_{cav,i}$  was calculated by APEAM, but  $T_{g,i}$  was determined from the solution of one-dimensional heat conduction in the guide tube wall.  $\Delta \dot{m}$  is the rate at which vapor was added or removed from the control volume, respectively:

$$\Delta \dot{m}_{v,i} = \dot{m}_{v,i-1/2} - \dot{m}_{v,i+1/2}. \quad (9.6)$$

Assuming a linear temperature change within the control volume in x-direction,  $T_{v,i-1/2}$  in Equation (9.4) can be substituted by:

$$T_{v,i-1/2} = 2T_{v,i} - T_{v,i+1/2}. \quad (9.7)$$

Combining Equations (9.3) through (9.7), the vapor temperature in the  $i$ th control volume was given as:

$$T_{v,i} = \frac{(Cp_i \Delta \dot{m}_{v,i} + h_{cav,i} A_{cav,i}) T_{cav,i} + h_{g,i} A_{g,i} T_{g,i} + (\dot{m}_{v,i+1/2} + \dot{m}_{v,i-1/2}) Cp_i T_{v,i+1/2}}{h_{cav,i} A_{cav,i} + h_{g,i} A_{g,i} + 2Cp_i \dot{m}_{v,i-1/2}}. \quad (9.8)$$

The vapor temperature at the TC guide tube tip is equal to the evaporator temperature calculated using APEAM.

The heat balance in the  $i$ th control volume of the guide tube wall (Figure 9.3) is:

$$Q_{cond,i-1/2} - Q_{cond,i+1/2} + Q_{g,i} + Q_{g,rad,i} = 0, \quad (9.9)$$

where  $Q_{g,rad,i}$  is the net radiant energy received by the  $i$ th control volume surface on the guide tube from the cavity surface:

$$Q_{g,rad,i} = Q_{g,rad,i}^{in} - Q_{g,rad,i}^{out}, \quad (9.10a)$$

where  $Q_{g,rad,i}^{in}$  and  $Q_{g,rad,i}^{out}$  are the radiation reaching and leaving the surface of the  $i$ th control volume of the guide tube wall, respectively, and  $Q_{g,rad,i}^{out}$  includes the heat reflection of incident radiation (see Section 5.3):

$$Q_{g,rad,i}^{in} = \sum_{j=1}^{N_{tot}} F_{j \rightarrow i} Q_{g,rad,i}^{out} \quad (9.10b)$$

and

$$Q_{g,rad,i}^{out} = (1 - \epsilon_i) Q_{g,rad,i}^{in} + \sigma \epsilon_i A_{g,i} T_i^4 \quad (9.10c)$$

$F_{j \rightarrow i}$  is the radiation view factor from  $j$ th control volume surface on the cavity to the  $i$ th surface on the guide tube. The reflectivity of the guide tube and cavity walls are taken as  $(1 - \epsilon_i)$ . The subscript  $j$  changes from 1 to  $N_{tot}$ , the total number of control volume surfaces. Using Equations (9.10a) and (9.10b),  $Q_{g,rad,i}^{in}$  and  $Q_{g,rad,i}^{out}$  can be written as functions of  $T_i$ , then substituted back into Equation (9.10a) to get  $Q_{g,rad,i}$  as a function of  $T_i$ . Applying numerical differentiation into Equation (9.9), the discretized equations for solving the temperature distribution on the TC guide tube wall can be written as:

$$\begin{aligned} & k_{i-1/2} \frac{A_{cond}}{\Delta x} T_{g,i-1} - (k_{i-1/2} \frac{A_{cond}}{\Delta x} + k_{i+1/2} \frac{A_{cond}}{\Delta x} + h_{g,i} A_{g,i}) T_{g,i} + k_{i+1/2} \frac{A_{cond}}{\Delta x} T_{g,i+1} \\ & = -h_{g,i} A_{g,i} T_{v,i} - Q_{g,rad,i} \end{aligned} \quad (9.11)$$

where the vapor temperature,  $T_{v,i}$  was calculated using Equation (9.8), and  $Q_{g,rad,i}$  was calculated by Equation (9.10a). Thermal conductivities and emissivities were taken to be functions of temperature. Equation (9.11) was solved subjected to the following boundary conditions:

$$T_g(x=0) = T_{hot} \quad \text{and} \quad Q_{cond,tip} = Q_{g,rad,tip} \quad (9.12)$$

The second boundary condition is the energy balance on the last control volume, the TC guide tube tip.

Equations (9.8) and (9.11) were solved using an iterative solution procedure to determine the axial temperature distribution along the guide tubes of the TCs, in the BASE tube and evaporator cavities. The FIN model also calculated the readings of the TCs in both cavities, as function of the length (or placement).

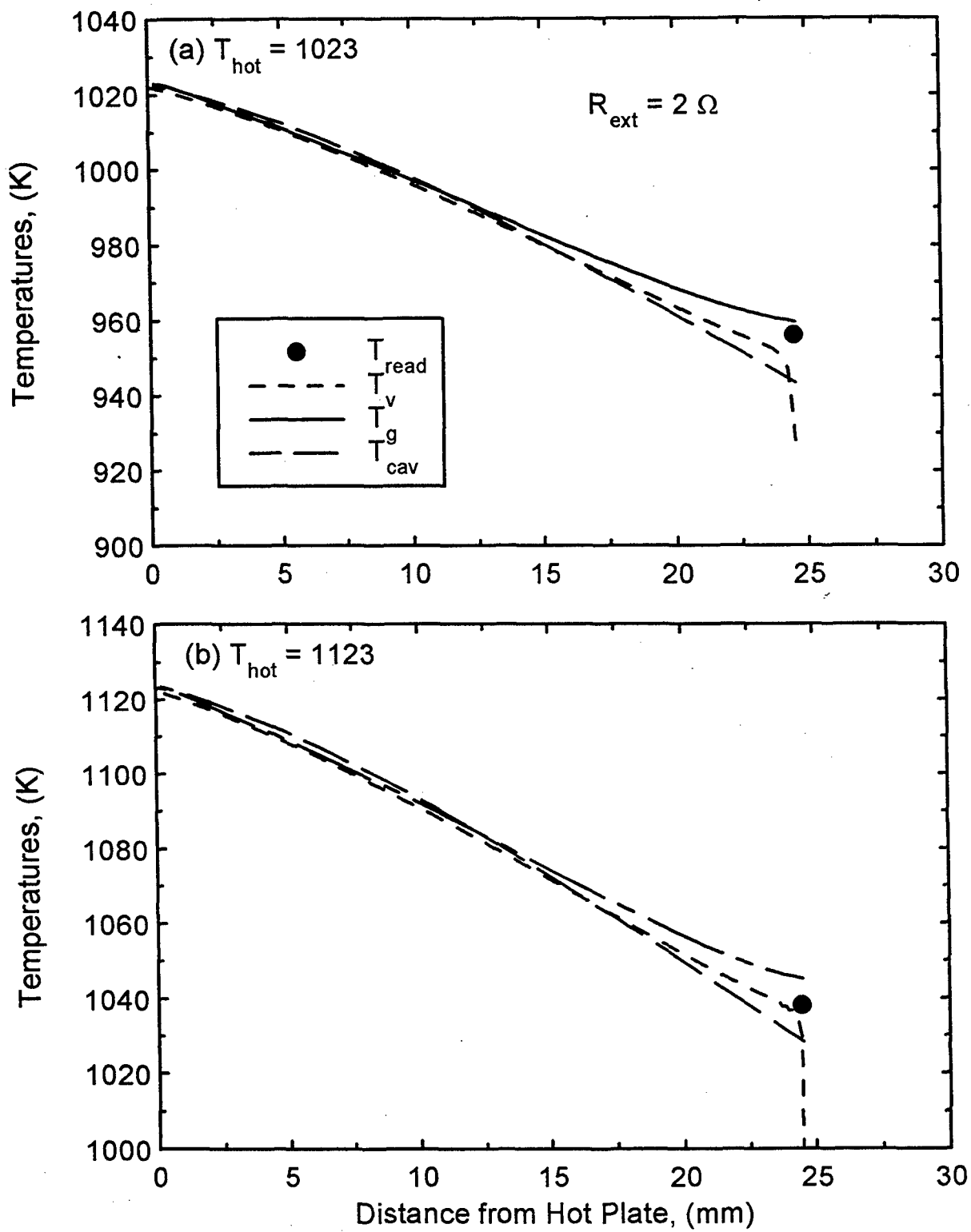


Figure 9.4. Comparison of Predicted and Measured Evaporator Temperatures in PX-5A.

## 9.5 COMPARISON OF FIN MODEL WITH EXPERIMENTAL MEASUREMENTS

Figure 9.4 shows the predicted axial temperature distribution along the guide tube of the TC placed in the evaporator cavity of the PX-5A cell. This figure shows that FIN predictions of the temperatures of the free-standing end of the guide tube was generally in good agreement with the TC readings. At hot plate and condenser temperatures of 1023 and 623 K, respectively, the predicted temperatures were higher than the readings of the evaporator TC, by 2–5 K, depending on the cell electric current (Table 9.2). When the hot plate temperature of the PX-5A cell was increased to 1123 K, the difference between FIN's predictions and TC readings varied from +7 K, at high cell current to -2.2 K at low cell current.

Similar comparisons of the FIN's predictions and the readings in the BASE tube cavity were performed, and results are presented in Figure 9.5 and Table 9.2. The FIN model's predictions were in good agreement with the TC readings. At a hot plate temperature of 1023 K, the difference between FIN's predictions and the readings of the TC in the BASE tube cavity varied from 0.9 K, at low cell current, to 3.1 K, at high cell current. At a higher hot plate temperature of 1123 K, this difference varied from 0.2 to 7 K.

Table 9.2. Comparison of BASE and Evaporator TC Readings and Predictions of APEAM Model and Fin Model for PX-5A.

Load Resistance, [ $\Omega$ ]	0.5	2.0	4.0
(a) $T_{\text{hot}} = 1023 \text{ K}$			
Cell Current (A)	2.05	1.0	0.61
$(T_{\text{read}} - T_{\text{APEAM}})_{\beta} \text{ (K)}$	17	18	18
$(T_{\text{read}} - T_{\text{APEAM}})_{\text{ev}} \text{ (K)}$	4	28	47
$(T_{\text{read}} - T_{\text{fin,tip}})_{\beta} \text{ (K)}$	3.1	6.8	0.9
$(T_{\text{read}} - T_{\text{fin,tip}})_{\text{ev}} \text{ (K)}$	-5.1	-3.5	-2.2
(b) $T_{\text{hot}} = 1123 \text{ K}$			
Cell Current (A)		1.28	0.77
$(T_{\text{read}} - T_{\text{APEAM}})_{\beta} \text{ (K)}$		23	15
$(T_{\text{read}} - T_{\text{APEAM}})_{\text{ev}} \text{ (K)}$		55	77
$(T_{\text{read}} - T_{\text{fin,tip}})_{\beta} \text{ (K)}$		7.0	0.2
$(T_{\text{read}} - T_{\text{fin,tip}})_{\beta} \text{ (K)}$		7.0	0.2
$(T_{\text{read}} - T_{\text{fin,tip}})_{\text{ev}} \text{ (K)}$		-7.1	2.2

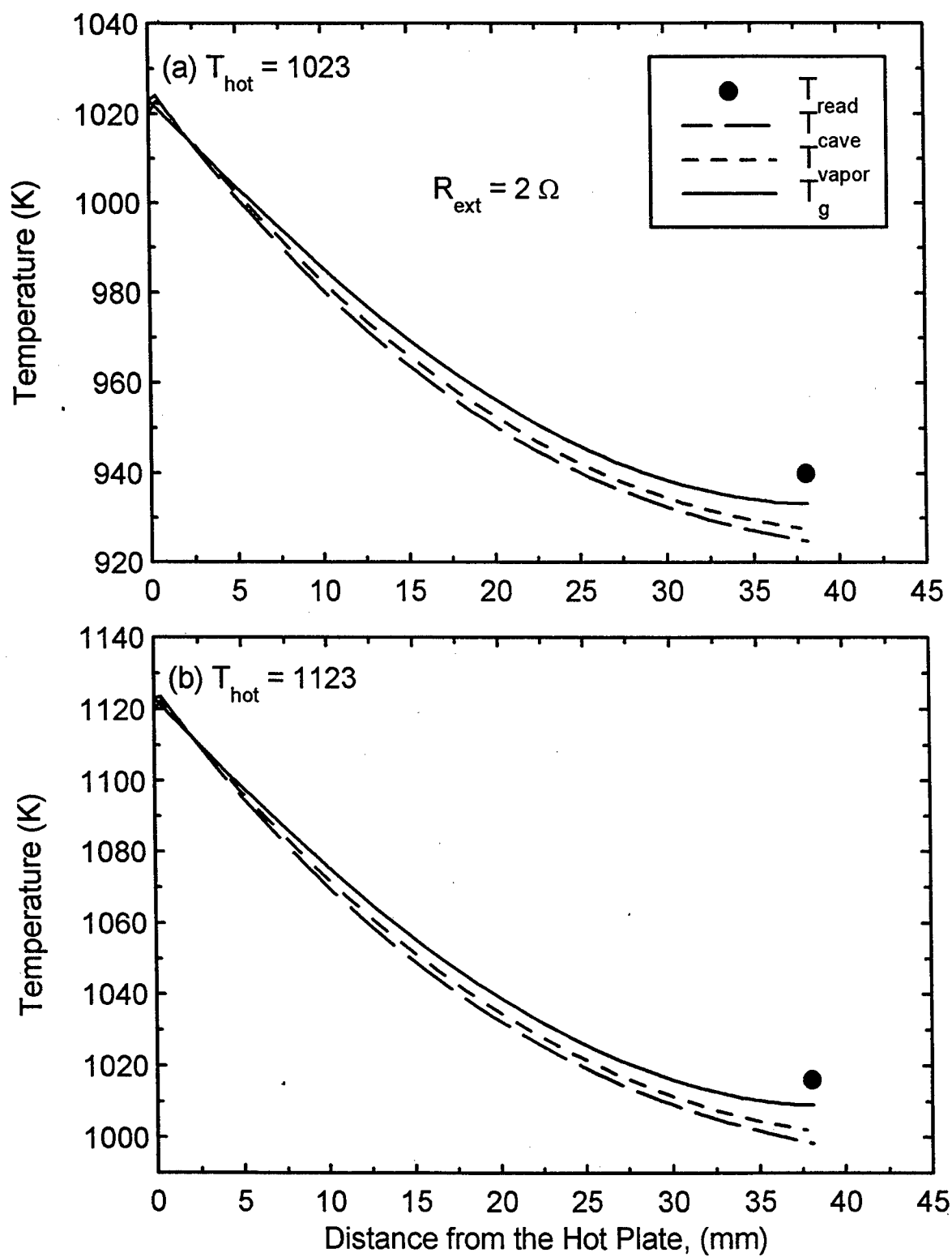


Figure 9.5. Comparison of Predicted and Measured BASE Tube Temperatures in PX-5A.

Figures 9.4 and 9.5 also show that the readings of the TCs in the evaporator and the BASE tube cavities were consistently higher than the BASE tube cold end and evaporator temperatures predicted by APEAM. These predictions were based on the best comparison with the cell electric power values. The evaporator TC readings in PX-5A could have been 4–47 K and 55–77 K, higher than the evaporator temperature, at hot plate temperatures of 1023 and 1123 K, respectively (Table 9.2). Similarly, the BASE tube TC readings were also higher than predicted temperature at the cold end of the BASE tube by as much as 18 K and 23 K, at hot plate temperatures of 1023 and 1123K, respectively. Based on the calculated temperatures of the evaporator and the BASE tube (Chapter 11), at a hot end temperature of 1023 K, the temperature margin in the cell varied from -25 to 4 K, at high and low cell current, respectively. When the hot end temperature increased to 1123K, this temperature margin varied from -21 to 27 K.

## 9.6 EFFECT OF THERMOCOUPLE PLACEMENT

Figure 9.6 shows that increasing the length of the TC guide tube, from 12.7 mm to 38.1 mm, lowered the TC reading, and decreased the difference between it and the predicted evaporator temperature, using FIN, from 12.7 K to only 2 K. Similar results are shown in Figure 7, for the placement of the BASE tube TC. At  $T_{\text{hot}} = 1023$  K, increasing the length of the guide tube of the BASE TC from 12.7 mm to 38.1 mm, decreased the difference between the TC reading and the temperature predicted by FIN from 15 K to 6 K.

## 9.7 SUMMARY AND CONCLUSIONS

The uncertainties associated with the performed measurements in the vacuum tests of the PX-series AMTEC cells were calculated. The experimental measurement uncertainty was the greater of  $\pm 1.1\%$  or 1.7 K in temperature;  $\pm 1.2\%$  in the cell electric power output,  $\pm 0.7\%$  in the heat input,  $\pm 6.2\%$  in air flow rate, and as much as  $\pm 6.5\%$  in heat rejection. Another uncertainty associated with the measurements of the BASE tube and evaporator temperatures in these tests was caused by the placement of the TCs in the respective cavities and the fin effect of the TC guide tubes.

In order to calculate the uncertainty associated with the placement of the TCs in the BASE and evaporator cavities, a heat transfer model was developed. This model coupled heat conduction in the TC guide tube, to forced convection, and thermal radiation to the walls of the evaporator and the BASE tube cavities. The model predictions were in good agreement with the readings of the BASE and evaporator TCs in PX-5A cell. However, the TC readings of the BASE and evaporator temperatures in PX-4C cells were about 15–18 K and 4–47 K, higher, respectively, than what they might have been, depending upon the TC placement, cell electric current, and the hot and cold temperatures in the tests. Results of a parametric analysis indicated that increasing the length of the TC guide tubes for the BASE and evaporator cavities would reduce the readings of the TCs, to be more representative of the actual BASE tube and evaporator temperatures.

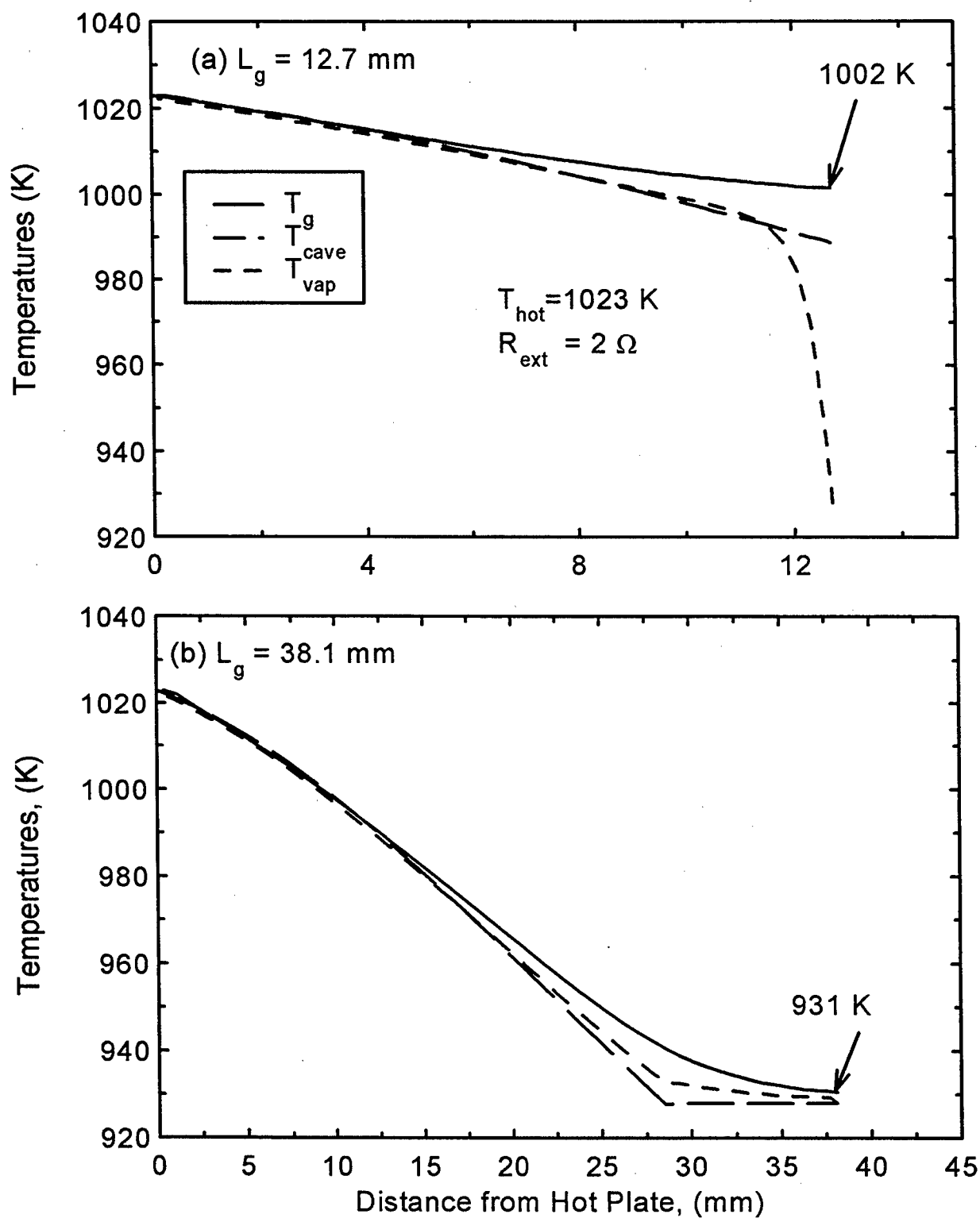


Figure 9.6. Effect of Guide Tube Length in Evaporator of PX-5A.

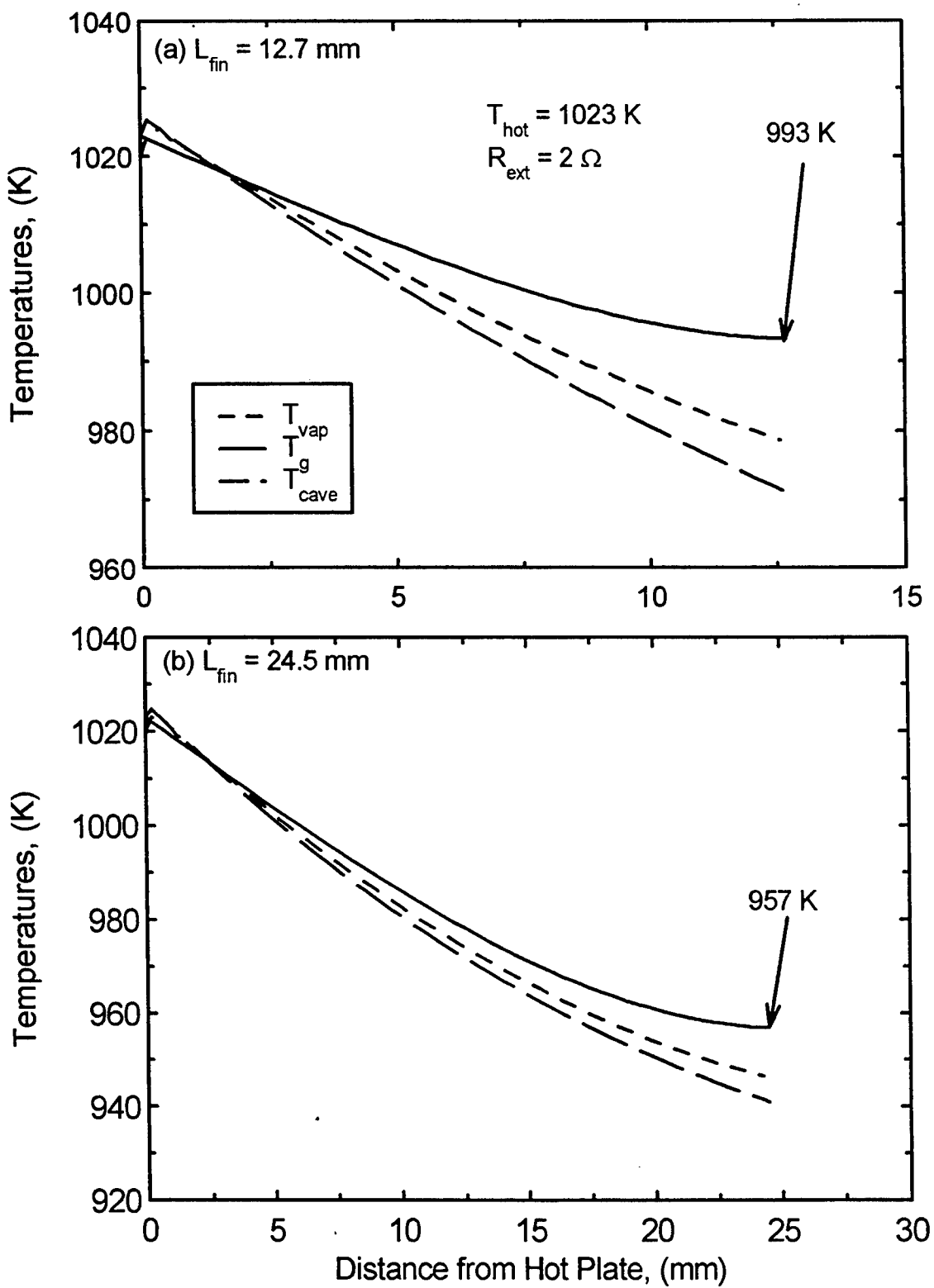


Figure 9.7. Effect of Guide Tube Length in BASE Tube of PX-5A.